IPP-Report

Max-Planck-Institut für Plasmaphysik

David M. Rittich

Quantification of Neutral Beam Driven Current and the effect of radial fast ion transport in ASDEX Upgrade

IPP 2018-24
November 2018

Quantification of Neutral Beam Driven Current and the effect of radial fast ion transport in ASDEX Upgrade

Dissertation

zur Erlangung des Doktorgrades

Dr. rer. nat.

eingereicht an der

Mathematisch-Naturwissenschaftlich-Technischen Fakultät

der Universität Augsburg

von

David M. Rittich

Augsburg, Dezember 2017

Vorgelegt am: 18.12.2017
Tag der mündlichen Prüfung: 19.04.2018

Erste Gutachterin: apl. Prof. Dr.-Ing. U. Fantz
Zweiter Gutachter: apl. Prof. Dr. H. Karl

Contents

1. Introduction

The worldwide energy consumption increases strongly. To illustrate this with a number, the worldwide generation of electricity increased between 1973 and 2014 from 6 131 TW h to 23 816 TW h, an increase of 388% [1]. The main source of electricity generation, with a fraction of 67% in 2014 [1], is combustion of fossil fuels. The combustion of coal, gas and oil produces CO_2, which causes global warming. Furthermore, these fuels are finite and not equally distributed. Therefore alternatives are necessary to replace these fossil energy sources.
Examples for presently used CO_2-free alternatives are nuclear fission, hydroelectric power, photo-voltaic systems and wind turbines. However, all these alternatives have also disadvantages, such as the risk of an uncontrollable fission chain-reaction or the necessity of large storage for weather-dependent renewable energy. Therefore a balanced energy mix of all CO_2-free power plants is advisable.
An attractive future CO_2-free alternative to combustion power plants is the thermonuclear fusion power plant. In this inherently safe system the fusion of hydrogen isotopes to helium is used to produce energy.

1.1. Thermonuclear Fusion

The fusion process is well-known from the sun. In the sun hydrogen is fused to helium in the proton-proton reaction chain. The main reaction chain is

$$\begin{aligned} {}^1_1\mathrm{H} + {}^1_1\mathrm{H} &\rightarrow {}^2_1\mathrm{D} + e^+ + \nu_e + 0.42\,\mathrm{MeV} \\ {}^2_1\mathrm{D} + {}^1_1\mathrm{H} &\rightarrow {}^3_2\mathrm{He} + \gamma + 5.493\,\mathrm{MeV} \\ {}^3_2\mathrm{He} + {}^3_2\mathrm{He} &\rightarrow {}^4_2\mathrm{He} + 2{}^1_1\mathrm{H} + 12.86\,\mathrm{MeV}. \end{aligned} \tag{1.1}$$

The energy produced at the different reaction steps is a consequence of the mass defect. The equivalence of mass and energy was first formulated by Albert Einstein [2] and is given by

$$E = mc^2 \tag{1.2}$$

with the energy E, the mass m and the speed of light c.
The conversion of a proton to a neutron in the first step of the shown reaction chain is a process of the weak interaction and has therefore a very small cross section. In the sun this small reactivity is compensated by the enormous pressure resulting from the high gravitational force. On earth such pressures cannot be sustained for sufficiently long times in

reasonably sized volumes, therefore this reaction chain is not suitable for a fusion power plant.
To avoid the process of the weak interaction, the protons are replaced by the two hydrogen isotopes deuterium and tritium, which already contain the necessary neutrons for the reaction. The resulting fusion reaction is

$$ {}^{2}_{1}\mathrm{D} + {}^{3}_{1}\mathrm{T} \rightarrow {}^{5}_{2}\mathrm{He}^{*} \rightarrow {}^{4}_{2}\mathrm{He} + {}^{1}_{0}\mathrm{n} + 17.6\,\mathrm{MeV} \tag{1.3} $$

with a reaction probability which is 10^{21} times higher than that of to the proton-proton reaction chain. The isotope deuterium is naturally available on earth, as 0.0115% of the hydrogen in water is deuterium. In contrast, the unstable tritium with a half life of 12.3 years exists only in negligible amounts (worldwide $\sim 3.5\,\mathrm{kg}$). Using the neutrons from the fusion reaction it can be bred from the stable element lithium, following

$$ \begin{aligned} {}^{6}_{3}\mathrm{Li} + {}^{1}_{0}\mathrm{n} &\rightarrow {}^{4}_{2}\mathrm{He} + {}^{3}_{1}\mathrm{T} + 4.8\,\mathrm{MeV} \\ {}^{7}_{3}\mathrm{Li} + {}^{1}_{0}\mathrm{n} &\rightarrow {}^{4}_{2}\mathrm{He} + {}^{3}_{1}\mathrm{T} + {}^{1}_{0}\mathrm{n'} - 2.5\,\mathrm{MeV}. \end{aligned} \tag{1.4} $$

The breeding of the tritium in the fusion power plant allows to keep the radioactive inventory of tritium small. The product of the fusion reaction, helium, is stable and not hazardous. Furthermore, deuterium and lithium are more or less equally distributed on earth and are close to infinitely available.
For the fusion reaction the Coulomb barrier of the positively charged nuclei must be overcome. This could be done in particle accelerators, but a net energy production is impossible due to the high power demand of the accelerator itself and the high losses due to the dominance of Coulomb scattering events without a fusion reaction. Instead of using directed bombardment of a tritium target with deuterium, a confined high temperature plasma is used in which the continuous collisions between the thermal ions provide a sufficient fusion rate. In combination with a high density of the reactants the reaction probability becomes high enough for a self sustaining fusion process. Taking also energy losses into account a threshold for a self sustaining fusion reaction can be formulated. This threshold is called the Lawson criterion [3]

$$ nT\tau_{\mathrm{E}} \geq 5 \cdot 10^{21}\,\mathrm{keV\,s\,m^{-3}} \tag{1.5} $$

with the density n, the temperature T and the energy confinement time τ_{E}, the characteristic energy transport time scale. The energy confinement time is defined as the ratio of the stored energy and the heating power.
As the cross section of the D-T-fusion reaction is strongly energy, and accordingly temperature dependent, the highest reactivity, assumed in the formulation of the Lawson criterion in equation (1.5), is reached at $T \approx 70\,\mathrm{keV}$.
Such high temperatures are not compatible with wall contact in a plasma chamber. Therefore a confinement concept is needed that avoids wall contact of the high temperature bulk plasma. Two concepts of confinement are commonly established, magnetic confinement, that this thesis deals with, and inertial confinement fusion. In the inertial confinement the Lawson criterion is fulfilled for a short time ($\approx$ ns) by a high power laser pulse where the confinement is achieved through the inertia of the reactants. Details can be found in

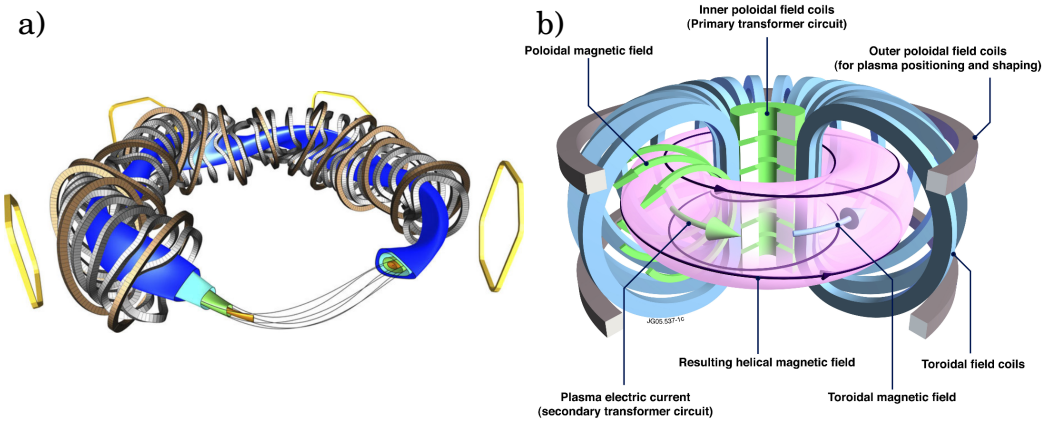

Figure 1.1.: Two concepts for the magnetic confinement. In a) the current free Stellarator and in b) the axisymmetric Tokamak. The pictures are adapted from the references [5, 6].

reference [4].
In magnetic confinement, magnetic fields are used to confine the charged plasma particles by the Lorentz force. As linear devices, for example with a magnetic mirror configuration, lead to insurmountable losses at the end plates a toroidal device is needed. However, in a pure toroidal magnetic field the field strength is proportional to $1/R$, with R the distance to the center of the torus, and this magnetic field gradient would lead to a drift of the charged particles in the plasma. This drift forces charge separation and prevents confinement of the plasma. A helical magnetic field is the solution for this problem. The two most promising concepts for the magnetic confinement are the Stellarator and the Tokamak, shown in figure 1.1.
In the Stellarator the helicity of the field is entirely created by the external coils that have a complicated, non-planar shape, which can be seen in figure 1.1 a). The magnetic field intrinsically enables steady state operation. However, the manufacturing of the optimized coils with the necessary precision is challenging and expensive. Details on the Stellarator concept can be found in reference [7].
In the Tokamak the coil configuration is axisymmetric. The resulting toroidal magnetic field is indicated by the blue arrow in figure 1.1 b). To form the necessary helical magnetic field, a poloidal magnetic field is superimposed which is created by a current in the plasma. Commonly this current is driven using the transformer principle with a central solenoid as primary coil and the plasma as secondary circuit. As the direct current induction requires a constant sign of the time derivative of the magnetic flux enclosed by the secondary circuit the time of inductive current drive is limited. As a consequence the Tokamak with inductive current drive can only be used in pulsed operation.
In a future fusion power plant the main objective is the economically efficient, continuous electricity production. Therefore pulsed operation like in a conventional Tokamak scenario has the disadvantages that a large energy storage is needed to buffer the down times and the mean output power is reduced in comparison with the peak fusion power. Furthermore, thermal cycling due to the pulsed operation leads to fatigue, which decreases the lifetime

of the power plant and increases the maintenance costs. To mitigate these problems, an increase of the duty cycle by extension of the pulse length is desirable. The optimum is infinite pulse duration, rendering energy storage dispensable and reducing the number of thermal cycles to a minimum, determined only by maintenance breaks.
In order to achieve long pulses the inductively driven current has to be replaced as much as possible by non-inductively driven current. The commonly used non-inductive driven currents are the intrinsic bootstrap current (BS), the neutral beam driven current (NBCD) and the electron cyclotron driven current (ECCD).
The BS is a consequence of the helical magnetic field in combination with a pressure gradient.
The electron cyclotron driven current can be actively controlled by tangential injection of electromagnetic waves at the electron cyclotron resonance frequency. Due to the Doppler shift electrons moving in a preferential direction gain more energy with respect to electrons moving in the opposite direction. This asymmetry leads to the driven current.
The neutral beam driven current can also be actively controlled and is a consequence of tangential injection of energetic neutral particles ($\sim 10 - 1000\,\mathrm{keV}$). After entering the plasma the particles are ionized and circulate several thousand times around the torus in a preferential direction until their thermalization. These supra thermal ions, also called fast ions, drag along some electrons from the bulk plasma leading to an electron shielding current. However, there are some electrons trapped, due to the magnetic field configuration, which can not participate to the shielding current. Beside ohter factors this complicates the calculation of the NBCD.

1.2. This Thesis

For the development of a plasma scenario for a Tokamak fusion power plant a valid quantitative neutral beam current drive (NBCD) model is necessary. Also for multiple scenarios of the Tokamak ITER (the Latin word for "The Way") [8–10], the next, large, international fusion experiment, which is in the construction phase, a large NBCD fraction is foreseen.
Therefore, experiments and quantitative comparisons with the common NBCD model are made. The experimental environment for this thesis, ASDEX Upgrade (chapter 3), is a medium size Tokamak with a very similar shape as ITER and $\sim 1/4$ of its size [11]. ASDEX Upgrade with its versatile neutral beam injection system and large diagnostic capability is well suited for studies of the NBCD.
The neutral beam driven current, like the other single contributions to the total plasma current, is not directly measurable. Therefore two strategies are used to investigate the NBCD. On the one hand for quantitative investigations of the total neutral beam driven current the reliably measurable total plasma current is compared with the sum of the reconstructed contributions. On the other hand the changes in the measured plasma current profile due to changes in the neutral beam injection are examined.

An issue for the quantitative approach are large uncertainties in the reconstruction of the inductive current. This hampers a reliable quantitative assumptions on the current composition. Therefore quantitative investigation of the non-inductive contributions are done in discharges with maximized neutral beam driven and bootstrap current fraction leading to an almost vanishing inductive current fraction (see chapter 7).
The changes in the total plasma current profile due to changes in the neutral beam injection had been examined in previous studies. At various fusion experiments the radial distribution of the neutral beam driven current and the fast ion distribution, carrying the current, had been investigated and in some cases deviations from the common description of the fast ion dynamics in the plasma, were found [12–16]. In other cases the measurements were in agreement with the common models [17, 18]. This apparent discrepancy raised the question if the commonly used neutral beam current drive model is correct.
This contradiction was also seen at the Tokamak ASDEX Upgrade. In two comparable discharges on the one hand the changes of the radial current profile were investigated and on the other hand the radial fast ion density was examined. While the measured radial fast ion distribution corresponded to the expectation, the changes in the radial current profile, carried by the fast ions, deviated from the common theory.
To investigate this apparent discrepancy experiments are made where, for the first time, the radial fast ion distribution and the radial current profile are measured simultaneously. The main diagnostic to gain information on local changes of the current profile is the motional Stark effect polarimetry (MSE). For example, these current profile changes could be forced due to a change of the neutral beam injection geometry. To increase the accuracy and reliability of the current profile reconstruction the MSE is absolutely calibrated (see chapter 4).
The information on the radial fast ion profile are gained by the fast ion D-alpha spectroscopy (FIDA) (section 3.3.8). With multiple lines of sight at different radial positions the local fast ion phase space is measured.
The transport code TRANSP, with its fast-ion module NUBEAM, (chapter 5) is used to examine various physical models. The output of the code is used to calculate synthetic diagnostics for comparison with measurements. The code is commonly used to calculate NBCD in many Tokamaks.

2. Theoretical Background

2.1. Magnetic Confinement

For a self sustaining burning fusion plasma the Lawson criterion equation (1.5) must be fulfilled. Therefore a hot and dense plasma needs to be confined, but on the one hand due to the high temperatures in the order of 100 keV no materials are and will be available that tolerate wall contact. On the other hand a plasma with wall contact would have large energy losses towards the wall and reasonable energy confinement and high temperatures would not be possible. The magnetic confinement avoids the wall contact by a magnetic field. The Lorentz force

$$\vec{F} = q(\vec{E} + \vec{v} \times \vec{B}) \tag{2.1}$$

is used to confine the plasma, which is composed of free charged particles. Due to the Lorentz force the plasma ions and electrons are bound to the magnetic field lines. For stable conditions the magnetic force must balance the force resulting from pressure gradients in the plasma

$$\vec{j} \times \vec{B} = \nabla p \tag{2.2}$$

with $\vec{j}$ the plasma current, $\vec{B}$ the magnetic field confining the plasma and p the kinetic pressure.
The confined electrons and ions are able to move along the field lines with velocities corresponding to their temperature, but the transport perpendicular to the field lines is strongly reduced. To avoid uncontrollable losses especially of fast ions and electrons at the ends of a linear magnetic system, the magnetic field is toroidal. However, in such an axisymmetric toroidal system, the field strength decreases with increasing radius R from the torus' axis. Together with the resulting curvature, this would lead to an unstable configuration due to charge separation by the curvature and the $\nabla\vec{B}$ drift. The resulting vertical electric field $\vec{E}$ in combination with toroidal magnetic field $\vec{B}$ leads to a further outwards directed $\vec{E} \times \vec{B}$ drift, explained in detail in the next section. To overcome this problem, the upper and lower half of the torus needs to be shortcut and therefore helical magnetic field lines are necessary. Regarding this demand two concepts for the magnetic confinement are established, the Tokamak and the Stellarator. In the Stellarator the helical field is realized by complex 3D magnetic field coils. A motivation and description of the concept can be found in reference [7]. As the experimental work of this thesis is done in an axisymetric Tokamak, only this second concept is explained in detail.
In the Tokamak concept the toroidal field is created by planar coils, whereas the poloidal field is created mostly by externally driven plasma current. This helical twist leads to field lines that circle the magnetic axis poloidally while going around the torus toroidally. Each

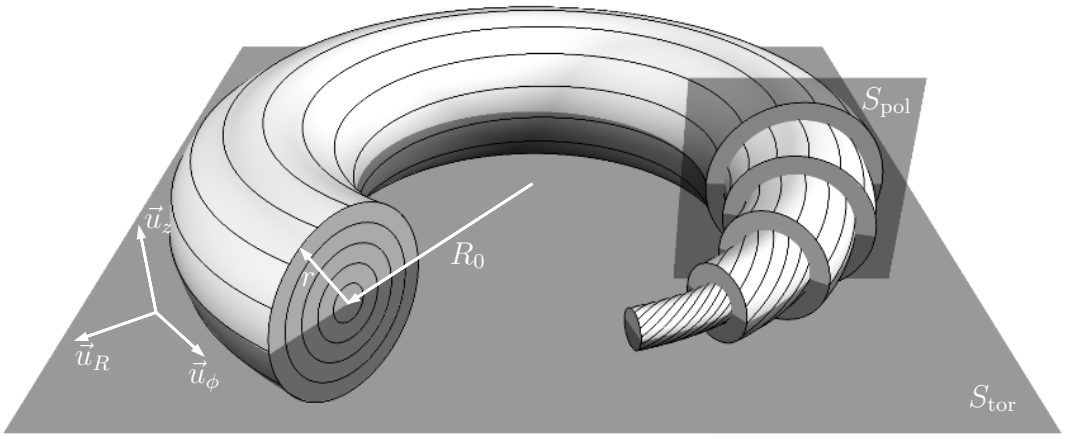

Figure 2.1.: Schematic of a circular plasma with five generic nested flux surfaces. On the flux surfaces the corresponding helical magnetic field lines can be seen. The figure is adapted from reference [19].

field line defines a surface, called flux surface. The flux surfaces are nested and each flux surface can be identified by the magnetic flux it encloses. In figure 2.1 five generic flux surfaces and the helical field lines on these flux surfaces are shown. Due to the fact that only the radial transport is strongly reduced and the velocities of the particles along the field lines are very high, an almost instantaneous equilibration of several plasma parameters such as temperature and density on a flux surface can be assumed.
For the case of a circular plasma, the relevant geometrical parameters are also shown in figure 2.1. The major radius R_0, the minor radius r and the direction vectors. Instead of a cartesian coordinate system one commonly uses a cylindrical system with the toroidal angle ϕ, the radius R and the vertical coordinate z. Due to axisymmetry most phenomena can be described two-dimensionally in the poloidal plane S_{pol} with the coordinates R and z. The magnetic field structure resulting from an equilibrium between the pressure and the poloidal magnetic flux in the poloidal plane is given by the Grad-Shafranov equation

$$\begin{aligned} -\Delta^*\psi &= \mu_0 R^2 \frac{\partial p}{\partial \psi} + f\frac{\partial f}{\partial \psi} \\ &= \mu_0 R^2 p'(\psi) + f f'(\psi) = \mu_0 R j_{\mathrm{tor}}. \end{aligned} \tag{2.3}$$

The Grad-Shafranov equation cannot generally be solved analytically. However, the solution of the Grad-Shafranov equation represent the magnetic field structure used as the natural coordinate system for multiple plasma quantities. An approach to solve the Grad-Shafranov equation to reconstruct the equilibrium is outlined in section 2.1.1. Here only the different terms are explained.
The term $\Delta^*\psi$ is the Stokes operator in cylindrical coordinates acting on the poloidal flux function. The poloidal flux function ψ is a 2D scalar field of all magnetic flux contributions. From the poloidal flux the magnetic field components in the poloidal plane can be calculated

by

$$B_R = -\frac{1}{2\pi R}\frac{\partial \psi(R,z)}{\partial z}$$
$$B_z = \frac{1}{2\pi R}\frac{\partial \psi(R,z)}{\partial R}. \tag{2.4}$$

The magnetic flux is measured externally by coils installed close to the plasma with different orientations. However, the coils can only measure the integral of the intersected flux. Nevertheless, for the numerical solution of the Grad-Shafranov equation these measurements are the main input.
The pressure gradient p' is the second term in the Grad-Shafranov equation. The pressure as well as its gradient are flux surface quantities, i.e. constant on a flux surface. The pressure is the product of individually measured density and temperature profiles. These measurements are also used to constrain the equilibrium, the solution of the Grad-Shafranov equation.
The poloidal current flux function $f = RB_{\text{tor}}$ with its gradient f' is the third and last term. This flux surface quantity describes the contribution of all poloidal currents. These currents are also measured integrally by magnetic coils surrounding the plasma and the vacuum vessel.
The solution of the Grad-Shafranov equation needs to be self-consistent in all three quantities and it describes the nested flux surfaces shown in figure 2.1.
The common plasma shape in today's Tokamaks, planed fusion experiments and also used in this thesis is the divertor configuration. Instead of the limiter configuration, where the last closed flux surface is defined by the intersection of field lines by a material object, scraping off the outermost flux surface, the divertor configuration uses magnetic fields from poloidal coils to form a separatrix. This last close flux surface forms at least one x-point and in the new areas this flux surface is directed onto panels. Over the separatrix energy and particles are transport out of the plasma. The advantage of this configuration is only a small wall contact leading to less impurity influx and a better confinement.
The solution of the Grad-Shafranov equation describe this plasma shape and can be used as natural coordinate system. Several plasma parameters, like the electron temperature or electron density, are flux surface quantities, but due to the fact that plasma is usually not circular, the minor radius is no suitable choice for the radial coordinate. However, instead the normalized magnetic flux of the flux surfaces can be used as defined by

$$\Psi_{\text{N}} = \frac{\psi - \psi_{\text{axis}}}{\psi_{\text{separatrix}} - \psi_{\text{axis}}}$$
$$\rho_{\text{pol}} = \sqrt{\Psi_{\text{N}}} \tag{2.5}$$

with Ψ_{N} the normalized flux and ρ_{pol} the radial coordinate.
Analogously, a toroidal flux coordinate ρ_{tor} can be defined, using the toroidal flux ϕ. However, the definition of the toroidal flux requires closed flux surfaces and it is therefore only defined inside the last closed flux surface, the last closed flux surface. However, ρ_{tor} does not depend on the toroidal current and is therefore more robust in the center, whereas ρ_{pol} is mostly used to describe edge phenomena, because it can be extended beyond the last

closed flux surface. Due to the fact that the studies in this thesis are related to the plasma center, ρ_{tor} is mostly used as coordinate.
One important flux surface quantity and figure of merit for the confinement is β. This quantity is given by the ratio of the average thermal pressure inside the surface and the magnetic pressure

$$\beta = \frac{\langle p \rangle}{B^2/2\mu_0}. \tag{2.6}$$

The magnetic field at the axis is represented by B. Also common is the normalization only to the poloidal magnetic field B_{pol} at the edge leading to the quantity β_{pol}. The value β is typically in the order of single percent, however it is typically given without the percentage symbol, for example $\beta = 2.5$ for 2.5%.
A further important flux surface quantity is the safety factor

$$q = -\frac{d\phi}{d\psi} \approx \frac{r}{R}\frac{B_{tor}}{B_{pol}}. \tag{2.7}$$

The safety factor represents the helicity of the field lines on a flux surface. It can be paraphrased with the number of toroidal turns per poloidal turn and is an important parameter for the stability of the plasma. Furthermore the $q = 1$ surface and the surfaces with rational q are of special interest, because field lines close on themselves after a small number of toroidal turns. A initial perturbation on such field lines can lead to the grow of instabilities. Some of those instabilities are discussed in section 2.5.

2.1.1. Equilibrium Reconstruction

The Grad-Shafranov equation, defined in the 2D poloidal plane, is not generally analytically solvable. Therefore a set of consistent ψ, $p'(\psi)$ and $ff'(\psi)$ is approximated on basis of several measured quantities. The most important measurements are the kinetic profiles and the magnetic flux measurement from poloidally, toroidally and radially oriented magnetic field probes outside the plasma.
In interpretive equilibrium reconstruction all input measurements are connected with their corresponding equilibrium quantities, for example the density measurement is used to constrain the pressure profile. In an iterative process, using Picard iterations [20, 21] and the χ^2-minimization process, a self-consistent set of ψ, $p'(\psi)$ and $ff'(\psi)$ is calculated. To deal with this underdetermined system, regularizations need to be applied. With less measurement constraints these regularizations become more important. The regularizations drive the iterative process towards a smooth and plain solution, but the regularizations are not based on a physical model or measurement. Therefore a solution constrained by measurements or physical models leads to a more accurate solution.
Within this thesis the ASDEX Upgrade equilibrium reconstruction codes CLISTE [22] and integrated data equilibrium (IDE) [23] are used.
A routinely written CLISTE equilibrium, available within minutes after the experiment, only takes the measurements of the magnetic probes into account. This equilibrium is available rapidly, but due to the increasing uncertainty of the magnetic measurements towards

the plasma center this equilibrium is not completely reliable. Especially the position of the magnetic axis is inaccurate in the range of cm, needed is $< 1\,\mathrm{cm}$. For example the Shafranov shift, the pressure induced radial shift of the magnetic axis, cannot be resolved.
In this thesis equilibria, the natural coordinate system of the plasma, are used that are calculated on the basis of a larger set of input data. Although CLISTE is in principle able to handle this task, the integrated data analysis equilibrium solver IDE was used in this thesis. To reduce the regularization, the standard equilibrium reconstruction with the IDE code takes, beside the kinetic profiles and magnetic measurements, also the current diffusion into account. This enables smoothing in time that is based on a physical model and replaces a part of the regularization. The current diffusion equation (CDE) is given by

$$\sigma_{\parallel}\frac{\partial\psi}{\partial t} = \frac{R_0 J^2}{\mu_0\rho_{\mathrm{tor}}}\frac{\partial}{\partial\rho_{\mathrm{tor}}}\left(\frac{G_2}{J}\frac{\partial\psi}{\partial\rho_{\mathrm{tor}}}\right) - \frac{V'}{2\pi\rho_{\mathrm{tor}}}\left(j_{\mathrm{bs}} + j_{\mathrm{CD}}\right) \tag{2.8}$$

with $\sigma_{\parallel}$ the parallel conductivity, J the poloidal currents, G_2 and V' geometry parameters of the flux surfaces, j_{bs} the bootstrap current density (see section 2.4.4) and j_{CD} the external non-inductively driven current density. The external non-inductive current contributions are the electron cyclotron driven current (see section 2.4.3, calculated with TORBEAM and implemented within IDE) and the NBCD (see section 2.4.2, the NBCD together with the fast ion pressure is calculated using TRANSP (introduced in section 5.1)).
A detailed description of the current diffusion equation can be found in reference [24] and the use in the IDE equilibrium reconstruction code is described in reference [23].
A further improvement of the equilibrium reconstruction with either IDE or CLISTE is possible by taking measurements into account that depend on the central current profile. The two available diagnostics at ASDEX Upgrade that are suitable for this purpose are the MSE (see chapter 4) and the Faraday rotation polarimetry (see section 3.3.3). Their inclusion strongly reduces the uncertainties of the reconstructed central q profile.
Figure 2.2 compares different equilibria reconstructed for the same discharge. Figure 2.2 a) and b) show the strong reduction of the uncertainties on the q profile and the current profile by taking the current diffusion equation and motional Stark effect measurements into account. Furthermore in c) the nested flux surfaces in a poloidal cut can be seen. At the separatrix all equilibria are equal, because the uncertainties on the magnetic measurements are small, but closer to the plasma center the deviations increase.

2.2. Transport

In the following section the motion of single charged particles in the magnetized plasma is discussed, beginning with the neoclassical transport, i.e. the radial transport derived from the particle orbits in a toroidal magnetic field. The strong underestimation of the measured radial transport by the neoclassical prediction makes an extension of the transport theory by turbulent transport necessary.

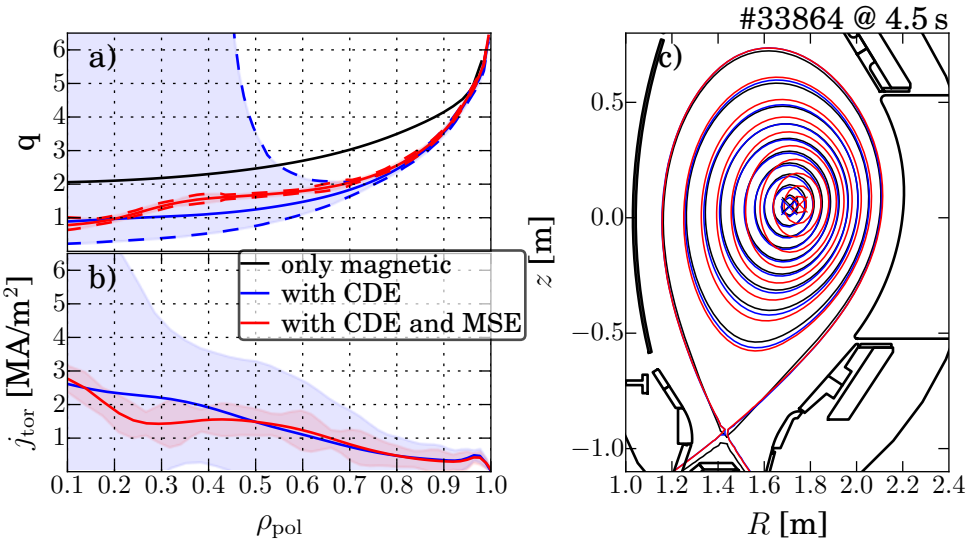

Figure 2.2.: Comparison of equilibria. Shown in black is the (Cliste) equilibrium only using magnetics, in blue the one additionally using the current diffusion equation (CDE) and the kinetic profiles and finally in red the equilibrium also constrain by the MSE measurement can be seen. In a) the reconstructed safety factor q and in b) the plasma current profile, for the equilibria using the CDE, is shown. In c) the flux surfaces for the different equilibria are compared.

2.2.1. Neoclassical Transport

The neoclassical transport theory is based on the ideal motion of charged particles in a magnetic field with a $1/R$ dependence due to the toroidal structure. A detailed description of the neoclassical transport can be found in references [3, 25, 26].
In this section the focus is on fast ions, as their orbits are larger and therefore easier to visualize, but the assumptions are also valid for thermal ions and electrons, where the different sign of the charge and the strongly reduced mass must be taken into account.
The charged particles are confined via the magnetic field by the Lorentz force. The particles gyrate around the field lines with the Larmor radius

$$\rho_{\mathrm{L}} = \frac{v_{\perp}}{\omega_{\mathrm{c}}} \tag{2.9}$$

with $v_{\perp}$ their velocity perpendicular to the field lines and ω_{c} the cyclotron frequency

$$\omega_{\mathrm{c}} = \frac{qB}{m} \tag{2.10}$$

with q the charge, B the magnetic field strength and m the particle mass. For fast deuterium ions and a magnetic field of 2.5 T $\omega_{\mathrm{c}} \approx 120$ MHz. With an injection energy of 60 keV the maximum Larmor radius is $\rho_{\mathrm{L}} \approx 2$ cm, if the velocity is perpendicular to the field lines.
The further motion of the gyrating fast ions can be understood using two constants of

motion. The first, an adiabatic invariant, is the magnetic moment from the gyromotion

$$\mu = \frac{m v_\perp^2}{2B} = \text{const} \tag{2.11}$$

connecting the local magnetic field B with the perpendicular velocity $v_\perp$.
The second constant of motion is the energy

$$E = \frac{m}{2}(v_\parallel^2 + v_\perp^2) = \text{const} \tag{2.12}$$

coupling the parallel $v_\parallel$ and perpendicular $v_\perp$ velocity. Due to the helical magnetic field and the $1/R$ dependence of the toroidal magnetic field, as follows from Ampere's circuital law, the strength of the magnetic field changes continuously along the field line. Therefore the perpendicular velocity of the fast particle must change. To fulfill the energy conservation the perpendicular velocity needs to be converted into parallel velocity at decreasing magnetic field and vice versa at an increasing magnetic field.
For a given ratio of $v_\parallel/v_\perp$ there is a maximum relative increase in field strength where $v_\parallel$ becomes zero. This is the mirror condition defined by

$$\frac{v_\parallel^2(R_0 + r)}{v_\perp^2(R_0 + r)} < \frac{B_{\max}}{B_{\min}} - 1, \tag{2.13}$$

with R_0 the major radius from the center of the torus to the axis and r the local minor radius with respect to the plasma axis. This condition divides the particles in two groups, trapped particle that fulfill the mirror condition and passing particle that do not. For trapped particles two mirror positions exist where all energy is in perpendicular velocity. After reaching one of the mirror point the particle is accelerated again in opposite toroidal direction. In contrast, passing particles always continue to move (anti-) parallel to the field lines in the same direction.
For a full understanding of the orbit, particle drifts need to be introduced. Generally an additional force $\vec{F}$ that is not parallel to the magnetic field, leads to a drift of charged particles perpendicular to the force and the magnetic field direction

$$\vec{v}_{\mathrm{D}} = \frac{\vec{F} \times \vec{B}}{qB^2} \tag{2.14}$$

which is a result of periodically varying gyro radii. To describe the neoclassical fast ion movement, the centrifugal force and $\nabla\vec{B}$ force are the important forces. As they point into the same direction, both drifts, the curvature drift and the $\nabla\vec{B}$ drift, can be formulated together as following

$$\vec{v}_{\mathrm{D}} = \frac{m}{qB^3}\left(v_\parallel^2 + 0.5 v_\perp^2\right)\vec{B} \times \nabla\vec{B}. \tag{2.15}$$

The superposition of the gyromotion with the drift velocity leads to the different orbits for passing and trapped fast ions shown in figure 2.3.
For the passing fast ion in the top row in blue as well as for the trapped particle in the bottom row in red, a 100 keV deuterium ion was implanted at the same position into a

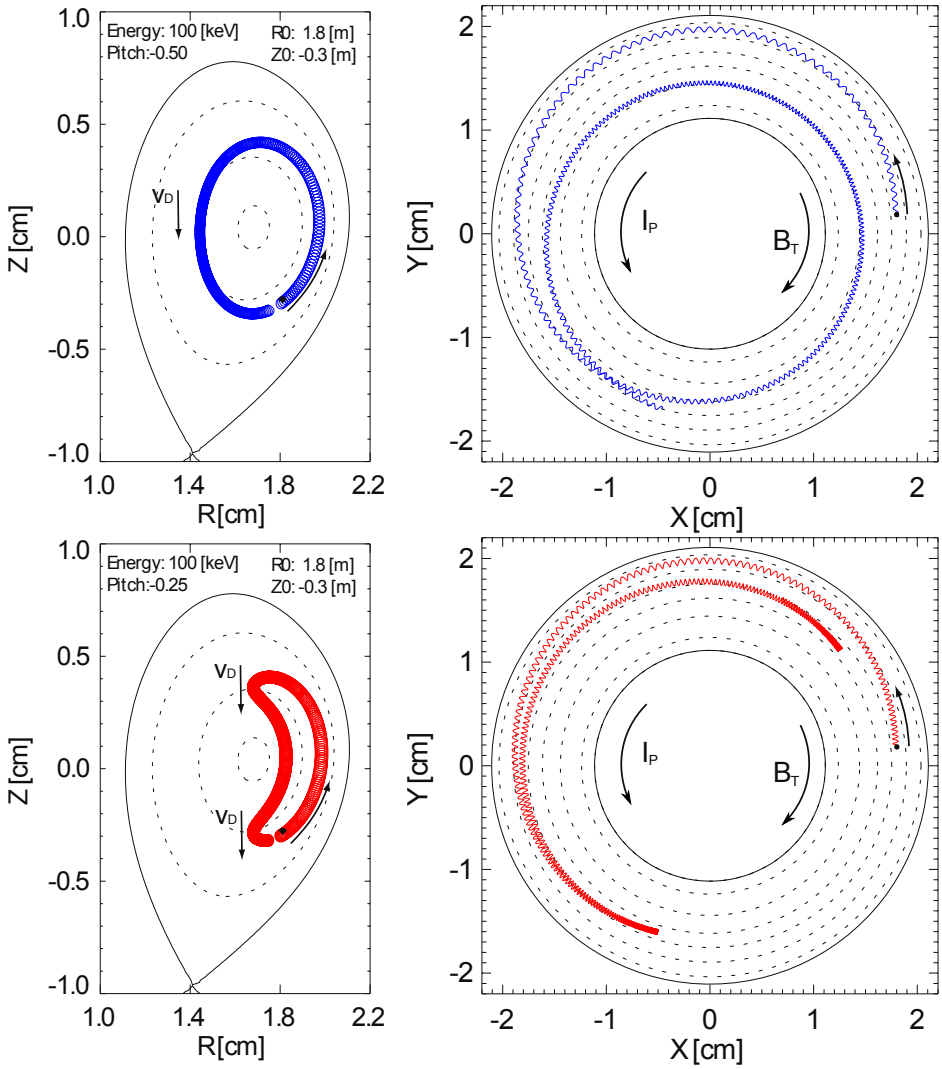

Figure 2.3.: Poloidal and top-down view on orbits of fast ions. In the top row in blue for orbits of a passing and in red in the bottom row for a trapped fast ion. The figures are adapted from reference [17]. The shown trajectories are calculated with the full orbit code GOURDON [27].

ASDEX Upgrade plasma. For the calculation of the orbits only the initial pitch angle is changed. The pitch angle is defined as

$$\xi = \frac{v_\parallel}{v_{\text{tot}}} \tag{2.16}$$

where $v_{\text{tot}} = \sqrt{v_\parallel^2 + v_\perp^2}$ is the total velocity of the fast ion.
The passing fast ion follows almost a field line and in the case shown in figure 2.3 in the top row revolves almost two times toroidally in co-current direction during one poloidal turn. The fast ion does not completely follow the field line, as the drift velocity displaces the orbit slightly, shown in the poloidal view, with the field lines as dashed lines. Fortunately the drift is at the top of the plasma towards the plasma center and in the bottom part in the opposite direction. Therefore the so called drift surfaces are only shifted with respect to the field lines.
In the bottom row of figure 2.3 the orbit of a trapped fast ion can be seen. Due to the reduced initial parallel velocity the particle fulfills the mirror condition. Before entering the high field side, defined by a radius smaller than the radius of the magnetic axis, the parallel velocity component vanishes. The fast ion bounces back and the parallel velocity increases again with the opposite sign. This can be seen in the top-down view in the lower right figure. Furthermore, due to the small parallel velocity, at both mirror positions the downwards drift of the fast ion is pronounced. After reaching the top mirror position, the particle moves into the counter current direction, but due to the drift closer to the center of the plasma. At the bottom mirror position the particle drifts again downwards, this time away from the center. A look at the projection of the trajectory in the poloidal plane gives these orbits their name: the banana orbit.

The movement along the orbits described above would not lead to a radial transport of particle and energy. In the classical theory this transport is a result of collisions between particles. This transport can be described by a random-walk diffusion model with the diffusion coefficient

$$D_{\text{classical}} = \frac{(\Delta x)^2}{\Delta t} \tag{2.17}$$

with Δx the typical scale length of the plasma, in this case the Larmor radius ($\Delta x = \rho_{\text{L}}$), and Δt the collision time, which is the average time between two 90° direction changing collisions.
Taking also the neoclassical orbits into account this diffusion coefficients strongly increases, depending on the collisionality ε. The collisionality is the reciprocal of the collision time, the time the trajectory of a particle undergoes a change of direction of 90° due to Coulomb interactions with typically small angle scattering events. Three different transport regimes were found. The banana regime, with low collisionality. In this regime the particle complete their orbit in less than the collision time. In the random-walk diffusion model the banana width is the typical scale length ($\Delta x = w_{\text{banana}}$). In the Pfirsch-Schlüter regime with the highest collisionality, the collision frequency is that high, that the particles are no longer able to complete single orbits. Here the random-walk cannot be used any longer, the diffusion is dominated by particle drifts, which also increases with the collisionality. In between there is

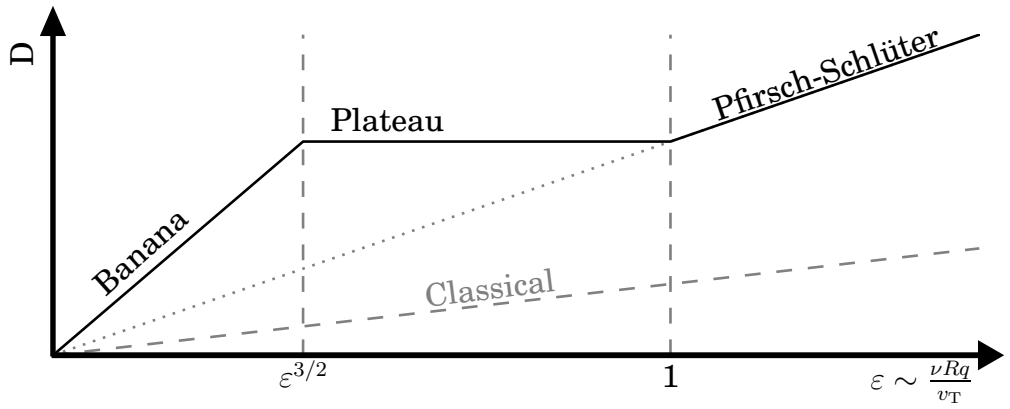

Figure 2.4.: Neoclassical Transport regimes. Variation of diffusion coefficient with collision frequency.

the plateau regime, where the radial transport does not change with increasing collisionality. In figure 2.4 the dependence of the diffusion coefficient with increasing collisionality is shown schematically. A more detailed description of the neoclassical transport can be found in reference [3].

2.2.2. Turbulent Transport

A comparison of the radial transport predicted by the neoclassical theory with experimental data [3,28] reveals a strong underestimation, for the electron heat transport up to 3 orders of magnitude (neoclassical electron heat diffusivity $\chi_{\mathrm{e,neo}} \sim 0.1\,\mathrm{m^2\,s^{-1}}$ [3]) and for the ion heat transport typically by a factor of 10 (neoclassical ion heat diffusivity $\chi_{\mathrm{i,neo}} \sim 0.3\,\mathrm{m^2\,s^{-1}}$ [3]). The reason for this strongly increased radial transport was identified to be microturbulent transport [29]. The microturbulence drives macroscopic eddies, increasing the radial transport.
It is commonly assumed that fast ions are unaffected by microturbulence. The large orbits and the fast motion lead to averaging over the turbulence. The important parameter for this assumption is the ratio E/T_{e}. The larger this ratio is, the less the ion will be affected by turbulence, typically the value of 10 is used as threshold. It is still an ongoing discussion if only time scale separation is required for the averaging, see reference [30], or whether also a separation of the equilibrium orbit size and the perturbation correlation length is needed [15, 31, 32].
In contrast to the common assumption that fast ions are unaffected by microturbulence, there is experimental evidence for a deviation of the fast ion dynamics from the neoclassical transport model [12]. One hypothesis is anomalous fast ion transport due to turbulent transport. A model, used within this thesis, can be found in reference [33].
The simulation of the turbulence and the turbulent transport uses gyro-kinetic codes. Gyrokinetic codes numerically solve the gyro-kinetic equation. This equation describes the temporal change of the particle distribution function in the five dimensions. The

expected three dimensions in the velocity space can be reduced to two, by averaging over the gyromotion. The particle velocity is described in this case by the motion of the guiding center with a charged ring around, representing the gyration radius. The gyro-kinetic codes consider changes of the particle distribution function on the scale of the Larmor radius and on timescales close to the cyclotron frequency. The codes take finite Larmor radius effects into account and also the variation of electromagnetic fields across the Larmor radius of the particles. The use of a gyrokinetic code comes with huge numerical costs, due to the single particle simulation, but with today's (super-) computers the investigation of the impact on the particle distribution function due to a change of microturbulence and their linear and also non-linear growth is possible. An overview on general turbulence and an overview on gyrokinetic codes can be found in reference [34]. The simulations are also compared with experiments which for example can be seen in references [35, 36].
The microinstabilities can be characterized depending on their perturbation of the magnetic field. In the case of small β the perturbation is negligible and the modes are essentially electrostatic. With increasing β the electrostatic modes become less unstable and a new set of electromagnetic modes appears, for example the so called kinetic ballooning modes.
The two most relevant instabilities, namely the interchange instability and the drift wave instability are predominantly electrostatic and discussed in the following sections.

Interchange Instability

The interchange instability is driven by a temperature-gradient either in the ions or the electrons. It resembles the Rayleigh-Taylor instability [37] and leads to an increase of the radial transport of ions and electrons. The mechanism of the ion-temperature-gradient-(ITG) and electron-temperature-gradient-mode (ETG) is the same, only the characteristic length scale, the Larmor radius, is different. The following description focuses on the ITG and is based on an article by Rosenbluth-Longmire [38].
In figure 2.5 a) a poloidal cut of an equalibrated plasma is shown, together with the gradient directions of the magnetic field and the temperature. The dominant magnetic field component from the toroidal field points into the plane. The starting point for the formation of an ITG mode is a periodic temperature fluctuation on a flux surface. This fluctuation periodically changes the drift velocity from the curvature and $\nabla\vec{B}$ drift, introduced in equation (2.15) and schematically shown in figure 2.5 b). In the cold region on the right the drift velocity is smaller with respect to the hot regions. This leads to a periodic accumulation and depletion of ions shown in figure 2.5 c). The local charge separation creates an electric field, leading to a force on the charged particles. From equation (2.14) it is known that a force, in this case the Coulomb force, leads to a drift of the plasma

$$\vec{v}_{\mathrm{D}} = \frac{\vec{E} \times \vec{B}}{B^2}. \tag{2.18}$$

This $\vec{E} \times \vec{B}$ drift leads to an outward transport of hot plasma and inwards transport of cold plasma, flattening the average temperature gradient.

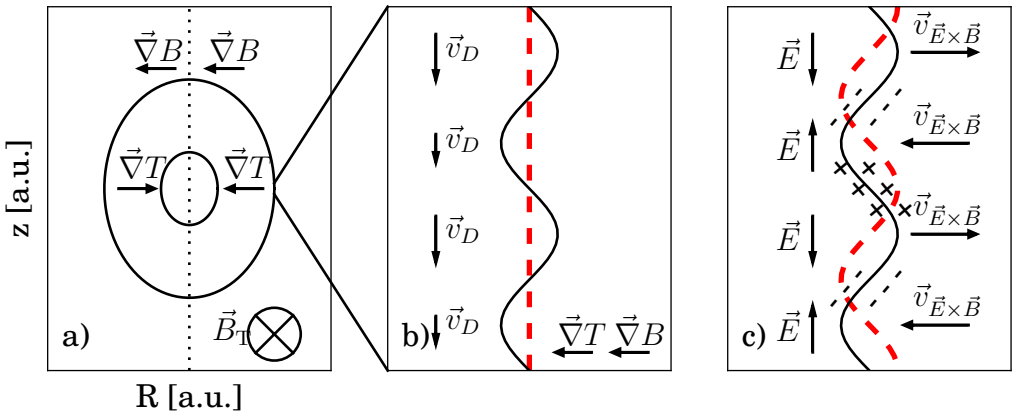

Figure 2.5.: Sketch of an ITG. In a) a poloidal cross section of a plasma can be seen, with the different gradient directions. The dashed line marks the radius of the magnetic axis. In b) a zoom on a field line can be seen, with an initial temperature fluctuation indicated by the black solid line of constant temperature and the resulting drift velocity vectors on the left side. In c) the periodical charge separation and the resulting change in the potential in red can be seen. The resulting radial $\vec{E} \times \vec{B}$ drift leads to a radial energy and particle transport. The figure is adapted from reference [19].

The shown example works on the low field side of the torus, as the temperature and magnetic field gradient point in the same direction, leading to an amplification of the initial perturbation. On the high field side, the temperature gradient has the opposite sign (figure 2.5 a)). The gradients point in opposite direction, and this leads to a damping of the perturbation. Due to the damping the high field is said to have 'good curvature', and due to the amplification on the low field side its curvature is called 'bad'.

Drift-Wave Instability

The drift-wave instability [39], giving rise to the trapped electron mode (TEM), also starts from an initial pressure fluctuation, but in contrast to the interchange instability the fluctuation on a flux surface is not perpendicular to the field lines. In figure 2.6 a 2D flux surface is shown with its field lines and the different pressure regions.
In a) the solid ellipse represent a region with a higher pressure with respect to the regions marked by the dashed ellipses. Assuming that the electrons are adiabatic, they will follow the gradient into the low pressure region. The heavier ions are not able to follow and the consequence is an accumulation of positive charges in the high pressure region and a accumulation of negative charges in the low pressure region, shown in b).
In figure 2.7 the same situation is sketched in a poloidal plane. In b) the black line sketches an perturbed isobar pressure line. In c) the periodic charge separation can be seen with the resulting electric field. In contrast to the ITG the electric field fluctuation is in phase with the pressure fluctuation. The resulting $\vec{E} \times \vec{B}$ drift leads to a downwards movement of the

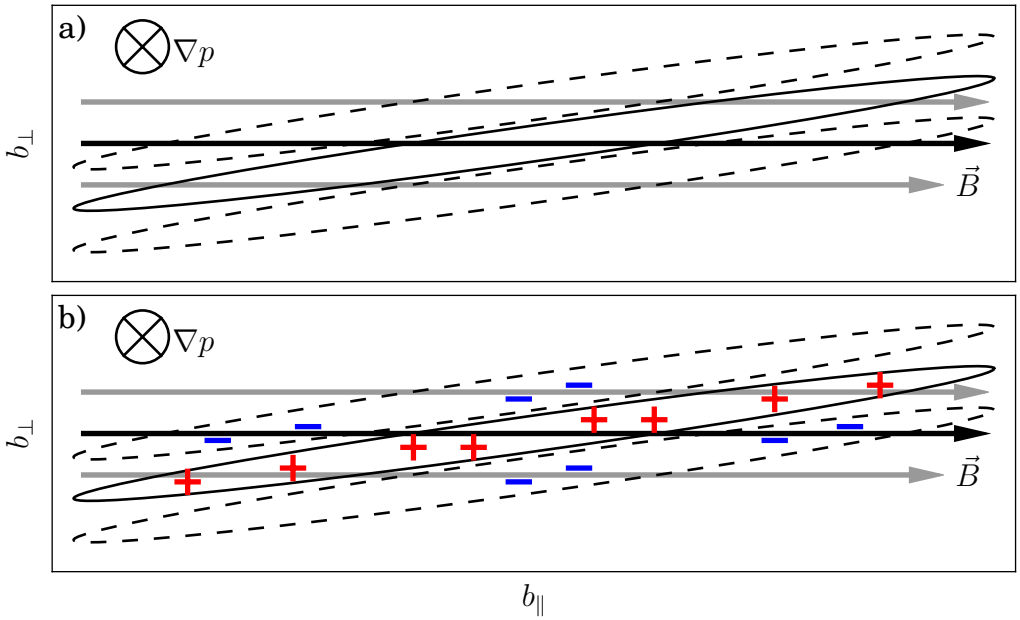

Figure 2.6.: Pressure perturbation in a plane parallel to the field lines and not perpendicular to them shown on an unrolled flux surface. The solid (dashed) ellipses present a region with high (low) pressure. The assumed adiabatic behaviour of the electrons leads to the charge separation shown in b). The figure is adapted from reference [19].

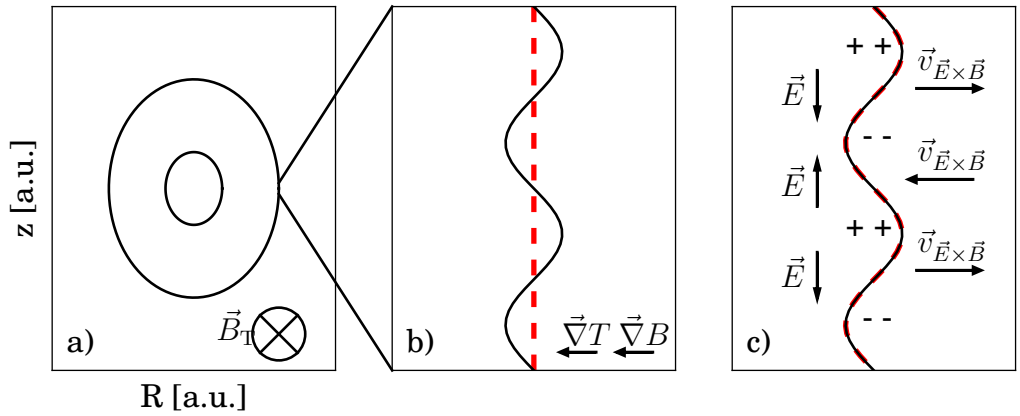

Figure 2.7.: The TEM in a poloidal cut through figure 2.6. The pressure perturbation due to the assumed adiabatic electrons, leads to a charge separation. The $\vec{E} \times \vec{B}$ drift from the resulting electric field leads to a downwards drift of the perturbation. The figure is also adapted from reference [19].

perturbation in this picture. In consequence the initial perturbation would rotate around the flux surface without any amplification or damping.
In this ideal case no anomalous radial transport would appear. However, the assumption of adiabatic electrons is not valid for all electrons at any position. Especially the trapped electrons cannot be assumed to be free. These non adiabatic electrons lead to a phase difference between the electric potential and the pressure fluctuation, resulting in (anomalous) radial transport. Therefore the instability is called trapped electron mode.

2.3. The H-Mode

The high confinement mode (H-mode) is a plasma regime with enhanced confinement, discovered at the Tokamak ASDEX in 1982 at the IPP in Garching [40].
This H-mode has approximately two times higher confinement times with respect to the low confinement mode (L-mode). The H-mode is accessed above a certain heating power threshold. As the underlying physics is not yet completely understood on a first-principles level, the scaling law was empirically derived from a multi-machine database. The resulting scaling [41, 42]

$$P_{\mathrm{thr,scal08}}[\mathrm{MW}] = 0.049\overline{n}_{\mathrm{e}}^{0.72}[10^{20}\,\mathrm{m}^{-2}]B_{\mathrm{tor}}^{0.8}[\mathrm{T}]S^{0.94}[\mathrm{m}^2] \tag{2.19}$$

was derived for the threshold with $\overline{n}_{\mathrm{e}}$ the line integrated density through the plasma center, B_{tor} the toroidal magnetic field and S the plasma surface.
The enhanced confinement is the result of a region with reduced transport, called edge transport barrier (ETB). This reduced transport is induced by a radially sheared $E \times B$ plasma flow, driven by a radial electric field. A detailed explanation on the mechanism can be found in reference [43].
The consequence for the pressure profile in an example discharge with a L- to H-mode transition is shown in figure 2.8. The ETB is formed in the region between approximately $\rho_{\mathrm{pol}} = 0.96$ and $\rho_{\mathrm{pol}} = 1.0$. In this region the pressure strongly increases in the H-mode in contrast to the L-mode. Inside the pressure profiles run almost parallel as they are expected to be 'stiff', which could also be expressed that the gradients of the temperature and density are constant [44, 45]. The pressure step within the ETB region is called pedestal.
The steep gradients of the H-mode at the edge leads to a further edge instability, only appearing in H-mode, the edge localized mode (ELM). This edge instability presents as a cyclical (10-200 Hz) flattening of the pedestal, forcing a fast (crash in ≤ 1 ms) outwards directed energy and particle transport. A detailed description on ELMs can be found in reference [46].
As the H-mode leads to a strong increase of the confinement, it is the favourable scenario for future fusion power plants, because it decrease the necessary machine size to fulfill the Lawson criterion (see equation (1.5)). All discharges in the framework of this thesis were in H-mode.

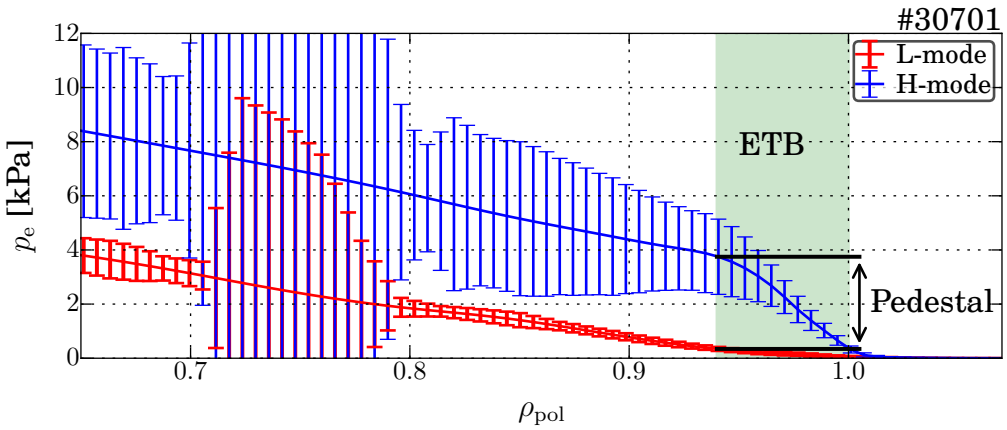

Figure 2.8.: Pressure comparison of an L-mode in red and an H-mode in blue. In the green shaded region the edge transport barrier (ETB) forms leading to a pronounced pressure step in this region, called the pedestal.

2.4. Heating and Current Drive

An ignited fusion plasma is mainly heated by the alpha particles, produced in the fusion reaction. However, before reaching a self sustaining plasma, the Lawson criterion must be fulfilled (see equation (1.5)). Therefore the plasma needs to be heated externally.
The intrinsic Ohmic heating (see 2.4.1) from the product of the plasma current squared and the plasma resistivity, is insufficient due to the fact that the resistivity of the plasma decreases with higher temperatures. Therefore different additional heating methods were developed.
Two concepts are established, on the one hand the injection of highly accelerated neutral particles (see section 2.4.2) and on the other hand the coupling of electromagnetic waves. The electromagnetic waves transfer energy at the resonance frequencies of either the electrons (see section 2.4.3) or ions. As ion cyclotron resonance heating is not used within this thesis, it will not introduced here. An overview can be found in reference [47].
Besides heating of the plasma, the systems are also able to drive a current in the plasma. Furthermore, neoclassical particle orbits give rise to the intrinsic bootstrap current (BS) (see section 2.4.4), driving also a current non-inductively.

2.4.1. Ohmic Heating

The confinement in a Tokamak relies on a current in the plasma ($I_p \sim 15\,\mathrm{MA}$ for ITER) that produces the helical twist of the field lines. This current is commonly inductively driven by a central transformer coil with the plasma as single-turn secondary coil. The current flows in toroidal direction around the torus, and due to the finite resistivity of the plasma a part of the current will dissipate as Joule heating. This heating power can be expressed by

$$P = 2\pi \cdot R \int_0^r \eta(r') \cdot j^2(r') \cdot r' dr' \tag{2.20}$$

with R the major and r the minor radius of the plasma, η the radially dependent resistivity and j the radially dependent current density. The resistivity is given by

$$\eta = Z_{\text{eff}}\eta_{\text{s}} \tag{2.21}$$

including the effective charge of the plasma which is defined as

$$Z_{\text{eff}} = \frac{\sum_j n_j Z_j^2}{\sum_j n_j Z_j} \tag{2.22}$$

with the sum over the density and charge number of all ion species (j) in the plasma and furthermore η_{s} the Spitzer resistivity

$$\eta_{\text{s}} = 0.51\frac{m_{\text{e}}}{n_{\text{e}}e^2\tau_{\text{e}}} = 0.51\frac{m_{\text{e}}^{1/2}e^2\ln\Lambda}{3\epsilon_0^2(2\pi T_{\text{e}})^{3/2}}. \tag{2.23}$$

The electron density (n_{e}) cancels out because the electron collision time (τ_{e}) is proportional to $1/n_{\text{e}}$. The Ohmic heating becomes more and more inefficient at higher temperatures due to the decreasing resistivity ($\eta \sim {T_{\text{e}}}^{-3/2}$). Therefore the Ohmic heating cannot increase the temperature up to ignition, the threshold for a self sustaining fusion reaction.

2.4.2. Neutral Beam Heating and Current Drive

Neutral beam heating is based on the injection of energetic neutral particles ($\sim 10 - 1000\,\text{keV}$) into the fusion plasma. The production of a high energy neutral particle beam is discussed in section 3.2.1. In the present section the heating and current drive mechanism is introduced following references [48, 49].
The fast neutral particles enter the plasma, are ionized by interaction with the plasma particles, and become confined as fast ions. Subsequently the heating occurs by thermalization of these fast ions through further collisional interaction with background electrons and ions. The fraction of energy transferred to electrons and ions is determined by the energy dependent cross sections. Two regimes exist: while at high energy ions transfer their energy dominantly to the electrons, the fast ions with lower energy increasingly transfer energy to the background ions. For deuterium injection into deuterium plasmas the critical energy where electrons and ions are heated equally is

$$E_{\text{c}} = 18.6 \cdot T_{\text{e}} \left(\frac{A^{3/2}}{n_{\text{e}}} \sum_j \frac{n_j \cdot Z_j^2}{A_j} \right)^{2/3} \tag{2.24}$$

with T_{e} the electron temperature, A the mass number of the beam, n_{e} the electron density (ITER $\sim 10^{20}\,\text{m}^{-3}$), j the index for the ion species of the plasma with density n_j, charge Z_j and mass number A_j.
Due to the fact that the fast ions starting in the electron heating regime during their slowing

down also transit through the ion heating regime, for the integrated power transfer over the full process the critical energy is 2.5 times higher.
The beam energy is the main control parameter for the penetration depth of the neutral beam into the plasma, that determines also the power deposition profile in the plasma. Higher energy leads to a deeper penetration and reduces the beam attenuation, resulting in a centrally increased power deposition. In contrast, too high beam energy leads to an increasing shine through, neutral beam power not absorbed in the plasma. This shine through power is lost and possibly resulting in damage of the inner wall of the vessel. The shine through depends strongly on the electron density of the plasma and should be avoided.
Besides the heating of the plasma neutral beam injection is able to drive non-inductively a current in the plasma. The following description of the neutral beam current drive (NBCD) follows the calculations of D. R. Mikkelsen [50].
Neutral beam current drive is based on the non-radial injection of hyperthermal energetic neutral particles into the magnetized fusion plasma. The fast ions, resulting from the ionization of the neutral particles, move along the field lines into a preferential direction during their slowing down. A simple estimate of the circulating current can be obtained by the injected current multiplied by the number of toroidal laps until the particles are thermalized,

$$I_{\mathrm{circ}} = I_0 \cdot \frac{\langle v_{\parallel} \rangle \tau_{\mathrm{s}}}{2\pi R_0}, \tag{2.25}$$

where I_0 is the injected particle current, $\langle v_{\parallel} \rangle$ the averaged toroidal velocity over the slowing down process, τ_{s} the time until the particle is thermalized (several 10s of ms) and R_0 is the major radius of the torus.
For a more accurate calculation correct averaging over the slowing down and the effect of pitch angle scattering must be taken into account. This transforms equation (2.25) to

$$I_{\mathrm{circ}} = Z_{\mathrm{beam}} \cdot I_0 \cdot \frac{v_0 t_{\mathrm{s}}}{2\pi R_0} \xi_0 I(x, y) \tag{2.26}$$

with Z_{beam} the charge number of the beam particles, v_0 the injection velocity, t_{s} the Spitzer slowing down time [48]

$$t_{\mathrm{s}}[\mathrm{s}] = 6.28 \times 10^{14}\,\mathrm{s} \frac{A_{\mathrm{beam}} T_{\mathrm{e}}[\mathrm{eV}]^{3/2}}{Z_{\mathrm{beam}}^2 n_{\mathrm{e}}[\mathrm{m}^{-3}] \ln \Lambda} \tag{2.27}$$

including all constants summarized in the beginning, the Coulomb logarithm $\ln \Lambda \approx 17$, $\xi_0 = v_{0_{\parallel}}/v_0$ the initial pitch angle and $I(x, y)$ the pitch angle scattering parameter

$$I(x, y) = \frac{1}{x} \left(\frac{1 + x^3}{x^3} \right)^y \int_0^x \left(\frac{u^3}{1 + u^3} \right)^{y+1} du. \tag{2.28}$$

This pitch angle scattering parameter depends on $x = \sqrt{E_0/E_{\mathrm{c}}}$ and $y = 4Z_{\mathrm{eff}}/5A_{\mathrm{beam}}$, with E_0 the injection energy of the neutral particles, E_{c} the critical energy, Z_{eff} the effective charge of the plasma and A_{beam} the atomic mass number of the beam particle.
Until now no electrons were taken into account. However, due to the Coulomb force the

light electrons of the bulk plasma are dragged along with the circulating ions leading to an electron shielding current that reduces the fast ion driven current to

$$I_{\mathrm{cd}} = I_{\mathrm{circ}} \cdot \left(1 - \frac{Z_{\mathrm{beam}}}{Z_{\mathrm{eff}}}\right). \tag{2.29}$$

This is valid for a cylindrical plasma. Fortunately, in toroidal geometry not all electrons are able to participate in this shielding current. Electrons on trapped orbits move equally in co- and counter current direction and cannot carry a toroidal net current. This leaves a non-zero driven current even for $Z_{\mathrm{beam}} = Z_{\mathrm{eff}}$ and transforms equation (2.29) into

$$I_{\mathrm{cd}} = I_{\mathrm{circ}} \cdot \left[1 - \frac{Z_{\mathrm{beam}}}{Z_{\mathrm{eff}}} \cdot (1 - G(Z_{\mathrm{eff}}, \epsilon))\right] \tag{2.30}$$

where G is the trapped electron parameter. This trapped electron parameter depends on the effective charge of the plasma and the inverse aspect ratio $\epsilon = r/R_0$. The trapped electron parameter is challenging to calculate and therefore multiple physics based approximations exist. In chapter 5 the simulation tool to calculate the neutral beam driven current and the different implemented physical models for the electron shielding current are introduced. Furthermore a benchmark study is presented calculating the neutral beam driven current on basis of a semi-analytic fast ion model.

2.4.3. Electron Cyclotron Resonance Heating and Current Drive

Electron cyclotron resonance heating (ECRH) is based on the coupling of electromagnetic waves to the plasma fulfilling a resonance condition with the gyrating electrons. The gyrofrequency of the electrons is given by

$$\omega_{\mathrm{c}} = e \cdot B/m_{\mathrm{e}} \tag{2.31}$$

with e the elementary charge, B the magnetic field and m_{e} the electron mass. In first approximation the frequency of the heating wave should be a harmonic of this gyrofrequency. At the fusion experiment ASDEX Upgrade with a magnetic field of 2.5 T at the axis the gyrofrequency is ≈ 70 GHz and the commonly used ECRH frequency is the second harmonic ≈ 140 GHz. The radial decrease of the magnetic field in combination with steerable mirrors allows to pinpoint the deposition of the power in the order of $1\,\mathrm{cm}^3$ along the plane fulfilling this resonance condition. The power absorbed by the now hot electrons is subsequently transferred via collisions, mainly with other electrons, in the plasma and increases the electron temperature while thermalizing the hot electrons.

Besides the heating, the ECRH system can be used to drive current. If the injection angle of the electromagnetic wave is not perpendicular to the current direction, the ECRH system is able to drive a current. This preferential direction allows either co- or counter-current drive. Due to the angle between the electron movement and the wave propagation direction the frequency of the wave is Doppler shifted in the frame of reference

of the electron. For electrons moving towards the emitter the wave frequency appears increased in their reference frame and vice versa for electrons moving in the opposite direction. In combination with the radially decreasing magnetic field the wave is first attenuated in a region were the electrons moving away from the emitter are resonant with the wave and the heating power is predominantly transferred to these electrons. Consequently, the collisionality for these electrons is reduced with respect to their counter-parts. Therefore these electrons circulate more often around the tours until they are thermalized, which leads to a net current. Due to the sharp resonance condition this current is driven in a narrow region and can be used for example to mitigate NTMs (see section 2.5.3) or locally tailor the q-profile.
More and detailed information about electron cyclotron resonance heating (ECRH) and electron cyclotron current drive (ECCD) can be found in reference [51]. TORBEAM is a tool to calculate the power deposition and current drive of the ECRH system, details on TORBEAM can be found in reference [52].

2.4.4. Neoclassical Bootstrap Current

The following overview of the bootstrap current (BS) mechanism is based on the description in reference [53]. The neoclassical BS current is a consequence of the neoclassical transport and especially of the trapping of particles on banana orbits. In combination with existing temperature and density gradients an intrinsic current in the plasma appears. In figure 2.9 a 3D visualization of the trajectories of the banana orbits can be seen. In the poloidal projection on the left side it can be seen, that the upwards movement of the particle is at a different radial position than the downwards movement. Furthermore a second banana orbit is shown with its outer leg at the same radial position as the inner leg of the first banana. As the center of the inner banana is closer to the center this banana is populated with more and faster particle due to the increasing density and temperature towards the center. This leads to a asymmetry of the parallel velocity of the particles at this radial position, leading to a net current. At almost all low field side positions a superposition of at least two of such bananas can be found. Furthermore due to the collisional coupling this asymmetry is also transferred to the passing particle fraction. This asymmetry in both fractions leads to a net current in toroidal direction, carried dominantly by the passing particle. This current is called the bootstrap current.
For a non-negligible trapped particle fraction an inverse aspect ratio $\epsilon > 0$. With this trapped particle fraction $\sqrt{\epsilon}$, the resulting BS density can be described by

$$J_{BS} = \frac{\sqrt{\epsilon} k_B}{B_{pol}} \left[2.44(T_e + T_i)\frac{dn}{dr} + 0.69n\frac{dT_e}{dr} - 0.42n\frac{dT_i}{dr} \right]. \tag{2.32}$$

The B_{pol} dependence takes the width of the banana orbit into account. In the square brackets the density and temperature gradients are considered, describing the different population and temperature of the inner and outer leg of the banana. Obviously the density gradient contributes stronger than the temperature gradients.
However, this approximation is not applicable in the complete plasma, particularly at the

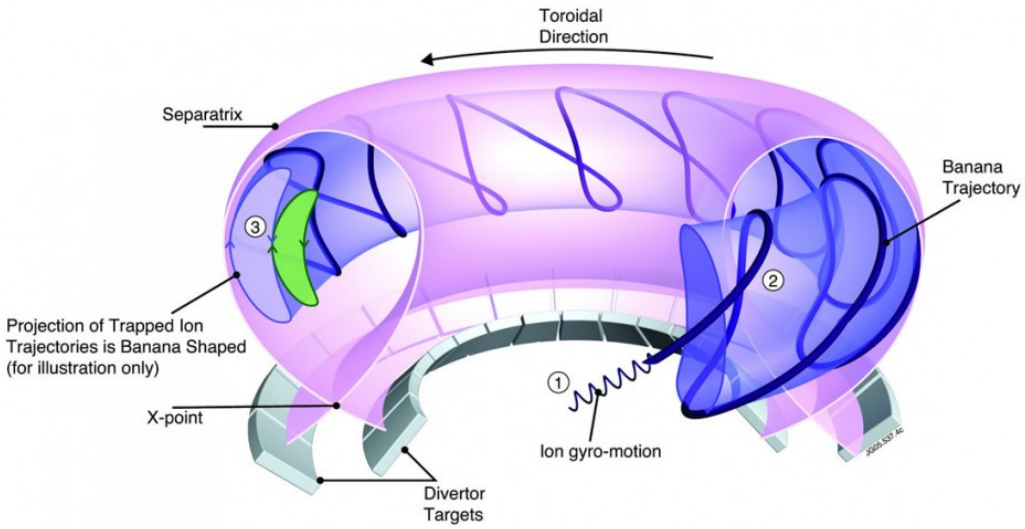

Figure 2.9.: 3D banana trajectory of a trapped charged particle in a Tokamak fusion plasma. In 1 the initial gyromotion can be seen overlapped with the movement of the guiding center in toroidal direction. In 3 the projection in the poloidal plane can be seen. Clearly visible is the toroidal precession. The figure is adapted from [54]

edge of the plasma some assumptions are no longer valid. However, especially at the edge in H-mode with its pedestal the strongest gradients are present. Therefore an improved description of the BS is needed and can be found in references [55, 56]

$$\langle j_{\mathrm{bs}} B \rangle = -I(\psi) p_{\mathrm{e}} \left[\mathcal{L}_{31} \frac{p_{\mathrm{e}}}{p} \frac{\partial \ln p}{\partial \psi} + \mathcal{L}_{32} \frac{\partial \ln T_{\mathrm{e}}}{\partial \psi} + \mathcal{L}_{34} \alpha \frac{1 - R_{\mathrm{pe}}}{R_{\mathrm{pe}}} \frac{\partial \ln T_{\mathrm{i}}}{\partial \psi} \right]. \tag{2.33}$$

I is the poloidal current, p_{e} is the electron pressure and R_{pe} is the electron pressure normalized to the total pressure. The other parameters depend on the plasma conditions and are discussed, together with the full model and restrictions, in detail in the references [55,56].

2.5. MHD Activity

In the following sections three different plasma instabilities from the magnetohydrodynamic spectrum and relevant for this thesis are discussed. The description of all three follows mainly the detailed summary on magnetohydrodynamics in reference [57]. Discussed are the sawtooth instabilitiy, the fishbone instability and the neoclassical tearing mode.

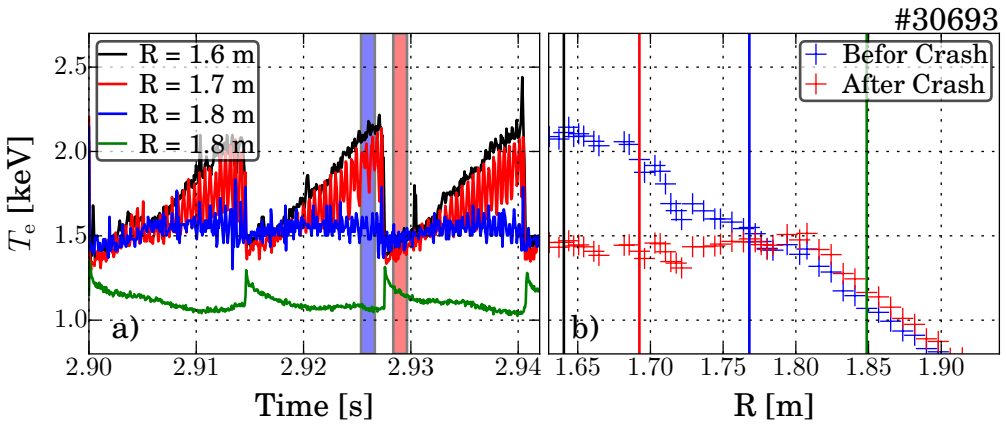

Figure 2.10.: In a) the time evolution of the temperatures during sawteeth at different radial positions can be seen. The eponymous sawtooth structure is clearly visible in the central channels. In b) the temperature profiles close before and after a sawtooth crash are shown. The figure is adapted from [19].

2.5.1. Sawtooth

The sawtooth instability is a cyclic instability at the q=1 surface. The sawtooth cycle can be illustrated by a periodic appearance of an mode at the q=1 surface. Subsequently this mode growths and at a certain point replaces the initial plasma center. The sawtooth behaviour can be identified by fluctuations in the central density and temperature. An example of the central temperature fluctuation can be seen in figure 2.10 a). In a first phase the central temperature starts to increase. With this temperature peaking due to $\sigma \propto T^{3/2}$ the central current increases, leading to a decrease of the safety factor q. If $q \leq 1$ an ideal m=1/n=1 kink or a resistive m=1/n=1 island can appear, leading to strong fluctuations that end up in a crash. The crash leads to a fast and strong diffusive transport of heat, particles, momentum and current, flattening the temperature, density and current profiles. The inversion radius is a radius where inside and outside the change in T_e and n_e is inverted and stays constant at this point. During the crash q_0 increase above unity and the cycle starts again with a slow density peaking.
The profile flattening shortly after the crash can be seen in figure 2.10 b). The timescale for the peaking of the kinetic profiles is much longer than the timescale of the crash, which is typically less than 100 µs for sawteeth in ASDEX Upgrade.
The exact reason for the crash is not fully understand yet, but fast reconnection described by the Kadomtsev model [58] is widely accepted as qualitative description of the phenomenon. In the Kadomtsev model a helical flux is defined, increasing from the plasma center up to a maximum value at the q=1 surface and decreasing again more outwards. The initial helical flux can be seen in figure 2.11 with ψ_*^i. During the crash flux surfaces with the same helical flux get connected and the kinetic and current profiles flatten out, until the maximum value of the helical flux is moving inwards to the magnetic axis and the $q = 1$ surface vanishes. This final helical flux is drawn as ψ_*^f. The time scale of a crash is approximated with $\tau_{\text{crash}} \approx \sqrt{\tau_A \tau_{\text{res}}}$, with τ_A the Alfven timescale and τ_{res} the resistive timescale. However,

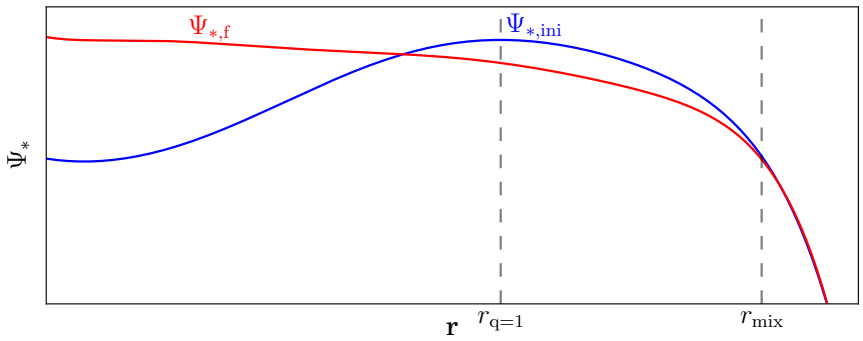

Figure 2.11.: The helical flux ψ_* assumed in the Kadomsev model [58] is shown, in blue before ($\psi_{*,\mathrm{ini}}$) and in red after ($\psi_{*,\mathrm{f}}$) the sawthooth crash. This figure is inspired from reference [59].

there are cases with $q_0 < 1$ right after the crash and for larger Tokamaks like JET, where the approximated time for the crash are to large with respect to the measurement ones. Therefore an extension for the Kadomtsev model is necessary, but not yet found. For a more detailed description of the sawtooth cycle see [57].
The sawtooth instability leads to a time averaged decrease of confinement, due to the cyclical decrease of temperature and density in the center. However, there is also a beneficial effect of sawteeth. During the crash, sawteeth lead to an outward-directed impurity transport, suppressing unfavourable impurity accumulation in the plasma center. For example in a fusion reactor, sawteeth can remove the He-ash from the center.
To use the beneficial properties of the sawteeth and additionally minimize the confinement degradation the sawtooth period needs to be controlled. The sawtooth period is increased by depositing a current close to the q=1 surface. This is typically done by ECCD deposition and is possible, as the onset criterion of sawteeth is connected to the magnetic shear. This increase of the sawtooth period leads to an increase of the sawteeth-averaged kinetic profiles, while the beneficial outward transport of impurities is retained. A more detailed description of sawtooth control and the onset criterion can be found in reference [57]. Furthermore an example for the sawtooth pacing in the TCV Tokamak is given in reference [60].
The sawtooth period can also be influenced by the injection geometry of the neutral beams and the resulting fast ion distribution. For example in ASDEX Upgrade the influence of the off-axis neutral beam geometry on the sawtooth period was studied in reference [61, 62].
Sawtooth are also able to redistribute fast ions from inside the q=1 surface outwards. This phenomenon was measured in several fusion experiments, examples are presented in references [63–66].

2.5.2. Fishbone Instability

The fishbone instability ordinarily lies on the q=1 surface and is driven by trapped fast particles, deposited next to the q=1 surface. Trapped fast particle can destabilize the

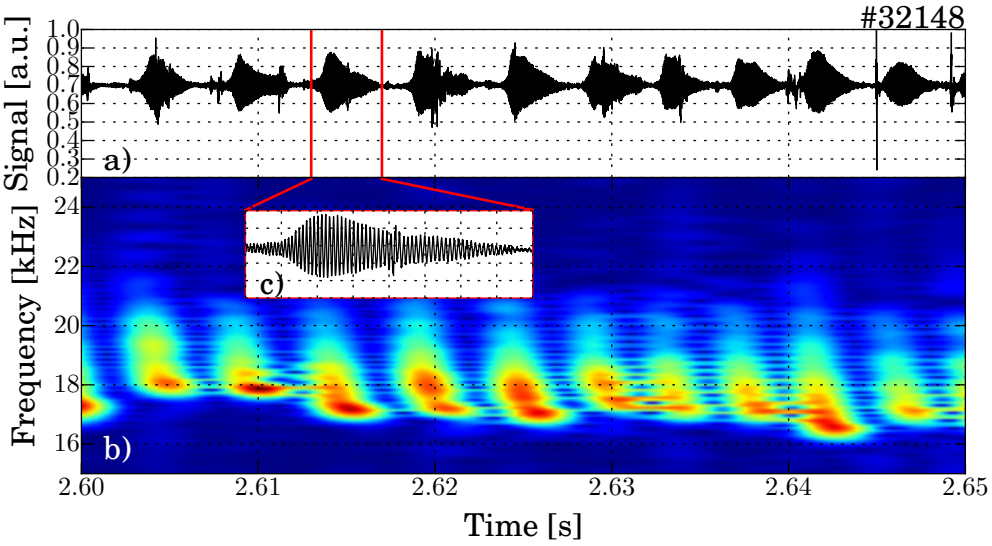

Figure 2.12.: Magnetic signature of fishbone instabilities, in a) the signal in Mirnov coil with a zoom on one fishbone with the characteristic structure in c) can be seen. In b) the Fourier transformed spectra of the signal with typical frequency chirping is shown.

m=1/n=1 internal kink mode if the following condition is fulfilled

$$\omega_{prec} = \frac{W_{ion}}{eR_0 r_1 B_t} \approx \omega_{mode}. \tag{2.34}$$

In this case the banana orbits precess toroidally around the q=1 surface, with a frequency close to the mode frequency leading to a growth of the m=1/n=1 internal kink mode. Neutral beam systems like the one at ASDEX Upgrade can lead to fast ions populations with energies around 100 keV which corresponds to frequencies in the order of tens of kHz. This frequency is in the range of the 'natural' frequency of the m=1/n=1 internal kink mode and fulfill the equation (2.34). This resonance effect can lead to a grow of the mode and above a critical value of the gradient of the fast ion density, the mode expels them starting from the ions with highest energy to the ones with lower energy. In the Fourier analysis of the magnetic signal this signature can be seen in a fast drop of frequencies called chirping. This growth and decay of the mode happens on a millisecond time scale. A look at the signals measured with the magnetic pick-up coils, shown in figure 2.12, indicates the characteristic structure, giving the name to the instability. Fishbones only appear if the fast ions from the neutral beams are deposited close to the q=1 surface and a strong gradient of fast ion density develops. Therefore in ASDEX Upgrade beside the ion cyclotron resonance heating only the neutral beam sources aiming close to the magnetic axis can induce fishbones. A more detailed description on fishbones can be found in references [57, 67].

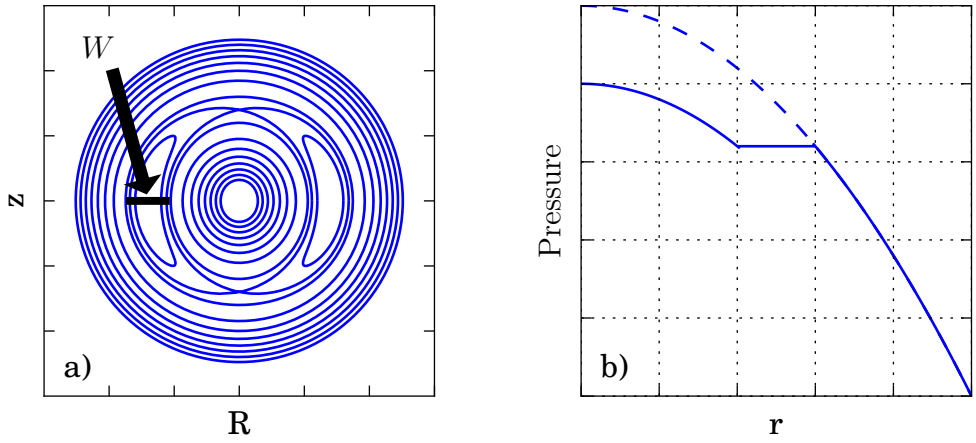

Figure 2.13.: In a) an idealized m=2/n=1 NTM in a cylindrical plasma is shown, with the clearly visible flux surface reconnection. In b) the corresponding pressure profile is sketched. With the dashed line the expected pressure profile without the NTM can be seen and corresponding with the solid line the change due to the NTM is shown. The figure is adapted from [68].

2.5.3. Neoclassical Tearing Modes

Neoclassical tearing modes (NTM) are confinement degrading, resistive magnetohydrodynamic (MHD) instabilities. They only exist on rational flux surfaces with $q = m/n$ with $m, n \in \mathbb{N}$. These NTMs, also called islands, are caused by reconnection of flux surfaces. The reconnection starts from an initial perturbation, flattening the pressure profile. This flattening of the pressure profile decreases locally the bootstrap current (BS). This missing current reconnects flux surfaces and strongly increases the radial particle and energy transport. In figure 2.13 a) the flux surfaces of a cylindrical plasma with an idealized m=2/n=1 NTM can be seen. The strongly increased radial transport leads to a further flattening of the pressure profile, visualized in figure 2.13 b). In consequence the pressure driven bootstrap current decreases further. As the local current decreases, the island width increases and with it the region with enhanced radial transport. The missing bootstrap current is called defect current.
NTMs grow from small seed islands, for example triggered by sawteeth, leading to the initial flattening of the pressure profile. Under unfavorable conditions NTMs can grow until they destabilize the complete plasma, forcing a disruption.
There are possible ways to stabilize NTMs, based on the compensation of the defect current. The compensation is realized by current deposition through external current drive, particularly by ECCD, inside the island position. This can be done preemptively, either aiming the ECCD at the expected position of rational flux surfaces or aiming at the expected localization of an NTM, detected in a reference discharge. A more advanced technique is the feedback controlled stabilization, using real time NTM localization and automated aiming of the ECRH to drive the current at the right location. A more detailed description of NTMs and the real time localization can be found in [68, 69]. An example

for real time NTM stabilization on TCV was published in reference [70].
The flattening of the pressure profile leads, beside the local pressure decrease, to a global decrease of the pressure profile towards the center, visible in figure 2.13 b). Beside this confinement degradation it was found that NTMs lead to anomalous fast ion losses. Qualitatively these losses were also measured at ASDEX Upgrade with the fast ion loss detector [71, 72].

3. Machine and Diagnostics

3.1. ASDEX Upgrade

The Tokamak ASDEX Upgrade (**AUG**) [73], successor of the fusion experiment ASDEX [74] (**A**xial-**S**ymmetrisches **D**ivertor-**EX**periment), which was operated from 1980 to 1990 at the IPP Garching, started its plasma operation in 1991. The experiment is situated at the Max-Planck-Institute for Plasma Physics in Garching bei München. ASDEX Upgrade is a medium size Tokamak with a major plasma radius of 1.65 m and a minor radius of 0.5 m. The toroidal magnetic field from 16 conventional copper coils can be chosen up to 3.0 T at the magnetic axis of the plasma. The upper limit for the plasma current is 1.4 MA. The main goals of ASDEX Upgrade are the study and improvement of the divertor in a Tokamak, the investigation of plasma facing components and the development of a ITER baseline scenario.

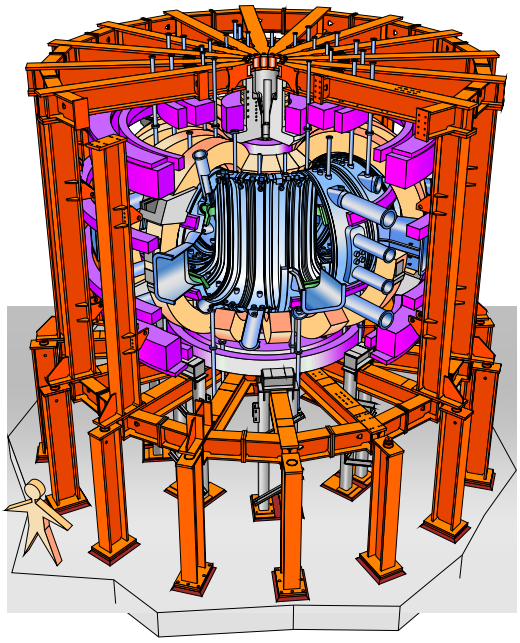

Figure 3.1.: Sketch of ASDEX Upgrade, with the support structure in orange, the poloidal field coils in magenta, the copper-colored toroidal field coils and the vacuum vessel with multiple diagnostic- and heating-ports in silver.

The divertor concept, for the first time successfully tested at the Tokamak ASDEX at the IPP [75], was improved several times within the lifetime of ASDEX and ASDEX Upgrade. Promising results lead to the result that all fusion relevant Tokamaks were built or upgraded with a similar divertor, especially ITER will be built with a full tungsten divertor based on the explorations and experience from ASDEX Upgrade. The main advantages of a divertor with respect to a limiter are a more localized and better controllable power exhaust and a smaller impurity influx towards the plasma center, leading to a better confinement.

The main physics program of ASDEX Upgrade is oriented towards the demands of ITER. As ASDEX Upgrade has a similar shape as ITER and a similar ratio of heating power normalized to the major radius, for example heat exhaust scenarios are under revision. Together with other medium size and even larger Tokamaks a ITER baseline scenario is in development. Originated with the high-confinement mode (H-mode see section 2.3), which originally was discovered at the ASDEX Tokamak 1982 in Garching [40], and which is the standard operational mode for all fusion relevant Tokamaks. The better confinement allows the same fusion conditions in an even smaller machine.

3.2. Heating and Current Drive Systems

In section 2.4 the heating mechanisms for a fusion plasma of the used external heating systems are introduced. At the time of the experiments reported in this thesis, at ASDEX Upgrade 20 MW of neutral beam heating, 5 MW electron cyclotron resonance heating and 6 MW ion cyclotron resonance heating are installed. Due to the fact that the ion cyclotron resonance heating was not used within the frame of this thesis, it will not be described here.

3.2.1. Neutral Beam Heating System

In section 2.4.2 the neutral beam heating and current drive mechanism was described. In this section the focus is on the production of high energy neutral beams [48, 49] and the implementation at ASDEX Upgrade [76, 77].
A high energy neutral beam is produced in four steps: production of thermal ions in a low temperature plasma; extraction and acceleration of these ions; neutralization of the fast ion beam by charge exchange; and deflection of the non-neutralized, residual ions out of the beam into an ion dump. As also molecular ions D_2^+ and D_3^+ are extracted from the source, the neutral beam has three energy components.
Figure 3.2 shows a CAD drawing of the first ASDEX Upgrade neutral beam injector, visualizing the individual steps.
The ASDEX Upgrade neutral beam system is organized in two beam boxes each with two pairs of sources with a comparable beam geometry, mirrored at the mid-plane. The injection geometry of the eight beams can be seen in figure 3.3. Sources 1 and 4 in the beam box 1 inject towards the magnetic axis almost radially, while sources 2 and 3 inject a bit more tangentially. The geometry of the sources of beam box 2 was readjusted in the year 2000, since then the geometry of the sources 5 and 8 is similar to the geometry of beam 2 and 3 and the beam 6 and 7 inject more tangentially than the other beam, enabling a higher current drive efficiency, and with respect to the magnetic axis they inject more off-axis. Furthermore, the off-axis steering angle of these two sources can be changed between plasma discharges in the order of $\pm 0.5°$.
All eight NBI sources of ASDEX Upgrade are able to heat the plasma with up to 2.5 MW

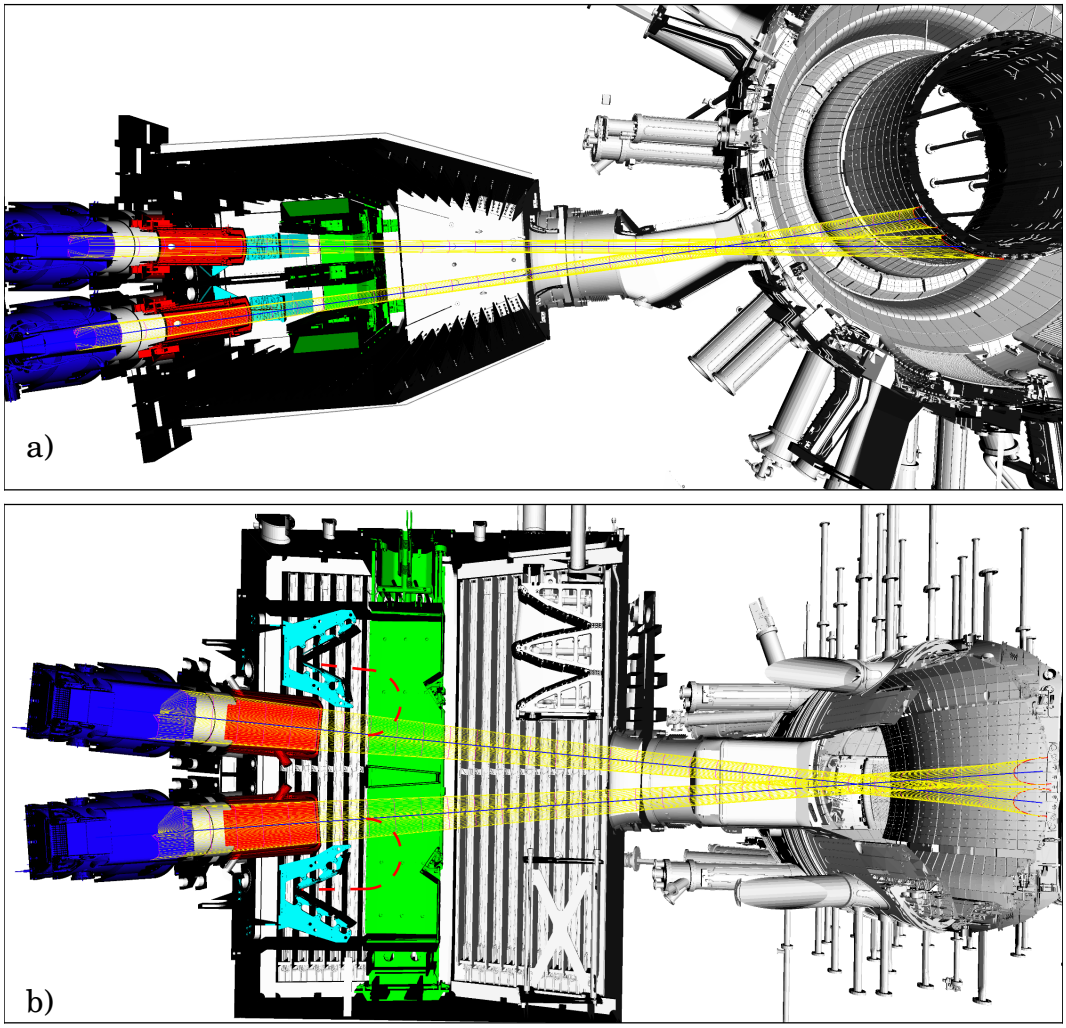

Figure 3.2.: a) Top down view and b) side view on the NBI box 1 of ASDEX Upgrade. The sectional plane were chosen almost horizontal a) and vertical b) oriented to the beam axis. The sources with the low temperature plasma and the grid system are shown in blue, downstream followed by the gas neutralizer in red. The bending magnet, shown in green, separating the ions from the neutrals of the beam into the ion dumps in cyan. The now pure beam of neutral particles enters through the duct into the ASDEX Upgrade vessel with the plasma.

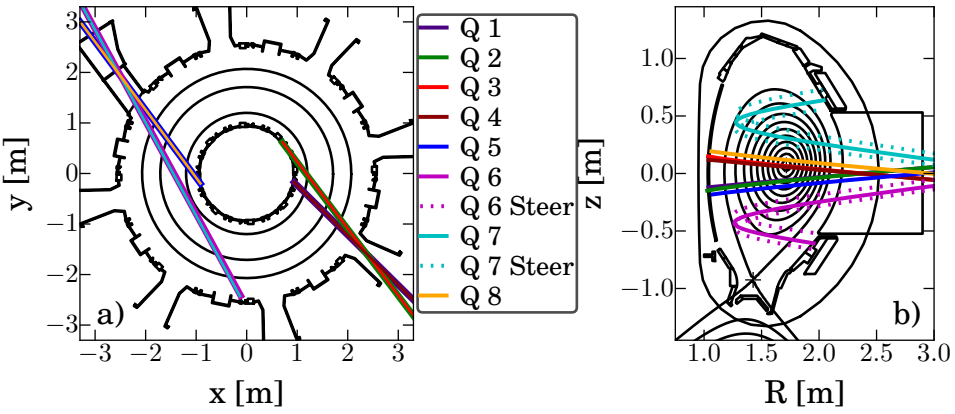

Figure 3.3.: a) Toroidal and b) poloidal view on the ASDEX Upgrade NBI system. Beam box 1 with the sources 1-4 is in the lower right quadrant and box 2 in the opposite diagonal one. While the sources 1 and 4 inject close to radial the sources 6 and 7 inject more tangential. The other sources are in between. The dotted lines show the steering ability of the off-axis beams 6 and 7.

neutral beam power each with the commonly used deuterium isotope. The grid systems are optimized for deuterium operation in the beam box 1 with a acceleration voltage of up to 60 kV and up to 93 kV for box 2.

3.2.2. Electron Cyclotron Resonance Heating System

The physical mechanism of the electron heating and current drive, with the electron cyclotron resonance heating (ECRH) system is described in section 2.4.3. Following the system of ASDEX Upgrade will be presented. This system hosts eight gyrotrons, which produce the electromagnetic microwaves. The four gyrotrons of the ECRH2 system deliver 800 kW at either 105 GHz or 140 GHz each for up to 10 seconds. At 105 GHz the resonant surface is formed by a magnetic field equipotential surface of 1.9 T and for 140 GHz the magnetic field is 2.5 GHz. The four gyrotrons of the ECRH1 system deliver 500 kW only at 140 GHz each for up to 2 seconds. At the end of 2015 the ECRH1 system was shut down. It is replaced by the ECRH3 system which starts operation in 2017 and will have, in its final stage, a similar performance as the ECRH2 system. The gyrotrons are placed outside the torus hall and the waves are transmitted via waveguides and mirrors into the torus. The last mirror to the plasma is steerable and allows a change of the power deposition along the resonance surface within a shot. The prediction of the deposition is made by the analysis tool TORBEAM using additionally to the ECRH parameters an equilibrium and kinetic profiles (for details on TORBEAM see reference [52]). Such a calculated deposition can be seen in figure 3.4. An overview over the ASDEX Upgrade ECRH system can be found in reference [78].

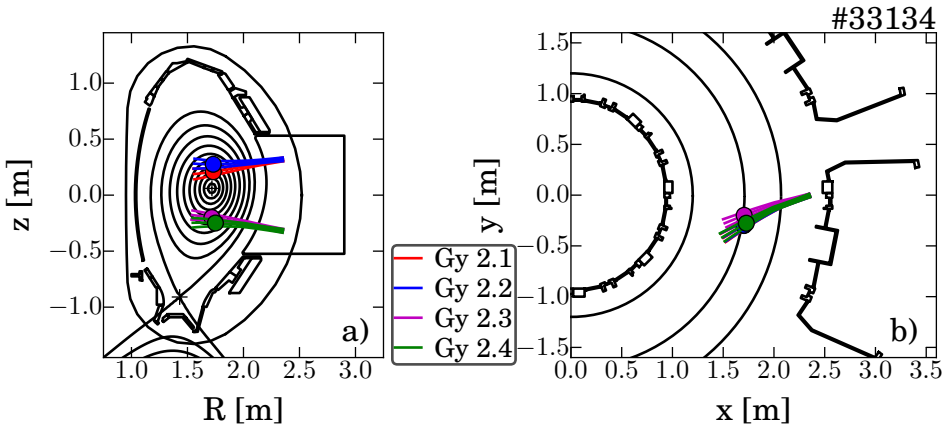

Figure 3.4.: a) Poloidal and b) toroidal view on the ASDEX Upgrade ECRH geometry for discharge #33134. The steerable mirrors of the gyrotrons of the ECRH2 are adjusted for co-current drive and off axis heating.

3.3. Diagnostics

The analysis of the plasma based on an accurate measurement of multiple plasma parameters. Most basic are the measurement of the magnetic field confining the plasma as well as the kinetic properties like temperature and density profiles.
These measured quantities are used, after a consistency check, as inputs for codes with complex physic models to be evaluated. The output of those codes can be used to calculate synthetic diagnostics to compare them with measurements of further diagnostics to evaluate the physics models. The most relevant diagnostics for this thesis are presented in this section.

3.3.1. Magnetic Measurements

Multiple magnetic coils within and around the vessel are used to measure the magnetic field of the plasma created by the superposition of the external toroidal field and the poloidal field induced by the plasma current. Furthermore the external correction and external and internal perturbation fields. They are also used as control parameter for the real time positioning of the plasma in the vessel by changing currents in the positioning coils. In the post processing the measured values are used as constraint for the equilibrium reconstruction by solving the Grad-Shafranov equation.
The measurement principal follows the inductive law

$$U(t) = -\frac{d\Phi}{dt} = -\frac{d}{dt}\int_A \vec{B}\cdot d\vec{A} \tag{3.1}$$

with U measured voltage in the coil, ϕ the magnetic flux, B the magnetic field vector and A the enclosed area of the coil. In ASDEX Upgrade several pick up coil with different orientations, probing different magnetic field com-

ponents, are installed. These coils can be seen in figure 3.5. The sampling rate of the coils is up to 2 MHz. For more details to this coils see [79].

Due to the fact that closer to the plasma core the distance to the coils increases and therefore also the uncertainties. This result in a week magnetic constrain for the plasma center by the coil magnetic measurements. For a proper equilibrium reconstruction in this area further measurements and physical models, like the current diffusion are needed to constrain the magnetic field structure. One of this diagnostics is the motional Stark effect polarimetry (MSE), discussed in detail in chapter 4.
Additionally to the magnetic field constrain there are multiple more coils to measure further plasma parameters like the surface voltage of the plasma, the plasma current or perturbations of the magnetic field for example due to magnetohydrodynamic activities like neoclassical tearing modes.

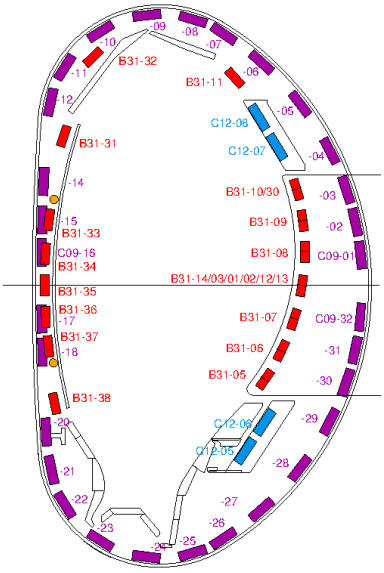

Figure 3.5.: Poloidal view on the ASDEX Upgrade magnetic field coils. The red coils measuring the poloidal field, while the purple ones measuring the radial field. The four blue coils measuring in the passive support loop at the top and at the bottom. Figure adapted from reference [19].

Diamagnetic Flux Loop

One special magnetic measurement in ASDEX Upgrade is the real-time diamagnetic flux loop. The diamagnetic flux is the difference of the measured total toroidal flux with and without the plasma. The diamagnetic flux is strongly correlated with the poloidal beta. The setup of the real-time measurement at ASDEX Upgrade can be seen in figure 3.6. The green coil measures the total flux, while the yellow coils measures the flux from the external coils. The two loops enables a real-time compensation and increase the accuracy with respect to small changes in the toroidal field coil current. The used coils were placed outside the vacuum vessel and are mounted together on the same frame to avoid independent deformation of the coils. The flux measurements of the coils can be expressed as followed

$$\Phi_{\mathrm{m}} = \int_{S_{\mathrm{meas}}} B_{\phi} dS \tag{3.2}$$

$$\Phi_{\mathrm{c}} = \int_{S_{\mathrm{comp}}} B_{\phi} dS. \tag{3.3}$$

thus the diamagnetic flux is defined as

$$\Delta\Phi = \Phi_{\mathrm{m}} - \alpha_{\mathrm{c}}\Phi_{\mathrm{c}} \tag{3.4}$$

with α a geometrical correction factor for the difference between the areas of the different coils. Due to the beta correlation, the comparison of the diamagnetic flux measurement with simulations, for example from TRANSP (see section 5.1), gives a good indication of deviations in the fast ion pressure, assuming accurate kinetic profiles. For more details on the diagnostic and a further fields of application see reference [80].

3.3.2. DCN Interferometer

Interferometry using sub-millimeter waves enables the measurement of the line integrated electron density in a fusion plasma. In ASDEX Upgrade a deuterium cyanide laser (DCN) with a wavelength of 195 µm is used. The real time density signal is used for density feedback control and is also coupled with the safety system. The passing of such an electromagnetic wave through a plasma with non-zero electron density leads to a phase shift with respect to a reference wave through a vacuum. The phase shift $\boldsymbol{\phi}$ can be expressed as follows

$$\phi = \lambda_0 r_{\mathrm{e}} \int n_{\mathrm{e}}(x)dx. \tag{3.5}$$

The wavelength of the laser is given by λ_0, the classical electron radius is donated by r_{e}, x gives the integration variable along the line of sight and the electron density is given by n_{e} . To measure this phase shift, a Mach-Zehnder-type interferometer with a heterodyne detection system is used.

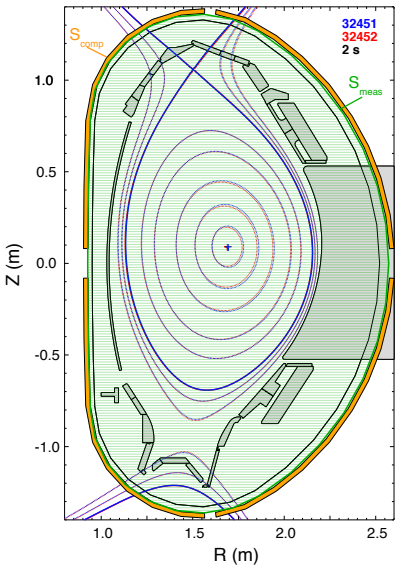

Figure 3.6.: In green the diamagnetic flux measurement coil is shown and in yellow the external compensation coils mounted on the same frame outside the vacuum vessel can be seen. The figure is adapted from reference [80].

A phase shift of 2π in the ASDEX Upgrade system corresponds to a line integrated density change of $5.72 \cdot 10^{18}\,\mathrm{electrons/m^2}$. Due to the fact that ASDEX Upgrade reaches line integrated densities of $10^{20}\,\mathrm{electrons/m^2}$, this leads to a phase shift of up to 20 times 2π. However, only a change of 2π can be measured and therefore the measurement is history dependent and an accurate counting of phase flips is necessary.
In reference [81] a more detailed description for the DCN interferometer of ASDEX Upgrade can be found and in figure 3.7 the line of sight geometry is shown.

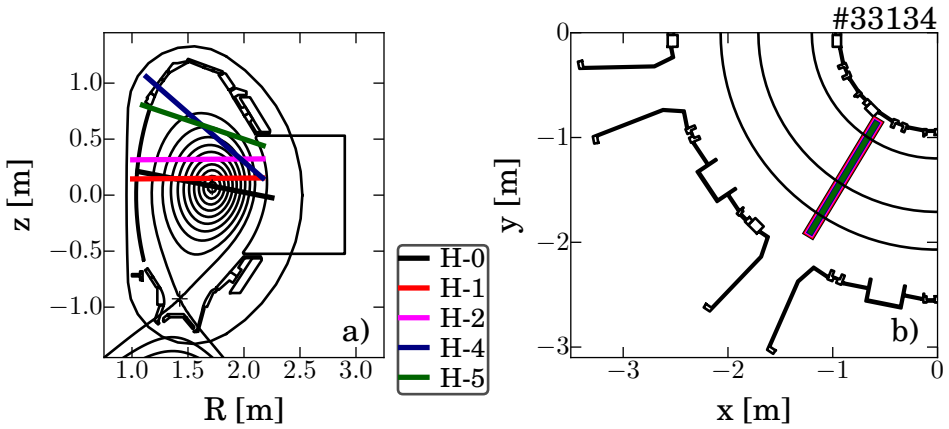

Figure 3.7.: (a) Poloidal and (b) toroidal view on the ASDEX Upgrade DCN lines of sight. The lines of sight H1 and H2 are in addition to the interferometer equipped with a polarimeter.

3.3.3. Faraday Rotation Polarimetry

From 2014 on the DCN interferometer (see section 3.3.2) is upgraded with an additional polarimeter, first on the H-1 and from 2015 on also on the H-2 line of sight. The polarimeter measures the Faraday rotation of electromagnetic waves passing through the magnetized plasma. The Faraday rotation is described by

$$\beta_{\text{Faraday}} \propto \lambda^2 \int n_e(x) B_{\parallel}(x) dx \tag{3.6}$$

where λ is the wavelength of 195 µm from the DCN laser, n_e is the electron density and $B_{\parallel}$ is the magnetic field component parallel to the line of sight.
For a simultaneous measurement with the interferometer a gold coated, off-axis parabolic and polarization conserving mirror is used, to redirect a part of the probed light into the polarimeter. The polarimeter is a rotating polarizer in front of a pyro-electric detector. The rotating polarizer in presence of a strong magnetic field is realized by an air-bearing pneumatically driven rotor. The rotation speed is in the order of 7500 RPM and the mounted rotating disc with the polariser is equipped with an encoder disc. The encoder disc, to measures the orientation of the polarizer, is read out by a light emitter and a receiving photo diode with a precision of 1° and a 0° marker. For further details about the polarimeter see reference [82].
The polarimeter measures the change in the polarization, with respect to a reference angle, measured before the plasma discharge. The changes are in the order of several degrees.
The used lines of sight are almost radial and therefore perpendicular to the toroidal magnetic field, see figure 3.7 b). Only the parallel poloidal magnetic field component leads to the measured Faraday rotation. The poloidal view on the geometry in figure 3.7 a) reveals that only in a small central area the H-1 and H-2 lines of sight are parallel to the poloidal field. This localized information can be used as constraint for the equilibrium reconstruction. The signal can also be used to investigate localized changes in the poloidal field structure,

directly related to changes in the local current distribution.

3.3.4. Electron Cyclotron Emission Diagnostic

The measurement of the electron cyclotron emission (ECE) of the plasma gain information on the electron temperature (T_e). The electrons in the plasma are trapped by the magnetic field and gyrate around the magnetic field lines. This rotation movement leads to a continuous centrifugal acceleration of the charged particle resulting in cyclotron emission. The frequency of this electromagnetic emission is described by

$$\omega = l \cdot \frac{eB}{m_\mathrm{e}} \tag{3.7}$$

with l the harmonic number, the measurement is typically at the second harmonic, e the elementary charge, B the magnetic flux density and m_e the electron mass. The magnetic flux density exhibits a spacial dependence dominated by the toroidal field decrease with $\sim 1/R$, which is used to map the single measured frequencies to a radial position. The toroidal field of ASDEX Upgrade is typically in the order of 1 T to 4.9 T, leading to frequencies from 55 to 270 GHz.
The information of the electron temperature is encoded in the intensity, by the assumption of a black-body radiator. This temperature is associated with the Maxwellian distributed velocity perpendicular to the magnetic field. Planck's law describes this black-body intensity

$$I d\omega = \frac{h\omega^3}{8\pi^3 c^3} \frac{1}{\exp(hf/k_\mathrm{B}T_\mathrm{e}) - 1} d\omega. \tag{3.8}$$

With some approximations valid for fusion plasmas, $\mathrm{h}\nu < 1\,\mathrm{meV}$, $\mathrm{k}T > 10\,\mathrm{eV}$, known as the Rayleigh-Jeans approximation, the equation simplifies to

$$I = \frac{\omega^2}{8\pi^3 c^3} k_\mathrm{B} T_\mathrm{e}. \tag{3.9}$$

With a combination of the equations (3.7) and (3.9) the radially dependent electron temperature can be determined with the assumptions of an optically thick emission and that the relativistic frequency shift is small. A more detailed description, discussion of limitations and a widening of the operational range, for example handling of non optically thick plasmas, can be found in references [83] and [84].
In ASDEX Upgrade a 60-channel heterodyne radiometer receiver is used to measure in three groups an electron temperature profile. In figure 3.8 the radial viewing positions used in most of the analyzed discharges can be seen.

3.3.5. Thomson Scattering System

The Thomson scattering system is an active measurement of the electron temperature and density. In ASDEX Upgrade two powerful laser beams with a pulse energy of 1.2 J and a

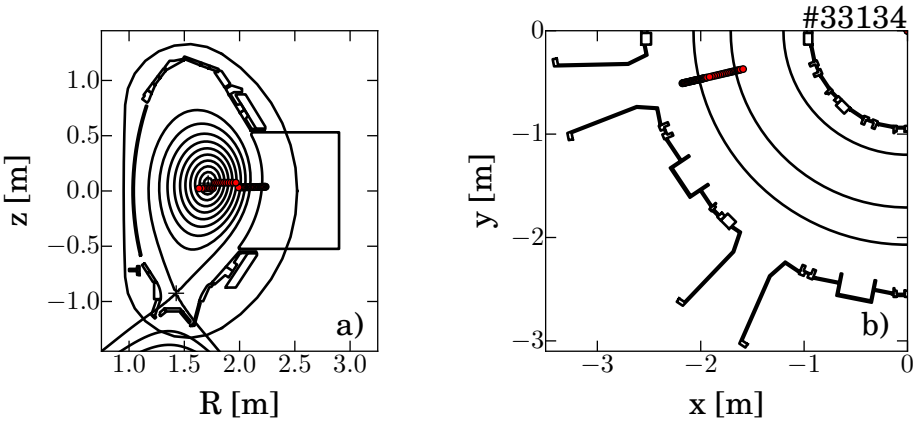

Figure 3.8.: a) Poloidal and b) toroidal view on the measurement positions of the ASDEX Upgrade 60-channel heterodyne ECE-radiometer.

repetition rate of 80 Hz in the core and 120 Hz at the edge are vertically coupled into the plasma vessel. Some photons are scattered by electrons through Thomson scattering and are collected by 16 lines of sight for the core laser beam and ten lines of sight for the edge laser beam. The collected light afterwards is analyzed individually for each line of sight in a polychromator. The electron temperature at the intersection of a line of sight and the laser beam can be determined by the width of the measured light from many photons. The electron density is directly correlated with the intensity, due to the density dependency of the scattering cross section. A sketch of the system at ASDEX Upgrade can be seen in figure 3.9. For more Information see reference [85].

3.3.6. Charge Exchange Recombination Spectroscopy

The charge exchange recombination spectroscopy (CXRS) is the most common plasma diagnostic to measure the ion temperature (T_i), the rotation velocity (v_rot) and also impurity densities, which can be used to reconstruct the effective ion charge (Z_eff) of the plasma. The measurement is based on the observation of hydrogen like line emission from impurity ions that have undergone a charge exchange reaction with a neutral particle from the NBI beams. The Doppler shift, width and intensity of the emission line gives information on the rotation velocity, the ion temperature and the densities of the observed species, respectively. In general it is a good assumption that the impurity ion temperature is equal to the main ion temperature due to the short impurity ion equilibration time.
The corresponding main ion density is challenging to obtain experimentally. It can, however, be approximated with the concept of the effective ion charge Z_eff in combination with the measured electron density n_e. Through a measurement of the densities of the main impurity species and the assumption of the quasineutrality, the effective ion charge can be estimated. The main impurities in ASDEX Upgrade are boron, nitrogen, carbon and helium and with

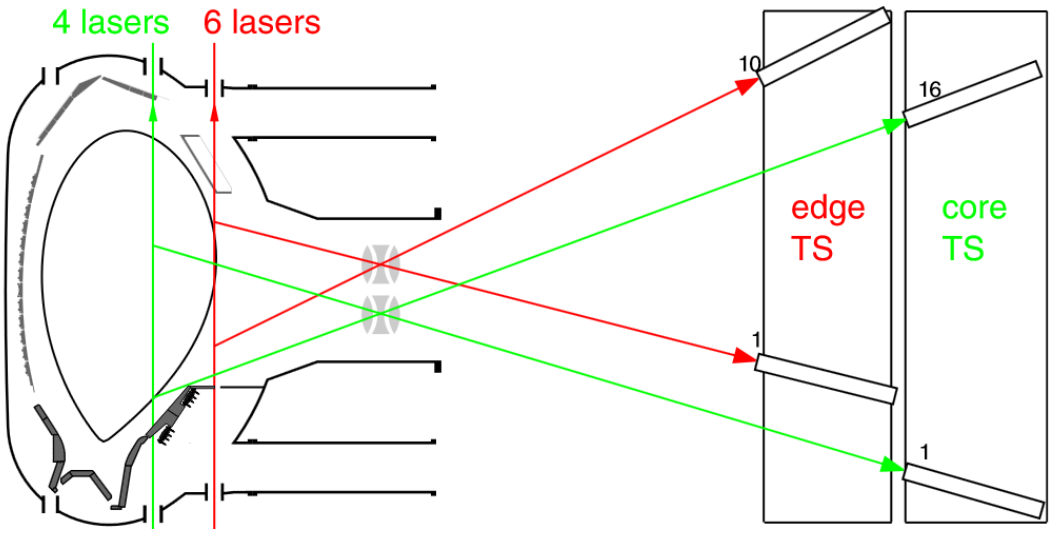

Figure 3.9.: Thomson Scattering system of ASDEX Upgrade. The core laser beam is a combination of four and edge system of six lasers, with ten lines of sight at the edge and 16 lines of sight on the core laser beam. The figure from B. Kurzan is adapted from reference [85].

the following equation the effective ion charge can be approximated

$$Z_{\mathrm{eff}} = \frac{\sum n_{\mathrm{i}} \cdot Z_{\mathrm{i}}^2}{n_{\mathrm{e}}} \approx \frac{n_{\mathrm{H/D}} \cdot 1^2 + n_{\mathrm{He}} \cdot 2^2 + n_{\mathrm{B}} \cdot 3^2 + n_{\mathrm{C}} \cdot 6^2 + n_{\mathrm{N}} \cdot 7^2}{n_{\mathrm{e}}} \tag{3.10}$$

All of these impurities have to be measured individually, with different spectrometers due to the fact that the characteristic line radiation is in different wavelength regions. ASDEX Upgrade is equipped with several different spectrometers for the charge exchange recombination spectroscopy with diverse viewing geometries, mainly on the neutral beams 3 and 8, routinely measuring boron, nitrogen, carbon and helium. The viewing geometry can be seen in figure 3.10 and a more detailed description on charge exchange recombination spectroscopy can be found in reference [86]. Additionally the effective charge can be measured by the bremsstrahlungbackground see reference [87]. Unfortunately at ASDEX Upgrade these measurement overestimate the effective charge, therefore only the method described above is used within this thesis.

3.3.7. Integrated Data Analysis

The integrated data analysis (IDA) at ASDEX Upgrade is designed to combine a set of different heterogeneous profile diagnostics and map them on a common coordinate system with Bayesian probability theory. At ASDEX Upgrade the electron temperature and electron density is estimated by the combination of the Thomson scattering spectroscopy, the DCN interferometry, the electron cyclotron emission and the lithium beam emission spectroscopy. The combination of diagnostics brings several advantages: a consistency check

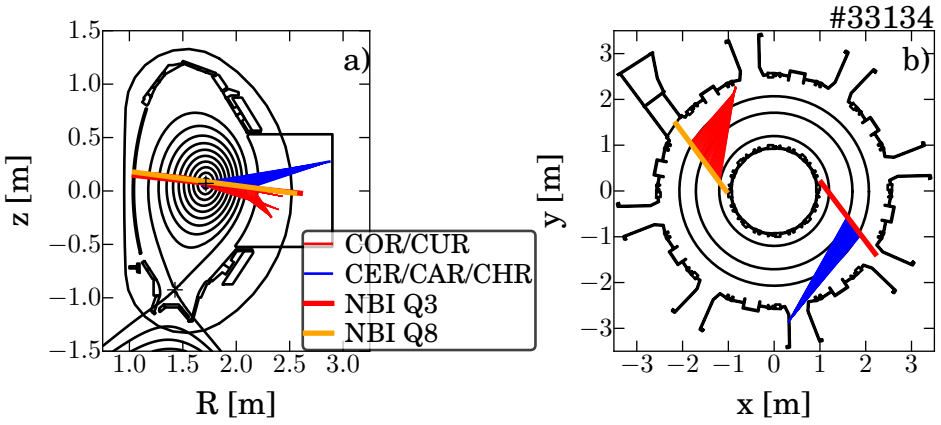

Figure 3.10.: a) Poloidal and b) toroidal view on the geometry of some ASDEX Upgrade charge exchange systems. The blue lines of sight are connected to the CER, CAR and CHR spectrometer and measures on NBI beam 3 and the red lines of sight intersecting NBI beam 8 are connected to the COR and CUR spectrometer.

can be performed and the larger set of data allows to reduce the uncertainties. Additionally the advantages of the different diagnostics can be taken into account, for example the better special resolution of the Thomson scattering and the intrinsic absolute calibration of the DCN interferometry. Furthermore, outliers can be identified and corrected more easily. Due to the fact that the reconstruction of a magnetic equilibrium, which is used for a mapping of the different diagnostics, also depends on the kinetic input data, the equilibrium reconstruction and the integrated data analysis should be coupled. At the moment the interplay of IDAand the equilibrium reconstruction IDE is tested and a better interchange is on the way to be implemented.
The integrated data analysis is built up modular so the included diagnostics can be easily switched on and off. Additional constraints, for example the exclusion of negative values for temperature or density or a monotonic increase to the center of the plasma, can also be switched on. Additionally systematic Gaussian error propagation is implemented. Up to now the data were mapped on the normalized poloidal flux radius of a standard Cliste equilibrium (see reference [88]). The temporal resolution is in the order of $\sim 100\mu s$. Further information about the integrated data analysis can be found in reference [89].

3.3.8. Fast Ion D-alpha Spectroscopy

Fast ion D-alpha spectroscopy (fast ion D-alpha spectroscopy (FIDA)) evaluates the light emitted by fast deuterium ions after charge exchange with neutrals of the neutral beam to extract information on the fast ion distribution. As already described in section 3.3.6, the ions in the plasma interact with the neutral atoms of the neutral beam by charge exchange and are neutralized into an excited state. Subsequently by emitting light the now fast neutrals transit into the ground state and the emitted photons are collected by optics and

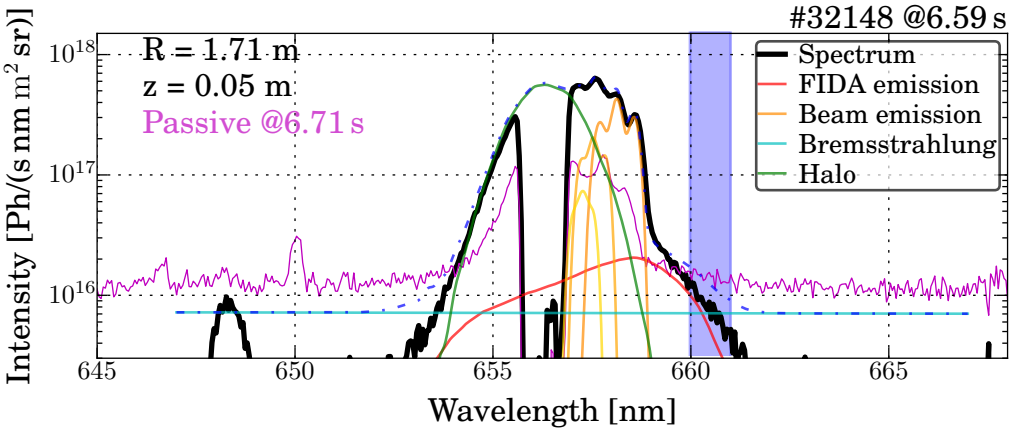

Figure 3.11.: In black, the spectrum measured with the FIDA spectrometer is shown. The unshifted deuterium Balmer-alpha line is blocked with a wire in the spectrometer. The different colored components come from a TRANSP run processed with FIDASIM (see reference [90]) and taking the instrument function into account. The fast ion tail is investigated further in the region between the dotted lines.

measured with a spectrometer. Due to the initial velocity of the (fast) ions parallel to the line of sight, the measured light is Doppler shifted. This Doppler shift of the emitted light contains information on the projected velocity of the fast ions onto the line of sight. Spatial resolution is obtained using several lines of sight that intersect the neutral beam, in the ASDEX Upgrade case the beams 3 and 8, at different locations.
Figure 3.11 shows an example spectrum for one line of sight together with a synthetic spectrum calculated with the analysis tool FIDASIM [90] that uses the fast-ion distribution calculated by TRANSP (see section 5.1). The measured spectrum in black is a superposition of multiple components and the single contributions are individually simulated with FIDASIM. FIDASIM uses, besides the fast ion density, multiple information from the TRANSP simulation for example the beam geometry and beam parameters like the beam energy as well as additional plasma parameter such as the electron density and temperature. From this set of information and the line of sight geometry the individual spectral components are calculated.
First, and for the diagnostic most important, in red the emission of the fast ions can be seen. The fast ions are produced by neutral beam injection and/or ion cyclotron resonance heating. In TRANSP the fast ion distribution is calculated down to thermalization of the fast ions assumed at $1.5 \cdot T_i$. It can be seen that for the given line of sight these fast ions emit Doppler shifted light with a preferential Doppler shift towards higher wavelength, but there is also emission of fast ions with almost no Doppler shift or Doppler shift towards lower wave length. This behaviour is due to the fact, that the fast ions with the same energy, but different pitch angles have a different velocity component along the line of sight, which only can be probed. This Doppler broadening towards lower wavelength is emitted from trapped fast ions moving partially parallel to the line of sight away from the optics on their orbits. For the measurement of the FIDA emission only wavelength regions

can be used, which does not overlap with other contributions, like the beam emission. The chosen region in the spectrum is marked in blue. As only the parallel velocity component to the line of sight can be measured, the lower wavelength gives only a minimum energy for the measured fast ions. The preferential emission towards higher wavelength came from the non-radial injection of the neutral beams in ASDEX Upgrade in this case producing the fast ions.
The green contribution, named halo, is the contribution of the thermal ions. It is the emission from the same process as described for the fast ions, only for the thermal ions and represents the Doppler broadening of the Balmer-alpha peak according to the ion temperature. According to the Maxwell distribution the halo wavelength Doppler shift is symmetric. The transition from thermal-ion to fast-ion emission is only given by an arbitrary energy threshold, in TRANSP at $1.5 \cdot T_\mathrm{i}$. In the measured spectrum the central unshifed Balmer-alpha peak is cut out by a wire in the spectrometer to avoid over-exposure and cross-talk on the CCD as this component would be very dominant.
The beam emission is shown in yellow to orange. The three Doppler shifted emission peaks from the three energy components are also subject to Stark splitting. This splitting is caused by the Lorenz electric field from the Lorenz transformation of the magnetic field in the frame of reference of the fast neutral particle. The motional Stark effect polarimetry uses this radiation to measure the magnetic field pitch angle. A detailed description of this emission can be found in section 4. A proper prediction of this emission can be used as qualifier for a simulation.
The last modeled contribution is the bremsstrahlung in light blue, which is broad band radiation of the plasma and independent of the neutral beam.
Additionally there is radiation, which is almost impossible to be simulated, for example emission from the charge exchange process of fast ions with neutrals along the line of sight, which are not from the neutral beam. The neutral particle background density is at maximum known very inaccurate especially beyond the separatrix. Therefore, the so called passive radiation needs to be measured and for a proper comparison with the simulation should be subtracted from the measurement. The measurement of the passive radiation takes place at a point in time, where the diagnostic beam 3 is shortly switched off, furthermore this point in time should be close to the point of interest.

The number of photons in the FIDA wavelength region, in the blue shaded area, is now integrated for the synthetic diagnostic and the measurement. For several radial lines of sight at one point in time these integrated intensities are plotted versus the radial intersection of the line of sight with the neutral beam 3. For a radial comparison of the predicted fast ion distribution and the measurement. Such a radial FIDA profile can be seen in figure 3.12.
In figure 3.12 a) the radial distribution of the integrated number of photons can be seen. The data for 4 points in time in the black points are already corrected for the passive radiation in red. These points are now compared with the FIDASIM processed TRANSP simulation. However, the neutral beam used as doner for the neutral particle is attenuated towards the plasma center and this reduces the number of emitted photons from the fast ions. Therefore the measured profile is not proportional to the radial fast ion distribution.

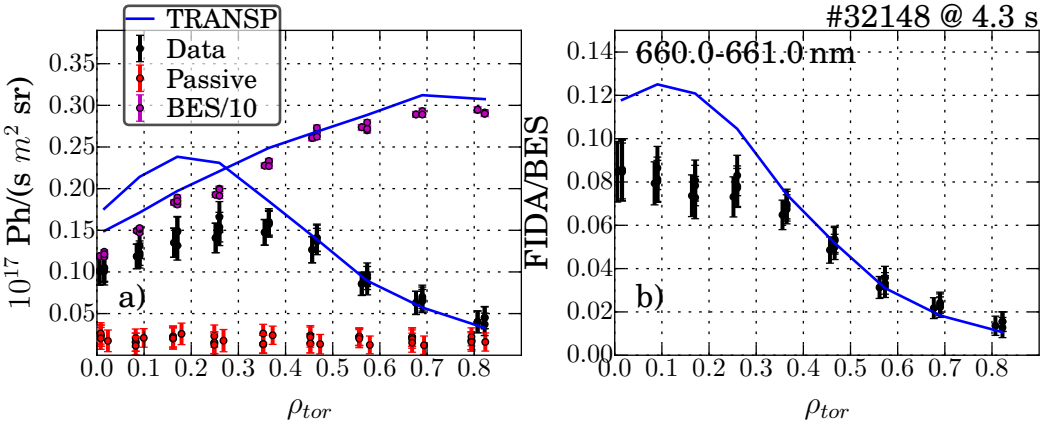

Figure 3.12.: a) Radial profile of the integrated number of photons from the FIDA region in black the measurement. In red is the passive radiation and in magenta the photon integration from the beam emission. b) The FIDA emission normalized by the beam emission together with the corresponding FIDASIM postprocessed TRANSP simulation.

To overcome this problem and reduce the influence of inaccurate calibrations of the spectrometer, the integrated FIDA emission is normalized to beam emission, represented by the Stark split high energy π-emission of the full energy component. The radial profile of the integrated photons from beam emission can be seen in magenta, and there is also a comparison with the TRANSP calculation. The resulting radial distribution of this FIDA emission normalized to the beam emission can be seen in figure 3.12 b). This dimensionless value corresponds more closely to the radial fast ion density profile.
The ASDEX Upgrade FIDA system consists of five optical heads with multiple radial views pointing on NBI beam 3 and one optical head on NBI beam 8. In figure 3.13 the five different groups of lines of sight on beam 3 can be seen.
The different view geometries enable tomographic reconstruction of the 2D fast-ion velocity distribution, measuring fast ions with at different positions in the fast ion velocity space. For more details on this 2D reconstruction see reference [91] and for more detailed description of the FIDA diagnostic, FIDASIM and the ASDEX Upgrade FIDA system see reference [17].

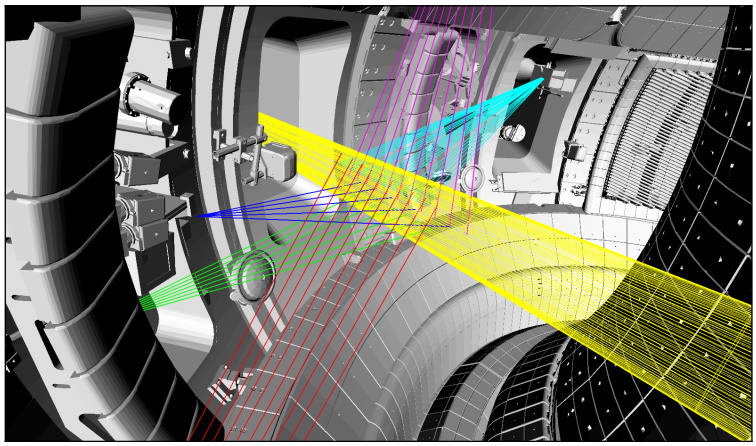

Figure 3.13.: In yellow the neutral beam 3 and the different lines of sight intersecting the beam which are used for FIDA measurements. The different colors indicating different optical heads with lines of sight with a comparable viewing geometry.

4. Upgrade of the ASDEX Upgrade Motional Stark Effect Polarimetry

Motional Stark effect polarimetry (MSE) is one of the main diagnostics to obtain information on the internal magnetic field structure of a fusion plasma. This is directly correlated with the safety factor and current distribution. The measurement can be used as a constraint for equilibrium reconstruction to gain information mainly in the core of a plasma, because closer to the center the uncertainties of the equilibrium derived from magnetic probe measurements increase very strongly (see figure 2.2). This non-invasive technique is based on the polarization measurement of Balmer alpha line radiation from excited atoms of a high energy neutral beam that interacts with plasma atoms. The Stark splitting of the line emission is mainly caused by the Lorenz electric field ($\vec{E} \sim \vec{v} \times \vec{B}$) seen by the fast beam atoms in a magnetic field. The resulting radiated π- and σ-lines are polarized perpendicular to each other. From the polarization measurement the projection of the magnetic field vector can be calculated.

4.1. Diagnostic

Motional Stark Effect polarimetry (MSE) is based on the injection of fast neutral particles of velocity $\vec{v}$ into a magnetic field $\vec{B}$. A Lorenz electric field $\vec{E_{\mathrm{L}}} = q \cdot (\vec{v} \times \vec{B})$ appears in the frame of reference of the moving particle. For a typical ASDEX Upgrade beam energy of 60 keV and magnetic field of 2.5 T, the electric field strength is around $5 \cdot 10^6\,\mathrm{V\,m^{-1}}$. Through collisions of a given fast neutral particle with plasma electrons and ions, the atom becomes into an excited state. The Balmer alpha emission is subject to Stark splitting due to the electric fields, dominated by the Lorenz electric field and the radial electric field. Zeemann splitting is negligible. For a non-perpendicular view with respect to the beam axis this light is also Doppler-shifted and hence separated in wavelength from the bulk plasma emission.
Commonly, in magnetic fusion experiments hydrogen isotopes are used as neutral beam particles. The ASDEX Upgrade MSE system is optimized for the standard deuterium injection with 60 keV beam energy and a magnetic field around 2.5 T at the magnetic axis. The Balmar alpha n=3 to n=2 (λ_{D_α}=656.1 nm) transition is used, with the transition from five to three excited states. Restricted by selection rules nine distinct transitions are allowed. The three central lines are polarized perpendicular to Lorentz electric field and called σ-lines (German “senkrecht”). The other six lines are polarized parallel to the Lorentz field and called π-lines (German “parallel”).

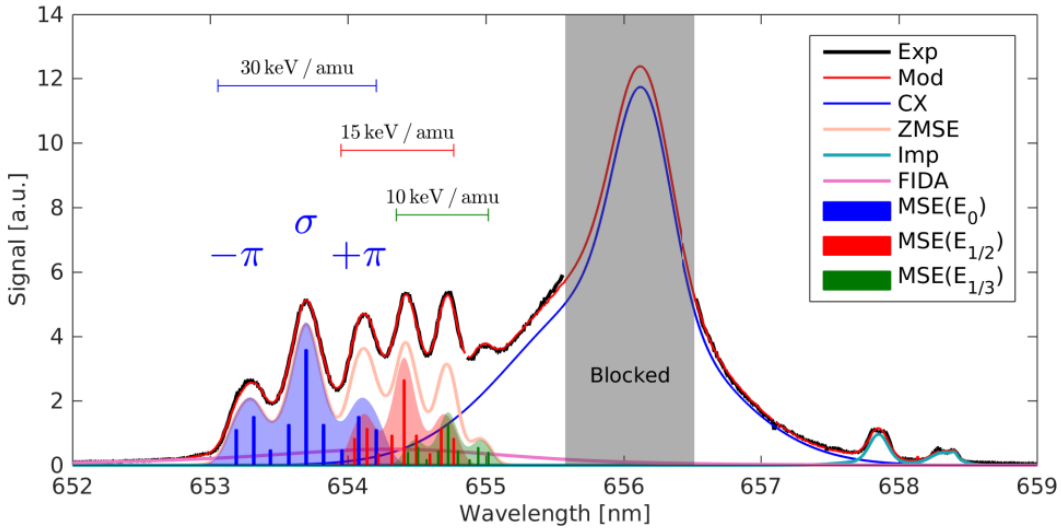

Figure 4.1.: Calculated spectrum for the Balmer-alpha emission of a 60 keV deuterium beam with the viewing geometry of a MSE line of sight of ASDEX Upgrade. Clearly separated are the π- and σ-line of the full-energy component (30 keV/amu). This figure is adapted from reference [92].

The measurement of the projection of the polarization vector onto the plane perpendicular to the line of sight in combination with the known beam velocity vector allows the reconstruction of the projection of the magnetic field vector in this plane. In combination with the known vacuum toroidal magnetic field and information on the diamagnetic contribution, the MSE measurements are a good indication for the poloidal magnetic field, which is induced by the plasma current. At the different radial positions, the measurements constrain the enclosed poloidal magnetic field, improving the current profile reconstruction, in the equilibrium reconstruction (see section 2.1.1).
The line of sight geometry of ASDEX Upgrade's MSE system leads to a blue shift of the beam emission. In figure 4.1 a calculated ASDEX Upgrade spectrum in comparison with a spectral measurement is shown for one MSE line of sight. The central Balmer alpha light in this measurement is blocked, but the charge exchange halo next to it can be seen. The halo is the emission of thermal ions which are neutralized into an excited state by a charge exchange process with a beam neutral, followed by a de-excitation cascade into the ground state. The same process with fast ions produced by the neutral beam leads to emission with a stronger Doppler shift, into the same wavelength region as the Stark emission. This radiation is called FIDA radiation and is measured by the FIDA diagnostic (see section 3.3.8). Fortunately the FIDA radiation is unpolarized and therefore does not interfere with the MSE measurement. The three different Stark multiplets, shown in blue, red and green, correspond to the three energy components of the 60 keV neutral beam 3, introduced in section 3.2.1. Obviously, due to the spectral broadening the emission of the half- and third-energy component overlap with each other. Also the lower energy π-lines of the full-energy component overlap with the half-energy component. Therefore only the σ- and the high-energy π-lines ($-\pi$ in figure 4.1) of the full-energy component are used.

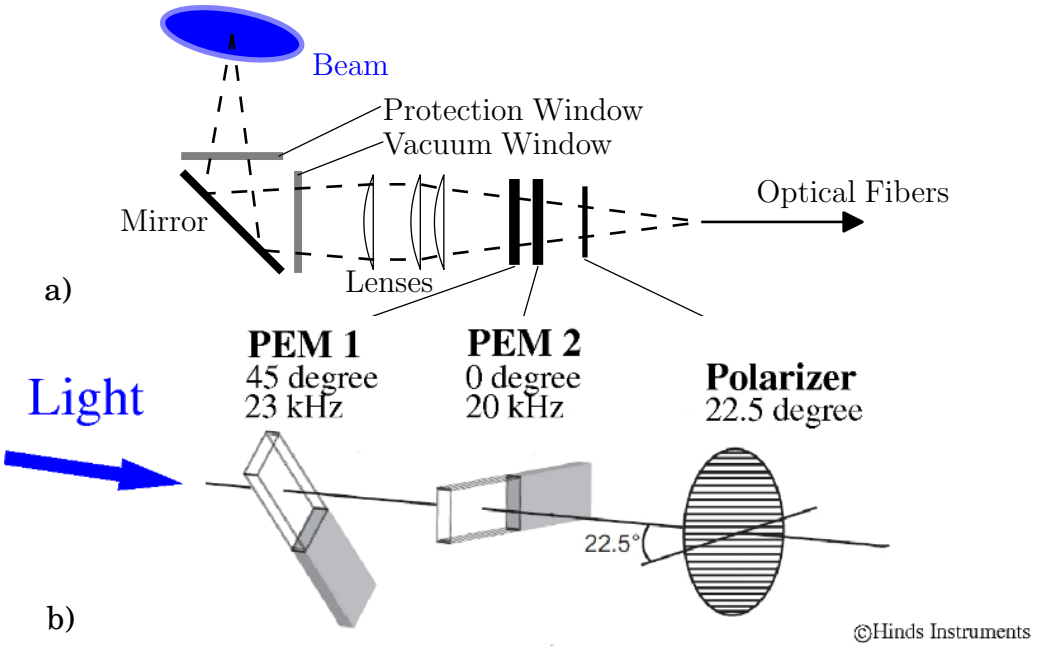

Figure 4.2.: a) Optical system to guide the polarized light from the plasma to a PEM system encode the polarization to intensity modulation. These light is transmitted by optical fibers to the detector unit. b) Schematic of the PEM system encoding the polarization into an intensity modulation. This figure is adapted from reference [19].

There are multiple techniques to determine the orientation of the electric field causing the Stark effect, for example by the ratio of the intensities of the π- and σ-line or by the measurement of the polarization direction of one of the lines. In ASDEX Upgrade the polarization measurement method is used. A detailed description of this technique, also known as Stokes polarimetry, and a description of other methods can be found in reference [92].
In Stokes polarimetry [93] a rotating polarizer is used encoding the polarization information into an intensity modulation. Figure 4.2 a) shows the implementation of the optical system in ASDEX Upgrade from the plasma to the optical fibers. After a protection window, made out of fused silica and used as transparent shielding for the mirror, the light is reflected through a vacuum window into a lens system that focuses the collected light into optical fibers. These optical fibers guide the light to the detector system placed outside the torus hall. Due to the fact that optical fibers do not conserve the polarization of light, the polarization must be translated into an intensity modulation that can be transferred by the optical fibers. In figure 4.2 b) the principle of such a conversion system can be seen. Polarized light is transmitted through two photoelastic modulators (PEMs) with their optical axes rotated by 45° with respect to each other and getting birefringent periodically with 20 kHz and 23 kHz due to a periodical activation of piezo crystals. Behind the two PEMs a polarizer is placed at an angle of 22.5°. This whole systems acts like a rotating polarizer in the kHz range.

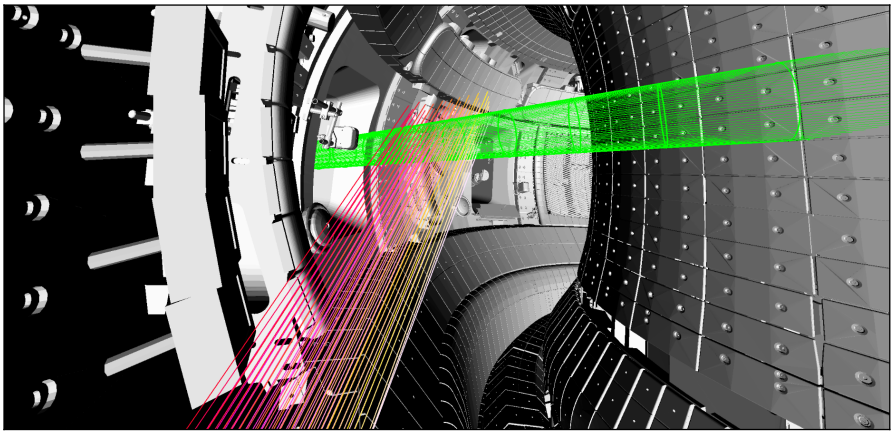

Figure 4.3.: Geometry of the 60 lines of sight, in six rows with ten columns, of the ASDEX Upgrade motional Stark effect polarimetry system from the top of the mirror box in sector 1 to the intersection with NBI beam 3 (green) in sector 15/16.

The state of polarization can be described by the 4-component Stokes vector

$$\vec{S} = \begin{pmatrix} S_0 \\ S_1 \\ S_2 \\ S_3 \end{pmatrix} = I \begin{pmatrix} 1 \\ p\cos 2\gamma_\mathrm{m} \cos 2\chi \\ p\sin 2\gamma_\mathrm{m} \cos 2\chi \\ p\sin 2\chi \end{pmatrix} \tag{4.1}$$

where I is the total measured intensity, p the polarization fraction, γ_m the polarization angle and χ the degree of ellipticity. The first component corresponds to the intensity, the second and third component represents the degree of parallel and perpendicular polarization, while the fourth component covers the degree of circular polarization. With the ratio of the second and third component the polarization angle can be expressed as

$$\gamma_\mathrm{m} = \frac{1}{2} \arctan\left(\frac{S_2}{S_1}\right). \tag{4.2}$$

The modulus of the Stokes components S_1 and S_2 is proportional to the intensity modulation at twice the respective PEM frequency, i.e. $|S_1| \propto I(40\,\mathrm{kHz}) = I_1$ and $|S_2| \propto I(46\,\mathrm{kHz}) = I_2$, so the polarization angle can be calculated by

$$\gamma_\mathrm{m} = \frac{1}{2} \arctan\left(\frac{I_2}{I_1}\right). \tag{4.3}$$

Due to the fact that the measured intensities contain no information on the sign of S_1 and S_2 equation (4.3) covers only 45°. The phase difference of the two modulations is used to expand the 45° coverage for the polarization to the full 180°.

Figure 4.3 shows the viewing geometry of the ASDEX Upgrade MSE system. The NBI Beam 3 is intersected by 60 lines of sight arranged from the edge to the center of the plasma in ten columns with six rows each. The intersections with the beam are at equidistant

radial positions from $R = 1.65\,\mathrm{m}$ to $R = 2.05\,\mathrm{m}$ and vertical positions from $z = 0.0\,\mathrm{m}$ to $z = 0.12\,\mathrm{m}$. Due to the beam's finite width with a diameter in the order of 20 cm, the intersection with a line of sight covers a finite R and z range. This aspect is further investigated in appendix A.5.3. Additionally, the beam gets attenuated while propagating through the plasma depending on the electron density. This decreases the intensity of emitted light closer to the center and increases the susceptibility to distortion.
After transmission through the fibers behind the optical system described above, the modulated light signals are measured by ten detector units. In each of these units the light of two neighboring lines of sight, lying on top of each other is coupled for a better signal to noise ratio. From the equilibrium reconstruction it is known that the deviation in the angle between these two lines of sight is negligible. This light is parallelized and the light from a wavelength region corresponding either to the π- or σ-line (see figure 4.1) is transmitted through a temperature-controlled narrow band-pass filter. These filters are tuned individually for each line of sight and the width of the transmitted region is on the order of 0.2 nm to avoid light from the π component in the σ measurement and vice versa. However, such cross talk would only lead to an increase of noise, unless the wrong component becomes the dominant part. Behind the filters the light is focused and measured with photomultipliers with a sampling rate of 250 kHz. Due to the fact that the changes in the current profile and q profile are slow, multiple periods are taken for a more accurate phase and intensity reconstruction. Therefore the time resolution of the ASDEX Upgrade MSE system is 40 Hz and the statistical uncertainty is on the order of 0.2°.

4.2. Absolute Calibration

Most of the world wide used MSE systems are not absolutely calibrated. To use data of a not absolutely calibrated MSE system, individual shifts for each line of sight are necessary. Afterwards the dynamic in the measured angles can be used either to compare with synthetic diagnostics or to constrain an equilibrium. For trustworthy offsets the real value at one point in time must be known, for example from an otherwise constrained equilibrium. However, non-linear effects can distort the measured dynamics and lead to unknown systematic uncertainties. Therefore with an absolutely calibrated MSE system the measured angles can be used to constrain an equilibrium at every point in time without additional information.
The approach to get the first absolutely calibration of the ASDEX Upgrade MSE system consists of three steps. The first step is the quantification of one absolute offset (see section 4.2.1) with the measurement of a known source of polarized light. The second step is the measurement of the instrument function (see section 4.2.2), with the measurement of all possible polarization angles. The last step is a dedicated measurement of the effect of the magnetic field (see section 4.2.3) and further environmental factors (see appendix A.5) such as pumping down the vacuum chamber, which are not taken into account during the measurement of the instrument function.

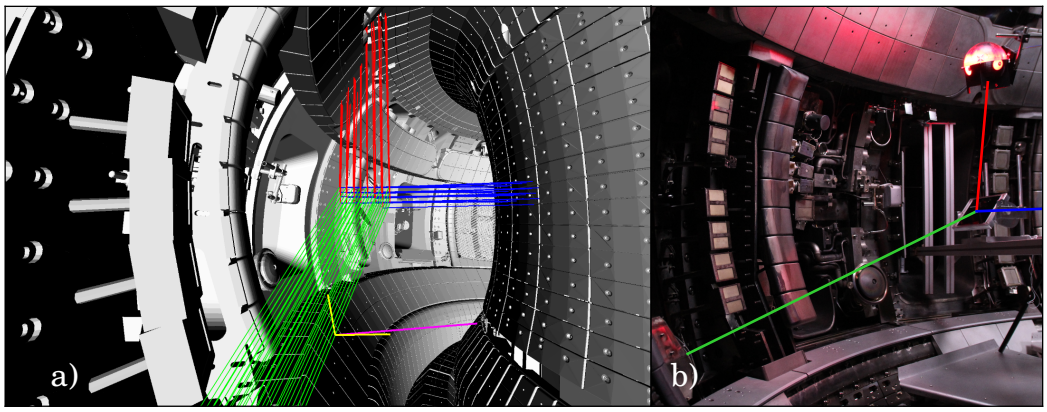

Figure 4.4.: Setup to measure an absolute offset of the MSE system. a) Shown in green are the 3D-FARO measured lines of sight and in red the similarly measured path of light from the light source to the mirror. In blue is the polarization vector. In magenta $\vec{u}_\perp$ for the common zero and in yellow $\vec{x}$ and $\vec{y}$ can be seen for one line of sight. b) Photo of the setup, at the top the integrating sphere for unpolarized light and below the mirror aligned according to the Brewster condition.

4.2.1. Absolute Offset

Before the measurement of an absolute offset is possible, a diagnostic coordinate system in the torus must be defined to obtain a zero degree marker. This coordinate system is individual for each line of sight, with $\vec{x}$ and $\vec{y}$ perpendicular to each other and to the line of sight $\vec{s}$, but with a common absolute zero angle for all lines of sight together. This coordinate system is given by

$$\begin{aligned} \vec{y} &= \vec{s}_{\mathrm{LOS}} \times \vec{u}_\perp \\ \vec{x} &= \vec{s}_{\mathrm{LOS}} \times \vec{y}. \end{aligned} \tag{4.4}$$

The common zero is a definition and introduced by $\vec{u_\perp}$. $\vec{u_\perp}$ can be seen in magenta in figure 4.4. For practical reasons this vector is chosen to be perpendicular to all lines of sight. Furthermore the ten radial lines of sight of each row lie in one plane and $\vec{u_\perp}$ is chosen to be as parallel as possible to the average of the six planes corresponding to the six rows of lines of sight. For one line of sight also the $\vec{x}$ and $\vec{y}$ can be seen in yellow. The conventional method to measure the line of sight geometry was not accurate enough, therefore a new method was developed and used. A description of this method can be found in appendix A.1. The intersection of the lines of sight with the neutral beam 3 can be seen in figure 4.3.

The determination of an absolute offset is achieved by the measurement of a known polarized light source in the torus. An unpolarized light source was adjusted in the torus in a way that light is reflected at a mirror, aligned within the Brewster condition, into each line of sight of the MSE system individually. The polarization of the now linearly polarized light is measured with the MSE system. This measured polarization angle is compared with the calculated polarization angle from the geometrical reconstruction. The setup and the

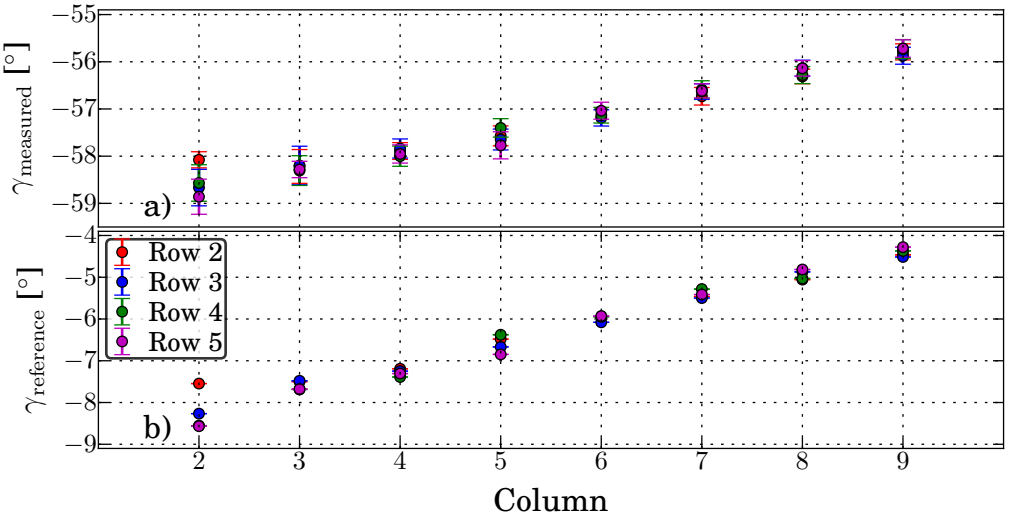

Figure 4.5.: Measurement of an absolute offset. a) Angle measured with the MSE system. b) Geometrical reconstructed reference angle in the torus coordinate system of the MSE diagnostic, see blue lines in figure 4.4.

geometrically reconstructed reference polarization vector can be seen in figure 4.4.
For the geometrical reconstruction the position of the light source and the reflection spot on the mirror were measured with the new evolved prototype probe head for the Nikon 3D-joint-measurement-arm [94]. The vector perpendicular to the line of sight and reflected path of light from the mirror to the light source is the polarization vector

$$\vec{x}_{\text{polarization}} = \vec{s}_{\text{LOS}} \times \vec{s}_{\text{Brewster reflected}}. \tag{4.5}$$

The angle of this vector with respect to the diagnostic coordinate system is used as reference angle

$$\gamma_{reference} = \arctan\left(\frac{\vec{y} \cdot \vec{x}_{\text{polarization}}}{\vec{x} \cdot \vec{x}_{\text{polarization}}}\right). \tag{4.6}$$

The difference of the reference and measured angle is the absolute offset for this specific polarization. In figure 4.5 the measured and reference angles are shown for 31 central channels. The channel of column 6 and row 2 is not measured because the light transmission is too low, probably due to a broken fiber. The distorted light beams of the unused channels can be seen in appendix A.3 figure A.6.
The uncertainty of the measured angle is given by the standard deviation of the measurement, based on the noise of the angle measurement. For the uncertainty of the geometrical reconstructed polarization the fact is used, that the polarization vector must be in the x-y-plane. Therefore the angle between the x-y-plane and the reconstructed polarization vector of each line of sight is taken

$$\sigma_{\gamma_{reference}} = \arcsin\left(\vec{x}_{\text{polarization}} \cdot (\vec{x} \times \vec{y})\right). \tag{4.7}$$

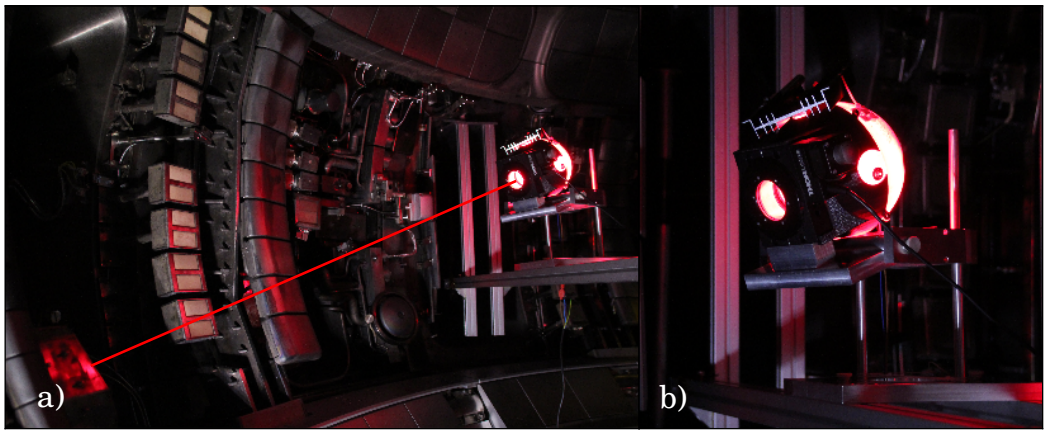

Figure 4.6.: Measurement of the non-linear part of the instrument function. a) Photo of the mounted setup on a rail at the expected neutral beam position. b) Enlarged image of the remotely controlled Thorlabs rotation stage NR360S [98] hosting the polarizer and backlit by an integrating sphere.

A difference between the reference and measured angle in the order of $\approx 50°$ can be found for all channels. Regarding this absolute offset the square error propagation leads to a mean uncertainty of $\pm 0.23°$, dominated by the uncertainty of the measured angle.

4.2.2. Correction of Non-Linear Effects

In former calibration measurements at ASDEX Upgrade [95] and at Alcator C-Mod [96], a non-linear behaviour in the instrument function was found. Multiple reasons for this behaviour were determinded or can be assumed, for example polarization aberrations in the optical system or a non-ideal polarimeter response. All these effects are discussed in reference [97].
To measure this non-linear part of the instrument function a rotating polarizer is used. This polarizer is aligned perpendicular to each single line of sight in the torus, at approximately the expected intersection position of the line of sight with the neutral beam 3. Behind this polarizer a uniform and unpolarized light source is mounted. This setup can be seen in figure 4.6. After the alignment, two measurements of a 400° rotation of the polarizer in 40 s were recorded individually for each line of sight.
In figure 4.7 the reconstruction of the the correction function for one line of sight can be seen. In the first row (a) the temporal evolution of the two measurements is plotted. In the second row (b) the time was translated into an angle of the polarizer via a linear regression to the measured angle. Due to the fact that only the angle measured for the absolute offset is known, the arbitrary angle of the polarizer was shifted such that it matches the reference angle of section 4.2.1 at the corresponding measured angle. In the last step the expected correction function

$$f(\gamma_\mathrm{m}) = a \cdot \gamma_\mathrm{m} + b \cdot \sin(4 \cdot \gamma_\mathrm{m} + \phi_1) + c \cdot \sin(2 \cdot \gamma_\mathrm{m} + \phi_2) + d \cdot \sin(8 \cdot \gamma_\mathrm{m} + \phi_3) + e \quad (4.8)$$

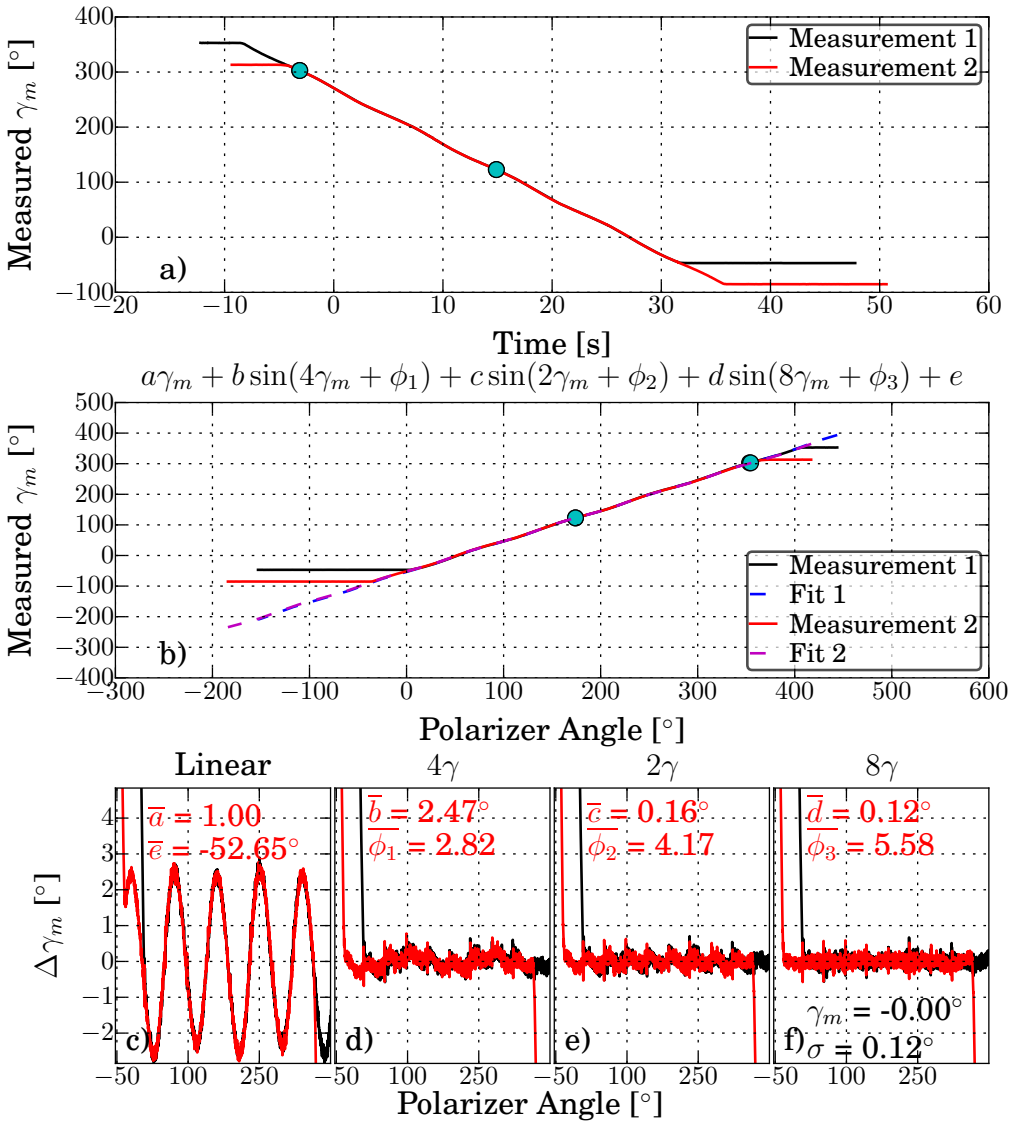

Figure 4.7.: Measurement of the non-linear instrument function. a) The measured angle versus time. b) Translation of time into angle of the polarizer and shift to match the reference angle by the corresponding measured one (see section 4.2.1). c) Subtraction of the linear part of the fit function (equation (4.8)). d) Additionally subtraction of the 4γ-periodic-part. e) Furthermore subtraction of the 2γ-periodic-part and f) finally subtraction of also the 8γ-periodic-part.

was fitted to the data. In the last row the four different terms in order of their impact were successively subtracted. Firstly, the linear part, secondly the 4γ-part, thirdly the 2γ-part and fourthly the 8γ-part. In the shown case the measurement subtracted by the extrapolated function is at an averaged angle of zero and the non-periodic noise is on the order of $0.1°$. The error on the fit parameters is less than 1%, therefore only the $\approx \pm 0.1°$ will be propagated further as statistical error. To correct the measured data the inverse function of $f(\gamma_m)$ is needed. The fitted function has no analytically solvable inverse function, therefore a numerical approach is used for the inversion.
In figure 4.8 a summary of all parameters can be seen. The column dependency of the parameters b, c and d is a sign for a geometrical contribution to the instrument function. Polarization rotation due to a difference in the transmission of the parallel and perpendicular component of the polarization expressed by the Fresnel equations can be a possible explanation. In this case the value of the parameters changes, due to the variation of the angle of incident for the different lines of sight in the optical components in front of the PEMs.

4.2.3. Further Effects

The determination of the non-linear effects and the measurement of the absolute offset of the MSE diagnostic were made in the field-free and vented torus. These two restrictions should be investigated next. On the one hand the effect of the Faraday rotation due to magnetic fields up to 3 T at the axis in the torus must be evaluated. On the other hand, it is conceivable that, for example, stress-induced birefringence of the vacuum window can lead to a polarization rotation when the vessel is under vacuum. Due to the fact that the Faraday effect is non-negligible in the absolute calibration it is discussed in the following section. In contrast the other examined effect are negligible. The description of these studies can be found in the appendix A.5.
In detail three further effects are investigated. Firth the influence of the vacuum is investigated in appendix A.5.1. However the change of $-0.02°$ during the change from the vented ($\sim$ 1000 mbar) to the mostly evacuated vessel ($\sim$1 mbar) is one order of magnitude smaller than the uncertainty of the measurement. Therefore the vacuum effect is negligible. Second the long-term stability is examined in appendix A.5.2. Fluctuations in the order of $1°$ were found, but the reason is not jet clear and therefore needs to be investigated further more.
Finally the influence of the finite beam diameter is evaluated in appendix A.5.3. This effect is also negligible with respect to the uncertainties of the diagnostic.

Faraday Effect

The Faraday rotation is a change of the polarization direction of linear polarized light in an optical medium exposed to a magnetic field oriented parallel to the propagation direction.

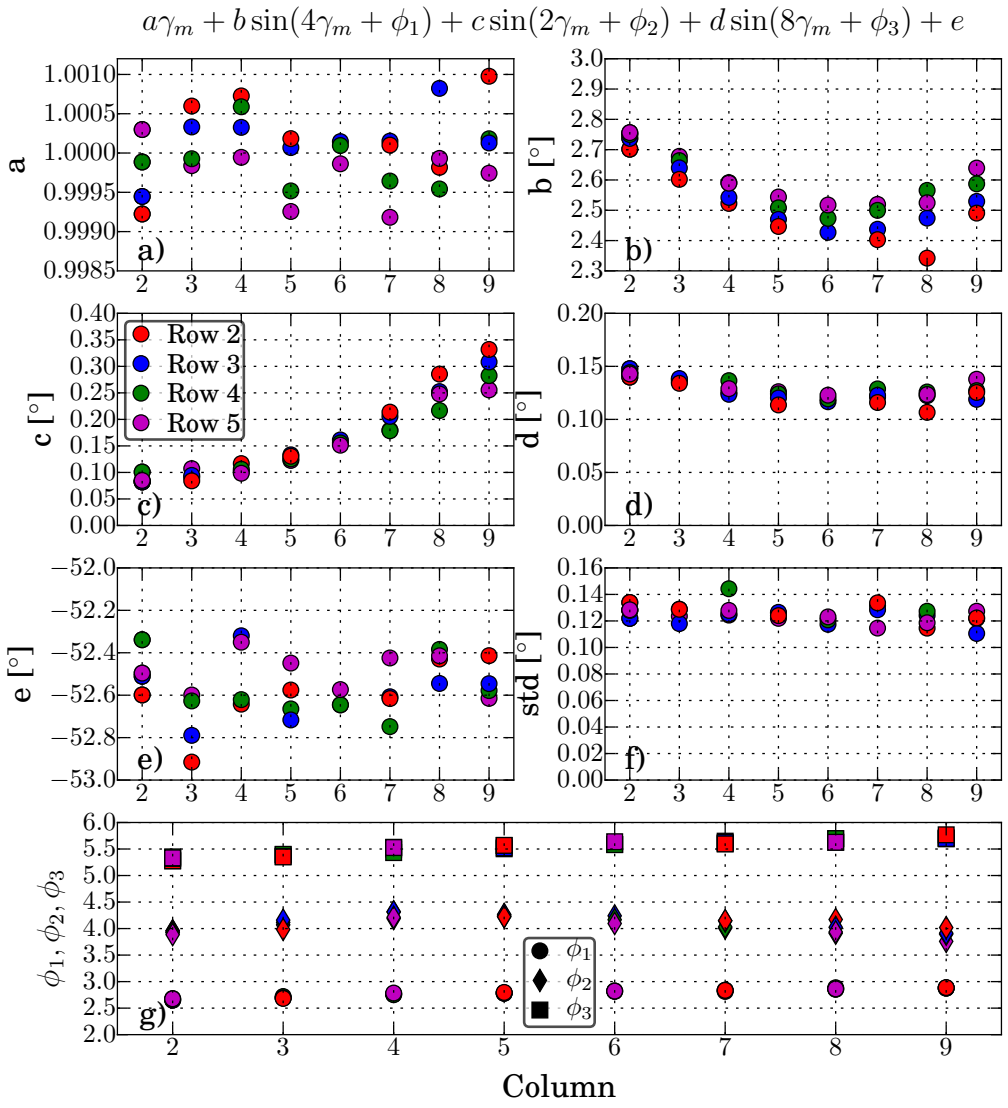

Figure 4.8.: Overview over the parameters to correct the instrument function for all lines of sight of the MSE system, corresponding to figure 4.7. a) Parameter a is the slope of the linear part expected to be one. b), c) and d) for the parameter b, c and d for the amplitudes of the 4γ, 2γ and 8γ-parts. e) The offset dominated by the measurements from section 4.2.1. f) The resulting standard deviation of the measurement, representing the statistical error for the non-linear correction. g) The three different phases for the sinusoidal contributions of the non-linear instrument function.

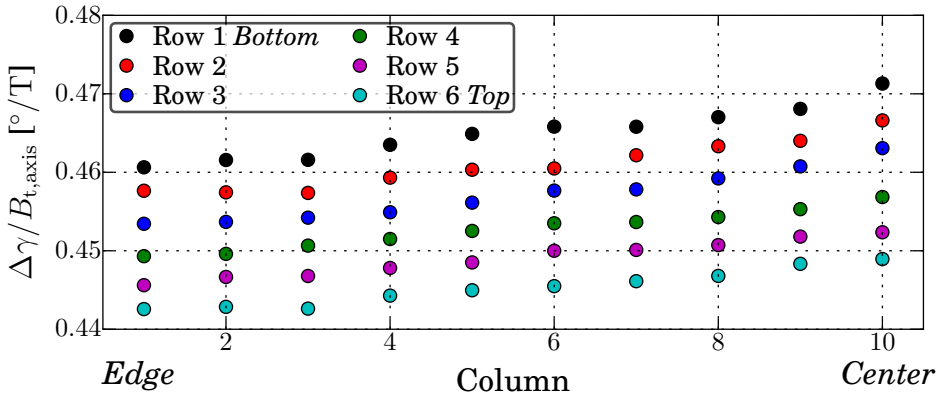

Figure 4.9.: Calculated Faraday rotation for each line of sight in the protection window normalized to the magnetic field on the axis.

This polarization rotation is given by

$$\Delta\gamma = V \cdot d \cdot B_{\parallel} \tag{4.9}$$

with the Verdet constant of the optical medium V and d the distance the light passes through the medium. For the MSE system at ASDEX Upgrade multiple optical components are involved before the polarization is transformed into a intensity modulation. The protection window in front of the mirror box is expected to be the main contributor to the Faraday rotation, a schematic illustration of the optical system can be seen in figure 4.2. As this is the only optical component where the path of light passes the optical component with a component parallel to the toroidal magnetic field, all other magnetic field components are orders of magnitude smaller and therefore negligible. Additionally the protection window is made out of fused silica with a Verdet constant of $3.67\,\mathrm{rad\,T^{-1}\,mm^{-1}}$ while the lenses are made of SF6L with a Verdet constant two orders of magnitude less.
With this assumption and the line of sight geometry the Faraday rotation in the protection window is calculated. In figure 4.9 the result normalized to the magnetic field at the magnetic axis can be seen.
The calculated Faraday rotation normalized to the magnetic field on the axis is on the order of $\approx 0.45°/B_{t,axis}[\mathrm{T}]$. The difference between the different lines of sight within a row is small due to the small change of the toroidal magnetic field within the protection window. The bigger changes between the different lines of sight within a column are due to the different angles of incidence (between 25-35°) at which the lines of sight enter the protection window, changing slightly the strength of the parallel magnetic field and the path length through the window.
A measurement of the Faraday rotation of the system was also performed in the vented torus during a technical shot day before the campaign 2017. For these measurements a polarized light source was mounted in front of the protection window. During the maintaining break before the 2017 campaign and before the calibration was made the protection window was permanently replaced by a thinner one with an anti-reflection coating. The shown

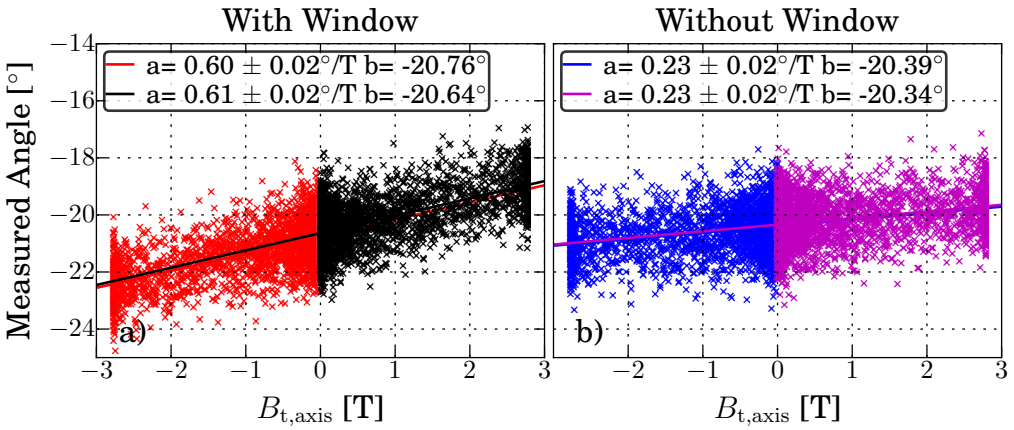

Figure 4.10.: Measurement of the Faraday rotation in a) with and in b) without the protection window for one channel. The toroidal magnetic field on the axis was either ramped up or down to ±2.8 T before returning to 0 T.

measurements and calculations are performed with the new window. All lines of sight were simultaneously illuminated with a polarized light source. The polarization was measured while the toroidal magnetic field of the vented ASDEX Upgrade was ramped up to 2.8 T and back to 0 T and in a second measurement ramped down to -2.8 T. In a third and fourth measurement the protection window was removed and the field was again ramped up and down to ±2.8 T. In figure 4.10 the non-linearly-corrected measured angles for one channel are plotted versus the toroidal magnetic field on the axis. The measured angles are plotted without any time averaging, leading to an increased statistical scatter on the measurements. A linear fit is made to estimate the amount of Faraday rotation.
Evidently the two measurements in the different field directions with and also without the protection window align well with each other. The uncertainty on the Faraday correction factor is $\pm 0.02°/B_{t,axis}[T]$. As expected the slope of the measurement without the window is smaller. Also the offsets are slightly higher with respect to the measurements with the window. One explanation for this behavior can be field independent polarization rotation of the protection window due to non-perpendicular incidence of the lines of sight on the protection window. From the Fresnel equations a different transmission coefficient for parallelly and perpendicularly polarized light appears. This leads to a rotation of the polarization of the superposition of both components. However, this effect is independent of the magnetic field and the vacuum and therefore part of the instrument function characterized in the sections 4.2.1 and 4.2.2.
In Figure 4.11 the slopes for the different columns are compared. The measurements take place in rows 3 and 4. The Faraday rotation of the complete system is on the order of $\approx 0.62 \pm 0.02°/B_{t,axis}[T]$. This is ≈ 35% higher than expected from the calculations for the protection window. However, the calculation is in agreement with the difference between the measured slopes with and without the protection window within the uncertainties. This supports the initial assumption that the main part of the Faraday rotation is caused by the protection window with ≈ 65%, but the Faraday rotation in other components is not

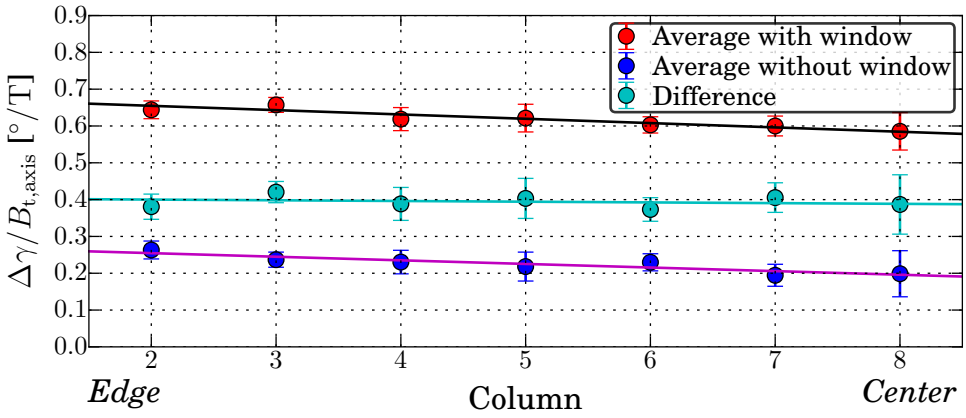

Figure 4.11.: Measured normalized Faraday rotation in the different columns. The red measurements correspond to the total Faraday rotation. The blue measurements represents the Faraday rotation without the protection window, while the difference plotted in cyan correspond to the dominant contribution of the protection window.

negligible. This fraction of the Faraday rotation can take place for example in the Vacuum window or the PEMs which lies outside the toroidal field coils and get disturbed by a diffuse magnetic field.

4.2.4. Combination of All Effects

In figure 4.12 the different corrections on one measured channel for the discharge #33864 from the campaign 2017 can be seen. Due to the fact that the correction of the absolute offset is in the order of 60°, the raw angles are not shown in this plot. Starting point is the offset corrected data to resolve the further corrections. This offset is a shift evaluated by the measurement from the known polarization (see section 4.2.1).
The correction of the non-linear part of the instrument function (see section 4.2.2) in this case contributes a reduction in the order of 2.4°. The fitted instrument function is not analytically invertible, therefore a numerical inversion of

$$f(\gamma_m) = a \cdot \gamma_m + b \cdot sin(4 \cdot \gamma_m + \phi_1) + c \cdot \sin(2 \cdot \gamma_m + \phi_2) + d \cdot sin(8 \cdot \gamma_m + \phi_1) + e \quad (4.10)$$

is used. The correction of the absolute offset is also covered within this correction in the factor e. For the visualization in figure 4.12 it was done once individually, in general the absolute offset correction is done within the instrument function.
The Faraday correction (see section 4.2.3) for the toroidal magnetic field of -2.6 T at the axis, leads in this case to a increase of the angles in the order of 1.9°. As the Faraday correction could not be measured as part of the instrument function and the instrument function is angle dependent, the sequence of correction could play a role. Due to the fact that the Faraday effect of the protection window can be separated from the further Faraday rotation, first the Faraday correction for the protection window is done, then the non-linear

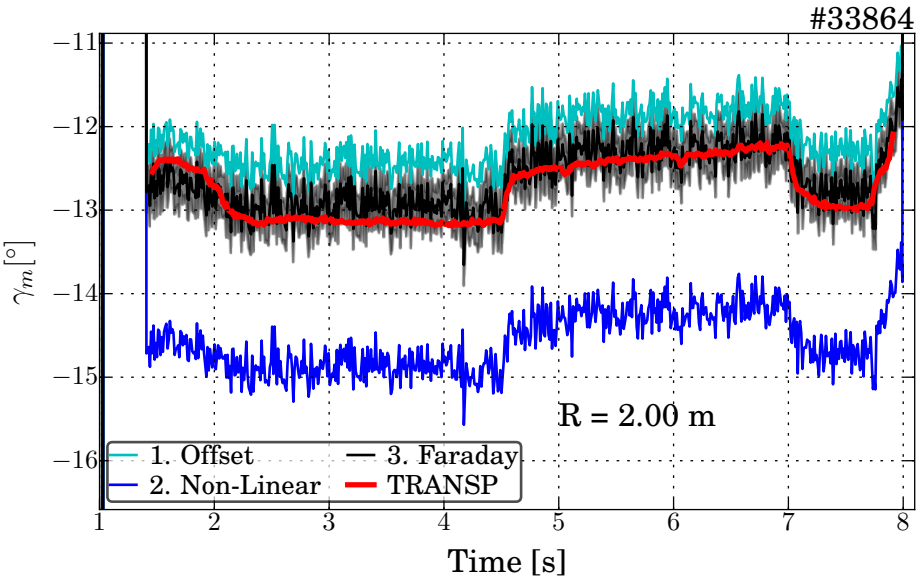

Figure 4.12.: Measured motional Stark effect angles of the discharge #33864 with successive corrections in comparison with a synthetic TRANSP prediction at an edge channel. Two lines of sight, lying at the same radial position vertically on top of each other, are combined. The uncertainty is only shown for the fully corrected measurement.

correction is performed and afterwards the remaining Faraday correction. This could lead to minor uncertainty, because the optical components, as well as the protection window covering the Faraday rotation are part of the instrument function and therefore the Faraday rotation and the non-linear changes in the polarization happen simultaneously.
Nevertheless a comparison between the corrected measurement and a calculation from a TRANSP equilibrium lead in this case for this combined lines of sight to a perfect agreement within the uncertainty of the measurement.
In figure 4.13 the comparison between the TRANSP simulation and all seven corrected measured σ channels in this discharge can be seen. The corrected measurements fit to the simulations, but from the edge towards the plasma center the deviation starts to increase up to more than $\pm 1°$, which is much larger than the uncertainties of the measurement. On the one hand the current distribution and the magnetic axis in the equilibrium from the simulation might be not completely correct, as it only depends on the pressure constraint. This hypothesis is investigated by constraining an equilibrium in IDE with the MSE angles (see section 4.3). On the other hand, interfering polarized background could play a role. As the beam gets attenuated towards the plasma center, the intensity of the emitted light decreases. These channels are therefore more susceptible to polarized background.
A further hint for polarized background can be found in the comparison between the measured and corrected π- and 90°-shifted σ component, which can be seen in figure 4.14. In this discharge seven lines of sight measure the σ component and three measure the corresponding π component. As there is at the moment no possibility to measure both components on the

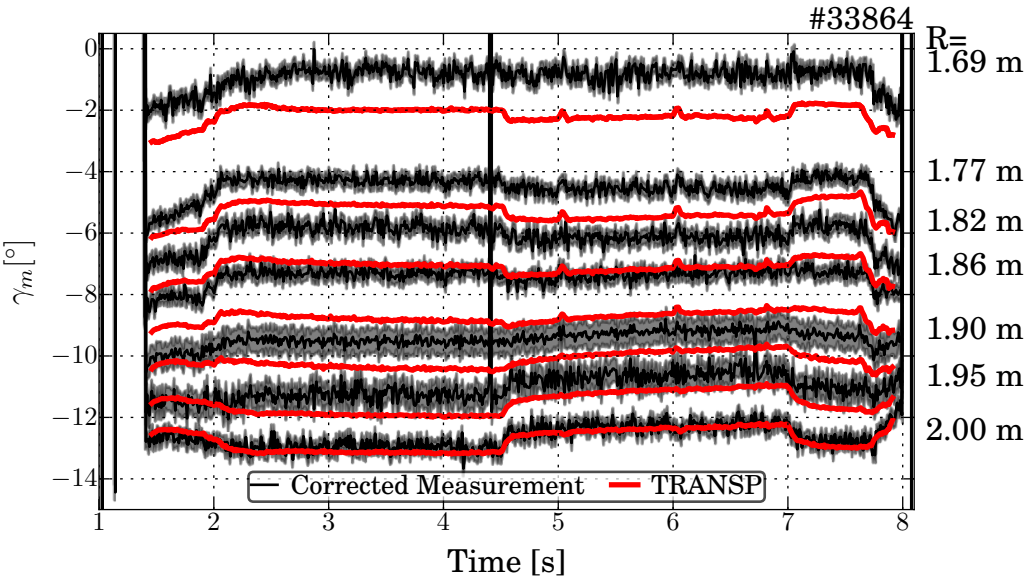

Figure 4.13.: Comparison of the corrected σ measurements with TRANSP simulated angles, for seven different radial channels.

same line of sight, two pairs of lines of sight were chosen vertically on top of each other, to measure the π- and the corresponding σ-component. The small shift in vertical direction close to the mid plane does not significantly change the expected polarization angle [19], which is in agreement with the TRANSP predictions shown in gray. Therefore the intrinsic 90° deviation is expected. In the case of these three channels the deviation is in the order of 87–88° in the beginning and starts to increase during the discharge. Simultaneously the deviation from the TRANSP predictions increases, especially for the π-components.
As mentioned before, a reason for this behaviour could be polarized background. The origin for this polarized light could be ASDEX Upgrade's full metal first wall on which unpolarized light can be reflected in a polarized state. This would lead to a broadband polarized background interfering with the measurement. Due to the fact that the intensity of the π-component is only half the intensity of the σ-component, the π-component is much more affected by polarized background. Additionally, the beam attenuation lead to a signal decrease towards the center, making them much more susceptible for interfering background. All this can be seen especially in the central π channel where the deviation strongly increases from 2 seconds on, while the TRANSP predicted angle does not change. The increase from 2 seconds on can be explained by increasing radiation from the plasma in this discharge.
The influence of polarized background on MSE angles was measured for the first time in the Alcator C-Mod Tokamak. To correct this effect a polychromator was designed to simultaneous measure the σ-, π-component and two times the polarized background on the same line of sight. With the assumption of a broadband polarized background, this background can be subtract in the signal region in the post processing [96].
In ASDEX Upgrade a similar polarized background was found in reference [19]. In cooperation with the MSE group of Alcator C-Mod and the Massachusetts Institute of Technology

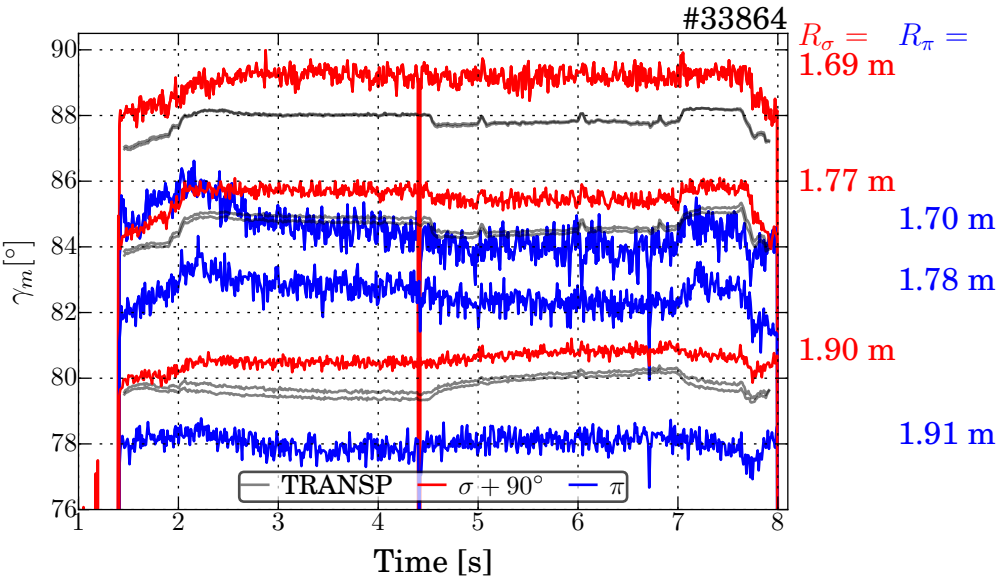

Figure 4.14.: Comparison of the corresponding π- (blue) and 90° upshifted σ-measurements (red) at similar radial positions, additionally in gray the predicted angles from TRANSP, where the π and σ channels lying perfectly on top of each other. Therefore the strongly increasing deviation in the central channel is unexpected from the equilibrium.

a polychromator for ASDEX Upgrade was developed. A short overview on the polychromator can be found in section 4.4, a more detailed description of the working principle, the technical implementation as well as first measurements is given in appendix A.6.
Nevertheless the deviation between π- and σ-component seems to be not completely based on the polarized background. A similar non-background effected deviation from the intrinsic 90° between the π- and σ-component was found at the DIII-D Tokamak, which has a full carbon wall. There the deviation from the intrinsic 90° were explained by a combination of the Stark-Zeemann effect and a non-ideal in vessel mirror [99]. This should be further investigated, particularly whether this deviation is still present after the correction of the polarized background with the polychromator.
As conclusion, the absolute calibration improves strongly the agreement of the measurement with a synthetic diagnostic from an equilibrium. For the σ-component at the edge the simulation agrees perfectly with the measurements within the uncertainties, but the deviation increases towards the center up to 1.°. This deviation could be explained either by an imperfect equilibrium or by interfering polarized background. This should be measurable by the new polychromator system explained in section 4.4. Also the deviations from the intrinsic 90° deviation between the π- and σ-component should be investigated further with this new approach.

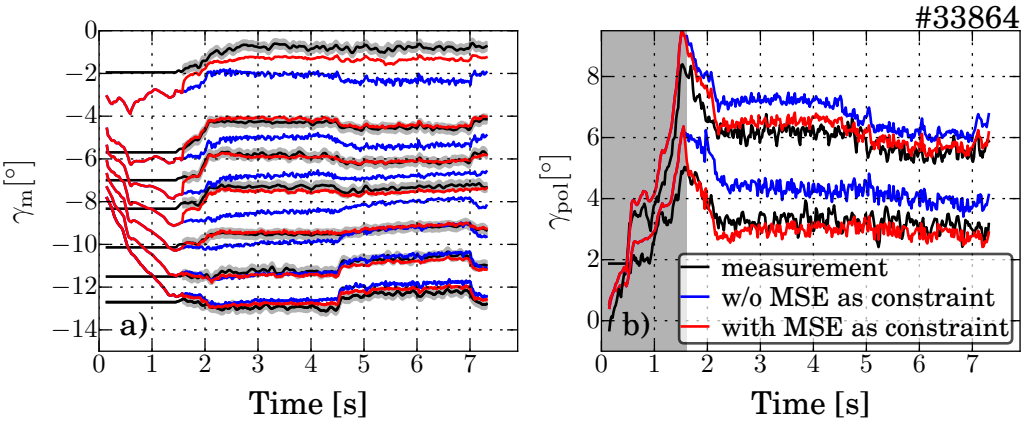

Figure 4.15.: a) Shows a comparison of the MSE angles, in black the measured ones with uncertainties and in blue and red the angles from the equilibrium reconstruction. The red prediction came from an equilibrium taking the MSE angles as constraint, while the blue ones does not. b) Shows the polarimetry angles in black the measurement and in blue and red the predictions. In both equilibria the polarimetry is not taken as constraint for the equilibrium reconstruction.

4.3. Equilibrium Constrained by MSE Measurement

The measured MSE angles can be used as a constraint for an equilibrium reconstruction. Before the absolute calibration was done, all measured MSE angles got an individual offset to match a short phase in time of an equilibrium calculated in advance. This technique is strongly restricted to one trustworthy phase in time during the equilibrium reconstruction and constitutes a source of strong systematic uncertainties. With an absolute calibrated MSE this is no longer necessary.
To demonstrate the benefit of constraining an equilibrium with MSE angles, two equilibria were calculated with the ASDEX Upgrade equilibrium code IDE [23] for the discharge #33864, for witch the absolute calibration is shown before. The first one takes only the magnetic and kinetic measurements to calculate the equilibrium in the second one the σ-MSE angles were taken as further constraint. Figure 4.15 shows the resulting comparison between measured and synthetic MSE and polarimetry diagnostics. Both diagnostics are sensitive to changes in the current profile. In figure 4.15 a) the measured MSE angles are compared with the calculated angles from the two equilibria. As expected the blue angles from the equilibrium reconstruction, which does not take the MSE as a constraint, deviates like the TRANSP reconstruction shown in figure 4.13. Also the agreement of the red predicted angels for the equilibrium reconstruction were the MSE angles were taken as constraint is expected. Only the central channel could not be matched within the uncertainties due to other constrains. Maybe this channel is affected by polarized background. Remarkable are the results from figure 4.15 b). There the measured polarimetry channels can be seen in comparison to the predicted ones from the equilibria. In this case the polarimetry is not taken as constraint for the equilibrium reconstruction. While the equilibrium without the

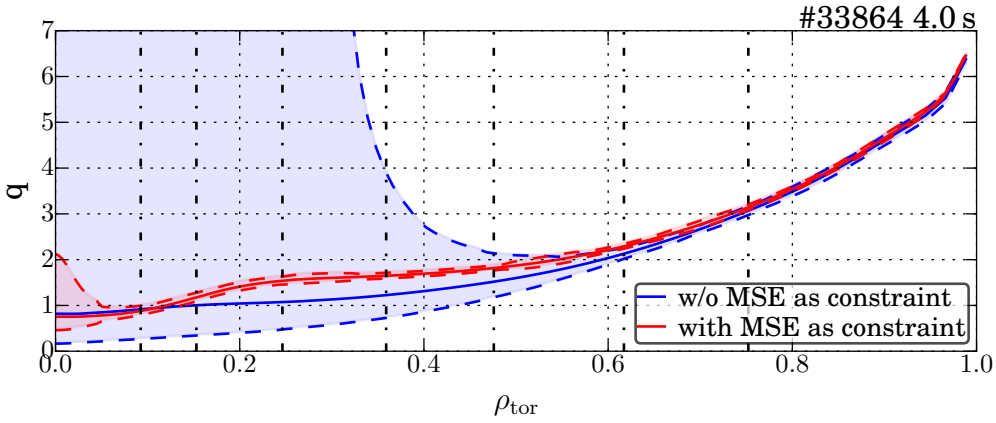

Figure 4.16.: Profiles of the safety factor q with uncertainties, in blue for an equilibrium reconstructed without and in red with the measured absolutely calibrated MSE angles as constraint. The dashed-dotted lines mark the radial MSE positions at this point in time.

MSE constraint overestimates the measured polarimetry angles, the constrained equilibrium predicts a match within the error bars of the synthetic polarimetry with the data. Clearly visible is the change in the predicted angle at the point in time when the MSE starts to constrain the equilibrium at the end of the gray bar in figure 4.15 b).
In figure 4.16 the corresponding profiles of the safety factor for the two equilibria at one point in time can be seen. The strongly increasing uncertainties towards the center in the blue equilibrium without the MSE constraint correlates with the uncertainty of the magnetic measurements. The black dash-dotted lines marks the positions of the MSE system at this point in time. In red the safety factor profile of the MSE constrained equilibrium can be seen. The uncertainties are strongly reduced up to the position of the central MSE channel.

4.4. Polychromator

The polychromator is foreseen as replacement and upgrade for the photomultiplier based detector units. The polychromator system enables parallel measurement of the π- and σ-component on a single line of sight. Furthermore the degree of polarization of the background radiation is measured, at wavelength above and below the signal region. Assuming uniform polarization of the broadband background radiation and only linear wavelength dependence, the contribution of the polarized background in the signal region can be interpolated and subtracted. The background is expected to be polarized due to polarizing reflection of light, for example from the divertor, on the metallic first wall into a line of sight. Such a polarized background was measured in the full metal first wall Tokamak Alcator C-MOD [96,97], and there is also indication in ASDEX Upgrade for such background polarization [19].
The polychromator design used at ASDEX Upgrade is adapted from the one used at Alcator

C-MOD. It was designed and constructed in cooperation with the MSE group of the MIT. Unfortunately the first ASDEX Upgrade polychromator became operational only after finalizing the experiments for chapter 6 and 7. However, the first measurements were successful and prove the principle. A detailed description of the working principle, the technical implementation in ASDEX Upgrade, the improvements with respect to the Alcator C-Mod system, the calibration and the first prove of principle measurements can be found in appendix A.6.

5. Simulation of Neutral Beam Current Drive

In section 2.4.2 an overview on the neutral beam driven current is given. In equation (2.30) the trapped electron parameter $G(Z_{\text{eff}},\epsilon)$ is introduced, which is challenging to be analytically calculate. The transport code TRANSP is used as multi-physics model, with the capability to calculate the neutral beam driven current. This code is introduced together with its module NUBEAM, which is used to calculate the neutral beam driven current and the fast ion distribution. Subsequent the three different, in TRANSP implemented, models to calculate the shielding current are presented and compared. Finally the TRANSP calculated neutral beam driven current is benchmarked by calculations using a semi-analytic fast ion model.

5.1. TRANSP

5.1.1. The Transport Code TRANSP

A general overview over the transport code TRANSP is given, based on the description from reference [100], which is a general introduction into the way of operation of a Tokamak transport code, where TRANSP is also used as example.
TRANSP [101,102] is an interpretative transport code for magnetic confined Tokamak fusion plasma. In general a transport code describes the heat and particle transport in a plasma by calculating transport coefficients for the electrons, ions and the energy. The simulations based on a set of measured values or synthetic data, like the kinetic profiles. Further non-measurable necessary quantities, like the neutral density profiles, are calculated using additional physical models.
For a proper description of the transport in the plasma several quantities are calculated (by the equations mentioned in parenthesis):

- Equilibrium (Grad-Shafranov-Equation see equation 2.3)
- Heat transport for electrons (electron energy conservation equation)
- Particle transport (particle balance equation)
- Heat transport for ions (ion energy conservation equation)
- Auxiliary heating

In a magnetic fusion device the transport along the field lines for particles and heat is high enough that the assumption of an immediate smoothing of these quantities on a flux surface is sufficient. For a Tokamak the axisymmetry allows to solve the transport problem in one poloidal cross section. The **Grad-Shafranov equation** (see equation (2.3)) is solved in this 2D coordinate system. With this magnetic equilibrium the flux surfaces can be defined and the transport problem can be solved in 1D as radial transport perpendicular to the flux surfaces. Due to the fact that the flux surfaces are not circular the code is categorized as 1.5D and the radial coordinate is given by the grid of the magnetic surfaces formed to a normalized magnetic flux.
The **electron energy conservation equation** is one of the central equations to solve, which enables the description of the electron movement and interactions with ions. This equation contains the interaction with the plasma, all energy sources, like auxiliary heating or energy transfer from ions, and energy loss channels, like radiation or the ionization of neutrals. The quantities necessary to solve this equation are the electron density profile, the electron and ion temperature profile, the profile of the radiated power and the plasma current profile. These are all measurable quantities, but furthermore some non-measurable quantities are necessary, like the profile of the plasma conductivity, the radial velocities of the electrons and ion, the neutral density profile and the auxiliary heating power transferred to the electrons. To get these quantities physical models are used. For example the auxiliary heating power is known, but the transferred power to the electrons has to be calculated by the assumption of a physical model.
Furthermore the global current profile has to be evaluated, which is also connected to the solution of the Grad-Shafranov equation. This is done by solving the poloidal magnetic field diffusion equation. Important parameters are the plasma resistivity which is strongly connected to the electron temperature and the effective charge of the plasma.
Until now only the confinement and the electron energy are presented, furthermore the **particle balance equation** must be solved representing the particle flux. In an interpretative run the sources, namely external heating with the NBI, gas inlet, pellets and the wall retention, are given together with the density profiles. This enables the calculation of the particle flux, but only by a connection of the diffusion and the convection, which is normally done defining an effective diffusion.
Analogous to the electron energy conservation equation there is an **ion energy conservation equation** that is needed to be solved. The differences of this equations are essentially the power gain and loss terms. Connected to this, the neutral transport in the plasma has to be modeled, as the neutral particle profile is not measurable and the neutrals are an important source for ions and electrons and also could lead to loss of energy and due to charge exchange losses of ions.
The last part is the simulation of the **auxiliary heating systems**. In TRANSP they are all covered by external modules. The ECRH is modeled by TORAY and the ICRH wave heating is modeled with TORIC, these modules calculate the power profile going to the different species. For the neutral beam injection the NUBEAM model is used. As this module plays an important role within this thesis a more detail description is given to this module. For more details to TRANSP see also reference [102].

5.1.2. The TRANSP Module NUBEAM

NUBEAM is a Monte Carlo based module to model the neutral beam heating of the plasma and the fast ion behaviour. The production of the fast ions is calculated and their interaction with the plasma down to their thermalization. The NUBEAM module calculates time-dependent the physics of the neutral beam deposition, a two-dimensional fast ion orbiting, the power deposition, the beam driven current and the momentum transfer to the plasma. Additionally the slowing down of the fast ions. Optionally the calculated full fast ion distribution and the fast ion birth location at a dedicated given point in time is written into an additional output file.
NUBEAM calculates the slowing down process of particles down to $1.5 \cdot T_\mathrm{i}$, below this threshold the ions are considered as thermalized. This threshold is important as NUBEAM is based on the assumption that the fast ion density is much lower than the thermal ion density $n_\mathrm{fi} \ll n_{,\mathrm{thermal}}$. This allows the approximation that fast ions only collide with thermal ions and that collisions with each other are negligible. The thermal ion content is described by a Maxwell distribution. This linearizes the collision operator for the fast ions. Furthermore, this limit the computational costs. Because to reduce the variance by a factor of N, N^2 Monte Carlo particles are needed. Therefore a Monte Carlo description of the thermal continuum and the particles below the threshold is impractical.
In NUBEAM the deposition of power and birth of fast particles is calculated by the expected time of flight of neutral particle considering the geometry, beam and plasma parameters. For the ionization process six mechanisms are taken into account: electron impact ionization, thermal ion charge-exchange, thermal ion impact ionization, high-Z thermal ion stopping also with impact ionization and non-neutralizing charge exchange, charge exchange with slowing down fast ions and impact ionization of slowing down fast ions. Necessary are the cross sections, the plasma density and the energy distribution, considering different energy components and fractions. In a step by step calculation including the slowing down a fast ion distribution is calculated. With the time of flight approach also the shine through could be calculated.
The TRANSP code and also the NUBEAM module are multiple times bench marked with other codes, for example see reference [103]. For more information to NUBEAM see reference [104].

5.1.3. NUBEAM NBCD Models

In NUBEAM three different models can be chosen to calculate the neutral beam driven current. As mentioned in section 2.4.2 one issue in the determination of the NBCD is the calculation of the electron shielding current.
The trapped electron parameter for equation (2.30) calculated by D. R. Mikkelsen [50] which used for the description in section 2.4.2 is defined as

$$G(Z_\mathrm{eff}, \epsilon) \approx (1.55 + 0.85/Z_\mathrm{eff})\sqrt{\epsilon} - (0.20 + 1.55/Z_\mathrm{eff})\epsilon \tag{5.1}$$

with Z_{eff} the effective charge of the plasma and ϵ the inverse aspect ratio. However, this approximation is only valid for $1 < Z_{\text{eff}} < 3$ and $0 \leq \epsilon < 0.2$. As ASDEX Upgrade as well as ITER have an inverse aspect ratio up to 0.3 this is not suitable for these devices.
The first model implemented in NUBEAM neglects the trapped electron correction completely and calculates the current with equation (2.29). Obviously this model underestimates the real current. The other two approaches differs in the calculation of the trapped electrons parameter. The first one based on calculations by Lin-Liu and Hinton [105], while the second one based on calculations from S. P. Hirshman [106, 107].
In their publication Lin-Liu and Hinton showed the similarity of the trapped electron parameter to a parameter of the neoclassical bootstrap current calculation and approximate the trapped electron parameter from equation (2.30) with

$$G = \frac{g(Z_{\text{eff}}^2 + 2.21Z_{\text{eff}} + 0.754) + g^2(Z_{\text{eff}}^2 + 1.243Z_{\text{eff}} + 0.348)}{(Z_{\text{eff}}^2 + 1.414Z_{\text{eff}}) + g(2Z_{\text{eff}}^2 + 2.657Z_{\text{eff}} + 0.754) + g^2(Z_{\text{eff}}^2 + 1.243Z_{\text{eff}} + 0.348)} \tag{5.2}$$

with g the ratio of trapped to non-trapped particle $g = f_{\text{t}}/(1-f_{\text{t}})$ including f_{t} as the trapped particle fraction. This approach is based on an approximation of the neoclassical bootstrap current by S. P. Hirshman [108]. It is valid for the assumption that the thermal electron velocity is much higher than the fast ion velocity, which is valid for fast ions from the neutral beams in ASDEX Upgrade ($v_{\text{e,3 keV}} = 32 \cdot 10^6\,\text{m}\,\text{s}^{-1} > 3 \cdot 10^6\,\text{m}\,\text{s}^{-1} = v_{\text{fi,100 keV}}$). The calculations are done in the banana regime (see section 2.2.1) for elliptical Tokamak plasma.

The second approximation is based on publications of S. P. Hirshman [106, 107], but is not very well documented. The formulas are reconstructed from the implementation in TRANSP. The starting point for the electron shielding factor is again a calculation of the neoclassical bootstrap current. In this case the normalized collisionality of electrons is included

$$\nu_{\text{e}}^* = 6.92 \cdot 10^{-18} \frac{q n_{\text{e}} \ln \Lambda_{\text{e}}}{T_{\text{e}}^2} \sqrt{\frac{R_0^5}{r^3}} \tag{5.3}$$

with q the safety factor, n_{e} the electron density, $\ln \Lambda_{\text{e}}$ the Coulomb-Logarithm of electrons, T_{e} the electron temperature and $R_{\text{min/maj}}$ the minor and major radius of the plasma. The trapped electron parameter depending on the normalized collisionality and the effective charge of the plasma and is defined as following

$$G = f_{\text{t}} \frac{1.5Z_{\text{eff}}(K_{12} - 2.5K_{11}) + (\sqrt{2} + 3.25Z_{\text{eff}})K_{11}}{Z_{\text{eff}}(\sqrt{2} + 3.25Z_{\text{eff}}) - 2.25Z_{\text{eff}}^2} \tag{5.4}$$

with

$$K_{11} = \frac{0.53 + Z_{\text{eff}}}{(1 + \sqrt{A_{11}\nu_{\text{e}}^*} + B_{11}\nu_{\text{e}}^*)(1 + \sqrt{C_{11}\nu_{\text{e}}^*\epsilon^{3/2}} + D_{11}\nu_{\text{e}}^*\epsilon^{3/2})}$$

$$A_{11} = 3.44Z_{\text{eff}} + \frac{0.52 - 0.42Z_{\text{eff}}}{1 + 1.35Z_{\text{eff}}}$$

$$B_{11} = 0.56 + 0.96Z_{\text{eff}}$$

$$C_{11} = 0.25Z_{\text{eff}} + \frac{0.14 + 0.55Z_{\text{eff}}}{1 + 5Z_{\text{eff}}}$$

$$D_{11} = 0.51 Z_{\text{eff}} + \frac{0.7 + 0.78 Z_{\text{eff}}}{1 + Z_{\text{eff}}}$$

and

$$K_{12} = \frac{0.71 + Z_{\text{eff}}}{(1 + \sqrt{A_{12}\nu_{\text{e}}^*} + B_{12}\nu_{\text{e}}^*)(1 + \sqrt{C_{12}\nu_{\text{e}}^*\epsilon^{3/2}} + D_{12}\nu_{\text{e}}^*\epsilon^{3/2})}$$

$$A_{12} = 0.31 Z_{\text{eff}} + \frac{0.1 + 0.084 Z_{\text{eff}}}{1 + 1.3 Z_{\text{eff}}}$$

$$B_{12} = 0.26 + 0.35 Z_{\text{eff}}$$

$$C_{12} = 0.081 Z_{\text{eff}} + \frac{0.072 + 0.15 Z_{\text{eff}}}{1 + 3 Z_{\text{eff}}}$$

$$D_1 = 0.29 Z_{\text{eff}} + \frac{0.42 + 0.62 Z_{\text{eff}}}{1 + 1.42 Z_{\text{eff}}}.$$

The differences of the two approaches are the use of the collisionality in the S. P. Hirshman approximation and the higher orders of the trapped particle fraction in the Lin-Liu and Hinton approach, from a later calculation of the neoclassical bootstrap current by S. P. Hirshman. The higher orders are the result from a more accurate numerical approximation.

The approximation of low normalized collisionality, like in most of the discharges in this thesis, lead in the limit of $\nu_{\text{e}}^* = 0$ and neglecting terms with $O(f_{\text{t}}^2)$ to an identical trapped electron parameter for both calculations. Same results were found in a detailed comparison of both approaches made by M. Kraus [109]. There is also a detailed comparison of the NUBEAM NBCD model with the IPP NBCD code FAFNER [110], which is not used within this thesis.
For an example discharge the comparison between the three different neutral beam current drive models in TRANSP can be seen in figure 5.1. As expected neglecting the electron trapping correction lead to a strong underestimation of the neutral beam driven current. As the collisionality in this discharge is low the difference in the integrated current between the two models is below 5%.
In this thesis, due to the fact that in all discharges the normalized collisionality is low, the Lin-Liu and Hinton model includes higher orders of the trapped particle fraction and that the Lin-Liu and Hinton model is better documented, the Lin-Liu and Hinton model is used for the TRANSP simulations.

5.2. Benchmarking of NUBEAM NBCD with a Semi-Analytic Fast Ion Model

In NUBEAM the NBCD calculation is carried out step by step along with the calculation of the full fast ion distribution function. It is therefore difficult to comprehend the NBCD calculation. Therefore a semi-analytic fast ion model that includes the same fast ion physics is used to check for consistency. Furthermore it is a computationally less expensive way

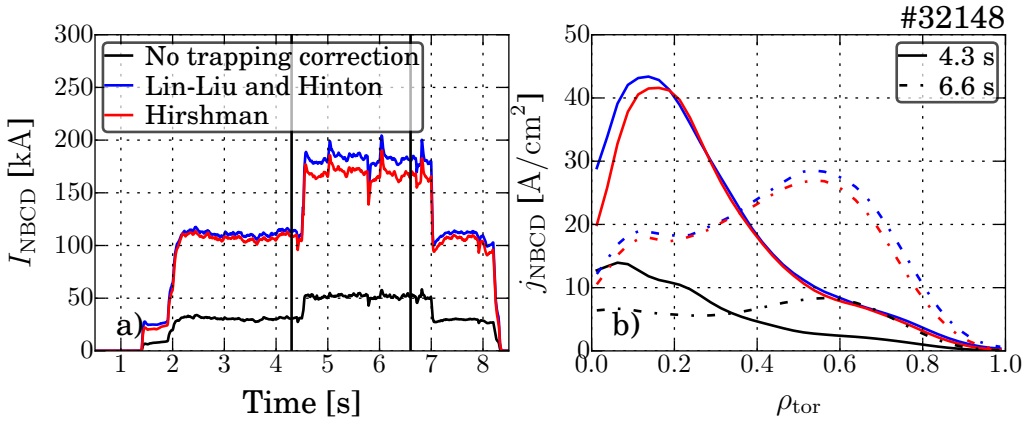

Figure 5.1.: a) Shows time trace for the integrated neutral beam driven current for the three different models in TRANSP. b) Shows the corresponding profiles of the current densities at two different points in time.

to calculate the NBCD independently from TRANSP. This fast ion model is developed by M. Weiland [111]. In this model the fast ion density is calculated from the kinetic profiles, the neutral beam injection geometry and power, using the same input data like a TRANSP/NUBEAM simulation. Additionally and in difference to the TRANSP calculation a prescribed equilibrium is required. The model calculates the fast ion birth locations and their initial pitch angle using the FIDASIM code [17, 90]. These fast ions afterwards are averaged over their first orbit taking their velocity (v) and pitch angle (ξ) into account. These information build the source term σ to calculate the fast ion distribution. Furthermore the slowing down distribution f of these fast ions is calculated by solving a Fokker-Planck equation in the velocity space

$$\frac{1}{t_{\mathrm{s}}}\frac{1}{v^2}\frac{\partial}{\partial v}\left[(v^3+v_{\mathrm{c}}^3)f\right]+\frac{\beta}{\tau_{\mathrm{s}}}\frac{v_{\mathrm{c}}^3}{v^3}\frac{\partial}{\partial \xi}\left(1-\xi^2\right)\frac{\partial f}{\partial \xi}+\frac{1}{\tau_{\mathrm{s}}}\frac{1}{v^2}\frac{\partial}{\partial v}\left[\left(\frac{T_{\mathrm{e}}}{m_{\mathrm{fi}}}v^2+\frac{T_{\mathrm{i}}}{m_{\mathrm{fi}}}\frac{v_{\mathrm{c}}^3}{v}\right)\frac{\partial f}{\partial v}\right]=\frac{\partial f}{\partial t}-\sigma \quad (5.5)$$

here the first term on the left side represents the slowing down as drift in the velocity space, the second term corresponds to the pitch angle scattering and the third term represents diffusion in the velocity direction due to accelerating collisions, which is typically less important. On the right side are the temporal change of the fast ion distribution function and the source and sink term for fast ions. A more detailed description of the equation and the solution is given in the reference [111].
The description only in the velocity space allows an analytical solution of the equation reducing the computational time. The terms describing orbits and movement in the real space are left out from the beginning. The fast ion distribution in the real space is given by the average over the first orbit, a redistribution in real space by scattering is neglected. Furthermore changes of the ion orbits during the slowing down process are neglected. These would lead to a special redistribution. The strongest redistribution would be expected when the orbit topology changes due to a collision for example form a passing to a trapped orbit or vice versa. In TRANSP/NUBEAM the fast ion distribution function is calculated in the

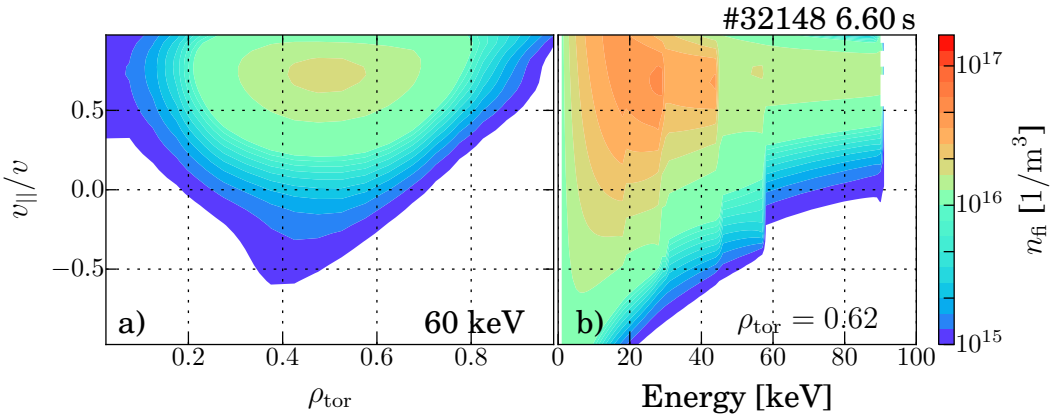

Figure 5.2.: Slices of the calculated 4D (time, space, energy and pitch angle dependent) fast ion distribution function in the real space at 6.6 s. a) Shows slice of the radial fast ion distribution function at 60 keV versus the pitch angle and b) shows energy resolved slice at the same point in time at $\rho_{tor} = 0.6$.

real space and also in the velocity space by a full Monte Carlo approach, leading to much higher computational effort. The movements in the real space and the transfer from passing to trapped orbits and vise versa are taken into account.
The fast ion distribution function is calculated for each radial position individually and depending on the pitch angle and the particle velocity tantamount the energy. In figure 5.2 for one point in time of discharge #32148 two slices of the fast ion distribution are shown. At this time the NBI sources 3, 6 and 7 produce the fast ions. Due to the fact that the NBI source 6 and 7, with 93 keV acceleration voltage, injecting tangential in the co-current direction, they produce mostly passing particle with a positive pitch angle. This can be seen in figure 5.2 b) above the threshold of 60 keV. Because at 60 keV the NBI source 3 injects neutral particles, but the injection is more radial with respect to the geometry of beam 6 and 7. This leads to a higher fraction of trapped fast ions with two and lower initial pitch angel values. Trapped particles with positive pitch angles move in co-current direction at the outer leg of the banana and in counter-current direction on the inner leg of the banana with negative pitch angle values. Along their banana orbit they reach the turning point with pitch angle zero. In the radial fast ion distribution in figure 5.2 a) this behaviour on the inner leg of the banana can also be seen, due to the fact that the low and negative pitch angles values appears closer to the center at smaller ρ_{tor} values. However, this shows also the neglected transformation of passing orbits to trapped orbits during the thermalization, as their are almost no trapped orbits above 60 keV in figure 5.2 b).
From these fast ion distributions the fast ion current can be calculated by integration in the following way

$$j_{\mathrm{fi}} = e \cdot \int \int f(\rho, t, E, \xi) \cdot (v_{||} - v_{\mathrm{rot},\varphi}) dE d\xi \tag{5.6}$$

with e the elementary charge, f the fast ion distribution function, $v_{||}$ the parallel velocity and $v_{\mathrm{rot},\varphi}$ the rotation velocity in current direction. The rotation velocity is necessary to

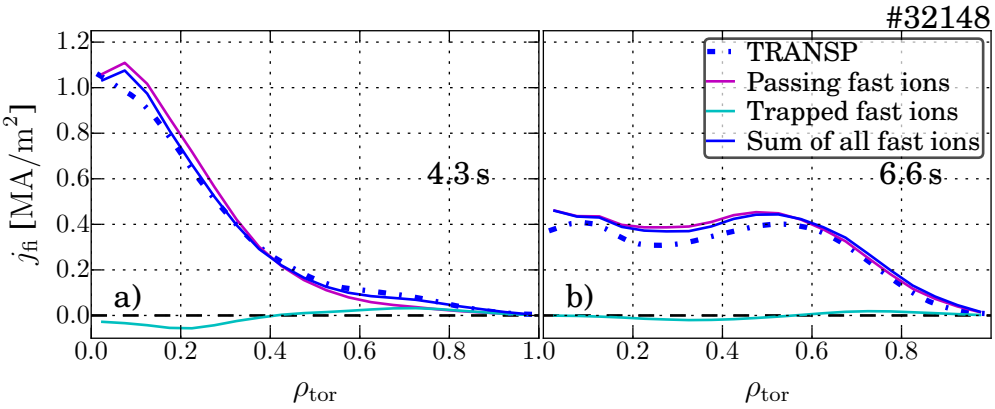

Figure 5.3.: Fast ion current density profile calculated with equation (5.6) in comparison to TRANSP predictions at two different points in time. In a) at 4.3 s the on-axis neutral beams are active and in b) at 6.6 s the off-axis beams are in use.

transform f from the lab frame to the rotating plasma frame. The differentials are the pitch angle ξ and the energy E. The energy dependent parallel velocity is calculated with $v_{||} = v_{\text{tot}} * \xi$ and $v_{\text{tot}} = \sqrt{2 \cdot E/m}$. The current density profile for two different points in time can be seen in figure 5.3. The calculated fast ion current density profile is in good agreement with the TRANSP predictions (dotted line) at both points in time. At 4.3 s the on-axis neutral beams 3, 5 and 8 are the source for fast ions, whereas at the second point in time at 6.6 s the fast ions came from the NBI sources 3, 6 and 7. The main contribution to the fast ion current came from the passing fast ions as expected. Furthermore also the trapped fast ions contribute in the radial distribution, but the small positive contribution closer to the edge is compensated by the negative contribution from the inner leg of the banana. Due to the fact that the volume towards the center is smaller the negative contribution of the current density towards the center mistakenly seems to be greater than their positive counterpart. The sum of passing and trapped particle contributions is in good agreement with the radial current density predicted by TRANSP.
The neutral beam driven current can be calculated from the fast ion current using

$$I_{\text{cd}} = I_{\text{circ}} \cdot \left[1 - \frac{Z_{\text{beam}}}{Z_{\text{eff}}} \cdot (1 - G(Z_{\text{eff}}, \epsilon))\right] \tag{5.7}$$

and taking the electron shielding current into account. To calculate the electron shielding current with equations (5.2) and (5.4) the trapped electron fraction is necessary. This can be calculated from the neoclassical theory from references [112, 113]

$$f_{\text{t}} = 1 - \frac{3}{4}\langle h^2 \rangle \int_0^1 \frac{\xi d\xi}{\langle \sqrt{1 - \xi h} \rangle} \tag{5.8}$$

with $\langle\ \rangle$ a flux surface average, $h = B/B_{\text{max}}$ with B the local magnetic field and B_{max} the maximum magnetic field on the flux surface and ξ the pitch angle. Solving this equation

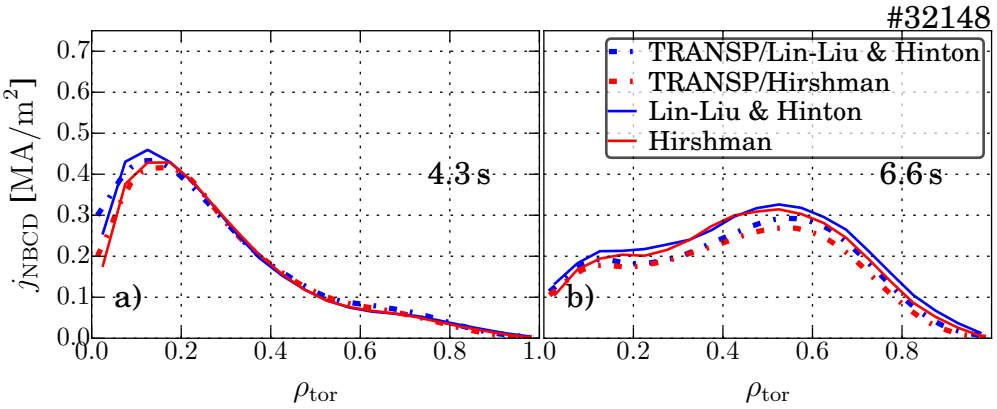

Figure 5.4.: In a) and b) the Neutral beam driven current profile calculated with equation (2.30) is shown, using the Lin-Liu shielding current from equation (5.2) and the fast ion current shown in figure 5.3. In comparison the TRANSP prediction for two different points in time are shown.

analytically with the double integration is time consuming and therefore an approximation, which is also taken in TRANSP, is used

$$f_{\mathrm{t}} \approx 1 - \frac{(1-\epsilon)^2}{\sqrt{1-\epsilon^2}(1+1.46\sqrt{\epsilon})} \tag{5.9}$$

with ϵ the local inverse aspect ratio $r_{\mathrm{minor,local}}/R_{\mathrm{major,axis}}$.
In figure 5.4 the resulting neutral beam driven current density profiles for the same two points in time shown before can be seen. Again a good agreement between the calculated and TRANSP predicted current density is achieved. Remarkable is the radial dependency of the electron shielding current, reducing the fast ion current from figure 5.3 to the neutral beam driven current in figure 5.4. While the central peak during the on-axis deposition at 4.3 s is reduced by a factor of 2, the peak around $\rho_{tor} \sim 0.6$ in the neutral beam driven current is around 80% of the corresponding fast ion current. The reason for this behavior is the much higher trapped electron fraction closer to the edge.
In conclusion good agreement between the TRANSP predictions and the calculations on basis of the Semi-Analytic Fast Ion Model was found.

6. Fast Ion Redistribution due to Plasma Perturbations

The neutral beam driven current is carried by fast ions. Redistribution of these fast ions due to perturbations in the plasma influences the current profile in the plasma. In future fusion devices such as ITER, neutral beam injection is one of the main heating systems and is used for active current profile shaping. For a reliable current profile prediction, crucial for the ITER scenario development, possible sources for anomalous fast ion transport need to be understood. For example, evidence for anomalous fast ion transport due to MHD activity such as neoclassical tearing modes [71, 72] or sawteeth [63, 66] was found.
A proper understanding of the fast ion confinement is also necessary as the fusion product, 3.5 MeV helium ions, needs to be confined in the plasma for self sustained fusion. Due to the fact that present fusion experiments do not run with tritium, as the benefit is not worth the afford, for example the strongly increasing safety issues, almost no fast helium is produced, the confinement of which could be studied. Therefore fast deuterium ions are used as test particles to investigate the fast ion confinement. These fast ions are produced either by neutral beam injection or ion cyclotron resonance heating.
In preparation of ITER the off-axis neutral beam driven current was studied. In several different fusion experiments deviations between the predicted current profile and the measurements were found in MHD-quiescent discharges. This behaviour was first published with experiments from ASDEX Upgrade [12]. Anomalous fast ion transport had been assumed to describe the current profile measurements. In another experiment, the Mega Amp Spherical Tokamak (MAST) [13], also a broadening of the current profile was measured. At the DIII-D experiment the necessity of the assumption of anomalous fast ion transport to describe the current profile was published in reference [14]. In addition, the measurement of the fast ion distribution at DIII-D also indicates anomalous fast ion transport [15, 16]. The influence of microturbulence was proposed as possible candidate for this fast ion redistribution.
In contrast at JT-60U the neoclassical prediction of the off-axis neutral beam driven current profile was in good agreement with the measurements [18], only a small shift in the location was found. An overview and comparison of all these studies can be found in reference [114].
In continuation of the experiments published by Günter et al. [12], using MSE (see chapter 4) as diagnostic to measure the current profile, the newly installed FIDA (see section 3.3.8) diagnostic was used to take a closer look to the radial fast ion distribution [17]. Interestingly the fast ion distribution, in comparable discharges, could be described perfectly by the neoclassical theory.
The present chapter focuses on the contradiction in the ASDEX Upgrade studies, intro-

duced in detail in section 6.1. To resolve this contradiction new improved experiments are performed to measure with both diagnostics simultaneously. These experiments are presented in section 6.2. This is followed by the presentation of some improvements to the simulations in section 6.3 and the discussion of the impact of these improvements in section 6.4. In section 6.5 the influence of fishbones and microturbulence on the fast ion distribution are discussed. Finally, before the conclusion, the lessons learned are projected onto the former experiments in section 6.6.

6.1. Initial Situation

The first comparison regarding the fast ion distribution and neutral beam current drive between on- and off-axis neutral beam injection at ASDEX Upgrade were published by Günter et al. in 2007 [12]. The experiments investigated the change of the total current profile by replacing 5 MW of on-axis neutral beam power deposition by 5 MW of off-axis neutral beam power and a switch back to the on-axis deposition. The changes in the current profile were measured with the motional Stark effect polarimetry (MSE). The measured angles were compared with synthetic angles from TRANSP simulations. This can be seen in figure 6.1, adapted from reference [12]. Due to the fact that the MSE diagnostic uses the on-axis NBI beam 3, measurements are only available in the on-axis phases. To study the influence of the off-axis beams on the current profile the relaxation of the MSE angles in the second on-axis phase from 7 seconds on were compared with TRANSP predictions. While the neoclassical TRANSP predictions overestimate the change in the off-axis phase coupled with a different relaxation behaviour, the predictions assuming anomalous fast ion diffusion are in much better agreement with the data. As no MHD activity besides type-I ELMs was measured in the discharge, the reason for the anomalous fast ion transport was assumed to be microturbulence.
The fast ion D-alpha spectroscopy (FIDA) was installed at ASDEX Upgrade by B. Geiger in 2011 [17]. In comparable discharges to the ones published in 2007 the measured signal during the on- and off-axis deposition was compared with a synthetic diagnostic from TRANSP simulations postprocessed with FIDASIM. The result could be seen in figure 6.2 which is adapted from reference [17]. A good agreement of the measurement with the neoclassical TRANSP predictions can be seen, while the simulations assuming anomalous fast ion diffusion underestimates the measurements.
In conclusion, the current profile measured with the MSE diagnostic published in 2007 deviates from the neoclassical TRANSP predictions. For a proper description of the current profile fast ion redistribution by anomalous fast ion diffusion was assumed. In contradiction to that result, the fast ion distribution published in 2012 measured with the FIDA diagnostic seems to be in perfect agreement with the neoclassical predictions.

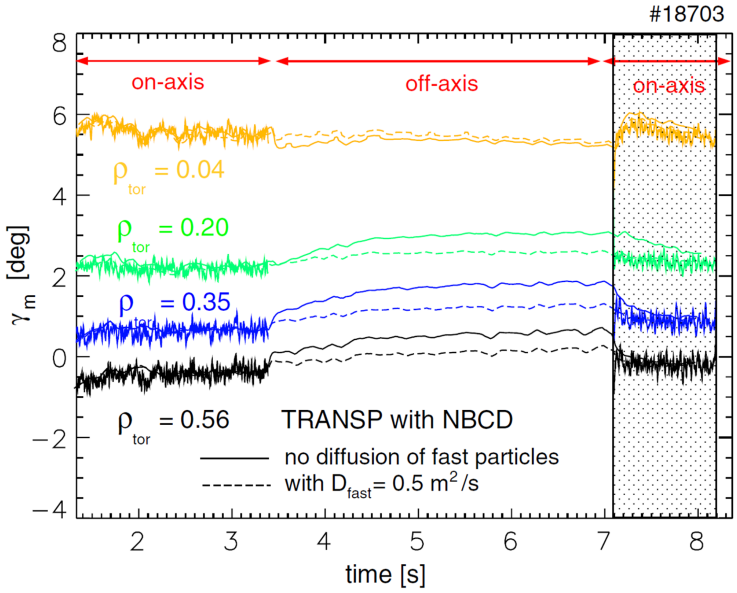

Figure 6.1.: Comparison of the measured MSE angles with TRANSP simulation in discharge #18703. The figure is adapted from the publication of Günter et al. [12].

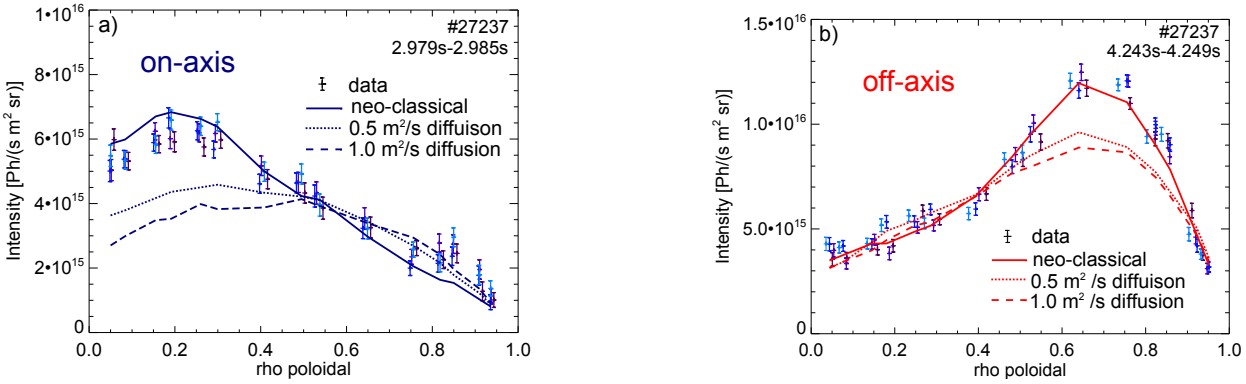

Figure 6.2.: FIDA results from the thesis of B. Geiger [17] comparing the measurements with TRANSP predictions assuming different levels of anomalous fast ion diffusion in discharge #27237. The figure is adapted from the thesis of B. Geiger [17].

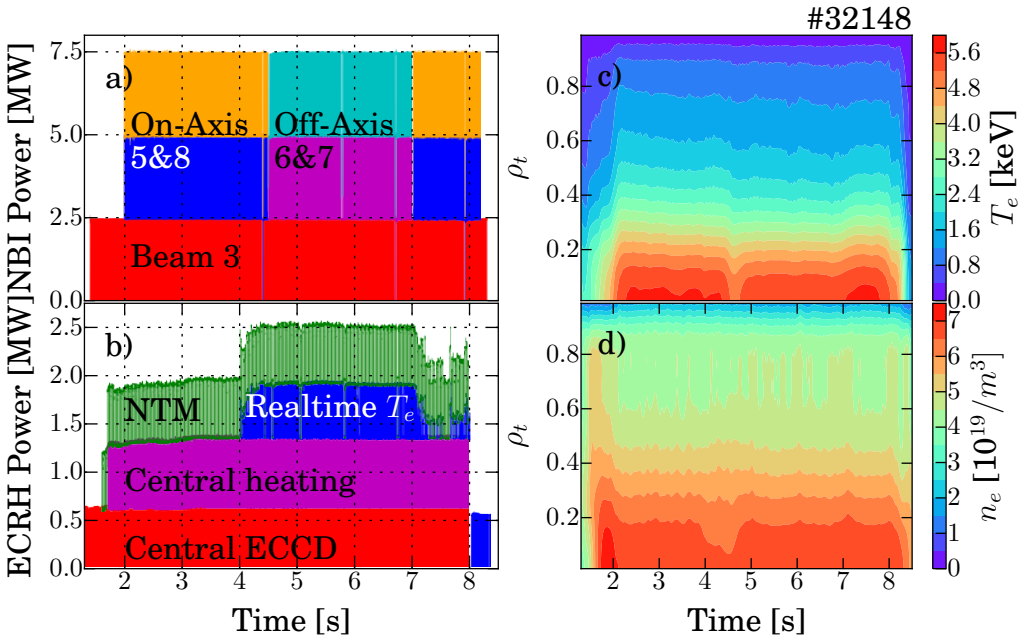

Figure 6.3.: In a) the NBI power, switching from on- to off-axis sources and back is shown and in b) the ECRH power with use of all available Gyrotrons. c) Shows the feedback controlled electron temperature and d) electron density evolution during the discharge.

6.2. New Series of Experiments

6.2.1. Experimental Setup

The new experiments are similar to the old discharges, but incorporate several improvements. The main element, the NBI sequence of 5 MW of on-axis deposition replaced by 5 MW of off-axis deposition and back to the 5 MW of on-axis NBI, is conserved. The 93 keV NBI sources 5 and 8 are used for the on-axis deposition and the sources 6 and 7 with maximum off-axis steering, were used during the off-axis phase. The injection geometry can be seen in figure 3.3. Additionally the NBI beam 3 with 60 keV beam energy is switched on during the whole discharge, to enable MSE and FIDA measurements during the off-axis phase as well. In figure 6.3 a) the time trace of the NBI can be seen.
The increased NBI power from 5 MW to 7.5 MW leads to the appearance of a m=3/n=2 neoclassical tearing mode (NTM), which can be seen in the spectogram of a magnetic signal in figure 6.4 a). The global toroidal phase reconstruction is used to fit the toroidal mode number of the perturbation. Therefore the amplitude and phase of a set of toroidally arranged coils at a certain frequency at the same point in time is used to fit the global toroidal mode number. To avoid this mode the first gyrotron of the ECRH is used for preemptive NTM stabilization by localizing the m=3/n=2 NTM and overcome the defect current by localized ECCD at the same position. In figure 6.4 b) the successful stabilization can be

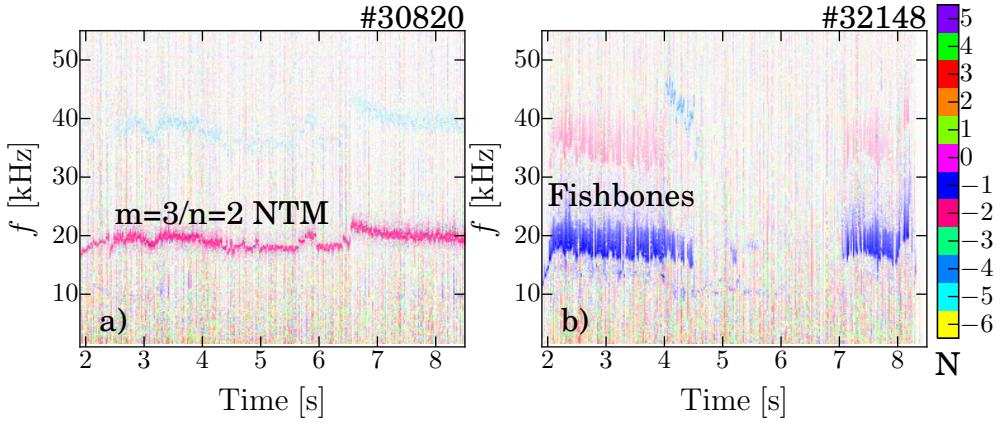

Figure 6.4.: Spectrogram of the activity in the magnetic signal, cross correlated with the electron temperature fluctuation measured with the ECE diagnostic to identify the toroidal mode number of the activity. In a) discharge #30820 with a m=3/n=2 NTM at 20 kHz is shown and in b) discharge #32148 using the preemptive NTM stabilization for the m=3/n=2 NTM can be seen. However, instead of a NTM fishbone activity appears during the on-axis NBI phases.

seen, but instead of the NTM fishbones with a high repetition rate appear during the on-axis phase.
Furthermore a second gyrotron is used with central ECCD to increase the saw tooth period, the time between two crashes in #32148 is between 200 ms and 300 ms, which is much longer than the slowing down time of the fast ions. This is necessary for useful FIDA measurements, as saw tooth redistribute fast ions, therefore profiles are compared with a long enough temporal distance to the last saw tooth to avoid the measurement to be modified by the saw tooth.
A third gyrotron is used for central heating to avoid tungsten accumulation in the center. The fourth last available gyrotron is used in a power feedback real time electron temperature control mode, to compensate the missing central electron heating by the NBI during the off-axis phase. The ECRH time traces can be seen in figure 6.3 b).
The almost constant electron temperature profile can be seen in figure 6.3 c), indicating that the temperature control works well. In figure 6.3 d) the electron density can be seen, which is also constant through out the discharge using a feedback controlled gas inlet. The constant electron density and temperature are beneficial as the measurements in the on- and off-axis phase are directly comparable with each other.
The discharge runs at a toroidal magnetic field of $B_T = -2.6\,\mathrm{T}$ at the magnetic axis, a total plasma current of $I_p = 800\,\mathrm{kA}$, a q_{95} value of 5.3 and a β_N between 1.5 and 2.

6.2.2. First Results

For the improved discharge #32148 the measured MSE angles can be seen in figure 6.5. Unfortunately the absolute calibration of the MSE system described in chapter 4 is not com-

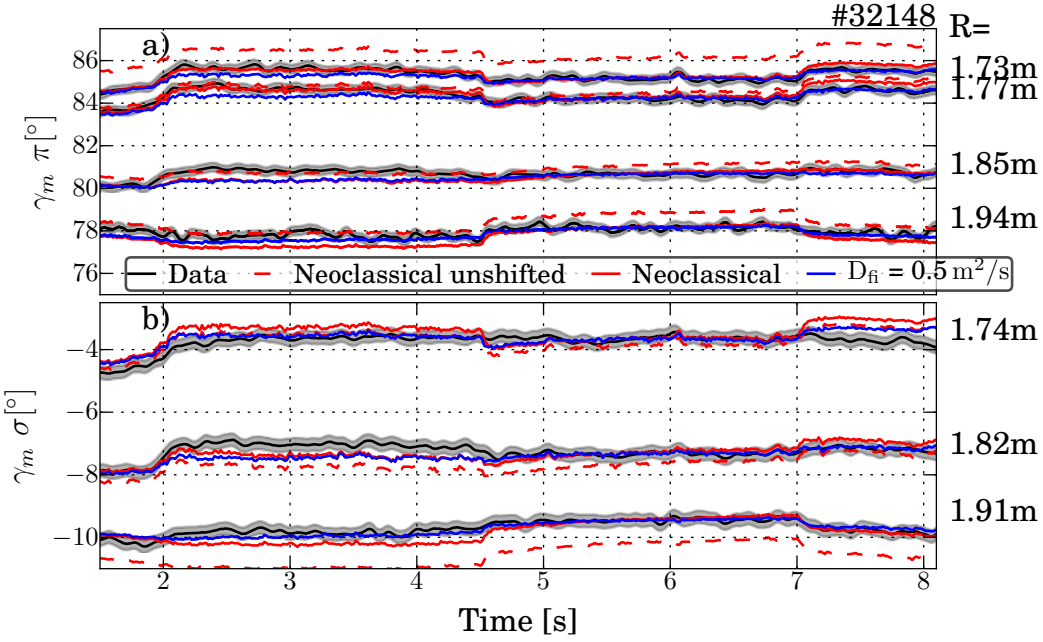

Figure 6.5.: Comparison of the measured and TRANSP predicted MSE angles in a) for the four π channels and in b) for the three σ channels. Due to the incomplete calibration the predictions have to be shifted and are offset-corrected to match in the off-axis phase from 4.5 to 7 s. The red dashed lines are the unshifted predictions.

pletely retroactive, as the protection window towards the plasma was changed. Therefore the first try with an incomplete calibration for the campaign 2015/2016 with less accuracy was used. This can be seen in the deviation between the synthetic TRANSP angles in the dashed red lines and the measurement in black. To compare the measurements with the simulations, the synthetic angles are shifted to match the measurements in the off-axis phase.
The MSE configuration with respect to the equilibrium can be seen in figure 6.6 with the four π and three σ channels. Also the Shafranov-shift at the switch from the on- to the off-axis phase can be seen, explaining the step in the MSE angles. Only minor changes in the dynamics of the MSE angles are measured and predicted. The changes due to the assumption of anomalous fast ion diffusion are in the order of 0.3°, only slightly above the uncertainty of the MSE measurement. The simulation with the assumption of anomalous fast ion diffusion seems to agree better. However, with respect to the earlier experiment in figure 6.1 the deviation of the neoclassical prediction is much smaller.
In figure 6.7 the corresponding measurements with the fast ion D-alpha spectroscopy (FIDA) can be seen. In a) an b) the intensity of the FIDA emission can be seen in analogy to figure 6.2. In c) and d) the beam emission is plotted. The normalized profile of the FIDA emission, introduced in section 3.3.8, can be seen in figure 6.7 e) for one point in time during the on-axis phase and in f) at a point in time during the off-axis phase.
The comparison with the synthetic diagnostic, based on TRANSP simulations, and shows a

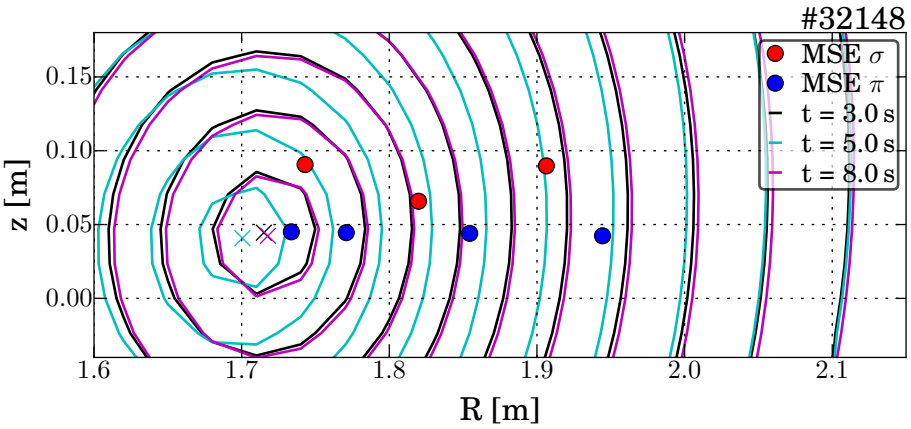

Figure 6.6.: Configuration and position of the useful MSE channels in comparison to the equilibria in the on- and off-axis phase. The inwards Shafranov shift of the magnetic axis in the off-axis phase can be seen in cyan with respect to the black and magenta flux surfaces in the on-axis phases.

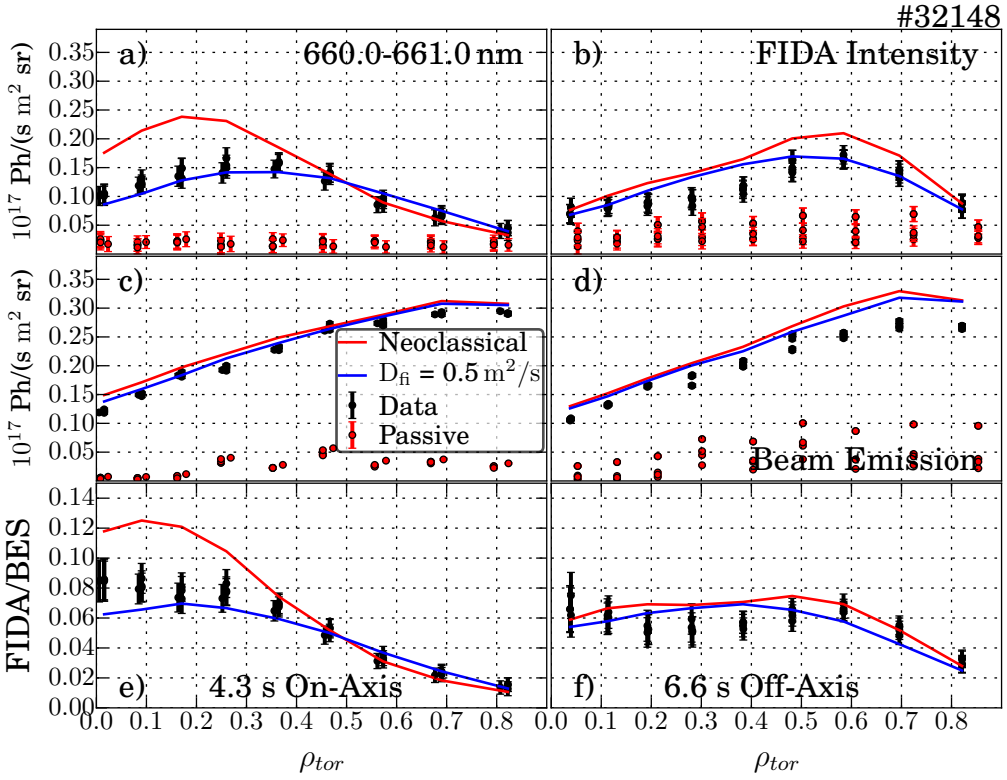

Figure 6.7.: Measured radial FIDA profiles in comparison with TRANSP predictions post-processed with FIDASIM. In a) and b) the integrated intensity of the FIDA emission and in c) and d) the beam emission can be seen. In e) and f) the FIDA emission is normalized to the beam emission for points in time in the on- and off-axis phase.

central overestimation of the fast ion profile during the on-axis phase, where the assumption of anomalous fast ion diffusion fits much better to the data. In the off-axis phase on the one hand the influence of the anomalous fast ion diffusion is small, as the fast ion profile is almost flat, on the other hand the shape of the normalized FIDA emission is not well described by the synthetic diagnostic. Neither is the off-axis peak described well nor the measured dip around $\rho_{\mathrm{tor}} = 0.3$.
In conclusion, there are hints for anomalous fast ion diffusion, especially during on-axis deposition. However, in the off-axis phase the disagreement of the shape of the FIDA profile between measurement and TRANSP prediction seems to be an issue. Therefore the simulations are revised, to identify the reasons for the deviations.

6.3. Review of Simulation Inputs

6.3.1. Geometry

A possible source of disagreement between measured and simulated FIDA profiles are differences between modeled and actual beam geometry, maybe differing from the designed one. The following section describe a measurement based revision of the beam geometry, a necessary input for TRANSP simulations. In this section, firstly the measurement with the infrared camera is presented. Secondly the modeling of the 3D geometry of the neutral beams is introduced. Thirdly the modeled geometry is superimposed with the infrared measurement and a correction of the assumed geometry input for the simulations is done. Finally a further approximation, necessary for the geometrical neutral beam simulation in TRANSP, is discussed.
With an infrared camera, the footprint of the neutral beams on the inner wall was measured in the empty torus. As the energy density of the neutral beams is able to melt the inner wall, the exposure time is limited to 60 ms (200 ms) on the target wall material stainless steel of the inner heat shield (tungsten coated carbon of the passive stabilizer loop). An infrared camera is only available in sector 9, shown in figure 6.8 a), therefore only the beams of NBI box 2 could be revised. Additionally in figure 6.8 b) the head of the immersion tube with its steerable mirrors can be seen.
For a proper comparison of the measured footprint, the neutral beams needs to be modeled as 3D objects to subsequently superimpose them with the infrared image in a CAD model of ASDEX Upgrade. The NBI model was built in cooperation with N. den Harder. In a first step the beamlet origins were taken from the datasheet of the grids, describing the source geometry. Then the beamlet normals were calculated with IBSimu, an ion optics simulation code [116]. The calculated beamlet normals for a NBI source of box 2 can be seen in figure 6.9, the corresponding calculations for box 1 are shown in appendix B.1.
The two grid halves have different vertical and horizontal focal lengths. Due to the fact that the optimization of the beam optics was only performed for the 60 keV beams of box 1. For the beams of box 2 only the distance between the grids was increased for the high voltage demands of 93 kV acceleration voltage.

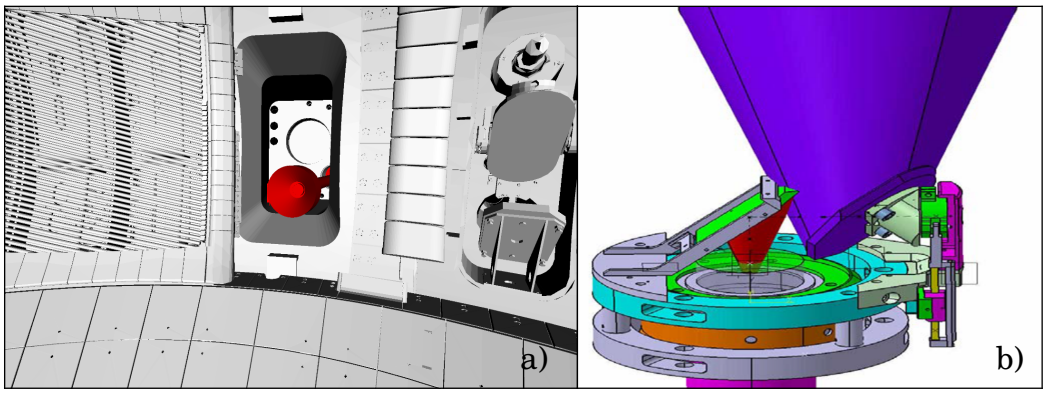

Figure 6.8.: a) shows the invessel rotatable immersion tube positioned in sector 9 with the infrared camera mounted at the end outside the vessel. In a) the red cone at the plasma side can be seen, representing the possible mirror positions realized by the rotatable and steerable mirrors at the head of the immersion tube, which can be seen in b). For further information see reference [115].

For a proper description of the neutral beams the single beamlets must be superimposed with the divergence of the beam. A definition of the divergence and the way to determine it can be found in F. Minks master thesis [117]. There the Doppler broadening of the beam emission spectroscopy is used to determine the divergence to a value of 0.8° for the NBI sources of NBI box 2. In figure 6.10 the calculated power densities at four different distances from the source along the beam axis and perpendicular to it for a single beam can be seen. The beam changes its shape from an initial more or less rectangular shape in a), inherited from the grid geometry, to a circular one inside the torus shown in b), c) and d). The red contour lines mark the equipotential line of $21\,\mathrm{MW\,m^{-2}}$ power density which will become important in the 3D model of the beam.
The final step of the beam modeling is the positioning of the beam model in a 3D model of ASDEX Upgrade. The construction sheet of the neutral beam boxes of ASDEX Upgrade is taken to determine the axes of the single beams. Furthermore the two possible degrees of freedom in movement, horizontal and vertical rotation around the mounted ball joint, were implemented.
In figure 6.11 the resulting superposition of the measured infrared image with a 3D CAD model of ASDEX Upgrade [118, 119] together with a modeled neutral beam can be seen. In this example the NBI beam 6 steered to the maximum off-axis position can be seen. The review of the other beams is shown in appendix B.1. The positioning of the infrared image based on the known camera position and the view direction, the image size and the aspect ratio is chosen by a proper overlap of visible components, like screw holes and tile gaps. The shown 3D neutral beam model in figure 6.11 a) is build by the central beam axis and is surrounded by the $21\,\mathrm{MW\,m^{-2}}$ power density equipotential lines. Also the intersection with the wall is shown.
The comparison of the nominal beam geometry with the infrared image in figure 6.11 a) reveal a deviation. Due to the fact that the positioning of the single sources was made in

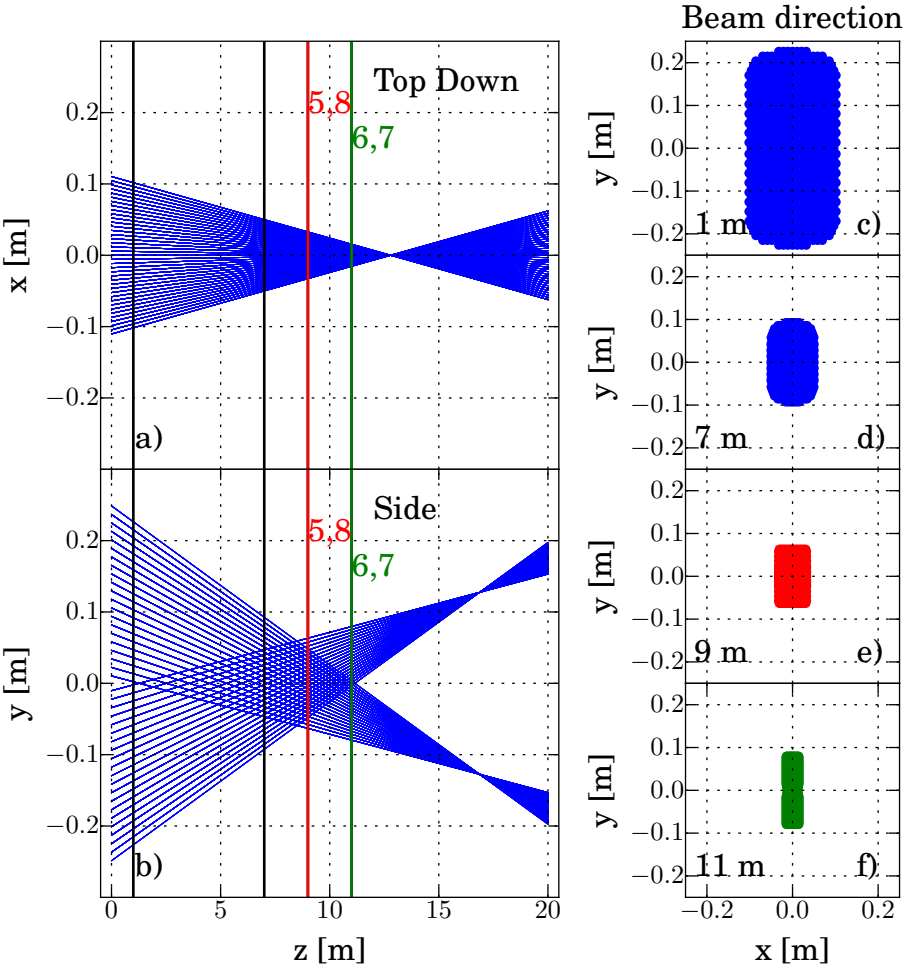

Figure 6.9.: Geometry of all beamlets of a NBI source of box 2. In a) the top-down view with the horizontal focus at 12 m can be seen. In b) the side view of the vertical foci at 17 m and their deviation from the beam axis can be seen (note the non-equal aspect ratio). The deviation arises from the initial design for 60 keV of beam box 1 only modified with respect to the high voltage demands to 93 keV without a review of the grid design. In c)-f) the overlap of the beams from the single beamlets at four different distances from the source along the beamline can be seen.

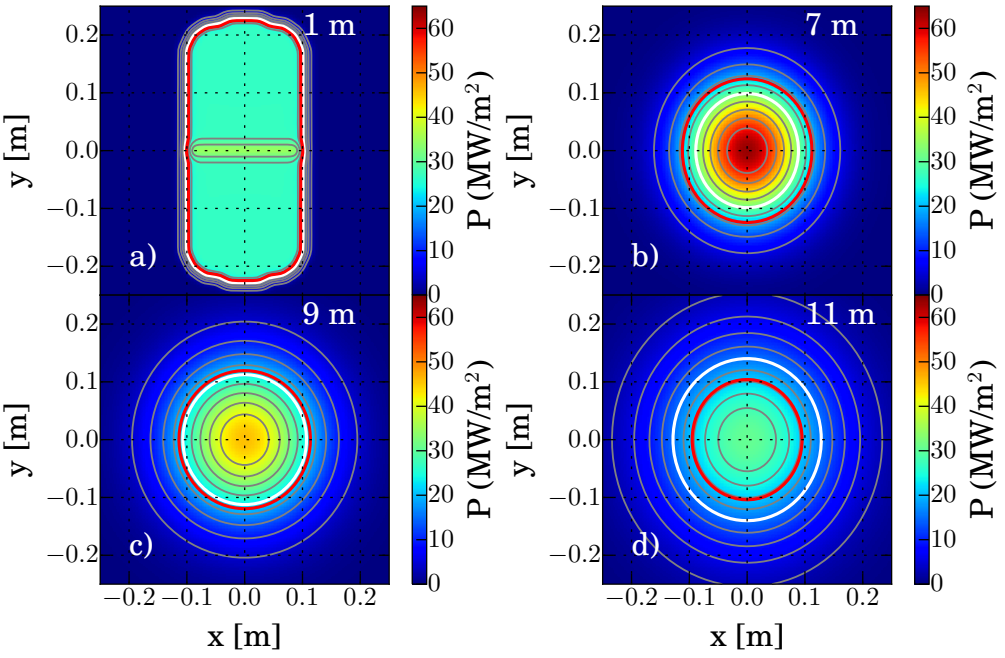

Figure 6.10.: Power density profiles perpendicular to the beam axis at four different positions along this axis of a beam of box 2 can be seen. After 1 m in a) the rectangular shape of the grids is still visible, but after several meters, where the beam intersects the plasma, the shape of the beam is almost circular also at the wall intersection in b), c) and d). The red lines indicates the equipotential line of 21 MW m^{-2} power density. These lines are used for the evaluation of the infrared images. Due to the fact that these equipotential lines decreasing their radius the overall beam extension at reasonable power density is increasing. The central power density decreases and this is illustrated by the white lines indicating the equipotential line of 50% of the maximum power density.

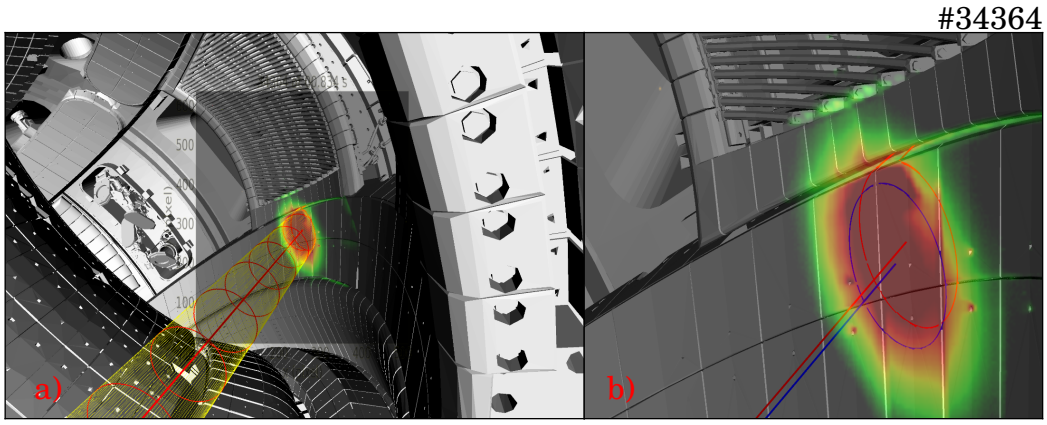

Figure 6.11.: Superposition of the infrared image with a 3D-CAD model of ASDEX Upgrade and the modeled beam geometry. The comparison shows the revision of neutral beam 6 in off-axis position. In a) the modeled neutral beam in the nominal position, with its 21 MW m^{-2} equipotential contour lines can be seen. In b) a zoomed view on the wall intersection and for the modeling the surface line of the 21 MW m^{-2} equipotential contour and the central axis can be seen. In red the nominal geometry and in blue the optimized geometry is shown.

a very accurate procedure, but without a measurement of the precise beam axis a small tilting of the sources with respect to their nominal direction is possible and also a grid displacement. The single NBI sources are mounted with a ball joint, with a fixed and well known position, and two tilting screws for vertical and horizontal steering, enables small tilting adjustments along two axis. In figure 6.11 b) the zoomed superposition of the infrared measurement with the modeled wall intersection is shown. In red the nominal geometry is shown and in blue the geometry optimized by view, with -0.20° horizontal and +0.40° vertical tilting. These tilting angles are in agreement with the tolerances in the construction phase. In table 6.1 the corrections for all four sources of box 2 can be found. Of special interest are the sources 6 and 7 which are steerable, the nominal steering range is from -0.50° to +0.30° for beam 6 and -0.50° to +0.50° for beam 7. This angle change between the different vertical steering positions was remeasured with a protractor at the source with an accuracy of 0.01°. These measured values fit perfect to the set values.
A closer look at the result table 6.1 shows only small deviations for the fixed neutral beams 5 and 8. The steerable beams 6 and 7 got a small horizontal tilt and also all their vertical angles are slightly tilted with respect to the nominal values. Nevertheless the differences between the different steering positions are in agreement with the nominal differences within the uncertainties. This uncertainty is expected to be ±0.05°. In total the off-axis beams 6 and 7 are generally steered a bit more off-axis with respect to their nominal positions.

A further issue in the simulation of the neutral beams with TRANSP appears from the different vertical focus positions of the two grid halves for beam box 2. These can be seen for a single beam in figure 6.9 b). In TRANSP, two focal lengths, the source size and

NBI Source	horizontal tilt	vertical tilt	nominal vertical tilt
Q5	-0.10°	+0.05°	+0.00°
Q6 On-Axis	-0.20°	-0.40°	-0.50°
Q6 Reference	-0.20°	+0.10°	+0.00°
Q6 Off-Axis	-0.20°	+0.40°	+0.30°
Q7 On-Axis	-0.10°	-0.25°	-0.50°
Q7 Reference	-0.10°	+0.20°	+0.00°
Q7 Off-Axis	-0.10°	+0.75°	+0.50°
Q8	-0.10°	+0.10°	+0.00°

Table 6.1.: Horizontal and vertical correction angles for the NBI sources of box 2 to optically match the infrared measurements, with an accuracy in the order of ±0.05°.

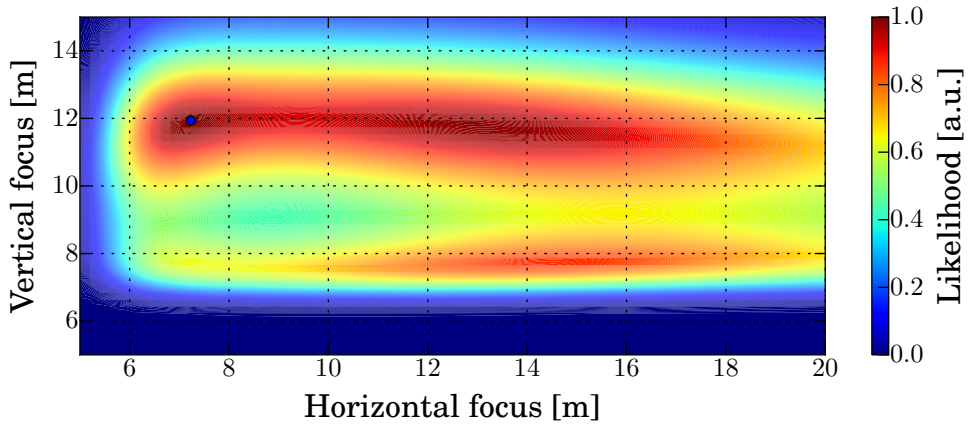

Figure 6.12.: Likelihoods for different combinations of vertical and horizontal focal length to match the power density distribution between 8 to 11 m with the assumption of a single source of box 2 in contrast to the real power density from the individual grid halves with the real focus length.

the divergence is used to define the neutral beam source. However, only one combination of vertical and horizontal focal length per source is possible, because TRANSP does not simulate the grid half individually. As consequence for beam box 2 each grid half has to be defined as individual neutral beam source with adapted geometry, position and the power of the source needs to be bisect. This adaption is time consuming and an increased number of NBI source with a factor of 1.5 increases the computational costs of a TRANSP simulation. However, these adaptions enable the use of the measured focal lengths.
An alternative approach, simulating both grids together as single source, can be found defining effective focal lengths for the whole source. The calculation of this effective focal lengths based on a 2D parameter scan in both focal lengths. For this scan beams are simulated assuming an equal vertical and horizontal focus point for both grid halves, with different combinations of vertical and horizontal focal lengths. These beams are compared in a further step with the exact simulation of a neutral beam source, taking the vertical focus point deviation of the different grid halves into account.

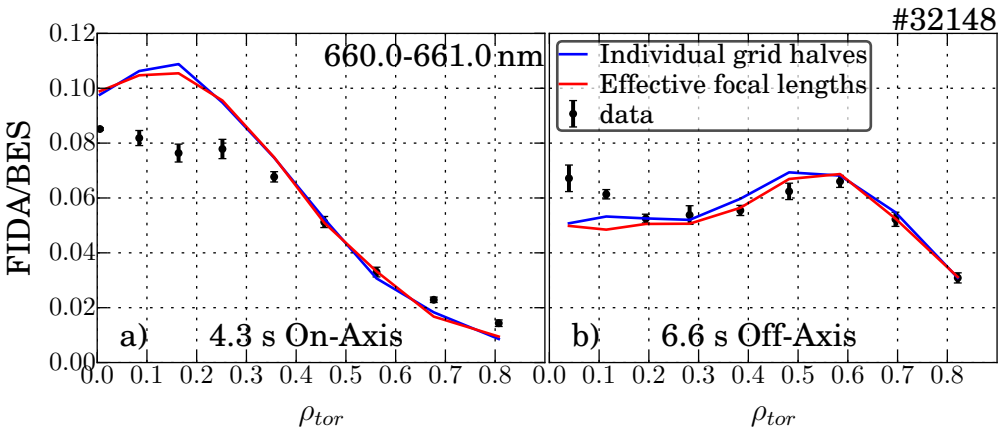

Figure 6.13.: Comparison of the TRANSP predicted FIDA profiles either simulating each grid half of the beams of box 2 individually or assuming an effective focal length.

Practically 20 slices of the power densities along the beam axis between 8 m and 11 m downstream, where the beam intersects the plasma, are compared. The comparison is done in multiple steps, first the squared difference of the 2D power densities in a single slice are calculated, summed up and normalized to the number of grid points in the slice. In the second step the 20 slices are averaged. In the third step the likelihood for the combination of focal lengths is calculated using reference [120]. Finally the likelihood is normalized to the maximum value. In figure 6.12 this 2D contour of the normalized likelihood for different combinations of focal lengths is shown. The best agreement is reached for an effective horizontal focal length of 7.23 m instead of the real 12.80 m and a vertical focal length reduced from real 16.80 m to effective 11.94 m.
To crosscheck the comparison in a practical example the two cases were compared. In figure 6.13 the TRANSP predicted synthetic FIDA profiles assuming the real geometry and the geometry with the effective focal lengths can be seen. The simulation in blue calculating the geometry of the neutral beams of box 2 individually for each grid half with the measured focal lengths. In red the simulation assuming the effective focal lengths, simulating both grid halves together, is shown. As the results of both simulation are in almost perfect agreement, the approach with the effective focal length works well and is therefore used henceforth.

Finally, because of the changed geometry also the beam power, transmitted through the duct towards the plasma, was revisited. The former value was 85% for all beams based on approximations from the commissioning phase of the neutral beams of beam box 1 at ASDEX Upgrade. A detailed description of the calculation and the attempt to validate the calculation with measurements can be found in appendix B.1.1. The result of the new calculations for the geometrical transmission can be seen in table 6.2. The attempt to validate the calculation with measurements, using the diamagnetic flux loop, however, was not conclusive.

NBI Source	Geometrical Transmission	New new Scraper
Q1	98.0%	-
Q2	92.0%	-
Q3	92.0%	-
Q4	98.0%	-
Q5	96.5%	95.5%
Q6 On-Axis	92.0%	92.0%
Q6 Reference	92.0%	92.0%
Q6 Off-Axis	91.5%	91.5%
Q7 On-Axis	93.5%	93.5%
Q7 Reference	93.0%	93.0%
Q7 Off-Axis	90.0%	90.0%
Q8	97.0%	95.5%

Table 6.2.: The resulting geometrical transmission from appendix figure B.13 at the end of the duct. Also the calculations for the new beam exit scraper installed in beam box 2 before the campaign 2017.

6.3.2. Sensitivity Analysis

TRANSP does not take uncertainties of the input quantities into account and also calculates no uncertainties for the output quantities. To get an error estimation a set of simulations are performed, with minor changes of the input profiles in the order of their uncertainties. The TRANSP input profiles are given as a function of the normalized toroidal flux ρ_{tor}, with the advantage, that all profiles are given in the same universal radial coordinate system. A possible source of systematic uncertainties is the mapping on a non-accurate equilibrium.
The equilibrium reconstruction in ASDEX Upgrade is described in section 2.1.1. Standardly the routinely written and fast available Cliste EQH equilibrium, which is only uses magnetic measurements as constrains, is used to map the TRANSP input profiles. However, especially centrally the uncertainty of these equilibria is high. Therefor in this case an IDE equilibrium, taking also the kinetic profiles, the current diffusion equation and internal constrains like the MSE and the Faraday rotation polarimetry into account, is used for a comparison.
In figure 6.14 a) and b) the R and z position of the magnetic axis predicted by the different equilibria can be seen. The movement in R of the magnetic axis in the phase from 4.5 to 7 s is not reproduced by the EQH equilibrium, as the magnetic measurements does not change, but the pressure profile is changing. In figure 6.14 c) and e) temperature profiles are shown, mapped on the EQH and IDE equilibria at two different points in time. In 6.14 d) and f) the corresponding relative changes can be seen, with differences up to 30%.
Furthermore the uncertainties of the measurements of the different input quantities must be taken into account. For the ion temperature and rotation velocity of the plasma only data from the CXRS (charge exchange recombination spectroscopy) were taken into account.

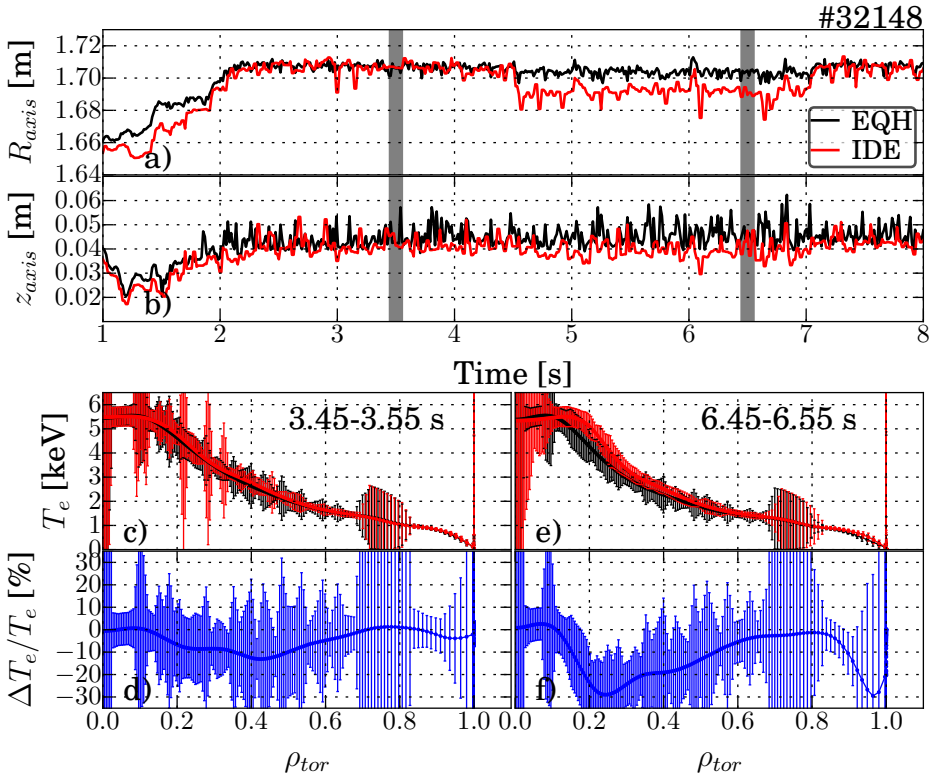

Figure 6.14.: In a) and b) the predicted position of the magnetic axis by the equilibria EQH (Cliste) and IDE is shown. In c) and d) the electron temperature profile mapped on this equilibria with error bars from IDA and the relative difference between the different equilibria is shown. In e) and f) the stronger temperature profile differences at a later point in time, with larger deviations in the prediction of the magnetic axis is shown.

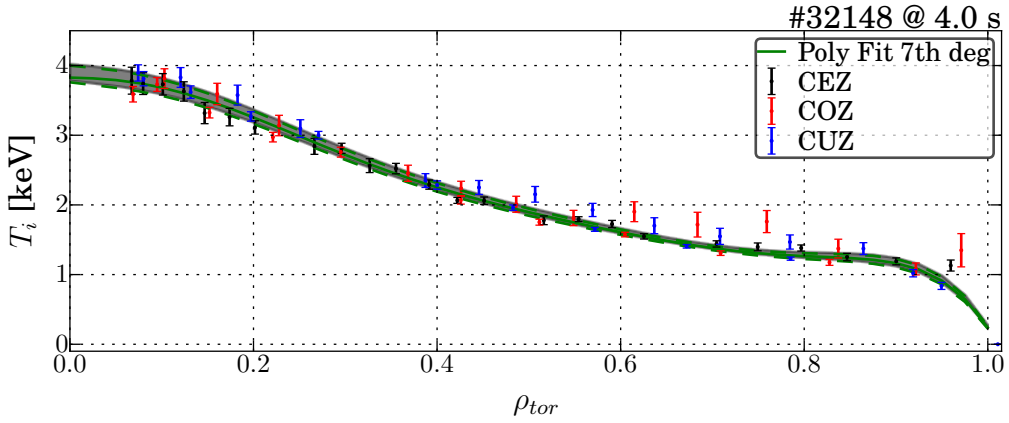

Figure 6.15.: Example for fitting the ion temperature profile at one point in time from CXRS measurements. All data were once up and once down shifted by their uncertainties and fitted again to get an estimation for the uncertainty of the profile. The different colored data points are from different optical heads and spectrometers shown in section 3.3.6.

To test the influence of a variation of the inputs on the TRANSP outputs, all data points were individually shifted up or down by their uncertainties at once and then fitted by a 7th order polynomial fit. The different fits for the ion temperature can be seen for one point in time in figure 6.15. A similar behaviour is found for the rotation velocity. The different modified input files were used in a set of individually calculated TRANSP simulations.
The profile of the effective charge of the plasma is calculated following the description in section 3.3.6, equation (3.10). The spectroscopically measured impurity densities of helium, boron, carbon and nitrogen have an uncertainty of ±10%. Therefore the uncertainty of the effective charge is also assumed to be in the order of ±10%.
Assumptions on the uncertainty of the electron density and electron temperature are more complicated. As the electron density and electron temperature profiles from IDA are calculated from a combination of multiple diagnostics (see section 3.3.7) a general uncertainty on these profiles is hard to get. To overcome this problem at a representative point in time the input data for the IDA calculation, in this case the DCN interferometry, the Lithium Beam data, the ECE measurement and the Thomson scattering data, were randomly shifted 600 times within their uncertainties and then the electron density and temperature profiles were evaluated. All these profiles can be seen in figure 6.16 a) and b). In figure 6.16 c) and d) the relative changes can be seen and colored also the maximum uncertainty. Obviously the uncertainties in the electron temperature measurements are smaller than for the electron density. Furthermore the central electron density measurement has large uncertainties due to the defect central DCN channel during the whole 2015/2016 ASDEX Upgrade experimental campaign.
Finally the time dependent input electron density and temperature profiles were up and down shifted pointwise by their maximum relative changes and individual TRANSP simulations were started for each case. The 3D electron density and temperature profiles used as input in TRANSP can be seen in figure 6.17.

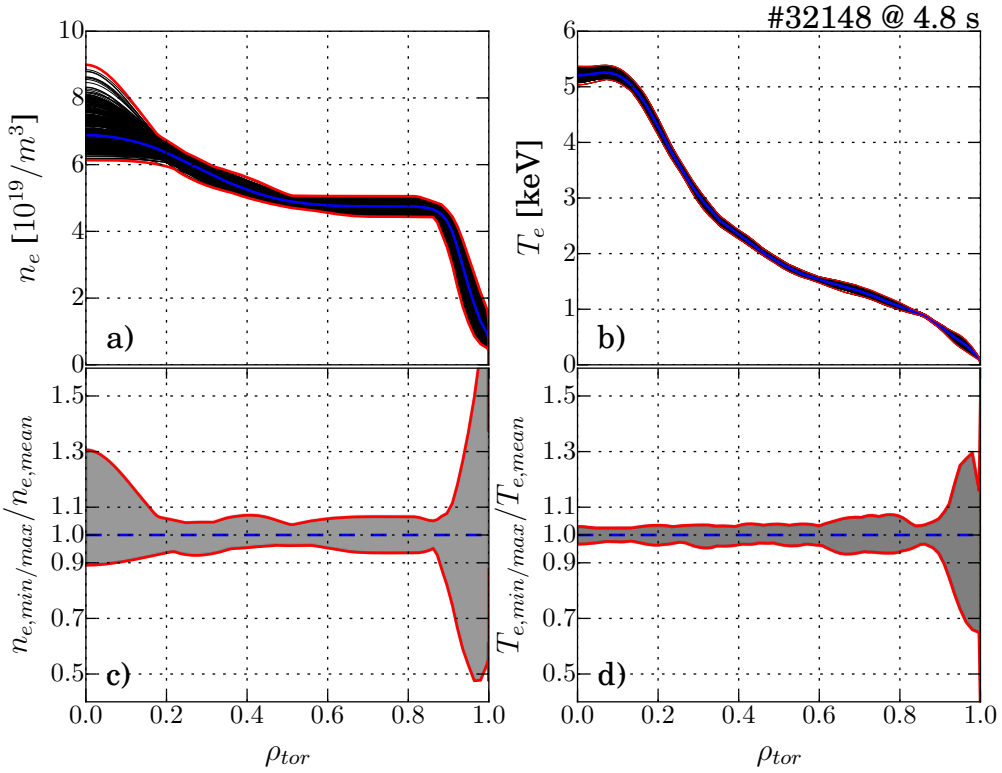

Figure 6.16.: In black, in a) 600 electron density and electron temperature profiles in b) from IDA at 4.8 s are shown. All profiles are calculated by a random variation of all IDA input diagnostic within their uncertainties at this point in time. The maximum deviation is shown in red and the average in blue. In c) and d) the maximum relative deviation of the profiles from the average is shown.

Following the influence of the individual varied kinetic input profiles on the different important diagnostics are investigated. Combined effects due to the simultaneous variation of multiple kinetic profiles are not taken into account.

In figure 6.18 the influence of the kinetic profile uncertainty scan on the synthetic FIDA diagnostic can be seen. The combined uncertainty from the square root sum of the relative individual uncertainties is in the order of up to 20% and is dominated by the uncertainty of the electron density. Due to the missing central DCN channel the uncertainty increases in the center of the plasma. The strong influence of the density fluctuation on the FIDA diagnostic is connected to the change in the slowing down time of the fast ions, given by equation (2.27), with $t_s \sim T_e^{3/2}/n_e$. As the uncertainty on the electron temperature is smaller, its influence on the FIDA diagnostic is small.
The result of the sensitivity scan for the synthetic MSE diagnostic data can be seen in figure 6.19. While figure 6.19 a) shows the π channels, figure 6.19 b) shows the σ channels.
Figure 6.20 shows the deviation of the synthetic MSE angles, due to the variation of the kinetic profiles from the reference simulation for the different radial channels averaged over

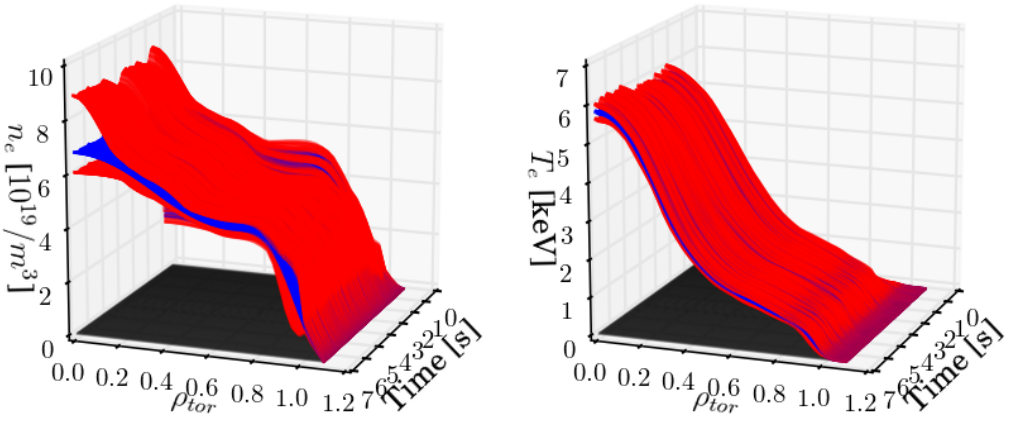

Figure 6.17.: In blue the best estimation of the time-dependent electron density in a) and electron temperature profiles in b) in discharge #32148 is shown. Furthermore in red their upper and lower lines representing the conservative assumption of the uncertainties of the single profiles are shown.

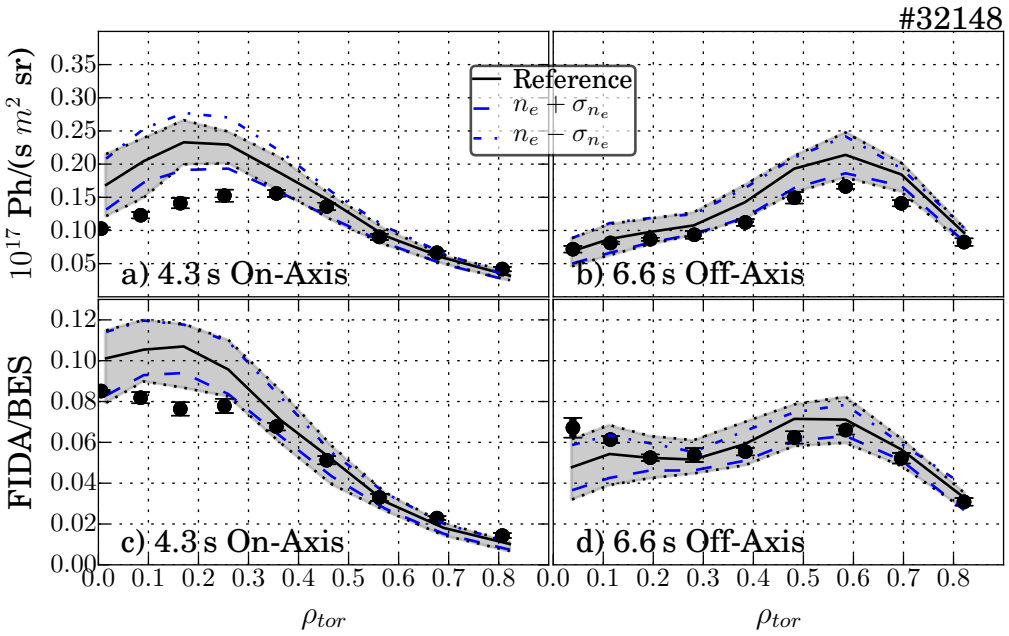

Figure 6.18.: Influence of the profile uncertainties on the synthetic FIDA diagnostic for an on-axis and off-axis point in time. As the electron density has the major influence, only changes due to the variation of this profile is shown. The influence of the variation of all other profiles can be seen in appendix B.2 in figure B.15.

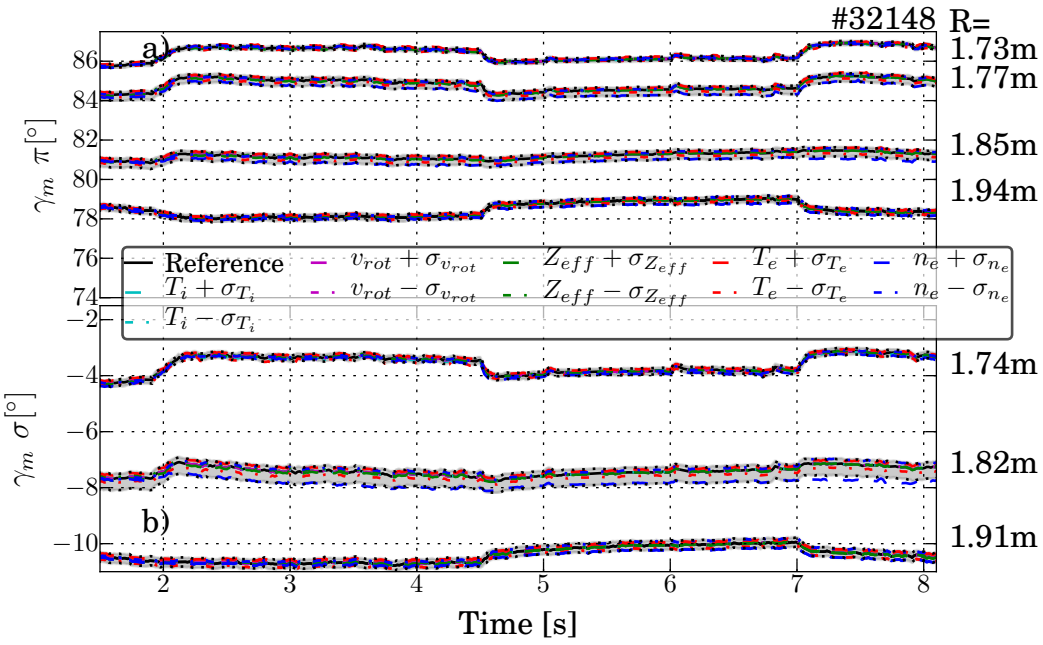

Figure 6.19.: Result of the sensitivity scan on the synthetic MSE diagnostic. Only TRANSP predictions are shown.

the whole discharge. With a mean deviation of lower than 0.05° the influence is small with respect to the uncertainty of the measurement in the order of 0.2°. But the strongest impact comes from the electron density uncertainty with an angle change up to 0.4° and from the electron temperature variation with an angle uncertainty of 0.15°. The influence can be explained by a change in the gradient of electron density or electron temperature, leading to a change in the pressure gradient. These changes in the pressure gradient change the strength of the bootstrap current locally explaining the local sensitivity of the synthetic MSE to the changes in the electron density and electron temperature profiles.
In figure 6.21 the influence on the predicted synthetic diamagnetic flux can be seen. The uncertainty in the order of 0.5 mWb from the kinetic uncertainty scan in TRANSP seems to be dominated by the uncertainty of the electron density, but the reason for this behaviour is the higher relative uncertainty on the electron density compared with the electron temperature. One expects a similar influence of electron temperature and electron density as the diamagnetic flux is proportional to the plasma pressure, which in first order is the product of electron density and electron temperature.
The influence on the loop voltage can be seen in figure 6.22. The uncertainty is dominated by the variation of the electron temperature, due to the fact that changes in the electron temperature have a strong impact on the resistivity of the plasma. Furthermore the loop voltage is sensitive to changes in the effective charge of the plasma, but due to the fact that the effective charge in this discharge is small with ~ 1.3, the change of $\pm 10\%$ does not have a big influence.
The influence of the uncertainties of the input kinetic profiles on the polarimetry is shown in figure 6.23. As expected, the dominant influence leading to the diagnostic uncertainty of

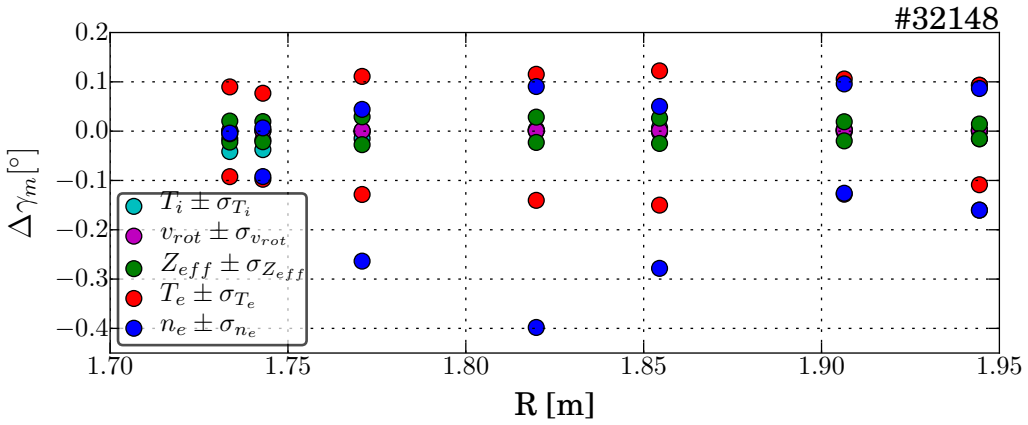

Figure 6.20.: Radially resolved deviation of the MSE angles from the reference simulation due to the kinetic profile variation, averaged over the whole discharge. The time evolution of the angles and uncertainties can be seen in figure 6.19.

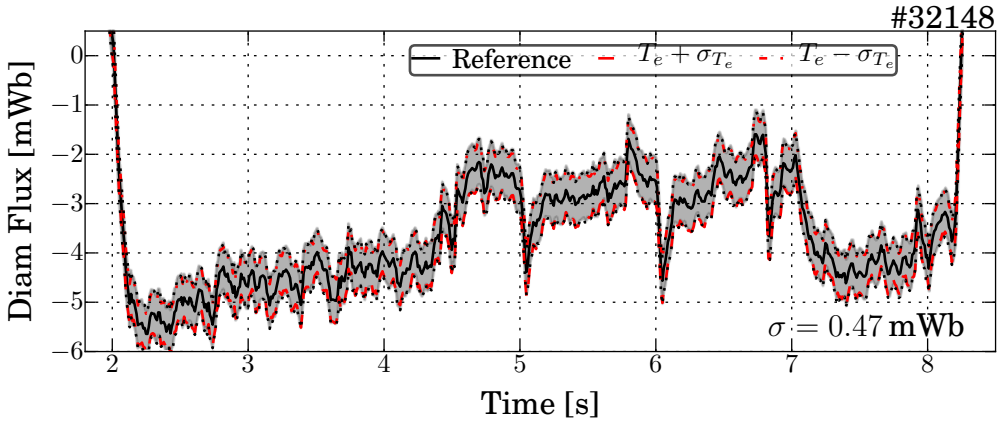

Figure 6.21.: Influence of the assumed uncertainties of the kinetic profiles on the diamagnetic flux prediction. Dominated by the electron temperature uncertainty leading to a deviation of up to 0.47 mWb. The measured diamagnetic flux is not shown. The influence of the variation of the other profiles can be seen in appendix B.2 figure B.16.

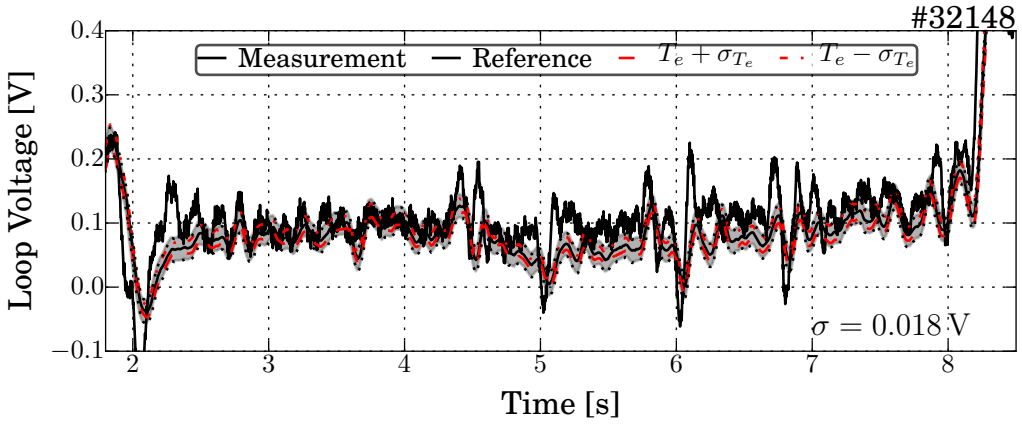

Figure 6.22.: Sensitivity of the TRANSP predicted loop voltage due to variations of the kinetic profiles with respect to their uncertainties. The influence of the variation of the other profiles can be seen in appendix B.2 figure B.17.

$\sim 0.6°$, comes from the electron density, because, as mentioned in section 3.3.3 in equation (3.6), the angle is proportional to the integrated density along the line of sight times the parallel magnetic field. The other kinetic profiles have only higher order effects regarding changes in the magnetic field, by their influence on the current profile.
Finally the influence on the predicted neutral beam driven current can be seen in figure 6.24. The uncertainty on the NBCD in the order of 10% is dominated by the uncertainty of the electron density, but also the variation of the electron temperature seems to change the neutral beam driven current. As mentioned in section 2.4.2 an important parameter for the calculation of the neutral beam driven current is the Spitzer slowing down time in equation (2.27) proportional to $T_e^{3/2}/n_e$. Together with the smaller relative uncertainty on the electron temperature, see figure 6.16 c) and d), this is consistent with the expectation. Also visible is the small influence of the variation of the effective charge on the neutral beam driven current through the change in the electron shielding current. The effect is in the same order of magnitude as the influence of the change in the electron temperature.

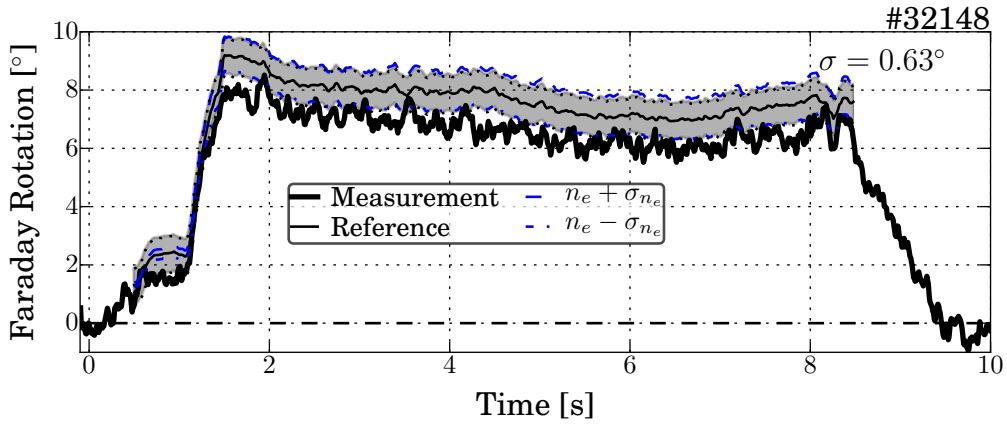

Figure 6.23.: Sensitivity off the single polarimetry channel on the variation of the kinetic profiles with respect to their uncertainty. As expected the dominant influence came from the electron density variation. The influence of the variation of the other profiles can be seen in appendix B.2 figure B.18

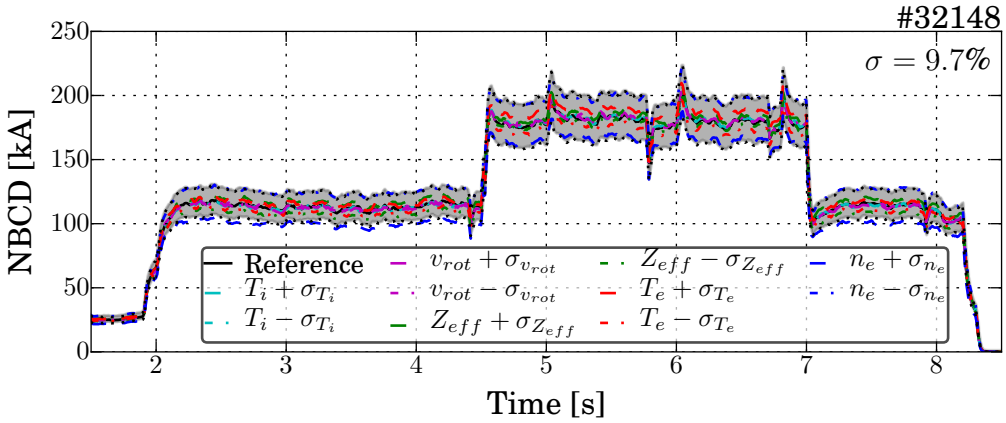

Figure 6.24.: Influence of the variation of the kinetic profiles with respect to their uncertainties on the TRANSP predicted neutral beam driven current.

6.4. Comparison with Improved Simulations

In section 6.3 several improvements with respect to the simulations in section 6.2.2 were made. The four main improvements are

Neutral Beam Injection Geometry: The revision of the geometry using the infrared camera is described in section 6.3.1.

Geometrical Beam Transmission: In combination with the geometry revision the geometrical power losses in the beam duct are calculated (see table 6.2) and point towards a higher injected beam power.

Remapping of the kinetic profiles: During the sensitivity analysis (see section 6.3.2) a non-negligible influence of the mapping of the kinetic profiles on a proper equilibrium was found. Therefore the more reliable IDE equilibrium is used for the mapping.

Effective charge profile: The calculation of the effective charge from the impurity densities measured with the CXRS (see description in section 3.3.6) reduce the mean value from 1.6, calculate from the evaluation of the bremsstrahlungs measurement, to 1.3, the two time dependent effective charge profiles can be seen in the appendix B.3 in figure B.19.

In the following, the comparison of synthetic diagnostics, calculated from the TRANSP output, with their corresponding measurements will be shown. Starting with the MSE, figure 6.25 shows the temporal evolution of seven different radial MSE channels. As the MSE was not in the perfect shape, only seven channels were useful. The radial intersections of the lines of sight with the beam 3 in front of the flux surfaces can be seen in figure 6.6. Unfortunately the absolute calibration presented in chapter 4 cannot be applied retroactively, as the MSE protection window towards the plasma was changed during the maintenance break, prior to the calibration measurements. Therefore the simulations still need to be offset corrected. From the experience that the TRANSP simulation have all almost the same value during the off-axis phase, the simulations are off-set corrected to match the measurement during the off-axis phase.
The most obvious change of the MSE angles occurs immediately after at the switch from the on- to the off-axis NBI phase and vice versa. It is caused by the change of the radius of the magnetic axis due to the Shafranov shift. In the measured and predicted angles the change is in the order of $\pm 0.2°$. This change is in the same order of magnitude as the statistical uncertainty of the measurement, but is not a statistical fluctuation as it only change in one direction for each line of sight. Also the maximum deviation due to the assumption of global anomalous fast ion diffusion in the order of $0.5\,\mathrm{m}^2/\mathrm{s}$ leads to a change of the predicted MSE angle in the order of $\pm 0.2°$. In most of the channels the predicted angles are in agreement with the measurement. A tendentially better agreement is achieved with the assumption of anomalous fast ion diffusion, especially in the central channels. Overall, the agreement of all simulations with the measurement is slightly improved with respect to the initial comparison in figure 6.5. However, in conclusion the MSE diagnostic is not very sensitive to the assumption of anomalous fast ion diffusion, as the changes in the global current profile due to the redistribution of fast ions are small. This can be seen in the TRANSP simulations in figure 6.26. The neutral beam driven current is only a minor part of the total plasma

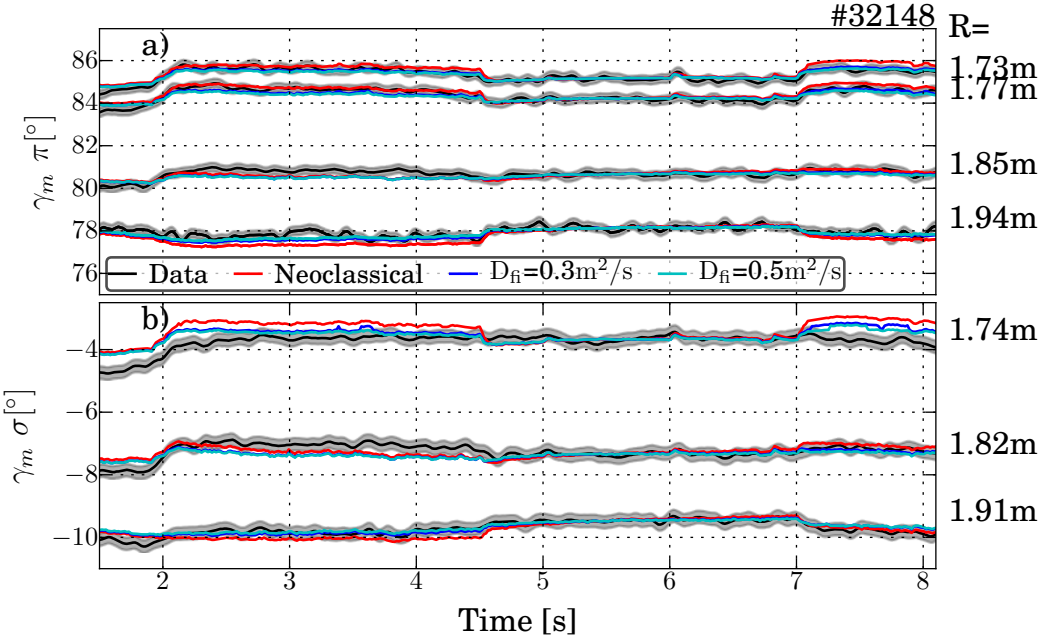

Figure 6.25.: Comparison of the TRANSP predicted MSE angles with the measurement. The predicted angles are individual off set corrected to match the measurement between 5-6 s, due to the missing absolute calibration. In a) four π- and in b) three σ-channels can be seen. Furthermore the assumption of global anomalous fast ion diffusion is shown.

current profile. Furthermore, as the change of the neutral beam driven current due to the anomalous fast ion diffusion is below 15%, and as the neutral beam driven current is below 25% of the total current, the effect on the total current is less than 3%.

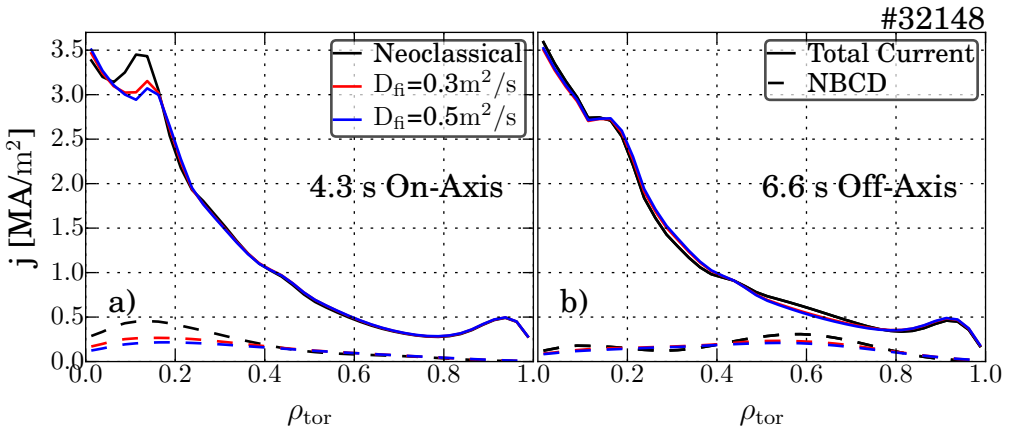

Figure 6.26.: Influence of the anomalous fast on diffusion on the TRANSP calculated current profiles. The dashed lines represents the neutral beam driven part of the current. In a) a point in time in the on-axis phase and in b) in the off-axis phase is shown. The change in the total current profile is small.

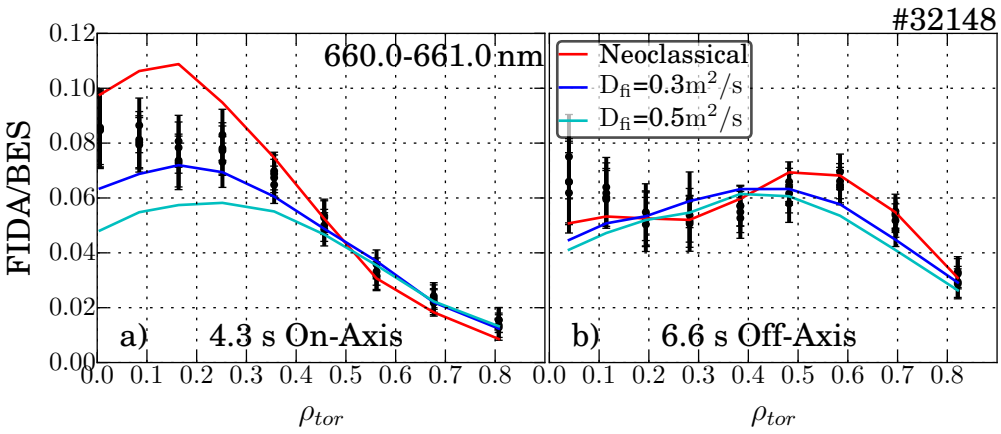

Figure 6.27.: Normalized FIDA measurement with statistical uncertainties in comparison to FIDASIM post processed TRANSP simulations. Shown are simulations assuming neoclassical transport and in contrast global anomalous fast ion diffusion. In a) a point in time in the on-axis phase and in b) in the off-axis phase is shown.

The second diagnostic that had motivated the review of the beam geometry is FIDA. The comparison between the synthetic diagnostic and the measurement is shown in figure 6.27. In the on-axis phase in figure 6.27 a) the central measurements are still overestimated by the neoclassical prediction, although less than in figure 6.7. In contrast, in the off-axis phase, shown in figure 6.27 b), the shape of the neoclassical prediction is in much better agreement with the data due to the revised geometry. In this phase the assumption of anomalous fast ion diffusion blurs the peak of beam 3 and the one from beam 6 and 7, leading to a disagreement in the shape of the prediction. Therefore the assumption of the anomalous fast ion diffusion is necessary during the on-axis phase, while the FIDA measurement in the off-axis phase are only in agreement assuming neoclassical transport.
A further diagnostic that is also sensitive to changes in the current profile is the DCN-Faraday rotation polarimetry (see section 3.3.3). The comparison of the synthetic diagnostic with the measurement of the single available channel is shown in figure 6.28.
The simulation assuming that no neutral beam driven current exists deviates from the measurement. This is a strong indication for the existence of non negligible neutral beam driven current. In contrast all other TRANSP simulations are in good agreement with the data. Unfortunately the difference between the simulations assuming neoclassical transport and the simulations assuming anomalous fast ion diffusion is too small to be resolved by the measurement. As shown before the change in the global current profile by redistribution of fast ions is too small. Therefore the diagnostic can only prove the existence of a change of the global current profile due to the neutral beam driven current, but can not resolve anomalous fast ion transport.
A similar conclusion is reached by the comparison of the loop voltage measurement with TRANSP predictions, as shown in figure 6.29. Again only the existence of the neutral beam driven current can be verified, but anomalous fast ion transport cannot be resolved.
Finally the measurement of the diamagnetic flux loop (see section 3.3.1) is compared with

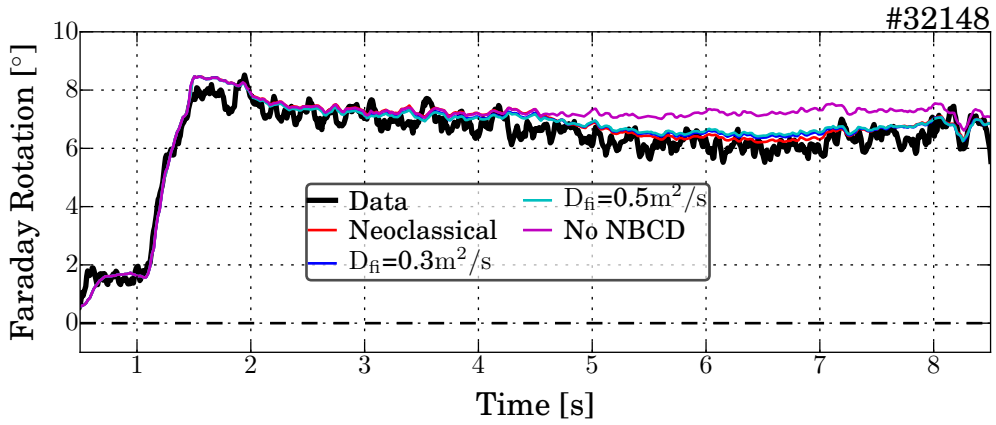

Figure 6.28.: Faraday rotation polarimetry measurement in comparison to TRANSP predictions. The current redistribution is measurable, but the assumption of anomalous fast ion diffusion could not be resolved.

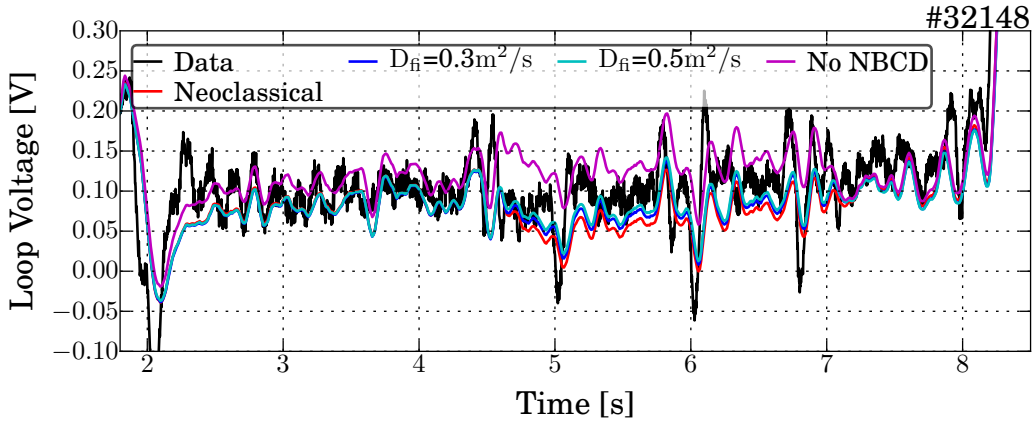

Figure 6.29.: Comparison of the measured loop voltage with TRANSP predictions. Only strong deviations could be seen, assuming the non-existence of neutral beam driven current. The other simulations are in agreement with the measurement.

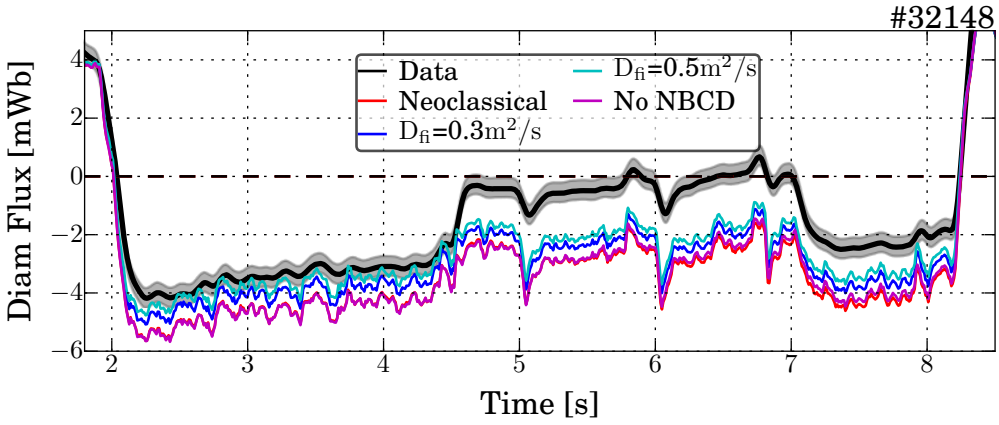

Figure 6.30.: Measurement of the diamagnetic flux loop in comparison with the corresponding TRANSP predictions. The strong deviation in the off-axis phase could not be explained yet, therefore the diagnostic could not be used for any possible conclusions about the anomalous fast ion diffusion, although it seems that the diagnostic could resolve the assumption of anomalous fast ion transport.

the TRANSP prediction in figure 6.30. Both predictions deviate from the measurement in the on-axis and even stronger in the off-axis phase. This deviation is also visible in other discharges using the off-axis neutral beams. One possible, not yet tested, explanation for this behaviour was found. The diamagnetic flux is very sensitive to the pressure profile including the fast ion pressure. An important part is the mapping of the pressure on an equilibrium, therefore the equilibrium reconstruction plays a major role in predicting the diamagnetic flux. A possible systematic uncertainty at this point can be found in the publications [121–124] about equilibrium analysis with anisotropic pressure. This uncertainty could maybe explain the difference between the measurement and the prediction, especially the off-axis phase is affected because the non-negligible fast ion pressure is shifted more outwards in regions which could be more affected by this anisotropy. However, as this explanation is not tested jet, no conclusion for this diagnostic is presented. Nevertheless, for future experiments, once the deviations in the off-axis phase could be explained, the difference between the neoclassical predictions and the predictions assuming anomalous fast ion diffusion seems to be strong enough to be conclusive. It should also be remarked that this diagnostic is used for the first time in the experimental campaign 2015/2016 and therefore systematic uncertainties could not be fully excluded.

6.5. Perturbation Induced Fast Ion Redistribution

The FIDA comparison in figure 6.27 clearly demonstrates the need for the assumption of anomalous fast ion transport. However, such an assumption is only required in the on-axis phase, while the off-axis phase agrees with the neoclassical simulation. The disagreement

in the on-axis phase did not vanish after applying all mentioned simulations improvements such as the revised geometry and error estimations due to the input kinetic profiles.
Besides microturbulence, the conclusion from reference [12], another reason for the observed anomalous transport could be localized fast-ion redistribution by MHD perturbations. In the following two sections both approaches are individually discussed.

6.5.1. Fishbone Induced Fast Ion Redistributing

In the following section the hypothesis of fast ion redistribution due to fishbone activity is investigated. After a characterization of the fishbones, the observed influence in other experiments is discussed. Following the modeling with several synthetic diagnostics assuming central anomalous fast ion transport due to the fishbones are compared with measurements. Finally the hypothesis for the ASDEX Upgrade results is evaluated.
The time evolution of the MHD activity in discharge #32148 can be seen in figure 6.31 a). It shows the time-dependent spectrogram measured with a set of magnetic coils, namely the B-coils. The n-number of the perturbation is calculated from the phase reconstruction. The color intensity corresponds to the amplitude of the perturbation. During the off-axis phase from 4.5 s to 7 s the discharge is MHD-quiescent. In the adjacent two on-axis phases n=1 activity can be seen. The activity at $\approx$ 20 kHz can be identified as fishbones (see section 2.5.2). The strongest indication is the frequency chirping, furthermore the phase reconstruction in the soft x-ray diagnostic identifies the mode number of the activity to m=1 and n=1. The fishbone repetition rate in the on-axis phase is stable between 250 Hz and 275 Hz only interrupted by single sawtooth every $\sim$ 230 ms and also the frequency chirp from 21 kHz to 17 kHz does not change during the on-axis phases.
From the fluctuation of the ECE measured electron temperature profile with the approximated mode frequency, the fishbones can be localized. These radial temperature fluctuation can be seen in figure 6.31 b), c), d) and e). The almost constant amplitude of the temperature fluctuation during the on-axis phase is a further indication for a constant fishbone strength.

There is evidence of fast-ion redistribution due to fishbones in the literature. At the MAST experiment a fast fast ion outward transport followed by a slow recovery using the FIDA diagnostic was observed [125], resolving the fast ion behaviour during single fishbones. However, no comparison with simulations were presented.
Also at ASDEX Upgrade the influence of fishbones on the plasma were studied in the past [126]. A redistribution of the fast ions was conclude by a time correlation between the fishbones and the signal of the charge exchange flux and also a temporally correlated drop of the neutron rate was measured.
A third publication from the JET experiment [127] concludes also with a redistribution of fast ions due to fishbone activity. In contrast to the publication before, the measured drop in the neutron rates was compared with predictions from a fast ion redistribution model due to fishbones, based on HAGIS and ASCOT simulations.

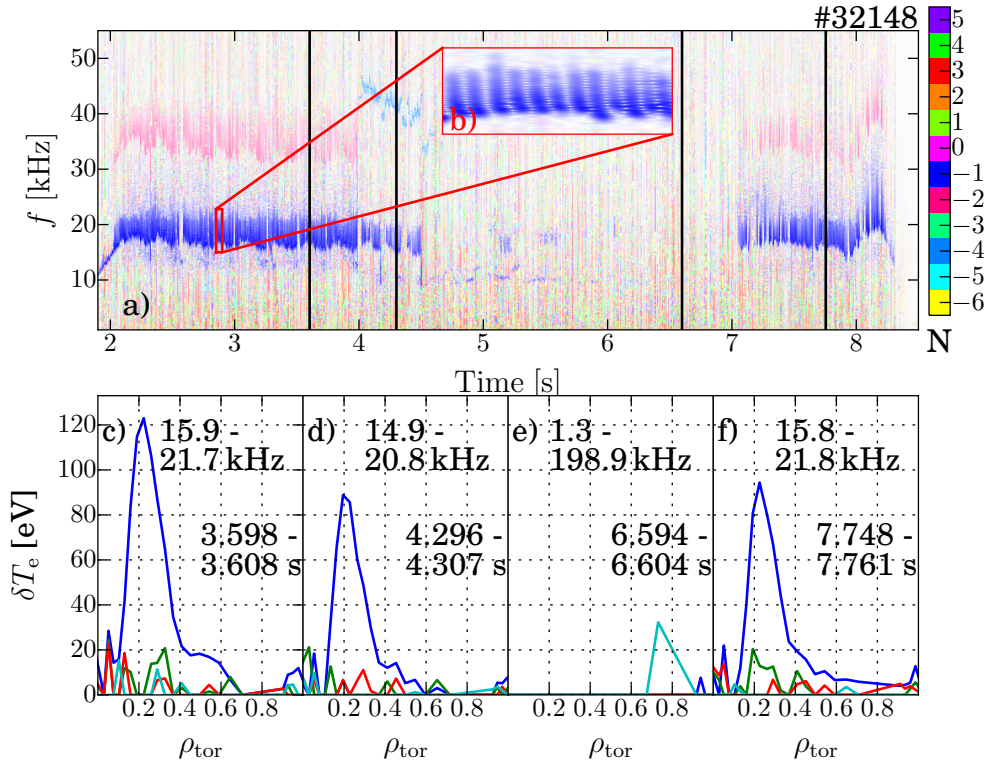

Figure 6.31.: In a) the spectogram of the magnetic signals, color coded for the different N-numbers the of the MHD perturbations can be seen. The n=1 mode number and the characteristic frequency chirping, visible in the zoomed part in b), identify the perturbation in the on-axis phases to fishbones. In c),d),e) and f) the temperature fluctuation at a dedicated frequency range can be seen, allowing the radial localizing of the fishbones.

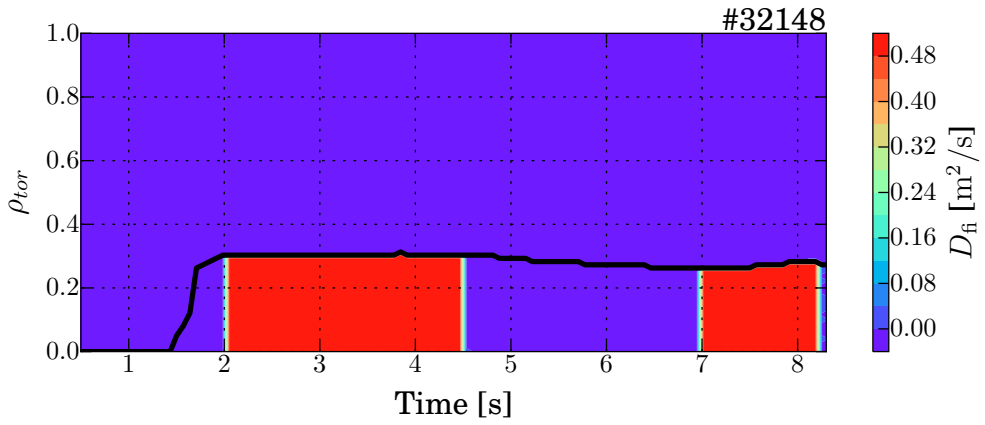

Figure 6.32.: Assumed anomalous fast ion diffusion within the q=1 surface, where the radial position of the q=1 surface is indicated by the black line. The anomalous diffusion is only switched on in phases with fishbone, identified in figure 6.31 a).

In the publication [128] also indication for a fast ion redistribution due to fishbones at the DIII-D experiment were presented. At DIII-D differences between the measured neutron rate and the TRANSP calculations were investigated and correlated with fishbone activity. The deviation were undermined by applying anomalous fast ion diffusion to the simulations. However, the neutron rate measurement is only an integral measurement.

In the FIDA measurements of ASDEX Upgrade the redistribution of fast ions due to a single fishbone cannot be seen in this discharge. Firstly the repetition rate of the fishbones is too high. Therefore the fast ion profile is not expect to completely recover between the fishbones. Secondly the time resolution of the FIDA diagnostic is too small.
For the same reason, the high repetition rate of the fishbones, no clear time correlation with the measured charge exchange flux could be resolved.
Also the ASDEX Upgrade neutron detector could not be used, as it was not properly calibrated. Furthermore the time resolution of the detector is not high enough to resolve single fishbones in this discharge. Therefore the focus is primarily on the FIDA diagnostic and on the small changes in the current profile measured with the MSE diagnostic.
To model the fast ion redistribution due to fishbones the common assumption of the fishbone mechanism, introduced in section 2.5.2, is used. There the fishbones are assumed to be triggered by an accumulation of trapped fast ions at the q=1 surface and a subsequent periodical expel of fast ions from inside this surface. Therefore a constant anomalous fast ion diffusion is assumed at $q \leq 1$, in the phases with fishbone activity. The resulting radial fast ion diffusion profile and the time evolution can be seen in figure 6.32.
The influence on the predicted FIDA profile can be seen in figure 6.33. The assumption of central anomalous fast ion diffusion of $0.3\,\mathrm{m}^2/\mathrm{s}$ and $0.5\,\mathrm{m}^2/\mathrm{s}$ in the phases with fishbones are both in agreement with the data within the uncertainties, in contrast to the neoclassical prediction. It should be mentioned that the error bars on the measurement only represent

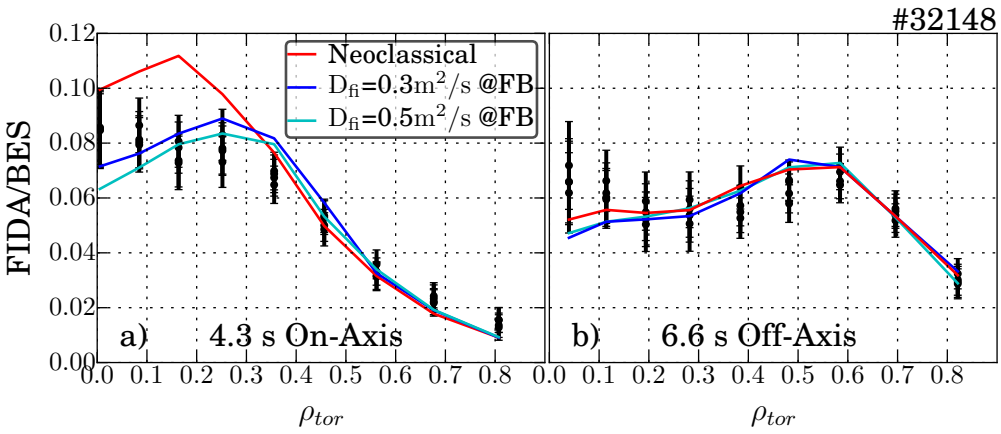

Figure 6.33.: FIDA profiles assuming the anomalous fast ion diffusion profile from figure 6.32 in contrast to the neoclassical simulation. In a) the on-axis phase with fishbones can be seen, while b) shows the MHD-quiescent off-axis phase.

the statistical uncertainties. Possible systematic uncertainties, for example from the calibration, should be canceled out by taking the ratio of the FIDA intensity to the beam emission.
It should be noted that the lines of sight of the FIDA diagnostic used for the shown radial profiles mainly probe the velocity space for the passing fast ions. This is shown in figure 6.34 for one central line of sight as an example. Figure 6.34 a) shows the TRANSP-predicted fast ion distribution at the position of the intersection from the line of sight with the beam. In b) the weight function of this line of sight can be seen. The weight function indicates that mainly particles with high energy and almost only passing particles, indicated by the high positive pitch angle, are observed. This is important as the fishbones are driven by the accumulation of trapped fast ions on the q=1 surface. Therefore the expectation indicates a redistribution mainly of the trapped particles, but the comparison in figure 6.33 indicates also a redistribution of passing particles.
A technique to look at a larger part of the velocity space of the trapped particles is FIDA tomography [91]. However, in this discharge the measurement of the vertical lines of sight, containing information on the trapped particle fraction, were disturbed irrecoverably by ELMs, therefor the comparison was not conclusive. The comparison can be seen in appendix C.1.
The influence of the assumed anomalous fast ion diffusion on the synthetic MSE diagnostic in comparison with the measurement is shown in figure 6.35. The differences between the assumption of neoclassical transport and the central anomalous fast ion transport due to fishbones are small as expected. The differences are also smaller than the uncertainties of the measurement. But in comparison to the measurements tendentially the assumption of the central anomalous fast ion diffusion agree slightly better.

In conclusion the fishbone activity seems to be able to redistribute fast ions from inside the q=1 surface outwards. The potential redistribution effects from fishbones, which are driven by trapped fast ions, also redistribute passing fast ions, this is measurable with

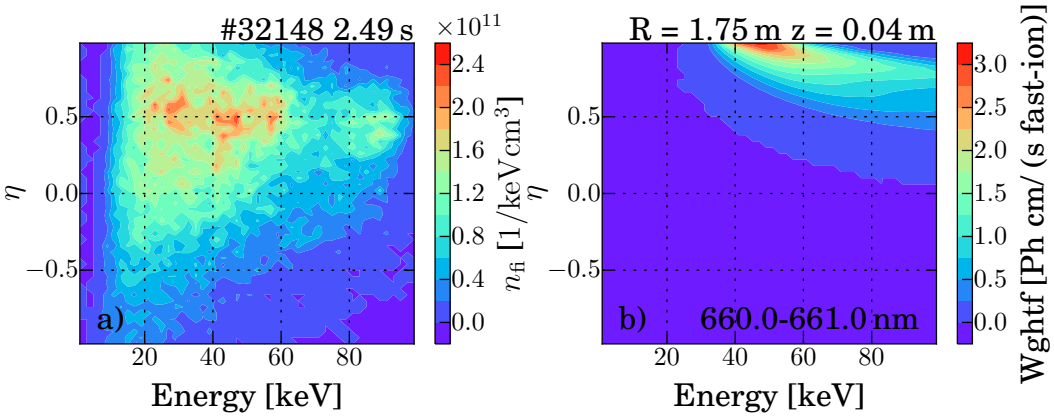

Figure 6.34.: In a) the fast ion distribution in the phase space at a dedicated point in time at the intersection of one FIDA line of sight with the neutral beam is shown. In b) the corresponding weight function of this line of sight in the phase space can be seen.

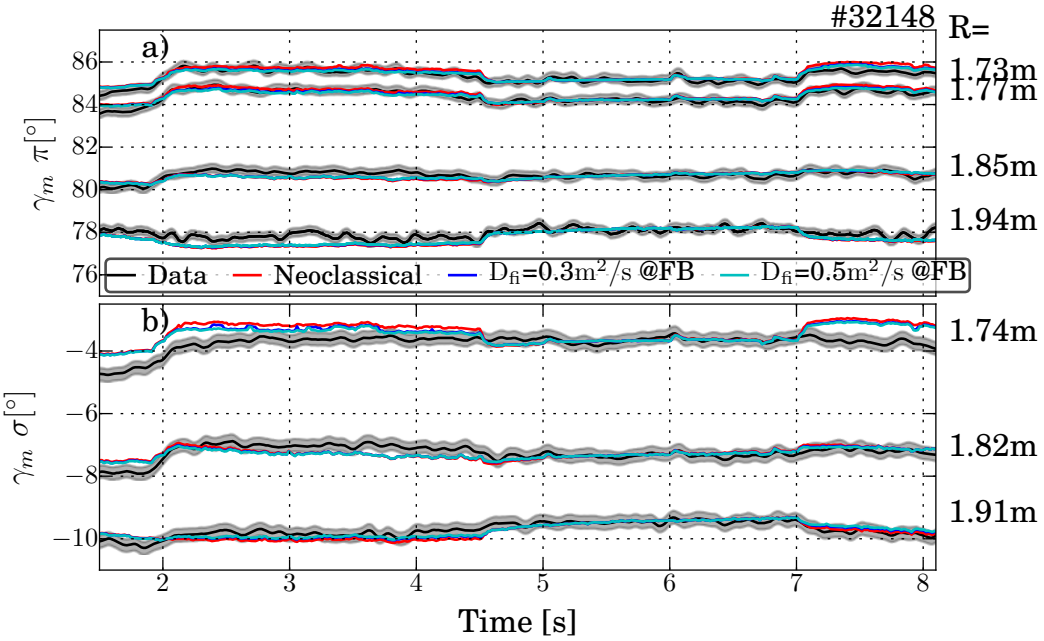

Figure 6.35.: Measured and predicted MSE angles comparing the neoclassical prediction with the assumption of anomalous fast ion diffusion from figure 6.32 due to the fishbone activity.

the FIDA lines of sight only measuring passing fast ions. In this case the FIDA tomography is not conclusive. It is also not possible to compare the measured fast ion distributions before and after a fishbone, as the repetition rate is to high. The influence on the current profile, measured with the MSE diagnostic can barely be seen. A tendential improvement of the agreement with the data due to the assumption of central anomalous fast ion diffusion in phases with fishbones was found.
For the redistribution of the fast ions due to fishbones no theoretical model was build. The anomalous fast ion diffusion profile used here is based on the simple assumption that fishbones redistribute fast ions from inside the q=1 surface outwards. This assumption makes no distinction between trapped and passing fast ions. In reference [127] a combination of HAGIS [129] and ASCOT [130] was used to model fishbone-induced fast ion redistribution based on more detailed physics model. For the discharge shown before, the gain from the use of these tools seems to be small, as only the FIDA diagnostic can be used as conclusive diagnostic and the measurement is well described also with the simplified model.

6.5.2. Fast Ion Redistribution due to Microturbulence

In the publication of Günter et al. [12] the proposed anomalous fast ion transport is founded on the assumed presence of microturbulence. A few years later a model to calculate anomalous fast ion diffusion coefficients due to electrostatic and electromagnetic turbulence was published [33]. The equations to calculate the anomalous fast ion diffusion coefficients from experimentally available quantities are based on non-linear gyrokinetic simulations with GENE [131, 132], a nonlinear gyrokinetic Vlasov code including full electromagnetic physics. Furthermore the data from ASDEX Upgrade discharges #18703 and #18383 and also from DIII-D discharge #134426 are used as database. The first two discharges are the examples given in reference [12]. This indicates, that the data used to develop the model are in a comparable regime as the discharges analyzed in this chapter.
The six equations for the diffusion coefficients are divided into trapped and passing particles and also into the electrostatic and electromagnetic contribution. Furthermore for the passing particles a finite larmor radius correction is applied. The six equations are

$$D^{\mathrm{es}}_{\mathrm{fi,p}} = \frac{\sigma_{\mathrm{es,p}} \cdot \chi_{\mathrm{eff}}}{\eta^2} \cdot \left(\frac{E}{T_{\mathrm{e}}}\right)^{-1} \tag{6.1}$$

$$D^{\mathrm{es}}_{\mathrm{fi,p-FLR}} = \frac{\sigma_{\mathrm{es,p-FLR}} \cdot \chi_{\mathrm{eff}}}{\eta^2 \cdot (1-\eta^2)^{1/2}} \cdot \left(\frac{E}{T_{\mathrm{e}}}\right)^{-3/2} \tag{6.2}$$

$$D^{\mathrm{em}}_{\mathrm{fi,p}} = \sigma_{\mathrm{em,p}} \cdot \chi_{\mathrm{eff}} \cdot \left(\frac{\beta}{\beta_{\mathrm{crit}}}\right)^{2} \tag{6.3}$$

$$D^{\mathrm{em}}_{\mathrm{fi,p-FLR}} = \frac{\sigma_{\mathrm{em,p-FLR}} \cdot \chi_{\mathrm{eff}} \cdot (\beta/\beta_{\mathrm{crit}})^2}{(1-\eta^2)^{1/2}} \cdot \left(\frac{E}{T_{\mathrm{e}}}\right)^{-1/2} \tag{6.4}$$

$$D^{\mathrm{es}}_{\mathrm{fi,t}} = \frac{\sigma_{\mathrm{es,t}} \cdot \chi_{\mathrm{eff}} \cdot \epsilon_{\mathrm{t}}^{1/2}}{\eta \cdot (1-\eta^2)} \cdot \left(\frac{E}{T_{\mathrm{e}}}\right)^{-3/2} \tag{6.5}$$

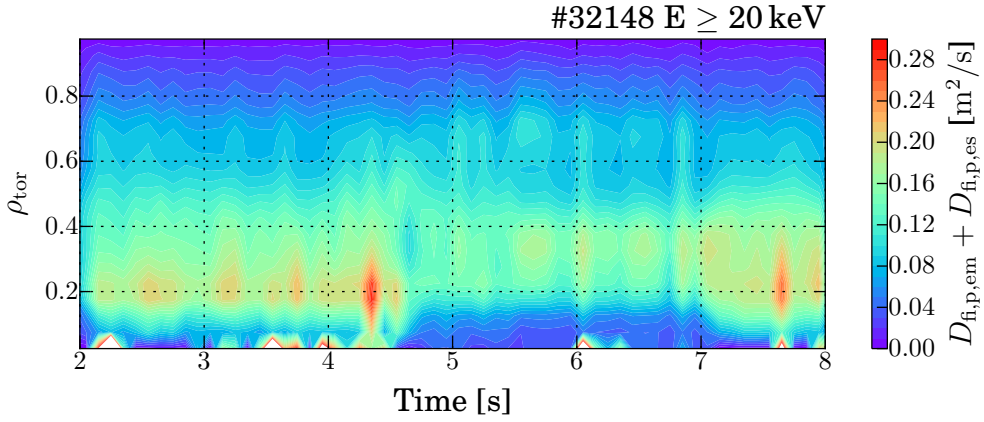

Figure 6.36.: Fast ion diffusion coefficients for the passing fast ion from the equations (6.1) to (6.4) describing the redistribution of fast ions in the plasma due to electrostatic and electromagnetic microturbulence calculated according to reference [33].

$$D_{\mathrm{fi,t}}^{\mathrm{em}} = \frac{\sigma_{\mathrm{em,t}} \cdot \chi_{\mathrm{eff}} \cdot (\beta/\beta_{\mathrm{crit}})^2 \cdot \epsilon_{\mathrm{t}}^{1/2} \cdot \eta}{1-\eta^2} \cdot \left(\frac{E}{T_{\mathrm{e}}}\right)^{-1/2} \tag{6.6}$$

where the indices p and t indicate passing or trapped particles, es and em "electrostatic" and "electromagnetic" and FLR indicates the finite Larmor radius approximation. The coefficients σ are given in the publication. The effective heat diffusivity χ_{eff} is calculated as sum of the ion and electron heat diffusivity. The two heat diffusivity profiles are calculated by TRANSP and the sum can be seen in appendix C.4, figure C.6. The local inverse aspect ratio is denoted by ϵ. The time and energy resolved local pitch angle of the fast ions is given by $\eta = v_{\parallel}/v$. The value used is the average from the multidimensional fast ion distribution function. The distribution function is calculated with the semi-analytic fast ion model from reference [111] which is also used and described in section 5.2. Energy averaged profiles of the calculated pitch angles can be seen in appendix C.4, figures C.4 and C.5. In this calculation the energy of the fast ions E, is bined in 1 keV steps from 20 keV to 110 keV. The electron temperature profile T_{e} is shown before in figure 6.3 b). Finally also the ratio of $\beta/\beta_{\mathrm{crit}}$ is needed, this ratio is calculated by calculation of β_{N}. The Troyon limit with a factor $g = 3.5$ is used as β_{crit} the calculated ratio can be seen in figure C.7.
The threshold condition for the finite Larmor radius correction from reference [33] is given by

$$\left(\frac{E}{T_{\mathrm{e}}}\right) \gg (1-\eta^2) \tag{6.7}$$

and is implemented if E/T_{e} is a factor 2 bigger than $(1-\eta^2)$. The energy averaged diffusion coefficent profiles from the equations (6.1) to (6.6) can be seen in appendix C.4, figures C.9-C.10. The electrostatic part determines for the passing particles as wall as for the trapped particles. This can also be seen by the comparison with the two sums for the diffusion coefficients. The energy averaged profiles for the passing and trapped particles are shown in figure 6.36 and 6.37. The influence of the estimated 3-dimensional anomalous fast ion diffusion on the fast ion distribution, for the high energy passing particle can be seen in

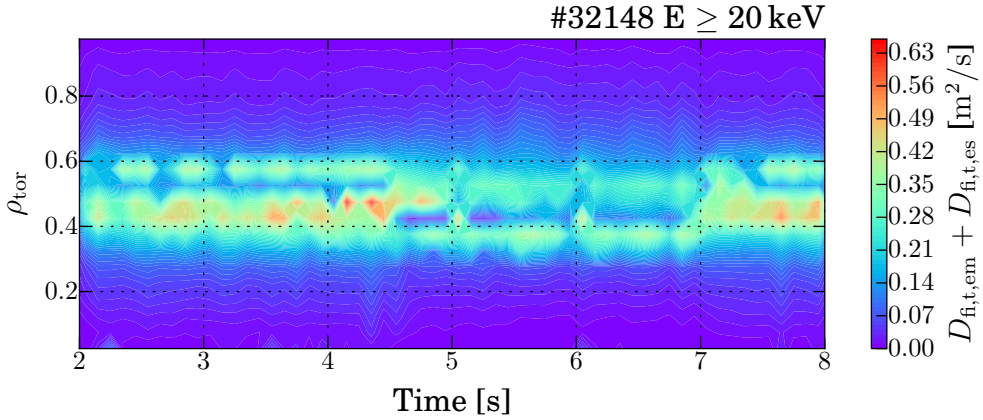

Figure 6.37.: Fast ion diffusion coefficients for the trapped fast ions calculated by equations (6.5) and (6.6).

figure 6.38. The comparison of the TRANSP predictions assuming neoclassical transport and the assumption of the shown diffusion profile with the FIDA measurement indicates a much better agreement for the assumption of the anomalous fast ion diffusion due to the microturbulence. Especially in the on-axis phase at 4.3 s the neoclassical prediction overestimates the central FIDA measurement. In the off-axis phase at 6.6 s the predictions are similar and both are in agreement with the measurement.
Different to the assumption in section 6.5.1 the assumed diffusion coefficients are different for trapped and passing particle and also energy resolved. The inconclusive FIDA tomography approach can be seen in appendix C.2.
In figure 6.39 the comparison of the MSE measurement with the TRANSP predictions can be seen. Unfortunately the predictions for the most central π and σ channel have some nonphysical fluctuation, most probably from a random, unintended amplification of statistical central fluctuations of the input profiles. However, the influence of the estimated anomalous fast ion diffusion on the other channels is small and within the uncertainties indistinguishable with respect to the neoclassical predictions. Therefore the MSE diagnostic is not very conclusive with respect to the assumption of the anomalous fast ion diffusion due to microturbulent transport. For proper validation of the model and crosschecking of the calculated anomalous fast ion diffusion coefficients, non-linear GENE calculation for the new discharge would be devisable. This calculations could not be done during this thesis.

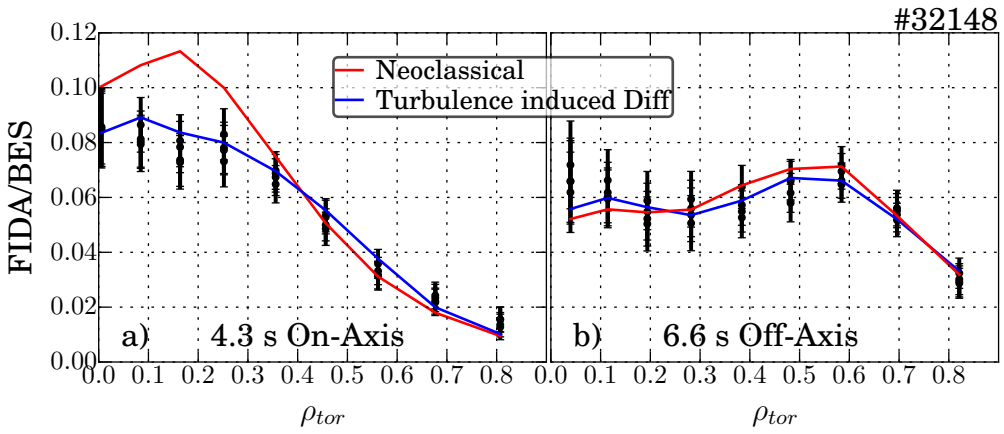

Figure 6.38.: FIDA measurement in comparison to TRANSP simulations with neoclassical transport and the assumption of the anomalous fast ion diffusion from figure 6.36 and 6.37. In a) a point in time in the on-axis phase can be seen and in b) the off-axis phase.

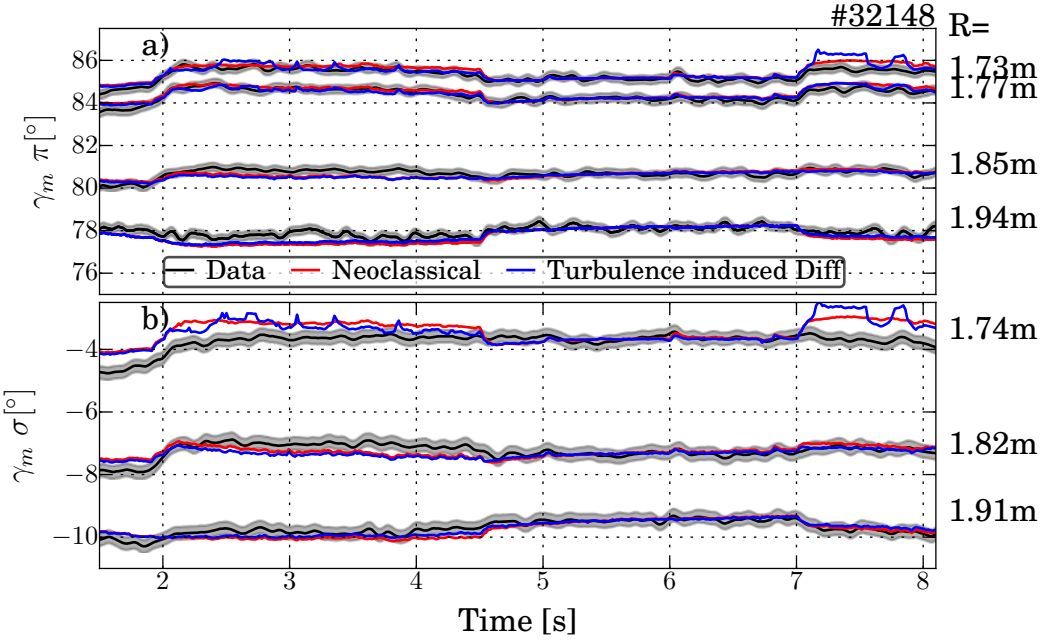

Figure 6.39.: Comparison of the measured MSE angles with TRANSP predictions, where the predictions are offset corrected to match the measurement during the off-axis phase between 4.5 s and 7 s. In a) the π-channels can be seen and in b) the 3 σ-channels.

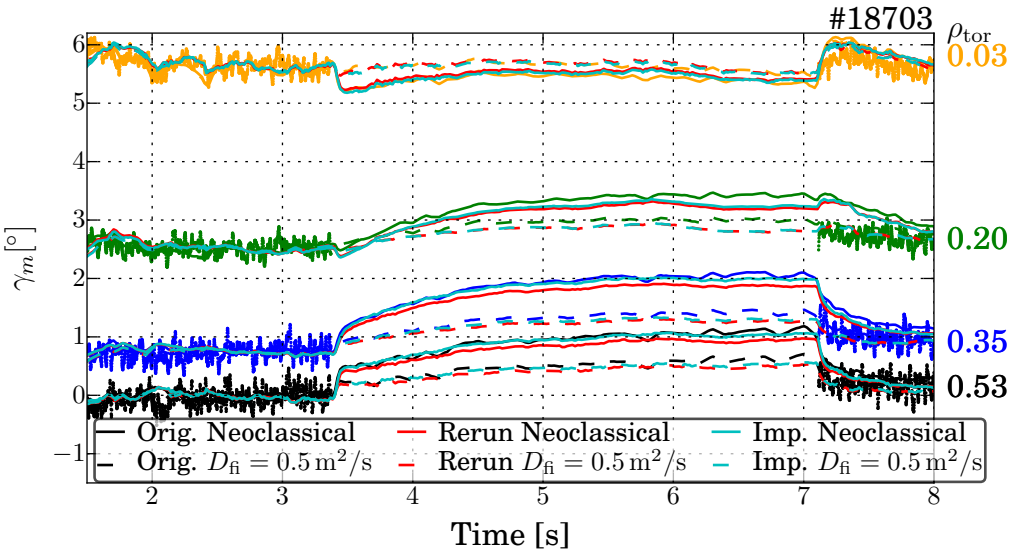

Figure 6.40.: Comparison of measured MSE angles with TRANSP predictions adapted from reference [12]. The original simulations are in the same color as the measurements. The influence of the radial electric field can be seen in the rerun simulations in red and furthermore the improvements in the geometry and transmission are considered in the new simulations in cyan.

6.6. Pre-2014 Discharges Revisited

Finally the discharges from the initial publications are simulated again, to see if the presented improvements lead to the comparable results and conclusions as written in the sections before. Furthermore, it was found in 2015 that the sign of the radial electric field in TRANSP, used only for the synthetic MSE angles, was wrong. The error was subsequently corrected. Additionally in 2008 the aiming of beam 3 was corrected by 0.1° in horizontal direction. This could have an impact on discharge #18703 which was performed in 2004. In the following sections the three discharges are presented chronologically.

6.6.1. Discharge #18703

The comparison of the measured MSE angle with TRANSP predictions of discharge #18703 in Günter et al. [12] and the apparent deviation from the neoclassical prediction provided the motivation for for the study of this chapter. This discharge is simulated again, taking the revised NBI geometry into account and also the geometry changes from 2008. Figure 6.40 shows the comparison of the MSE angles with the TRANSP predictions adapted from reference [12] together with a rerun of the old simulations and new simulations taking the improvements into account. The figure is an extension of figure 6.1, with minor differences, instead of an offset shift of the measurements to the simulations, the simulations are shifted with a temporal constant offset to match the measurement at 2.7 s.

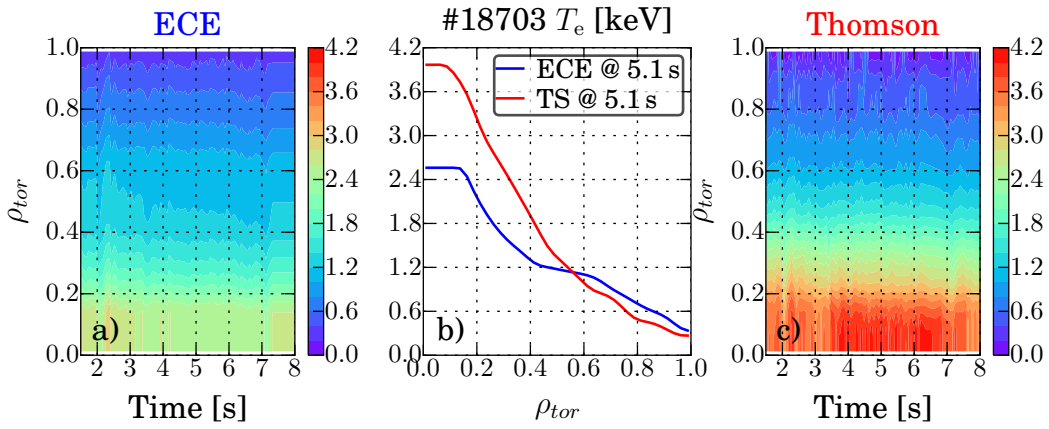

Figure 6.41.: Comparison of electron temperature profiles in a) measured with the electron cyclotron emission spectroscopy (see section 3.3.4) and in c) with the Thomson scattering diagnostic (see section 3.3.5). In b) a comparison of profiles from a single point in time is shown.

The comparison between the original and rerun simulations shows minor differences, due to the changed sign of the radial electric field, but as the simulations are shifted the influence is small. In contrast the comparison with the new simulations taking for example the revised geometry into account are comparable with the published results.
A closer look at the input kinetic profiles reveals some potential problems. Firstly, the assumed effective charge is fixed at 1.8. This value appears to be a reasonable assumption with the wall being mostly carbon in 2014. However, no temporal or radial variation was taken into account. The effective charge is an important parameter for the resistivity of the plasma and the current diffusion and also for the neutral beam driven current depends on the effective charge discussed in the sections 2.4.2 and 5.1.3. Therefore this can impact the MSE angles as the current profile depends on the effective charge. Secondly there are two issues with the used electron temperature input shown, in figure 6.41 a) taken from the ECE diagnostic (see section 3.3.4). On the one hand, the ECE measurement of the temperature ends at 7.3 seconds and the main conclusions from the comparison of the MSE angles are based on dynamics in the phase starting at 7 seconds. In TRANSP the temperature profile is kept constant for all times after 7.3 s. On the other hand a comparison of the electron temperatures measured with the ECE and the Thomson scattering diagnostic shows strong differences, shown in 6.41 b). The flat profile in the center from the ECE measurement is due to the fact, that the ECE in this case does not measure up to the center of the plasma. However, this alone cannot explain the strong differences of the profiles up to 1.5 keV. This should also have a major effect on the current profile, because all current drive mechanisms have a strong electron temperature dependence.
The expected strong influence of the different temperature profiles can be seen in figure 6.42. It could be seen, that especially in the channel at $\rho_{\mathrm{tor}} = 0.2$ strong deviations between the simulations are seen which are of a similar magnitude as the effect of the assumed anomalous fast ion diffusion. In the first on-axis phase the simulations using the temperature profiles from the Thomson scattering diagnostic exhibit different dynamics compared with

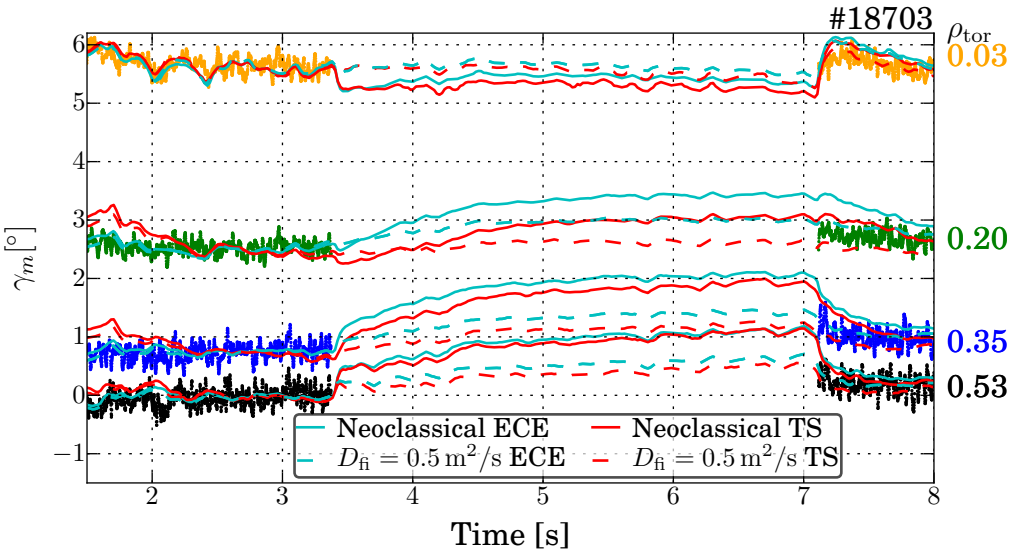

Figure 6.42.: Investigation of the influence of the different electron temperature profiles on the predicted MSE angles. ECE indicates temperature profiles from the electron cyclotron emission and TS profiles from the Thomson scattering measurement. The temperature profiles are shown in figure 6.41. Shown are the original simulations.

the measurements. The difference in the dynamics are also of similar magnitude as the described effect.
As expected, the channels at intermediate radii are the most sensitive to electron temperature variation. On the one hand, for the central channels the included current is small and therefore changes have a small impact. On the other hand, the closer the channel is to the edge the q value is more determined by the known separatrix position and the measured total plasma current. For comparison simulations have also been run using the electron temperatures measured with the Thomson scattering diagnostic and assuming anomalous fast ion diffusion based on the fishbone and on the microturbulent transport assumption.
Therefore a closer look at the perturbations in the discharge is necessary. Unfortunately the magnetic diagnostic used for the spectrograms shown before were not available. Therefore a spectrogram of a Mirnov coil is shown in figure 6.43, without n number determination from the phase reconstruction. Fishbone indications during the on-axis phases are seen, which are validated by experts, using the soft X-Ray diagnostic, to be m=1/n=1 activity. Also the characteristic frequency chirping can be seen. However, in contrast to the fishbones in discharge #32148 the repetition rate is reduced. The off-axis phase is MHD-quiescent similar to the discharges shown before. To test the hypothesis of a possible redistribution of central fast ions due to the fishbones simulations like in section 6.5.1 are performed. Therefore $0.3\,\mathrm{m}^2/\mathrm{s}$ anomalous fast ion diffusion in the on-axis phases within the q=1 surface is assumed.
In contrast also the anomalous fast ion diffusion coefficient profiles from the hypothesis of microturbulence induced anomalous fast ion transport from section 6.5.2 was simulated.

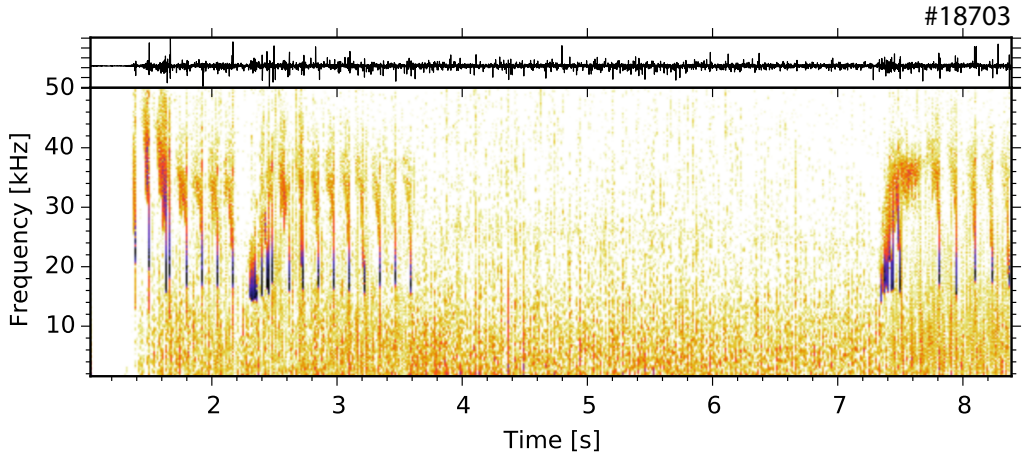

Figure 6.43.: Spectrogram of a Mirnov coil measurement, with m=1/n=1 magnetic activity in the on-axis phase, which could be identified to be fishbones. The off-axis phase is MHD-quiescent.

The assumed anomalous fast ion diffusion coefficient profiles can be seen in appendix C.5. The resulting predictions of the MSE angles in comparison to the measurements and the neoclassical prediction can be seen in figure 6.44. The influence of the expected anomalous fast ion diffusion is small. On the one hand it is much smaller than the effect of the overestimated global anomalous fast ion diffusion of $0.5\,\mathrm{m}^2/\mathrm{s}$. On the other hand in figure 6.42 it was shown, that in the most important channel the effect of the different measured temperature profiles is in the same order as the effect of global anomalous fast ion diffusion of $0.5\,\mathrm{m}^2/\mathrm{s}$. Therefore the effect of the expected anomalous fast ion transport is much smaller than the uncertainty of the simulation, due to the different measured temperature profiles. This leads to the conclusion that non-neoclassical fast ion redistribution cannot be resolved, if the discrepancies between the different measured temperature profiles is not resolved before. Therefore, using the same input data and profiles as in reference [12], the conclusions from this publication can neither be confirmed nor falsified.

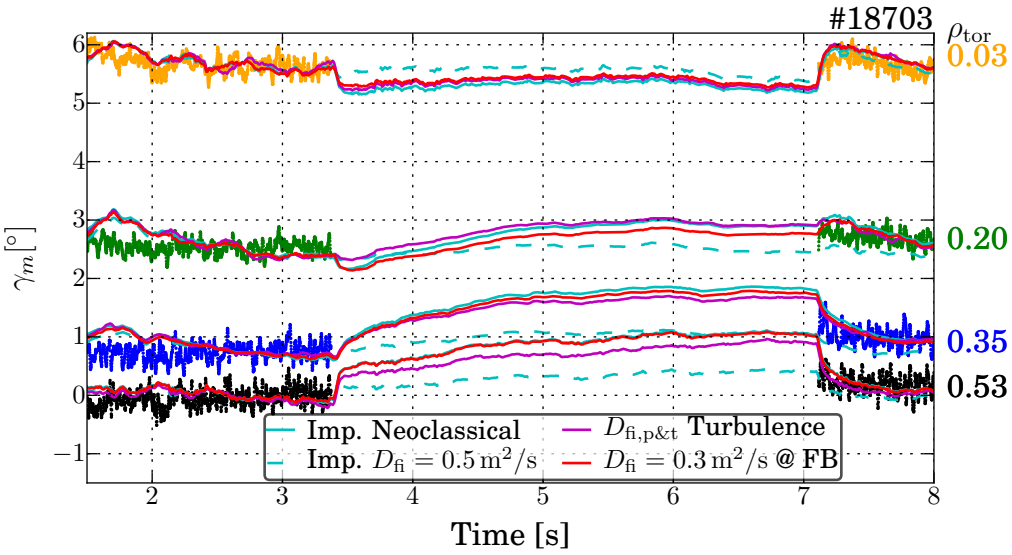

Figure 6.44.: Comparison of MSE angles, assuming fast ion redistribution due to fishbones or microturbulent transport.

6.6.2. Discharge #27237

In the thesis of B. Geiger [17] the discharge #27237 was used to show that the fast ion distribution is well described by the assumption of neoclassical transport. Furthermore the assumption of any global anomalous fast ion diffusion led to deviations from the FIDA measurements.
Figure 6.45 shows a comparison of the neoclassical simulation from reference [17] and new simulations with the corrected geometry with and without the assumption of anomalous fast ion diffusion. Furthermore, the FIDA intensity is now normalized to the beam emission to cancel out calibration issues. Unfortunately the amount of collected photons in the FIDA range is small, therefore only a measured profile averaged over 4 frames is shown.
In the on-axis phase shown, in figure 6.45 a), the conclusion could be confirmed. The neoclassical prediction, either the initial or the corrected, fit to the data, while the assumption of anomalous fast ion diffusion slightly underestimate the central fast ion density. Also the difference between the rerun simulation and the corrected one are small, due to only small changes in the geometry of beam 3 and 8, which were the only ones used. In the off-axis, phase shown in figure 6.45 b), the result is similar to the results from section 6.4. The prediction with the revised geometry is in good agreement with the data, while the initial geometry predicts a more inward-shifted peak. Again the assumption of global anomalous fast ion diffusion leads to a disagreement between the prediction and the measurement, with respect to the shape.
The calculation of the anomalous fast ion diffusion coefficient profile induced by microturbulence was also done for this discharge and can be seen in appendix C.5 in the figures C.14 and C.15. The comparison of these simulations with the data is shown in figure 6.45 in magenta. Similar to the results from section 6.5.2 the simulations are in agreement with

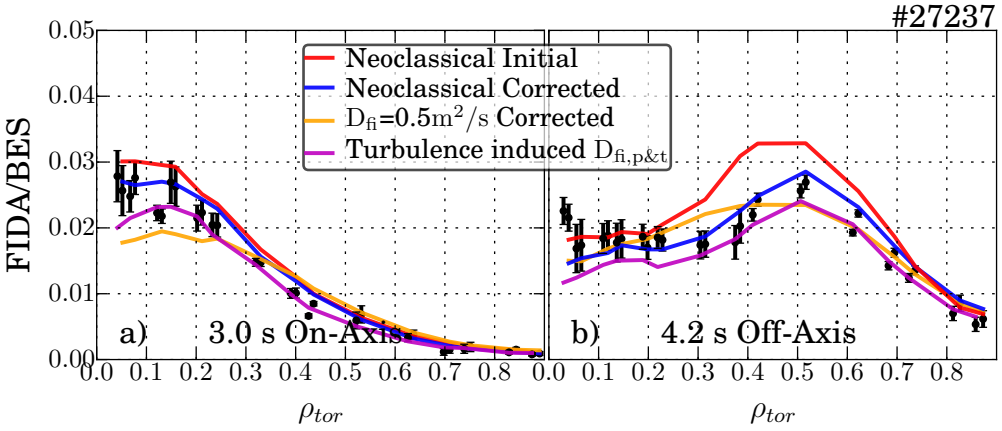

Figure 6.45.: Comparison of the synthetic FIDA diagnostic with a four frame averaged measurement, in a) for 5 MW of on-axis NBI and in b) for 5 MW off-axis NBI.

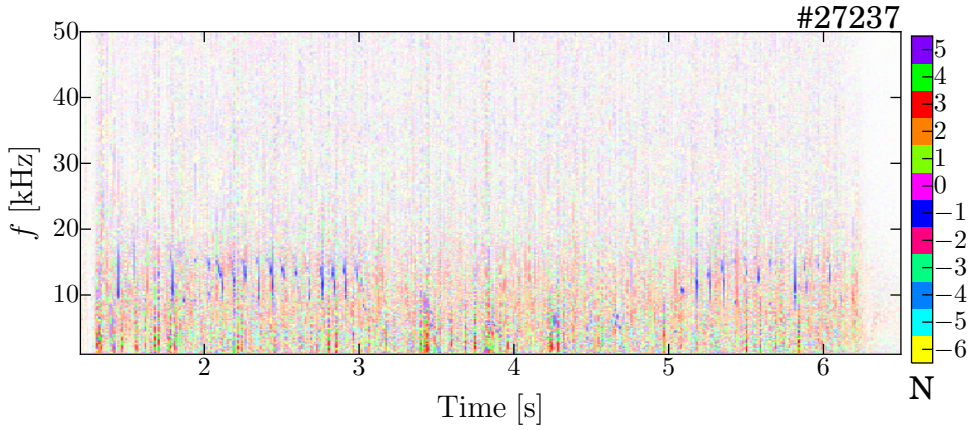

Figure 6.46.: Spectrogram of the measured MHD activity form the B-coils, showing an almost MHD-quiescent discharge, except small fishbones in the on-axis phases.

the data within the uncertainties. Only a slight underestimation in the off-axis phase can be seen.
A main difference between this discharge and discharge #32148 can be seen in the spectrogram in figure 6.46. This spectrogram seems to be almost completely MHD-quiescent, except some small fishbones, with low intensity and an erratic but long repetition rate. With respect to the fishbones in discharge #32148, shown in figure 6.31 a), these fishbones seems to be negligible. Therefore the result is in agreement with the hypothesis that fishbones redistribute fast ions from the center outwards. In the absence of strong fishbones the fast ion distribution is also in agreement with the assumption of neoclassical transport. In conclusion again both hypotheses, either the fast ion redistribution due to fishbones or the microturbulence induced fast ion transport are in agreement with the FIDA measurements in discharge #27237.

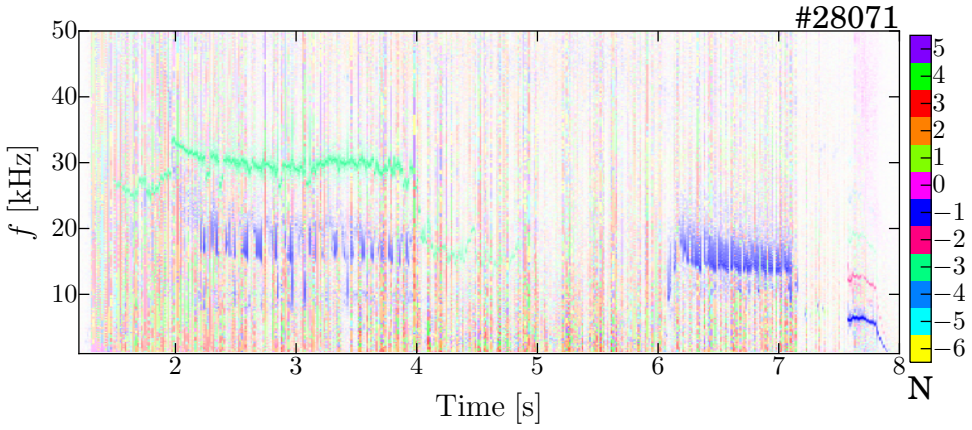

Figure 6.47.: Spectrogram of the measured MHD activity form the B-coils, showing an small m=4/n=3 NTM in the first on-axis phase, together with some fishbones, a MHD-quiescent off-axis phase and again fishbones in the second on-axis phase.

6.6.3. Discharge #28071

A second discharge #28071 was also discussed in the thesis of B. Geiger [17]. This discharge had lower collisionallity compared with discharge #27237. In this case only the FIDA comparison of MHD-quiescent off-axis phase was shown. A closer look at the spectrogram in figure 6.47 shows, besides the presence of a small m=4/n=3 NTM, fishbone activity is present. These fishbones are of a comparable magnitude as the ones in discharge #32148, but with lower repetition rate and intensity.
In figure 6.48 the comparison of the FIDA measurement with the TRANSP-predicted and FIDASIM-postprocessed simulations is shown. The result is similar to the comparison of discharge #32148, shown in section 6.5. The off-axis phase is again in a good agreement with the assumption of neoclassical transport with the revised geometry. However, again in the on-axis phase the neoclassical assumption overestimate the data centrally. Therefore again central anomalous fast ion diffusion is assumed in the phases were the fishbones are active, inside the q=1 surface.
As the fishbone intensity is smaller compared with discharge #32148 a value of $D_{\mathrm{fi}} = 0.3\,\mathrm{m}^2/\mathrm{s}$ is assumed. As expected, besides the off-axis phase also centrally the on-axis phase is matched by the simulation. In the on-axis phase between $\rho_{tor} = 0.2$ and $\rho_{tor} = 0.5$ the outwards diffused fast ions overestimate the measured fast ion density slightly.
Furthermore the hypothesis of anomalous fast ion transport due to microturbulence is tested. The assumed anomalous fast ion diffusion coefficient profiles can be seen appendix C.5 in the figures C.16 and C.17. Also these assumption leads to a good agreement of the simulations with the data either in the on-axis phase as in the off-axis phase. Therefore again, like in the sections before, both hypotheses reasoning anomalous fast ion diffusion yield agreement with the FIDA measurement.

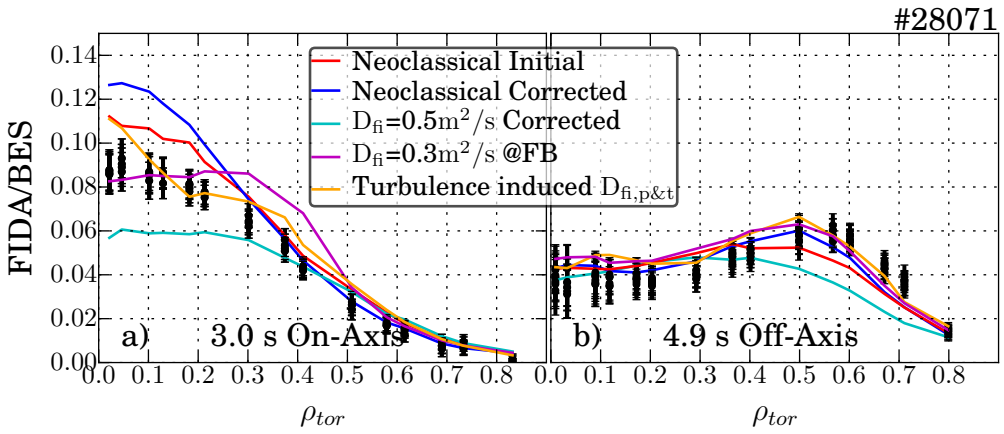

Figure 6.48.: Comparison of the FIDA measurements at two points in time with multiple TRANSP simulations. The influence of the improvements is shown. Also the comparison of the assumption of global anomalous fast ion diffusion and also the influence of the anomalous fast ion diffusion from the two models possibly reasoning the anomalous transport.

6.7. Influence on the Neutral Beam Driven Current

Finally the influence of the fast ion redistribution from the two models on the neutral beam driven current should be discussed. In figure 6.49 a comparison of different TRANSP NBCD predictions can be seen.

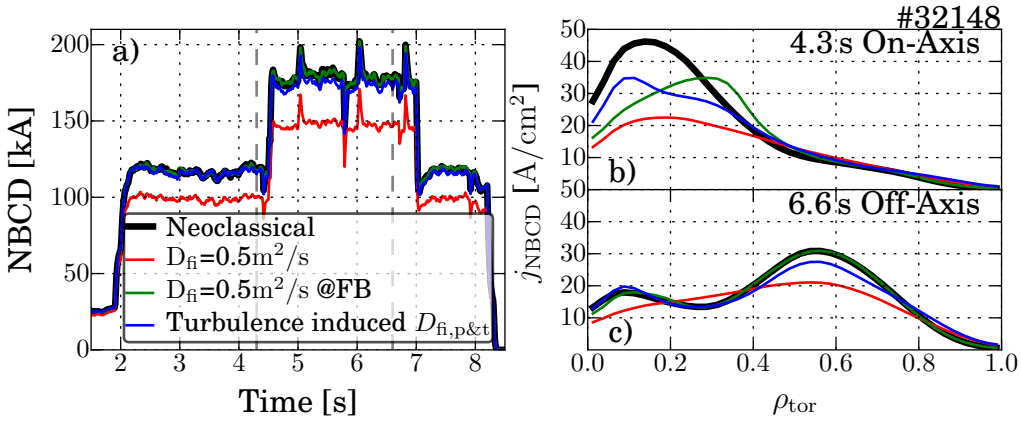

Figure 6.49.: TRANSP NBCD predictions. In a) the time evolution of the predicted current is shown, beside the assumption of neoclassical fast ion transport, three different fast ion redistribution models are assumed. In red global anomalous fast ion diffusion, in green localized anomalous fast ion diffusion induced by fishbones and in blue an anomalous fast ion diffusion profile, induced by microturbulence. In b) and c) corresponding profiles in the on- and off-axis phase are shown.

In figure 6.49 a) the time evolution of the neutral beam driven current integrated over the plasma volume can be seen. In the on-axis phase the current is around 120 kA, increases up to 180 kA in the off-axis phase, due to the tangential injection geometry of the off-axis sources, and is reduced again to the 120 kA in the second on-axis phase. The predictions assuming neoclassical fast ion transport (black) and the two fast ion redistribution models are almost indistinguishable, while the assumption of global anomalous fast ion diffusion reduce the predicted current in the order of 20%. The reason can be found in figure 6.49 b) and c), where the radial neutral beam driven current density profiles are shown for two points in time. The assumption of the global anomalous fast ion diffusion strongly changes the shape and also increase fast ion losses at the edge of the plasma. In contrast, the two approaches assuming fast ion redistribution due to perturbations only slightly change the profile. The changes are also mostly central. The total neutral beam driven current is calculated by integrating over the profile multiplied by the area of the flux surfaces. Due to the fact, that the central area is small, its effect on the integrated neutral beam driven current is negligible.

6.8. Conclusion

The contradicting results of Günter et al. [12] and Geiger [17] regarding anomalous fast ion transport in off-axis neutral-beam-heated discharges at ASDEX Upgrade were discussed and resolved within this chapter.
In improved experiments, a difference between measurement and prediction in the shape of the off-axis FIDA profile, was resolved mostly by a review of the neutral beam geometry. The resulting improved geometry description leads to an agreement of the FIDA data with neoclassical predictions in the off-axis phase and a disagreement with the assumption of global anomalous fast ion diffusion. In contrast the neoclassical FIDA predictions in the on-axis phase centrally overestimate the data. The comparison of the MSE measurement with TRANSP predictions proofs the existence of some anomalous fast ion transport, but due to missing absolute calibration is not able to resolve whether this transport is present in the on- or the off-axis phase. Furthermore the comparison of the predicted loop voltage and Faraday rotation polarimetry with measurements is not able to resolve anomalous fast ion transport. Synthetic diamagnetic flux loop data show that this new diagnostic should be able to resolve the anomalous fast ion diffusion. However, not yet fully understood systematic uncertainties in the comparison between predictions and measurement hampered this comparison. Therefore only the MSE and FIDA diagnostic could be used for the comparison.
Two hypotheses to explain the disagreements in the FIDA and MSE diagnostic were tested: The redistribution of central fast ions by fishbones, which are present in the on-axis phase, and anomalous fast ion transport due to microturbulence. For the fishbone hypothesis anomalous fast ion diffusion within the q=1 surface is assumed. This assumption leads to an agreement of the FIDA prediction with the measurement as well as the shifted MSE predicted time evolution with the measurement. However, also the assumption of the

microturbulence induced anomalous fast ion diffusion, on the basis of the model of Pueschel et al. [33], is able to resolve the disagreements.
A revision of the experiments of Geiger [17], taking the simulation improvements into account, and assuming both hypotheses, is also in agreement, although only one of the two discharges has fishbone activity in the on-axis phase. In contrast the revision of the experiments of Günter et al. [12] is less conclusive, as large uncertainties on the measured electron temperature profile avoid a reliable conclusion.
For an unequivocal identification of the source for the anomalous fast ion transport a discharge is needed with a phase with and without fishbones. This discharge needs to be similar to the ones shown before in this chapter and the phase must have a neutral beam configuration as in the on-axis phase. Furthermore in both phases FIDA and MSE measurements are crucial. The absolute calibration of the MSE system and a reliable combination of diamagnetic flux measurement and prediction, can strongly improve the validity of the comparison. The comparison with TRANSP calculations should reveal either the need of central anomalous fast ion transport in the phase with fishbones and a match with the neoclassical transport assumption in the phase without fishbones, or the assumed anomalous fast ion transport due to the microturbulent hypothesis should match in both phases. Such a discharge was attempted but could not be achieved within the limited number of allocated shots.
Finally it could be shown that the influence of both hypothesis on the global neutral beam driven current is negligible and that there are only minor changes in the central current profile.

For ITER there are fortunately almost no consequences. The common ITER scenarios are designed with $q_{\min} > 1$. In such scenarios no fishbones are present, as a $q = 1$ surface is a necessary prerequisite for fishbones. However, there are also scenarios with $q_{\min} < 1$. Fortunately in such scenarios a stabilizing effect of the internal kink mode that leads to fishbones by the α-particles from the fusion reaction is predicted [133–135]. Nevertheless, if against the expectation fishbones are present in ITER and the fishbones are the reason for the fast ion redistribution, the studies of this thesis indicate a increased fast ion transport in the center. This transport needs to be understood in detail, especially regarding the dependencies on plasma parameters, and the influence on the central heating should also be investigated.
The ansatz to describe the fast ion transport by microturbulence in this thesis uses $D_{\text{fi}^{\text{es}}} \sim (T_\text{e}/E)^x$ to calculate the diffusion [33]. In ITER the electron temperature is expected to be $T_\text{e} \approx 10 - 15\,\text{keV}$ and the energy of the injected beam particle is 1 MeV and the α-particles emerge with 3.5 MeV. With a similar expected effective heat diffusivitiy in ASDEX Upgrade and ITER, this diffusion model would lead to anomalous fast ion diffusion coefficients for ITER in the same order of magnitude as those calculated in this thesis. Furthermore in GENE based predictive studies for ITER also an influence of microturbulent transport on the fast ion distribution in the plasma was predicted. These predictions are in the same order of magnitude as the calculations in this thesis and are also energy and temperature dependent [136].

7. Quantitative Investigation of Non-Inductive Current Drive

The single current contributions to the plasma current are not measurable, in contrast to the total plasma current. To quantify the non-inductive contributions, like the NBCD, their fraction on the total plasma current needs to be large. This was not the case in the discharges of chapter 6, with a NBCD fraction of $< 25\%$. Furthermore the inductive contribution, quantifiable only with large uncertainties, should be small to reduce the absolute uncertainties. Therefore in this chapter ASDEX Upgrade discharges are studied in which the NBCD and the non-inductive current fraction as a whole is maximized. One suitable scenario with almost non-inductive current drive was developed by A. Bock [19]. While the studies of A. Bock focused on maximizing bootstrap current, the focus in this chapter is on the quantitative comparison of the non-inductive currents with models.
The almost fully non-inductive current drive in the experiments are a step towards stationary Tokamak operation. For these scenarios the intrinsic bootstrap current is of special interest, because it depends only on beneficial plasma conditions and not directly on external heating systems. High power demand of these external heating systems again would decrease the net output power of a power plant. However, besides the non-inductively driven plasma current several additional conditions [137] have to be taken into account in the scenario development of a fusion power plant. Some of them are in conflict with the beneficial bootstrap current conditions. For example the local safety factor is proportional to the bootstrap current but inversely proportional to the produced fusion power.
Also at other Tokamaks non-inductive scenarios were studied. In DIII-D, a Tokamak comparable with ASDEX Upgrade in shape and size, in fully non-inductive scenarios a current redistribution mechanism, called flux pumping, was investigated [138]. Studies at JT60-U focused on large bootstrap fraction and reached transient fully non-inductivity with 92% bootstrap fraction [139]. At JET an initial plasma current overshoot is used to transiently form the q-profile for a high bootstrap fraction, resulting in 40–60% non-inductive current [140]. Furthermore two super conducting long pulse Tokamaks EAST [141] and KSTAR [142] reached scenarios with fully non-inductive current drive, indicated by negative loop voltage measurements, but both with a reduced plasma current of 400 kA.

7.1. Experimental Setup

An ideally suited scenario for this study was one developed previously by A. Bock [19]. The goal of the scenario was a discharge with “centrally elevated and flattened q profile

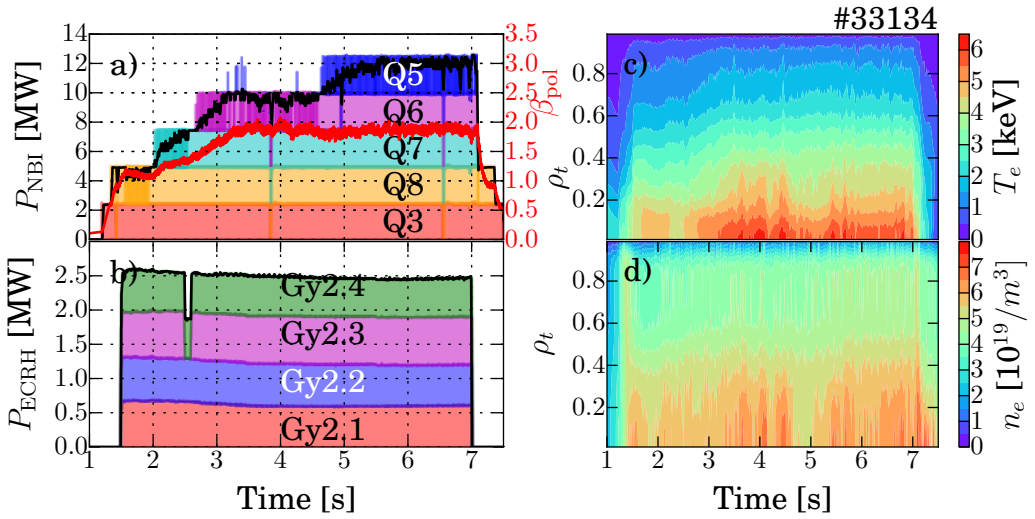

Figure 7.1.: Discharge overview, with the neutral beam power and the control parameter β_{pol} in a) and the electron cyclotron resonance heating power in b). In c) the electron temperature and in d) the electron density profiles are shown.

that promises better stability against low-helicity MHD instabilities while also maximizing bootstrap current." [143]. As the scenario is close to fully non-inductive, it is well suited for quantitative comparisons with predictions for the individual current contributions. Furthermore the scenario runs at reactor relevant parameters [137], for example $q_{95} \approx 5.3$. Further parameter are $B_T = 2.5\,T$ and a plasma current of 800 kA. The scenario is interesting due to the fact that it contains a high non-inductive current drive fraction and especially the NBCD fraction is in the order of up to 50% of the plasma current.
The scenario is presented in detail taking discharge #33134 as an example, which is derived from the initial discharges from A. Bock [19]. Figure 7.1 shows a discharge overview. The time trace of the neutral beam heating can be seen in 7.1 a). To maximize the bootstrap current, β_{pol} is increased close to the stability limit by a feedback controlled increase of the neutral beam power from 2 s to 3.5 s. The smooth neutral beam power regulation is realized by adding neutral beam sources with an adjustable duty cycle.
Additionally the four available ECRH gyrotrons are used for off-axis ECCD during the whole discharge in order to taylor a centrally elevated q profile. The time trace of the ECRH power can be seen in figure 7.1 b). The injection geometry, in a poloidal cross section, of the neutral beams and gyrotrons that were used is shown in figure 7.2 a). The predicted current profiles for the ECCD calculated by TORBEAM [51] and the NBCD calculated with TRANSP/NUBEAM for a representative point in time are plotted in figure 7.2 b). The neutral beam injection geometry leads to a broad, slightly off-axis shifted current profile, with the off-axis ECCD on top. The plasma volume is reduced to increase the distance to the inner wall of the torus, and thereby reduce gas influx from the wall and minimize the tungsten influx. Therefore the NBI sources 6 and 7 are not steered to maximum off-axis, because this would lead to high energy losses due to a strongly increased shine through. To maximize the bootstrap current by an elevation of the central q value, an active current

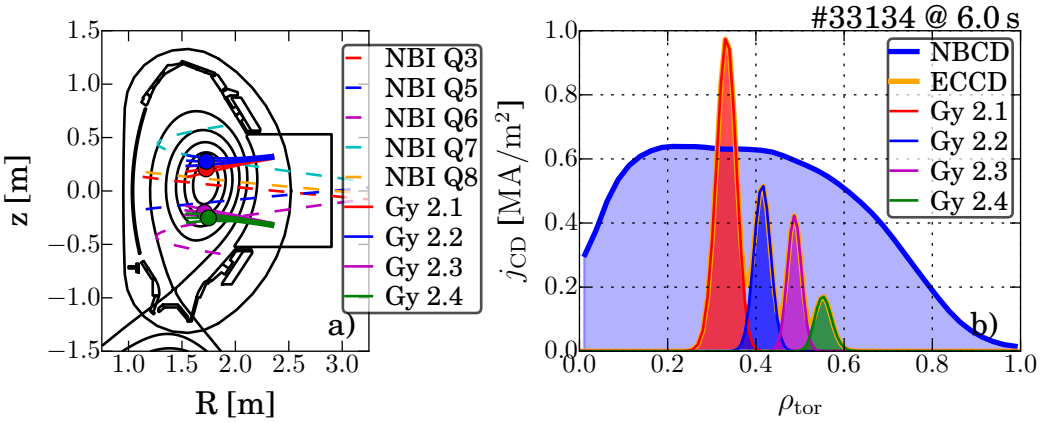

Figure 7.2.: Poloidal cross section of the NBI and ECRH power deposition, shown in a). In b) the calculated ECCD and NBCD current density profiles at 6 s can be seen. The ECCD current densities are calculated for all gyrotrons individually, while the NBCD is the current drive of all five beams together, marked in blue.

profile tailoring towards off-axis current profile is performed. This elevated central q profile increases also the stability against low-helicity MHD modes.
For ASDEX Upgrade, high central temperatures of $T_e \sim 6\,\text{keV}$ and $T_i \sim 9\,\text{keV}$ are reached by the combination of high heating power and a good confinement. Together with, a for ASDEX Upgrade low, central electron densities below $7 \cdot 10^{19}\,\text{m}^{-3}$ the conditions are beneficial for a high neutral beam current drive efficiency (see equations (2.26) and (2.27)) and the resulting steep gradients in the pressure profile, from the high central temperatures, increase the bootstrap current (see equation (2.33)).
The further plasma parameters are a plasma current of 800 kA, a toroidal magnetic field of -2.5 T at the magnetic axis and a $q_{95} \sim 5.3$ to be in a reactor relevant regime. The resulting $H_{98}((y,2)) > 1$ [144] indicates the good confinement.
The indication for a high non-inductive current fraction, close to full non-inductivity is the loop voltage measurement close to zero. This measurement can be seen in figure 7.3 a). In b) the current in the central solenoid, the Ohmic transformer, can be seen. In standard operation the slope of the current in the central solenoid is feedback controlled to keep the plasma current constant. This normally leads to a strongly negative slope in the order of several $\text{kA}\,\text{s}^{-1}$. However, in this discharge the current in the central solenoid is fixed from 4.5 s on to observe the resulting change in the measured plasma current. If the discharge were fully non-inductive and stationary the measured plasma current should not change at all. The small remaining current decrease of $45\,\text{A}\,\text{s}^{-1}$ is within the uncertainty of the controller and is still considered as a constant current in the central solenoid. The strong current increase in the Ohmic transformer from 2.5 s to 3.5 s correlates with the increasing neutral beam power. This at first sight surprising behaviour can be understood with figure 7.4. In a poloidal view in figure 7.4 a) the vacuum magnetic field of the poloidal field coils, calculated from the current through the coils, can be seen. While the primary function of the Ohmic transformer coil (OH1) is the inductive current drive, the other coils are used for the positioning of the plasma. During the β_{pol} ramp the plasma pressure increases. As

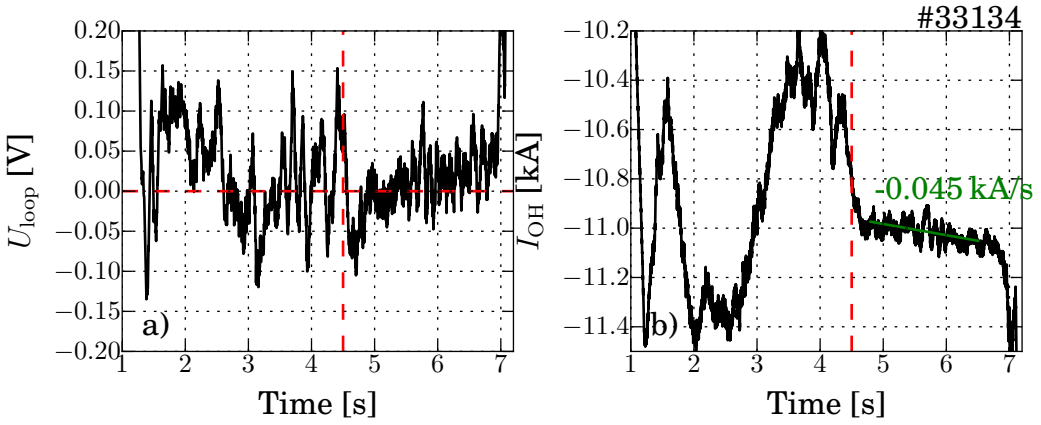

Figure 7.3.: In a) the measured loop voltage can be seen, which is most of the time close to zero, indicating a high non-inductive current fraction. In b) the current in the central solenoid is shown.

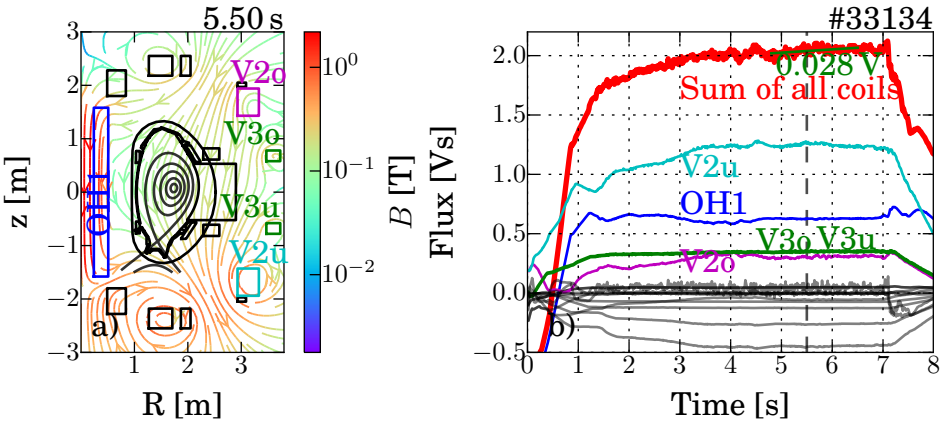

Figure 7.4.: In a) a poloidal view on the vacuum vessel and the poloidal field coils can be seen. The resulting vacuum magnetic field components from the external coils in the poloidal plane are indicated by the colored arrows, where the colors indicating the field strength. In b) the integrated vertical magnetic flux through the midplane from $R = 0$ up to the magnetic axis is shown. The most important coils and their contribution to the flux are colored and the sum of all coils is shown in red. The negative slope in the sum indicates inductive current drive.

reaction the positioning control increase the current in the outer poloidal coils to keep the plasma at its position. This change in the currents of the position control coils changes the poloidal magnetic flux enclosed by the plasma, resulting in an increase of the inductive current. This flux increase is compensated by a reduction of the current in the Ohmic transformer coil through the plasma current feedback control. In figure 7.4 b) the magnetic flux of the vertical magnetic field component through a plane at $z = 0\,\mathrm{m}$ from $R = 0\,\mathrm{m}$ to the magnetic axis for the different coils and the sum of all coils is shown.
At this point it should be noted that the inductive current needs time to decay especially in the high temperature center. The two seconds of fixed current in the central solenoid until the ramp down starts are much shorter than the relevant resistive time, which is in the order of 5 s for an average $T_\mathrm{e} \approx 2.5\,\mathrm{keV}$. The resistive time is calculated using

$$\tau_\mathrm{R} = \mu_0 \sigma L^2 \tag{7.1}$$

with the vacuum permeability μ_0, the conductivity σ and the system length $L = 0.5\,\mathrm{m}$. The conductivity can be approximated [3] with

$$\sigma = \frac{(1-\sqrt{\epsilon})^2}{\eta_\mathrm{spitzer}} \tag{7.2}$$

with the Spitzer resistivity (see equation (2.23) [3]) which could be further approximated by

$$\eta_\mathrm{spitzer}[\Omega\,\mathrm{m}] = \frac{2.8 \cdot 10^{-8}}{T_\mathrm{e}[\mathrm{keV}]^{3/2}}(1-\sqrt{\epsilon})^2. \tag{7.3}$$

Fully non-inductive current drive was not completely reached in discharge #33134, indicated by the still negative flux change. Therefore in a second discharge the plasma current was reduced to 600 kA, with a similar heating scheme. In this discharge the plasma current remains feedback controlled. It was anticipated that the total non-inductive current should exceed the feedback controlled plasma current. In this case the external flux should be reversed, i.e. positive. This is apparently not the case (see figure 7.5 b)) and in agreement with the measured loop voltage (see figure 7.5 a)) that remains positive. An overview of the plasma parameters of the discharge #33379 can be found in the appendix D.1 in figure D.1.

7.2. Current Prediction

The total plasma current can be measured with a poloidal magnetic loop, but the single contributions are not measurable. Therefore these contributions need to be calculated on the basis of physical models. In this section first the current calculations from the transport code TRANSP and the equilibrium solver IDE [23] are compared and second issues with the calculation of the inductive contribution are discussed.
The plasma current is composed of the neutral beam current drive (NBCD), the electron cyclotron current drive (ECCD), the bootstrap current (BS) and the inductive contribution.

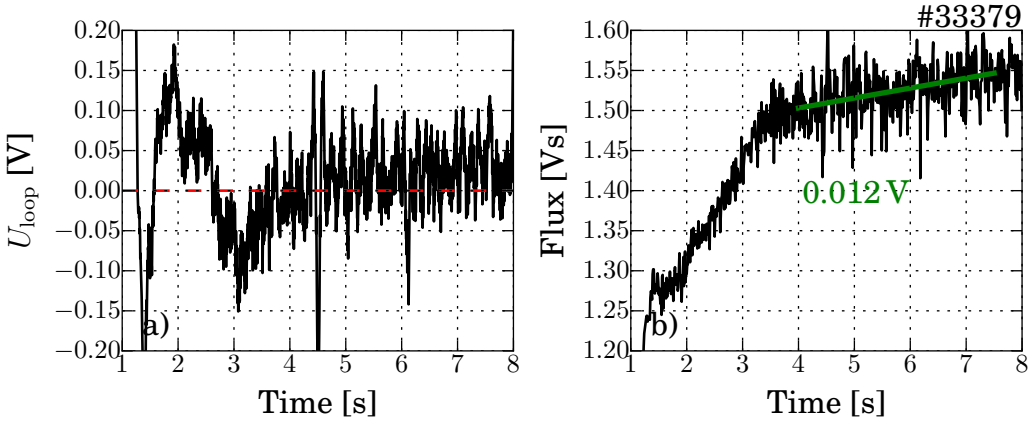

Figure 7.5.: In a) the measured loop voltage in the 600 kA discharge with feedback controlled plasma current is shown. In b) the integrated vertical magnetic flux from all external coils through the midplane from $R = 0$ to the magnetic axis is shown. The negative slope from 4.0 s on indicates no non-inductive current overshot.

TRANSP uses NUBEAM to calculate the NBCD contribution (see section 5.1.3) and TORBEAM to calculate the ECCD (see section 5.1). Furthermore different models to calculate the bootstrap current are implemented. For this study the model of O. Sauter [55] is chosen. Finally the inductive contribution is calculated as the difference between the measured total plasma current and all non-inductive contributions. It should be noted that TRANSP calculates all quantities on its self-consistent equilibrium, constrained only by the given separatrix position, the input kinetic pressure and the self calculated fast ion pressure.
In contrast to the TRANSP solution, **IDE** uses further constraints for the equilibrium reconstruction, for example the measurement of the magnetic probes and optional the MSE measurements (see section 4.3). The calculation of the current contributions in IDE is implemented in a comparable fashion as in TRANSP. The ECCD is also calculated using TORBEAM [52]. The NBCD and the full fast ion contribution to the equilibrium is taken from TRANSP, due to the fact that IDE does not contain an own fast ion model yet. The bootstrap current is calculated using the model of O. Sauter [55] and, as in TRANSP, the inductive contribution is calculated from the difference between the sum of the different non-inductive contributions drivers and the measured plasma current.
In the following it is shown, why a direct calculation of the inductive current from the change of the magnetic flux at the moment does not lead to reliable predictions. Figure 7.6 shows a comparison of an implementation of this ansatz within IDE from R. Fischer [145] (in blue) together with the conventional calculation from the difference of the plasma current and the calculated non-inductive contribution (in red). The large fluctuations from the calculation approach, despite using strong filter functions to reduce the fluctuations by about a factor of three, are due to events like ELMs or small changes in the shape of the plasma. In magenta a simplified approach is shown. In this case the shape of the plasma is kept constant and the change of the poloidal flux and the resistivity is averaged over 1.5 s, in this case this approximation is only valid for constant plasma conditions and if

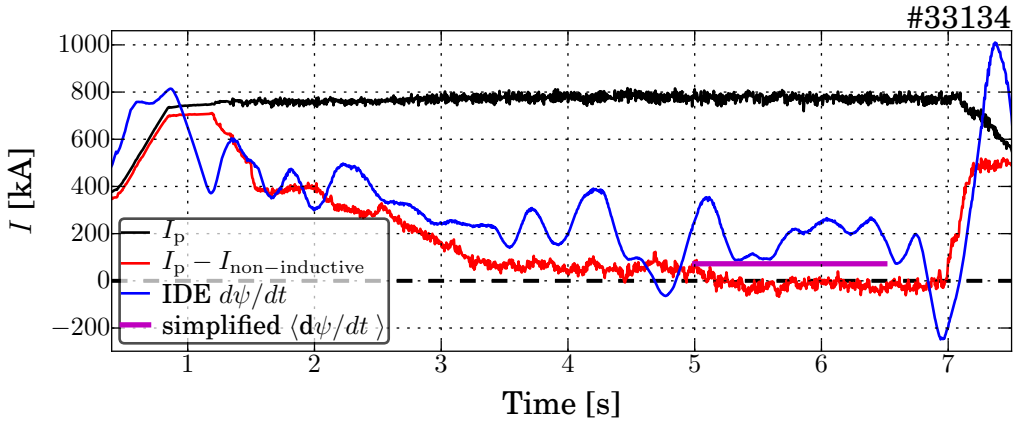

Figure 7.6.: Calculation of the inductive current. The red line indicates the conventional calculation from the difference of the plasma current (black) and the calculated non-inductive current drivers. In blue a calculation of the inductive contribution to the plasma current from the change in the magnetic flux is shown. In magenta the result from a second simplified ansatz, averaging over a longer period and assumed equalibrated conditions, is shown.

the derivative of the external flux is constant. However, for a quantitative analysis these current predictions can only indicate that the expected inductive current does not vanish completely. Both approaches have large uncertainties and are not useful for quantitative predictions. Therefore within this chapter only the inductive driven current from the difference of the plasma current and the calculated non-inductive driven current is used.
In difference to TRANSP, IDE calculates the total plasma current by integrating the current density inside the last closed flux surface ($\rho_{pol} \leq 0.995$). This current deviates from the measured plasma current as the contribution of current in the scrape-off layer is excluded. This current in the scrape-off layer is, besides other factors, due to thermoelectric effects and is described in references [146, 147].

In figure 7.7 the evolution of the different current contributions in the 800 kA discharge #33134 can be seen, in a) calculated with TRANSP and in b) by IDE. The difference in the total plasma current, shown in black, between TRANSP and IDE is in the order of 40 kA. Furthermore the biggest difference is the amount of predicted bootstrap current. Both calculations use the same model for the bootstrap current, but small differences in the fitting and smoothing of the kinetic input profiles together with a different mapping to the equilibria lead to the deviations that can be considered as the uncertainty of the bootstrap current prediction.
In the IDE approach in figure 7.7 b) the sum of the non-inductivly driven currents overestimates the plasma current, leading to a negative inductive current. Due to the fact that still inductive current is driven -indications were shown before- this should lead to an increase of the measured plasma current. However, the measured plasma current decreases from 4.5 s to 7.5 s about 30 kA and a negative inductive current is predicted.
This contradiction raises the question which of the non-inductive contributions is overes-

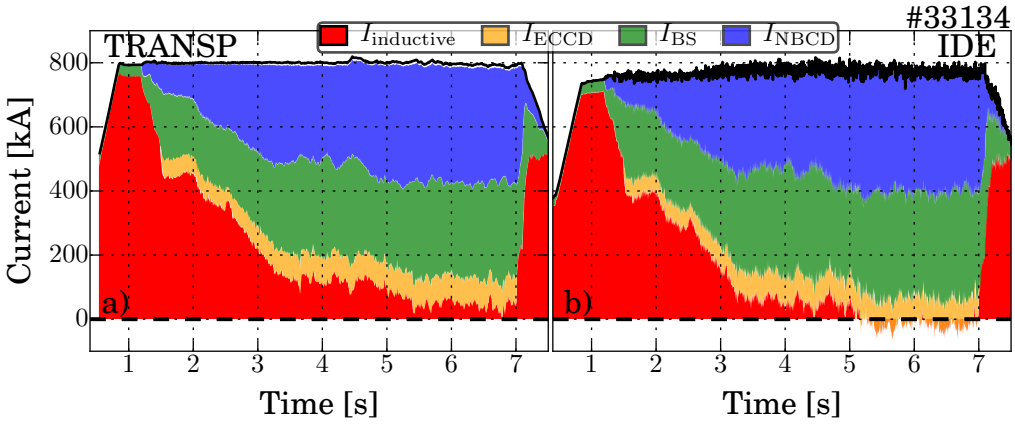

Figure 7.7.: Current composition calculated with TRANSP in a) and with IDE in b). The negative non-inductive current in the IDE calculation from 5 s on disagree with the decreasing plasma current, while the current in the central solenoid is fixed.

timated.
In both discharges the ECCD only contributes in the order of 10% to 15% to the plasma current. With a realistic uncertainty of ≈ 10%, the absolute uncertainty of ECCD plays only a minor role. Therefore the calculations of the bootstrap and neutral beam driven current are revisited in the following sections.

7.2.1. The Bootstrap Current

The overestimation of the predicted sum of the non-inductive currents triggered a reexamination of the bootstrap current calculation in IDE by R. Fischer [145] and finally led to the implementation of an modification to the commonly used bootstrap model of O. Sauter published in 2016 by R. Hager. This modification contains multiple extension to the Sauter model, for example taking the ion gyro radii into account. This and further contributions are described in detail in reference [148]. The differences between the different bootstrap current models can be seen in figure 7.8. Using the Hager modification reduces the bootstrap current by approximatly 15%. A more detailed comparison can be found in [145].
The non-inductive currents seem to be still slightly overestimated as the sum leads to negative inductively driven currents, contradicting the decreasing plasma current. The overestimation is even more pronounced in the 600 kA discharge #33379, shown in figure 7.9, where in IDE the modification by Hager is used.

7.2.2. The Fast Ion Content

The still predicted overestimation of the non-inductive contribution, lead to a quantitative revision of the NBCD prediction, which contribute with 50% to 60% to the total plasma current.

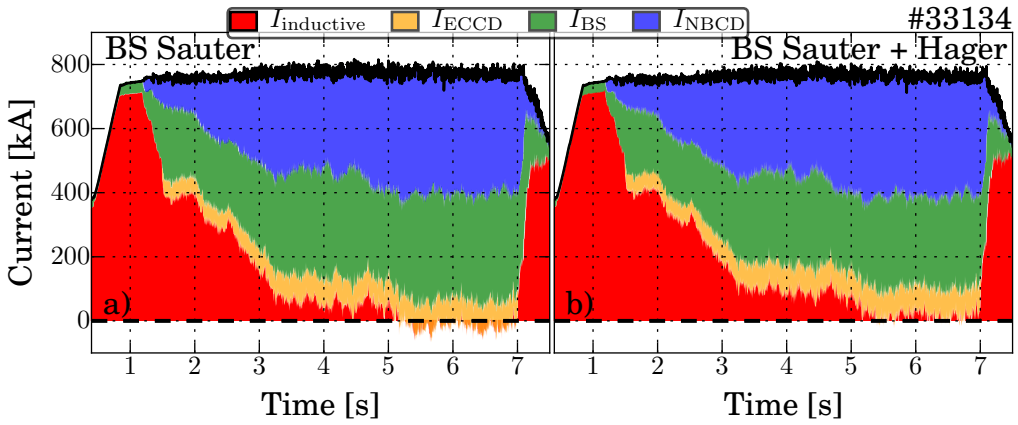

Figure 7.8.: Comparison of the current compositions calculated with IDE in a) using the bootstrap current model of O. Sauter and in b) taking the modification from Hager into account.

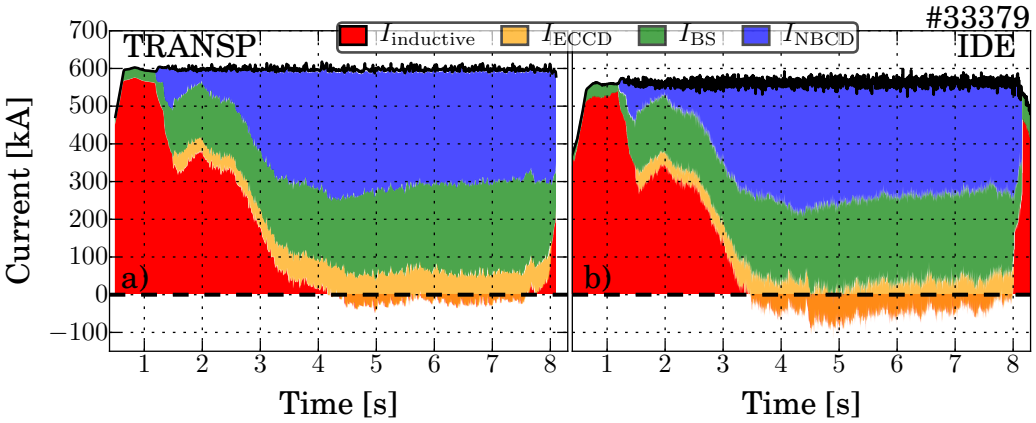

Figure 7.9.: Predicted current composition in a) from TRANSP and in b) from IDE using the modification of Hager for the bootstrap current prediction.

The TRANSP equilibrium solver assumes, besides the given separatrix position, an exact given pressure profile to constrain the solution of the Grad-Shafranov equation. The pressure contains the thermal pressure from the input kinetic profiles and the self calculated fast ion pressure.
In contrast, the IDE code, calculating all outputs using a Bayesian approach [89], uses the pressure with uncertainties, which are in the order of 20–30%. Furthermore, additional constraints for the equilibrium reconstruction are used and have a large impact, especially the magnetic measurements, with uncertainties in the order of 1–2 mT ($B_T \sim 2 - 3$ T). Both constraints enter the calculation of the stored energy (WMHD). Discrepancies in the pressure and magnetic constraints lead, primarily, to a deviation of the fitted pressure profile (from now on called IDE pressure) from the input pressure profile, as, due to the uncertainties, the weights of the magnetic measurements are higher. However, the magnetic measurements have only a small impact on the interior profile shape, as their influence is mostly on the integral quantities. The pressure profile shape is hence determined by the input pressure profile while the absolute pressure is determined by the combination of magnetic measurements and the pressure input. Such a deviation in the pressure is found in the 800 kA discharge #33134 as well as in the 600 kA discharge #33379. Of the two components of the input pressure, the kinetic pressure and the fast ion pressure, the first is assumed to be sufficiently accurate. Therefore the fast ion pressure, calculated with TRANSP, is assumed to be overestimated. Figure 7.10 shows the pressure used in TRANSP to constrain the equilibrium, divided into a contribution from the thermal (blue) and fast (red) particles. Also the IDE pressure (black), resulting from the equilibrium reconstruction, is shown.
Up to 3 s the time evolution of the IDE pressure is in good agreement with the sum of the thermal and fast particle pressure. However, especially in the phases with a high amount of non-inductive current drive, the pressure seems to be overestimated in TRANSP. This behaviour can also be seen comparing the radial profiles at three different points in time in b),c) and d). In the low beta phase in a) the pressure profile agrees almost perfectly with the TRANSP prediction, but in the phase with high beta in c) and d) the comparison indicates an overestimation of the TRANSP pressures.
Assuming an accurate thermal pressure profile, the comparison of the TRANSP predictions with the measurement indicates an overestimation of the fast ion pressure. Using FIDA as independent diagnostic, measuring an equivalent to the radial fast ion density, this hypotesis can be tested. In figure 7.11 this comparison is shown for six points in time.
The TRANSP predictions without or with a small amount of anomalous fast ion diffusion in the beginning of the discharge seem to be in agreement with the measurement. However, after 4.4 s the amount of anomalous fast ion diffusion that needs to be assumed increases. The observation of an overestimation of the fast ion content is in agreement with the overestimation of the IDE pressure shown before.
To quantify the overestimation and fit the amount of global anomalous fast ion diffusion which is necessary to reduce the fast ion content the fast ion pressure from IDE is compared with the TRANSP fast ion pressure prediction assuming anomalous fast ion diffusion. The global anomalous fast ion diffusion in TRANSP is used as modeling tool to reduce the simulated fast ion content in the plasma and potential reasons for the fast ion overestimation are discussed in section 7.2.3. In figure 7.12 the IDE fast ion pressure, the IDE pressure

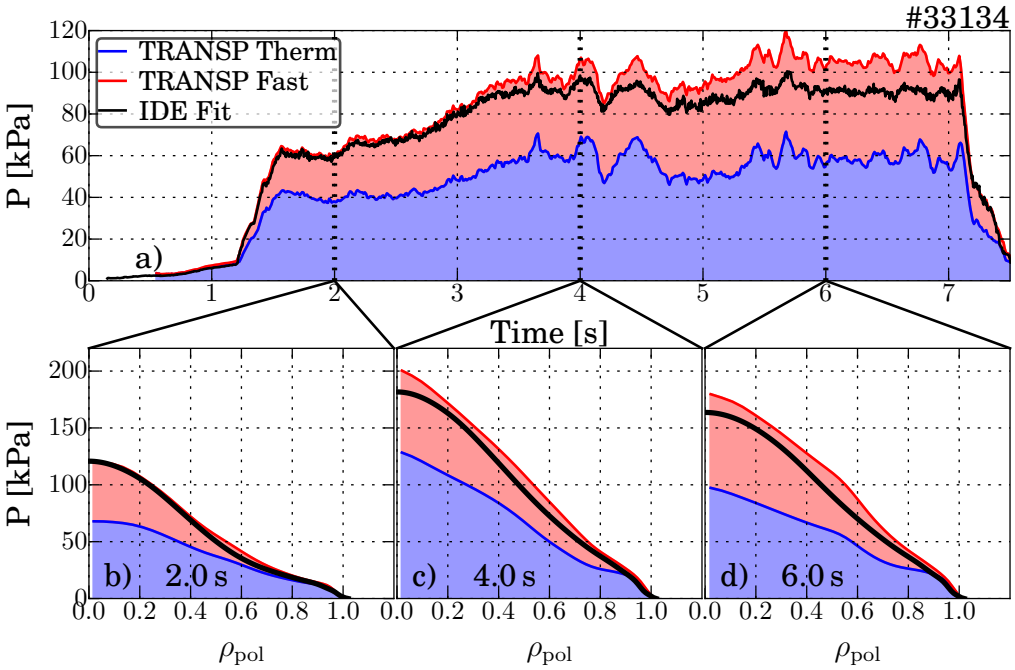

Figure 7.10.: Comparison of the IDE pressure in black and the pressure from TRANSP divided into a thermal (blue) and a fast ion (red) contribution. In a) the time evolution of the integrated pressure and in b)-d) a comparison of the pressure profiles at three different points in time can be seen.

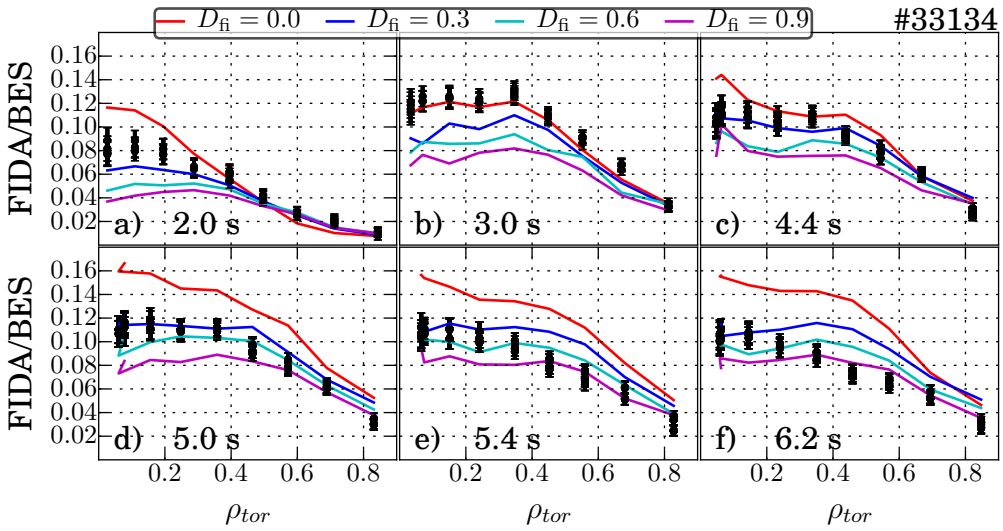

Figure 7.11.: FIDA profiles at several points in time comparing measurements and post-processed TRANSP simulations. In TRANSP anomalous fast ion diffusion is assumed to force fast ion losses, reducing the fast ion current.

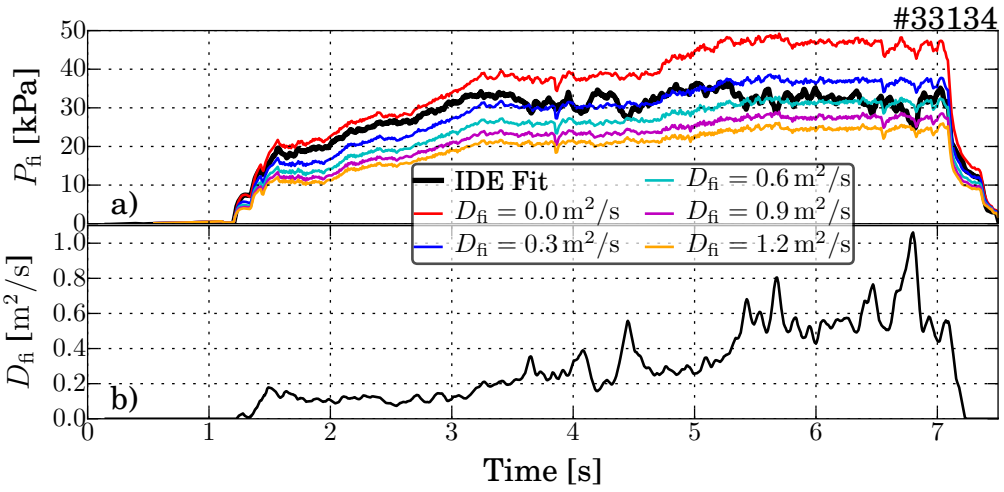

Figure 7.12.: The time evolution of the fast ion pressure is shown in a). The IDE fast ion pressure is the IDE pressure from figure 7.10 reduced by the thermal pressure. The fast ion pressure from TRANSP decreases with increasing anomalous fast ion diffusion. The time evolution of the anomalous fast ion diffusion that needs to be assumed to get to the IDE fast ion pressure is interpolated and shown in b).

without the kinetic pressure, is compared with fast ion pressures from TRANSP assuming different levels of global anomalous fast ion diffusion. From the comparison of the IDE fast ion pressure with different TRANSP predictions a time evolution of the global anomalous fast ion diffusion is interpolated, shown in b).
As written before, the global anomalous fast ion diffusion is used to force anomalous fast ion losses. In TRANSP the power distribution of the injected neutral beam power into the different possible channels is calculated. The channels are the fast ion heating and current drive, orbit losses, power losses due to shine through and charge exchange losses. In figure 7.13 the diversification of the injected power by the neutral beams is shown, in a) and c) for a TRANSP simulation without the assumption of anomalous fast ion diffusion. In this case a fraction of over 80% of the injected power goes into heating and current drive, the shine through and the charge losses are in a comparable range of 6% to 8% and the orbit losses are only in the order of 3% of the injected power. The assumption of anomalous fast ion diffusion, shown in b) and d) changes the distribution. The shine through is similar to the shine through without the assumption of anomalous fast ion diffusion, but the orbit losses as well as the charge exchange losses increase strongly with increasing anomalous fast ion diffusion. Due to the higher diffusivity the fast ion density closer to the edge increases and fast ions close to the separatrix are likely to be on orbits passing through the separatrix and possibly intersecting the wall. Furthermore the neutral pressure density at the edge is higher, originating mainly from wall recycling, leading to an increase of charge exchange losses as more fast ions diffuse outwards.
In the simulation assuming anomalous fast ion diffusion the absolute power going into heating and current drive is almost constant between the end of the β ramp at 3 s and the end of

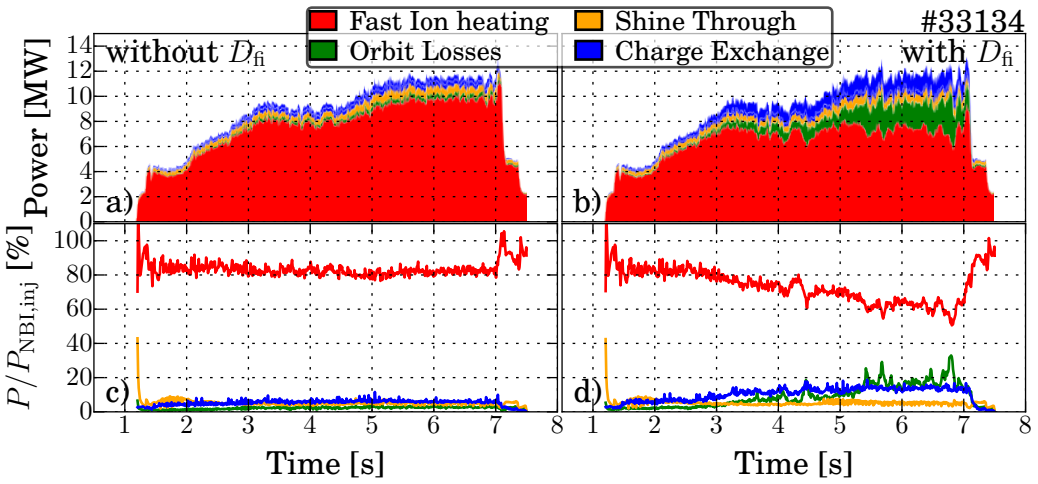

Figure 7.13.: The diversification of the neutral beam power in a) and b) in absolute values and in c) and d) relative to the injected power. In a) and c) the calculation for the TRANSP simulation assuming no anomalous fast ion diffusion is shown. In comparison in b) and d) the interpolated anomalous fast ion diffusion from figure 7.12 b) is assumed.

the discharge. Especially the additional NBI source, from 4.5 s onwards only compensates increasing fast ion losses in this simulation, explaining the constant β despite the increased injected neutral beam power (figure 7.1 a)).
Furthermore also in 600 kA discharge #33379 the assumption of anomalous fast ion diffusion is necessary to describe the IDE fast ion pressure. This can be seen in figure 7.14.
Before discussing the consequences of the assumption of a reduced fast ion content in the plasma, the potential reasons for the reduction are discussed in the following section.

7.2.3. Candidates for Fast Ion Overestimation

The most likely reason for the increasing fast ion losses from 4.5 s on in the 800 kA discharge #33134 is the appearance of a strong m=3/n=2 NTM, visible in the spectrogram in figure 7.15. It is known that neoclassical tearing modes lead to a stochastization of the fast ion orbits, increasing the fast ion losses. This is also qualitatively seen at ASDEX Upgrade [71, 72]. The pronounced 3/2 NTM is a source for anomalous fast ion losses.
Nevertheless, also up to 4.5 s the necessity of a small amount of anomalous fast ion diffusion is indicated by the pressure comparison in figure 7.12. Also in the 600 kA discharge #33379 the assumption of anomalous fast ion diffusion is necessary. However, in contrast to discharge #33134 no pronounced MHD activity is visible in the spectrogram in figure 7.16. Only some small fishbones with an erratic repetition rate are visible from 5 s on.
Assuming that up to 4.5 s the fast ion behaviour in both discharges is comparable, this indicates that either the NBI power, as the only source of fast ions, is overestimated or that there is another fast ion loss mechanism, which is not associated with a mode visible

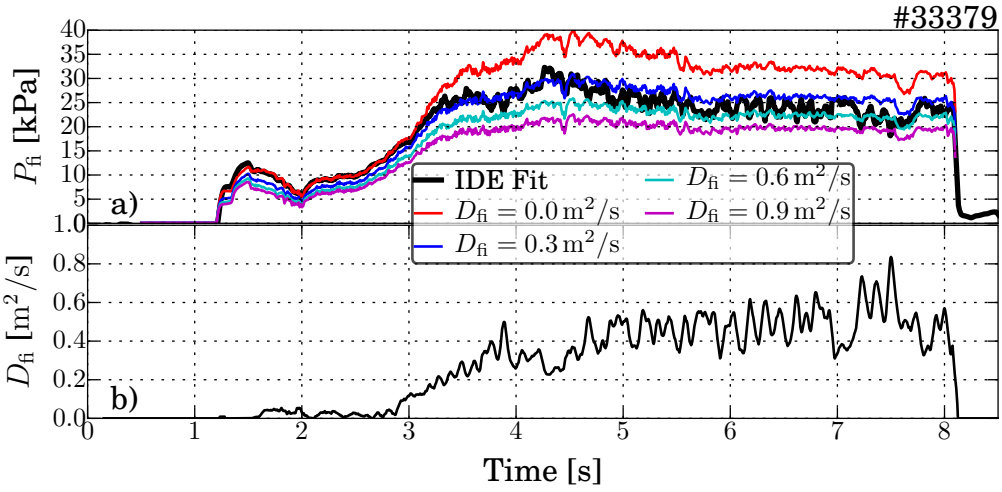

Figure 7.14.: In a) the time evolution of the fast ion pressure from the IDE fit in comparison to the TRANSP prediction assuming anomalous fast ion diffusion is shown. In b) the resulting interpolated global anomalous fast ion diffusion can be seen.

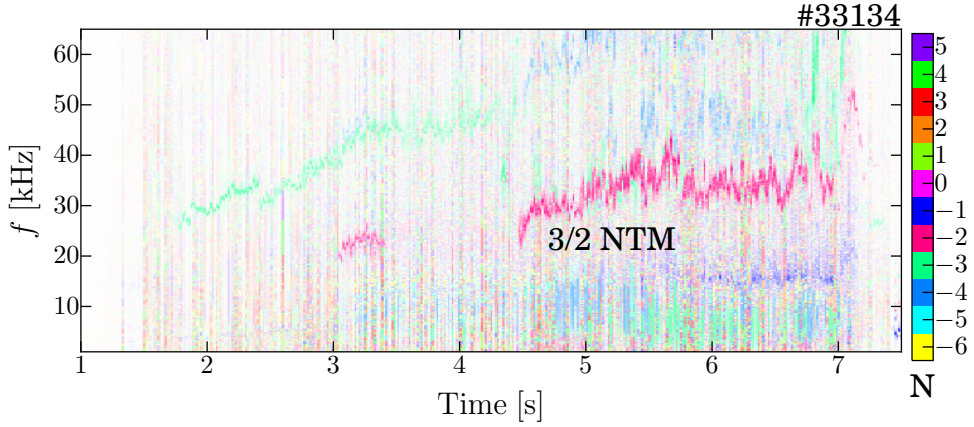

Figure 7.15.: Spectrogram of the magnetic measurements indicating MHD activity together with the n number of the activity. The strong m=3/n=2 NTM, shown in purple and pronounced from 4.5 s on, could force fast ion losses due to a stochastisation of the fast ion orbits.

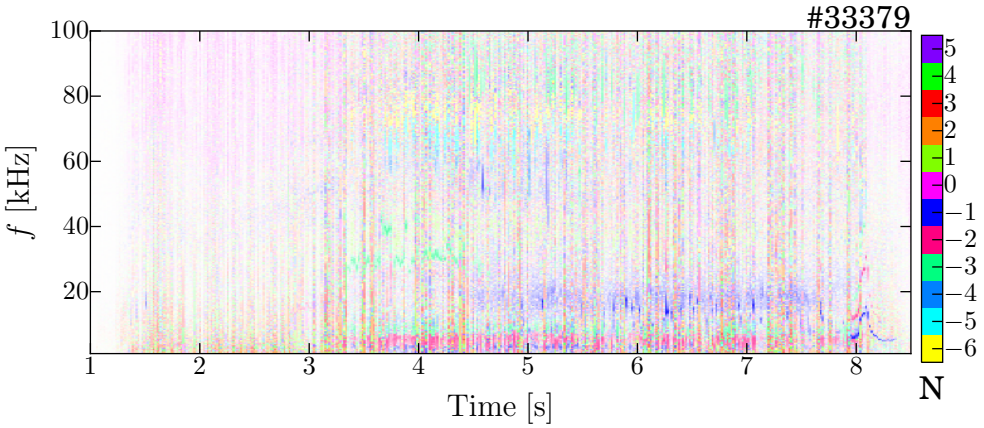

Figure 7.16.: Almost MHD-quiescent spectrogram of the 600 kA discharge, exceptional some small fishbones from 5 s on with an erratic repetition rate.

in the magnetic measurements. A distinct reason is not found, but some candidates were investigated.
A first candidate is the modulation of the neutral beam sources. From empirical studies it is known that the neutral beams need up to 10 ms to reach their full power, but for the β feedback the beam on times were often shorter than 10 ms. However, this cannot fully explain the fast ion overestimation, as the modulated neutral beam fraction decrease during the discharge, but in contrast the fast ion overestimation increases.
A second candidate is a potential pressure increase in the beam box and the duct. This would lead to an increase of reionization losses, reducing the neutral beam power. However a comparison of the absolute measured pressure values with other discharges can rule out this hypothesis.
A third candidate is an increased neutral gas pressure in the vessel, which would lead to increasing charge exchange losses. However, the discharges were performed soon after a boronization, cleaning the inner wall and reducing the wall recycling of gas.
A forth and last considered candidate is the fast ion redistribution due to microturbulent transport, discussed in section 6.5.2. However, no enhanced fast ion losses are found, using the anomalous fast ion diffusion coefficients expected from microturbulence, calculated using the model of Pueschel et al. [33] with equations 6.1–6.6 shown in appendix D.3. The calculated diffusion coefficients are in a similar order of magnitude, but only in the center of the plasma and decreasing towards the edge.
In conclusion the pronounced 3/2 NTM can explain a large fraction of the fast ion overestimation in the 800 kA discharge #33134, but for the overestimation seen without NTM, especially in the 600 kA discharge #33379, a unique explanation was not found. A combination of the four proposed candidates is a possible explanation, but further studies are needed.

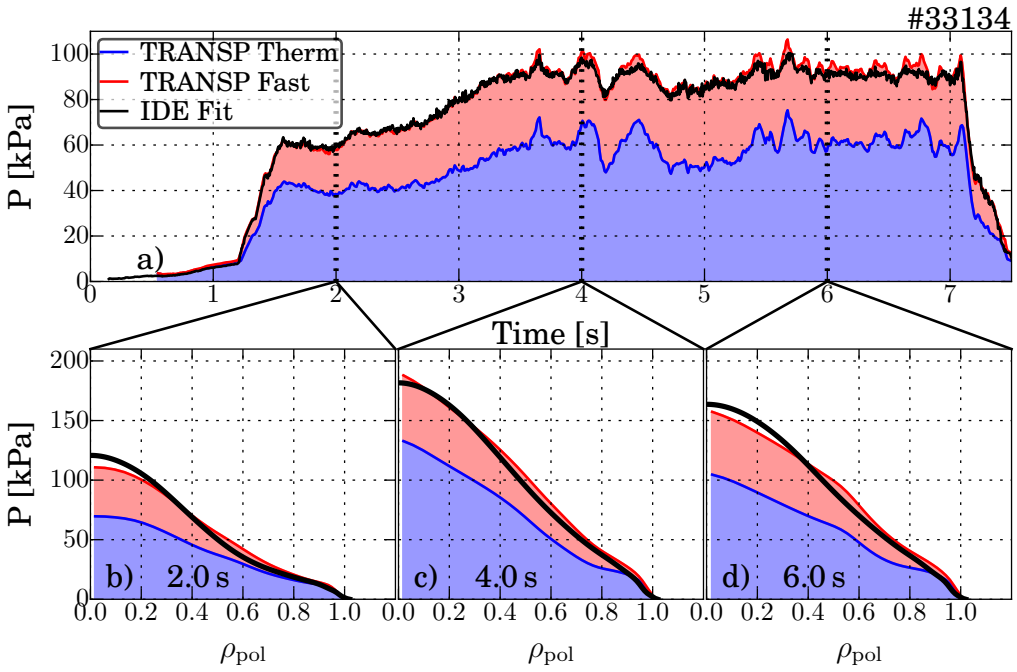

Figure 7.17.: Comparison of the IDE pressure fit with the TRANSP pressure prediction assuming the optimized anomalous fast ion diffusion, shown in figure 7.12. The integrated pressure in a) fits very well to the IDE fit, as expected, also the profiles in b)-d) have only minor deviation, but this deviations are within the uncertainties of the pressure profile.

7.2.4. Effect of the Forced Fast Ion Losses on the Modelling Results

Assuming the interpolated global anomalous fast ion diffusion to reduce the fast ions pressure in the plasma leads to the expected agreement of the integrated IDE pressure with the TRANSP pressure, shown in figure 7.17. This agreement in the integrated pressure is of course expected, as the time evolution of the global anomalous fast ion diffusion is calculated from the comparison of the TRANSP with the IDE fast ion pressure, shown in figure 7.12. The small deviation in the profiles in b)-d) are within the uncertainties of the pressure profiles.
The comparison of the measured FIDA data with the synthetic diagnostic from TRANSP, which is independent from the pressure fit, is in good agreement, shown in figure 7.18. Minor deviations in the shape could be explained due to the fact that the fit was done at the integrated pressure. The reasonable agreement in the shape is therefore a good indication for a conceptional right approach. In the FIDA comparison, two phases can be identified, the first before the appearance of the m=3/n=2 NTM in a)-c) and the second with the pronounced m=3/n=2 NTM active in d)-f). In the first phase the deviation between the simulations with and without anomalous fast ion diffusion is small, but the assumed anomalous fast ion diffusion agrees slightly better with the data. In the second phase the simulation assuming no anomalous fast ion diffusion overestimates the data

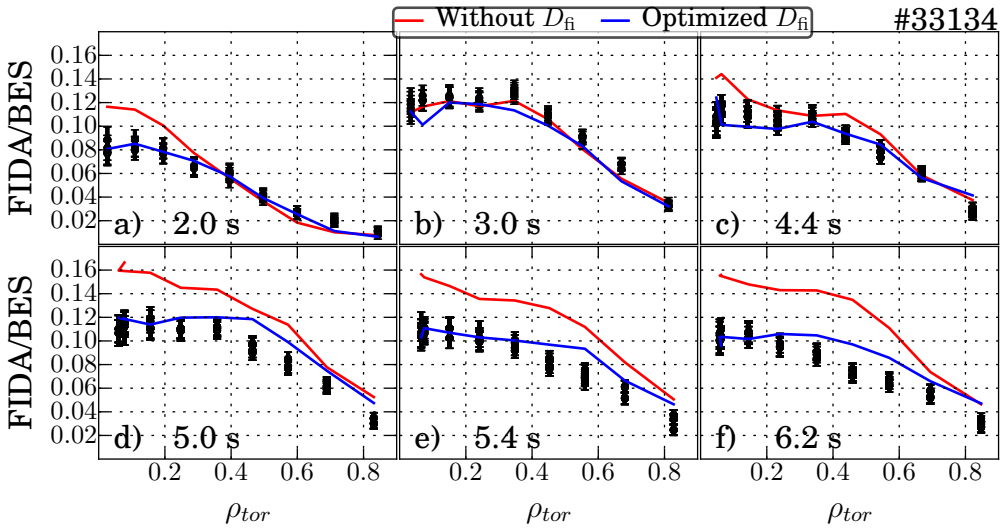

Figure 7.18.: FIDA profiles at six different points in time, comparing the TRANSP simulations assuming no anomalous fast in diffusion (in red), with the assumption of the optimized anomalous fast ion diffusion (in blue) and the data (in black).

and again the deviation is well compensated by the assumption of the anomalous fast ion diffusion. Only around $\rho_{\text{tor}} = 0.5$ does the simulation slightly overestimate the data, like the pressure profiles shown before.
A further indication is the comparison of the predicted and measured diamagnetic flux, but this comparison should be taken carefully. As a reminder of what was said at the end of section 6.4, the use of the off-axis neutral beam sources leads to not yet fully understood deviations between prediction and measurement. One potential explanation is an anisotropic pressure profile. This option is not taken into account in the simulation, and as the diamagnetic flux measurement is sensitive to such an anisotropy this would lead to such a deviation. Therefore only dynamics in phases with a constant power of the off-axis neutral beams should be compared. In figure 7.19 the comparison of the simulations with the measurement are shown.
Both simulations fit well to the data up to the point when the off-axis neutral beams are switched on. In the areas marked in red the power of at least one of the off-axis neutral sources changes within 30 ms, leading to an increasing deviation of both simulations from the data. However, from 4.5 s on the off-axis neutral beam power is constant and the simulation assuming anomalous fast ion diffusion does not further deviate from the measurements. This can also be seen in the magenta off-set corrected time trace, shifted to match between 4.6 s and 5.0 s. In contrast, the simulation without the assumption of anomalous fast ion diffusion - its shifted equivalent is shown in cyan - the deviation increases without a change in the off-axis neutral beam power. This comparison also indicates that the fast ion losses due to the NTM are well described by the assumed anomalous diffusion. It should be keep in mind that again only an integrated measurement is shown.
In figure 7.20 the comparison of the simulations with the FIDA measurement for the 600 kA

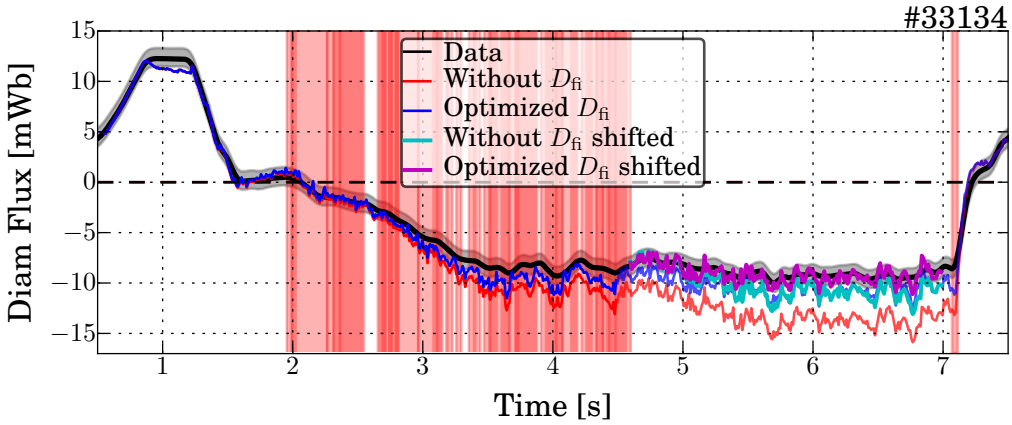

Figure 7.19.: Diamagnetic flux comparison of the measurement with simulations with and without the assumption of anomalous fast ion diffusion. The off-axis neutral beam sources 6 and 7 could lead to an anisotropic pressure, not taken into account in the simulations. Therefore phases with changing off-axis neutral beam power, marked in red, should be excluded in the comparison and only dynamics in the other phases should be compared. Therefore in magenta and cyan the simulations are shown off-set corrected to match the data from 4.6 s to 5.0 s.

discharge can be seen. In this discharge no passive background correction was possible, as the neutral beam 3 runs constantly throughout the whole discharge. Therefore the data are slightly overestimated. Nevertheless, the simulation assuming anomalous fast ion diffusion from the fit in figure 7.14 agree much better with the data, compared with the simulation without the assumption of anomalous fast ion diffusion.

Taking all previous results together, the anomalous fast ion diffusion from the interpolation to the IDE fast ion pressure seems to be in agreement with all data. Therefore finally in figure 7.21 the predict current distribution can be seen, assuming the interpolated global anomalous fast ion diffusion. In both calculations the inductive current is positive throughout the whole discharge. A slight decrease of the inductive current can be seen from the point on, where the current in the central solenoid is fixed. The inductive contribution of 80–120 kA is in an expected order of magnitude.
For an unequivocal comparison of the current predictions with the measurements the discharge is much to short. An equilibrated current distribution with a fixed current in the central solenoid is necessary, in which all inductive current has fully decayed, even in the plasma center. Then all non-inductive currents would add up to the full plasma current. The required time can be estimated by ≈ 3 resistive times - $\tau_{\mathrm{R}} \approx 10\,\mathrm{s}$ using equation 7.1 with $T_{\mathrm{e}} \approx 5\,\mathrm{keV}$ and $L = 0.5\,\mathrm{m}$ - and is approximately 30 s. In ASDEX Upgrade discharges are generally limited to 10 s and to even shorter time in these high power discharges. Hence these conditions cannot be reached in ASDEX Upgrade.
In figure 7.22 the corresponding calculated current distributions for the 600 kA discharge

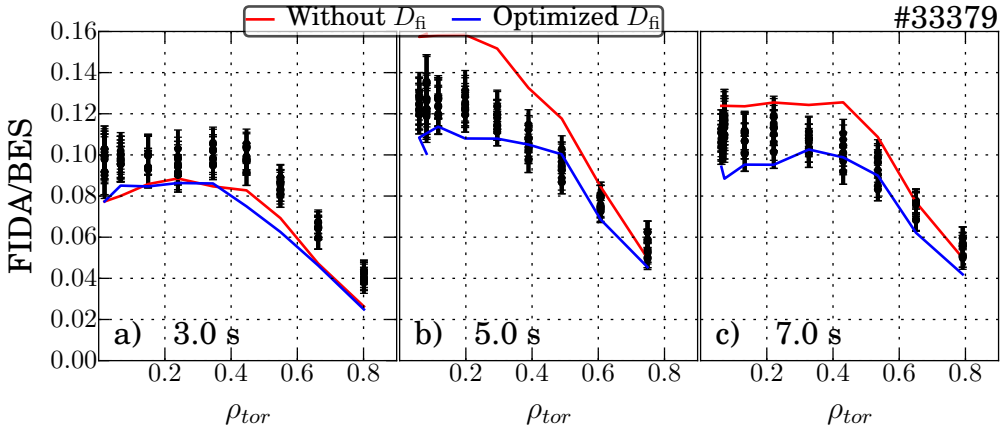

Figure 7.20.: Comparison of the measured and predicted FIDA profiles with and without the assumption of anomalous fast ion diffusion. No correction for the passive FIDA radiation was possible, as the neutral beam 3 runs uninterrupted throughout the whole discharge. Therefore the data could be slightly overestimated.

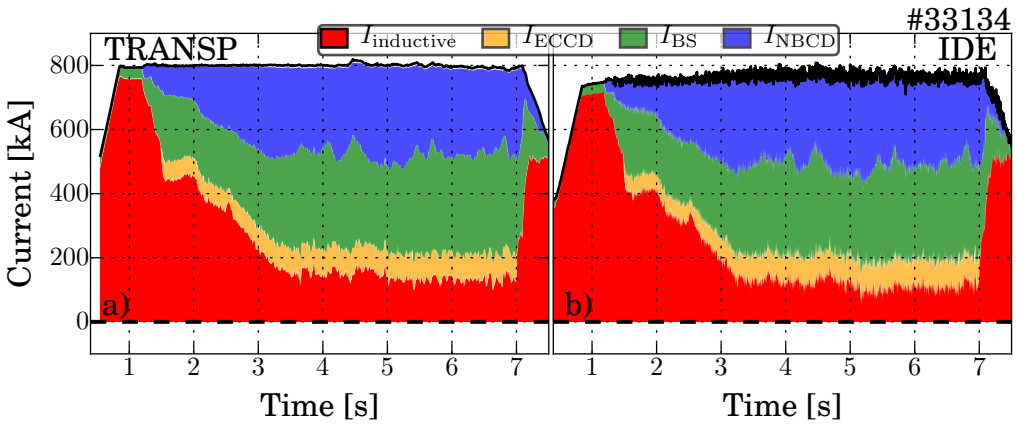

Figure 7.21.: Current composition calculated with TRANSP in a) and IDE in b) assuming anomalous fast ion diffusion from the interpolation in figure 7.12.

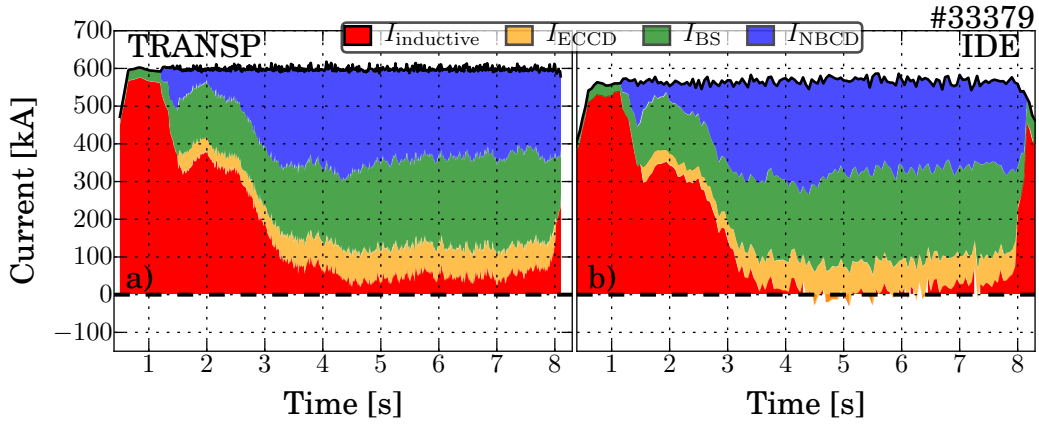

Figure 7.22.: Comparison of the TRANSP a) and IDE b) prediction of the current composition.

can be seen. In comparison to the initial predictions in figure 7.9 the negative inductive current almost vanishes. Within the uncertainties in the order of 10% the predictions seems to be in agreement with the indications for a discharge with a very small inductive current contribution.
The almost vanishing inductive current contribution in the 600 kA discharge enables a conclusive comparison of the MSE-based reconstruction of the current profile with the sum of the non-inductive contributions. In figure 7.23 the comparison of the profiles at two points in time is shown. The stiffness of the reconstructed current profile, due to radial limits in the spline fit, leads to a resolution which is to low to resolve narrow structures like the ECCD peaks. The limitation is connected with the finite radial resolution of the MSE diagnostic. An increased radial flexibility of the reconstructed current profile would lead to a strong increase of the uncertainties. Within the uncertainties and with the reasonable stiffness the reconstruction of the total plasma current profile and the sum of the non-inductive contributions are in good agreement. This good agreement in the shape of the profiles is another indication for a proper modeling of the non-inductive current drivers.

7.3. Summary and Discussion

A consistent prediction of the non measurable current contribution, in almost fully non-inductive discharges, was achieved. Furthermore a method to quantitatively calculate the fast ion content in the plasma in agreement with multiple diagnostics was introduced. In combination with the bootstrap current description by Hager [148] the initially found overestimation of the non-inductive driven currents vanishes assuming a fast ion content which is the result of a fit to the equilibrium pressure.
The considerable uncertainties of the direct inductive current calculation is suppressed in this study using almost fully non-inductive discharges.

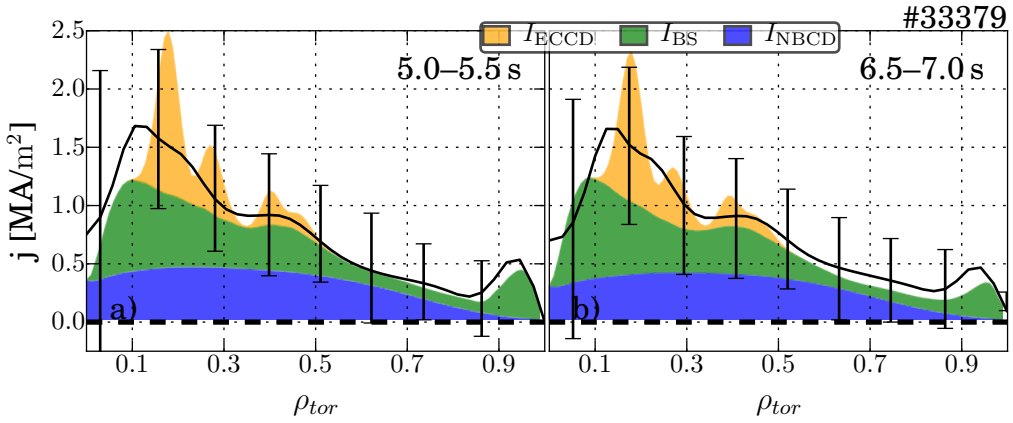

Figure 7.23.: Comparison of the reconstructed current profile on the basis of MSE measurements with the profile of the sum of the reconstructed non-inductive current contributions. The two points in time are averaged over 0.5 s in phases with predicted almost fully non-inductive current drive.

The improvement of the bootstrap current calculation is achieved by the implementation of the modifications of Hager [148] to the Sauter bootstrap current model. Nevertheless, the predicted non-inductive current fraction was still overestimated. This overestimation can be explained by an overestimation of the fast ion content in the plasma. From the (fast ion) pressure fit in IDE in comparison with the TRANSP (fast ion) pressure, the evolution of the global anomalous fast ion diffusion, used to induce fast ion losses, can be calculated. Applying this fast ion diffusion in the TRANSP simulation, the adjusted fast ion content is in agreement with the FIDA measurements and can also describe the dynamics in the diamagnetic flux measurement. The main reasons for the fast ion losses can be explained by an m=3/n=2 NTM in the 800 kA discharge #33134. The reason for the further necessary fast ion losses, especially in the 600 kA discharge #33379, needs to to be further investigated.
Nevertheless, assuming the fast ion losses, the prediction of the current contribution in both discharges is, within the uncertainties of $\approx 10\%$, in agreement with the measured plasma current and the loop voltage. The loop voltage as well as the approximation of the inductive contribution from the averaged values indicating a small inductive current contribution throughout the whole discharge.
Also at other Tokamaks, for example at JT60-U [149] and DIII-D [150], quantitative investigations of the non-inductive driven current were performed. The approach in these studies based on the method of C. B. Forest [151] and starts with a quantification of the inductive current contribution calculated from the reconstructed equilibrium and a calculated resistivity. Subsequently this inductive current is subtracted from the measured total plasma current to quantify the non-inductive contributions. In JT60-U the studies were made in L-Mode at reduced total plasma current, avoiding interfering ELMs, which was one of the sources of error in the calculation of the inductive current at ASDEX Upgrade. In DIII-D co- and counter-current drive by the neutral beam injection was compared. The quantification of the currents in both publications were in agreement with the neutral beam current drive theory, within the uncertainties of the measurement. One advantage of the study of this

chapter is that it uses the modified bootstrap current model by Hager. Another advantage is its reduced dependence from the still not accurately quantifiable inductive contribution, due to the small inductive contribution. The uncertainties on the inductive contribution were not discussed in the publications.
In conclusion there are no indications for quantitative disagreements of the NBCD model. This is a positive result for the scenario development for ITER and future Tokamak fusion power plants.

8. Summary and Conclusions

For ITER (the Latin word for "The Way") and future fusion power plants based on the Tokamak principle non-inductive current drive is essential to increase the pulse length towards stationary operation. In this thesis the active current drive with fast ions, produced by neutral beam injection, was studied.
While the total plasma current can be reliably measured, the individual contributions such as the beam driven current are not directly accessible through measurements. To investigate the influence of the neutral beam current drive (NBCD), changes of the plasma current profile due to changes of the neutral beam deposition were studied. Therefore a measurement-based reconstruction of the current profile in the plasma is important. Using motional Stark effect polarimetry (MSE) data as a constraint strongly reduces the uncertainties of the current profile reconstruction, especially in the plasma center, leading to an increased reliability of the reconstructed magnetic equilibrium, the natural coordinate system of the plasma. The achieved first absolute calibration of the ASDEX Upgrade MSE system, further improves the reliability of the reconstruction. However, a broad-band polarized background distorts the MSE measurement. This background originates from polarizing light reflections on metal surfaces, like the full tungsten plasma facing components in ASDEX Upgrade, into the lines of sight of the diagnostic. To correct for this distortion a polychromator was built, in cooperation with the MSE group at the Massachusetts Institute of Technology. This polychromator was successfully tested and enables the use of the MSE also in discharges with large radiative background. As ITER will have a full metal wall, and therefore a large polarized background, the work is also relevant for the implementation of an MSE system [152, 153] there.
As the NBCD contribution to the plasma current is not directly measurable, the NBCD was calculated using the Tokamak transport code TRANSP. The calculation of the NBCD in TRANSP was successfully compared with calculations based on a semi-analytical fast ion model. This ensures that the implementation of the NBCD in TRANSP was fully understood.
Improved experiments were carried out to investigate an apparent discrepancy between the radial current profile driven by off-axis NBI [12], that had been found to deviate from the neoclassical prediction, and the radial profile of the fast ions that drive it, which had been found to be in agreement with the neoclassical prediction. In the improved discharge design, for the first time, the current profile measurement, with MSE, and the fast ion profile measurement, with FIDA, was done in parallel. Improvements in the (synthetic-) diagnostics and simulations, like a remeasured neutral beam geometry, lead to simulations which are in agreement with measurements of both diagnostics. The fast ion profile during the phase with off-axis neutral beam current drive was in good

agreement with the neoclassical predictions. However, in the phase with on-axis neutral beam deposition a deviation from the neoclassical prediction was found in the center of the plasma. This deviation could be explained either by a redistribution forced by the magneto-hydro-dynamic fishbone instability or by microturbulent transport of the fast ions. For the fishbone redistribution increased central fast ion transport was assumed at the location of the fishbones. In contrast, the TRANSP simulation investigating the effect of microturbulence used anomalous fast ion diffusion coefficients calculated on basis of a published model, derived from gyro-kinetic calculations with the code GENE [33]. Each approach individually can explain the data within all diagnostics. However, an unequivocal identification of which of the two approaches force the minor deviations from the neoclassical theory is left to future experiments. The deviations from the neoclassical prediction in the former experiments can be explained by simulations using both hypotheses individually. The results of the earlier MSE based study [12] could neither be disproved nor confirmed due to large uncertainties in the electron temperature measurement in the presented discharges. In conclusion there are no longer indications for a discrepancy between the FIDA measured fast ion profile and the MSE measured, fast ion driven, current profile. Furthermore the determined deviation from the neoclassical theory does not change the amount of neutral beam driven current, only a small central current redistribution is predicted.

For a quantitative determination of NBCD its current fraction should be maximized. Furthermore, a larger non-inductive current fraction is beneficial, reducing the absolute uncertainty from the, only inaccurately quantifiable, inductive contribution. This was realized in discharges with a β increase close to the stability limit, feedback controlled by the neutral beam power. The large neutral beam power (12 MW) lead to a large NBCD fraction ($\sim 40\%$). The high β, in combination with a centrally elevated q profile, leads to a large bootstrap current fraction ($\sim 40\%$). In these experiments the inductive current fraction was proven to be small ($\sim 10\%$). However, the initial reconstruction of the current composition predicted a negative inductive current calculated as the difference between the total plasma current and all other contributions, as other quantification methods were not reliable. This raised the question which of the two main, non-inductive contributions to the plasma current was overestimated.

A revision of both lead to an agreement of the final current reconstruction with all diagnostics and the experimental evidence for a small inductive current fraction. The bootstrap current description was improved due to the use of the Hager addendum [148] to the commonly used Sauter model. The prediction of the NBCD fraction benefits from the new evolved technique to quantify the amount of fast ions in the plasma on the basis of the equilibrium reconstruction. The reconstruction of the equilibrium, between kinetic and magnetic pressure, enables the connection of the precise magnetic measurements with the pressure. The kinetic pressure is also based on measurements, but the pressure contribution from the fast ions is only the result of the modeled fast ion distribution. A comparison of the fast ion pressure reveals an overestimation of the fast ion content of up to 40%. The pressure-fit-based correction is independently confirmed with the FIDA measurements and other diagnostics. A magneto-hydro-dynamic instability was identified as a reason for the overestimation of the fast ion content. This instability, a neoclassical tearing mode (NTM),

is qualitatively known as fast ion loss mechanism. A further minor overestimation in phases without a NTM remains as open question for future experiments. In conclusion a reconstruction of the current composition with previously unknown precision at ASDEX Upgrade in agreement with all measurements, was achieved. In particular the NBCD fraction was quantitatively predicted, accounting for the correction of the fast ion pressure, and independently checked by the FIDA measurements, without indications for deviations from the used NBCD model.
In conclusion the NBCD is a good and robust tool to increase the pulse duration towards a stationary operation for ITER and a future fusion power plant based on the Tokamak principle. The work in this thesis has shown that the preexisting doubts regarding the qualitative and quantitative prediction of the amount and location of the NBCD can be removed.

9. Bibliography

[1] IEA. *Key World Energy Statistics 2009*. Key World Energy Statistics. OECD Publishing, 2016.

[2] A. Einstein. Das Prinzip von der Erhaltung der Schwerpunktsbewegung und die Trägheit der Energie. *Annalen der Physik*, 325(8):627–633, 1906.

[3] J. Wesson and D. J. Campbell. *Tokamaks*. International Series of Monographs on Physics. OUP Oxford, 2011.

[4] D. Keefe. Inertial Confinement Fusion. *Annual Review of Nuclear and Particle Science*, 32(1):391–441, 1982.

[5] EFDA. Tokamak principle, 2005.

[6] T. Sunn Pedersen, et al. Confirmation of the topology of the Wendelstein 7-X magnetic field to better than 1:100,000. *Nature Communications*, 7:13493, 2016.

[7] L. Spitzer. The Stellarator Concept. *Physics of Fluids*, 1(4):253, 1958.

[8] R. Aymar. ITER overview. *Fusion Engineering and Design*, 36(1):9–21, 1997.

[9] Y. Shimomura, et al. ITER overview. *Nuclear Fusion*, 39(9Y):1295, 1999.

[10] M. Shimada, et al. Chapter 1: Overview and summary. *Nuclear Fusion*, 47(6):S1–S17, 2007.

[11] O. Gruber. ASDEX Upgrade enhancements in view of ITER application. *Fusion Engineering and Design*, 84(2-6):170–177, 2009.

[12] S. Günter, et al. Interaction of energetic particles with large and small scale instabilities. *Nuclear Fusion*, 47(8):920–928, 2007.

[13] M. Turnyanskiy, et al. Study of the fast ion confinement and current profile control on MAST. *Nuclear Fusion*, 49(6):065002, 2009.

[14] J. M. Park, et al. Validation of on- and off-axis neutral beam current drive against experiment in DIII-D. *Physics of Plasmas*, 16(9), 2009.

[15] W. W. Heidbrink, et al. Beam-ion confinement for different injection geometries. *Plasma Physics and Controlled Fusion*, 51(12):125001, 2009.

[16] W. W. Heidbrink, et al. Evidence for fast-Ion transport by microturbulence. *Physical Review Letters*, 103(17):1–4, 2009.

[17] B. Geiger. *Fast-ion transport studies using FIDA spectroscopy at the ASDEX Upgrade*

tokamak. PhD thesis, Ludwig-Maximilians-Universität München, 2012.

[18] T. Suzuki, et al. Off-axis current drive and real-time control of current profile in JT-60U. *Nuclear Fusion*, 48(4):45002, 2008.

[19] A. Bock. *Generation and Analysis of Plasmas with Centrally Elevated Helicity Profiles in Full W ASDEX Upgrade*. PhD thesis, Ludwig-Maximilians-Universität, 2016.

[20] K. Lackner. Computation of ideal MHD equilibria. *Computer Physics Communications*, 12(1):33–44, 1976.

[21] M. Rampp, R. Preuss, and R. Fischer. GPEC: A real- Time-capable tokamak equilibrium code. *Fusion Science and Technology*, 70(1):1–13, 2016.

[22] W. Schneider, et al. ASDEX Upgrade MHD equilibria reconstruction on distributed workstations. *Fusion Engineering and Design*, 48(1):127–134, 2000.

[23] R. Fischer, et al. Coupling of the flux diffusion equation with the equilibrium reconstruction at ASDEX Upgrade. *Fusion Science and Technology*, 69(2):526–536, 2016.

[24] F. Felici, et al. Real-time physics-model-based simulation of the current density profile in tokamak plasmas. *Nuclear Fusion*, 51(8):083052, 2011.

[25] A. A. Galeev and R. Z. Sagdeev. Transport phenomena in a collisionless plasma in a toroidal magnetic system. *Sov Phys JETP*, 26(1):233–240, 1968.

[26] P. H. Rutherford. Collisional Diffusion in an Axisymmetric Torus. *Physics of Fluids*, 13(2):482–489, 1970.

[27] C. Marty, D. Maschke, E.K. Dumont, and J.O. Gourdon. *Plasma Physics and Controlled Nuclear Fusion Research*, 1:847, 1969.

[28] J. W. Connor, P. Buratti, B. A. Carreras, and R J Bickerton. Tokamak turbulence-electrostatic or magnetic? *Plasma Physics and Controlled Fusion*, 35(SB):B293, 1993.

[29] G. D. Conway. Turbulence measurements in fusion plasmas. *Plasma Physics and Controlled Fusion*, 50(12):124026, 2008.

[30] W. Zhang and Z. Lin. Does the orbit-averaged theory require a scale separation between periodic orbit size and perturbation correlation length? *Physics of Plasmas*, 20(10), 2013.

[31] F. Jenko, T. Hauff, M. J. Pueschel, and T. Dannert. Jenko et al. Reply:. *Physical Review Letters*, 107(23):239502, 2011.

[32] D.C. Pace, et al. Transport of energetic ions due to sawteeth, Alfvén eigenmodes and microturbulence. *Nuclear Fusion*, 51(4):043012, 2011.

[33] M.J. Pueschel, et al. Anomalous diffusion of energetic particles: connecting experiment and simulations. *Nuclear Fusion*, 52(10):103018, 2012.

[34] X. Garbet. Turbulence theory and Gyrokinetic Codes. In *22nd IAEA Fusion Energy Conference*, pages 1–16, 2008.

[35] T. Görler, et al. A flux-matched gyrokinetic analysis of DIII-D L-mode turbulence. *Physics of Plasmas*, 21(12):122307, 2014.

[36] A. E. White and T. Görler. Special issue on comparing gyrokinetic simulations to experiments. *Plasma Physics and Controlled Fusion*, 59(5):50101, 2017.

[37] D. H. Sharp. An overview of Rayleigh-Taylor instability. *Physica D: Nonlinear Phenomena*, 12(1-3):3–18, 1984.

[38] M. N. Rosenbluth and C. L. Longmire. Stability of plasmas confined by magnetic fields. *Annals of Physics*, 1(2):120–140, 1957.

[39] B. B. Kadomtsev, et al. Trapped particles in toroidal magnetic systems. *Nuclear Fusion*, 11(1):67, 1971.

[40] F. Wagner, et al. Regime of Improved Confinement and High Beta in Neutral-Beam-Heated Divertor Discharges of the ASDEX Tokamak. *Physical Review Letters*, 49(19):1408–1412, 1982.

[41] F. Ryter and the H mode database working group. H mode power threshold database for ITER. *Nucl. Fusion*, 36(9):1217–1264, 1996.

[42] Y. R. Martin, T. Takizuka, and ITPA CDBM H-mode Threshold Database Working Group. Power requirement for accessing the H-mode in ITER. *Journal of Physics: Conference Series*, 123:012033, 2008.

[43] J. Connor and H. Wilson. A review of theories of the L – H transition. *Plasma physics and controlled fusion*, 1(1):R1–R74, 2000.

[44] F. Ryter, et al. Experimental studies of electron transport. *Plasma Physics and Controlled Fusion*, 43(12A):A323–A338, 2001.

[45] F. Ryter, et al. Electron heat transport studies. *Plasma Physics and Controlled Fusion*, 48(12B):B453–B463, 2006.

[46] H. Zohm. Edge localized modes (ELMs). *Plasma Physics and Controlled Fusion*, 38(2):105–128, 1996.

[47] F.W. Perkins. Heating tokamaks via the ion-cyclotron and ion-ion hybrid resonances. *Nuclear Fusion*, 17(6):1197–1224, 2011.

[48] T. H. Stix. Heating of toroidal plasmas by neutral injection. *Plasma Physics*, 14(4):367–384, 1972.

[49] M. M. Menon. Neutral Beam Heating Applications and Development. *IEEE*, 69(8):1012–1029, 1981.

[50] D. R.. Mikkelsen and C. E. Singer. Optimization of Steady-State Beam-Driven Tokamak Reactors. *Nuclear Technology/Fusion*, 4(September):237–252, 1983.

[51] R. Prater. Heating and current drive by electron cyclotron waves. *Physics of Plasmas*, 11(5 PART 2):2349–2376, 2004.

[52] E. Poli, A. G. Peeters, and G. V. Pereverzev. TORBEAM, a beam tracing code for

electron-cyclotron waves in tokamak plasmas. *Computer Physics Communications*, 136(1-2):90–104, 2001.

[53] A. G. Peeters. The bootstrap current and its consequences. *Plasma Phys. Control. Control. Fusion*, 42(00):231–242, 2000.

[54] EFDA. Charged particles movement, 2005.

[55] O. Sauter, C. Angioni, and Y. R. Lin-Liu. Neoclassical conductivity and bootstrap current formulas for general axisymmetric equilibria and arbitrary collisionality regime. *Physics of Plasmas*, 6(7):2834, 1999.

[56] O. Sauter, C. Angioni, and Y. R. Lin-Liu. Erratum: Neoclassical conductivity and bootstrap current formulas for general axisymmetric equilibria and arbitrary collisionality regime (Physics of Plasmas (1999) 6 (2834)). *Physics of Plasmas*, 9(12):5140, 2002.

[57] H. Zohm. *Resistive MHD Stability*. Wiley-VCH Verlag GmbH & Co. KGaA, Weinheim, Germany, 2015.

[58] B. B. Kadomtsev. Disruptive instability in Tokamaks. *Soviet Journal of Plasma Physics*, 1:710–715, 1975.

[59] F. Porcelli, D. Boucher, and M. N. Rosenbluth. Model for the sawtooth period and amplitude. *Plasma Physics and Controlled Fusion*, 38(July 1995):2163–2186, 1996.

[60] T. P. Goodman, F. Felici, O. Sauter, and J. P. Graves. Sawtooth pacing by real-time auxiliary power control in a tokamak plasma. *Physical Review Letters*, 106(24):15–18, 2011.

[61] A. Mück, et al. Sawtooth control experiments on ASDEX Upgrade. *Plasma Physics and Controlled Fusion*, 47(10):1633–1655, 2005.

[62] I. T. Chapman, et al. The effect of off-axis neutral beam injection on sawtooth stability in ASDEX Upgrade and Mega-Ampere Spherical Tokamak. *Physics of Plasmas*, 16(7), 2009.

[63] Ya. I. Kolesnichenko, V. V. Lutsenko, Y. V. Yakovenko, and G. Kamelander. Theory of fast ion transport induced by sawtooth oscillations: Overview and new results. *Physics of Plasmas*, 4(7):2544–2554, 1997.

[64] S. K. Nielsen, et al. Fast-ion redistribution due to sawtooth crash in the TEXTOR tokamak measured by collective Thomson scattering. *Plasma Physics and Controlled Fusion*, 52(9):092001, 2010.

[65] B. Geiger, et al. Fast-ion D-alpha measurements at ASDEX Upgrade. *Plasma Physics and Controlled Fusion*, 53(6):65010, 2011.

[66] B. Geiger, et al. Fast-ion transport in the presence of magnetic reconnection induced by sawtooth oscillations in ASDEX Upgrade. *Nuclear Fusion*, 54(2):022005, 2014.

[67] L. Chen, R. B. White, and M. N. Rosenbluth. Excitation of internal kink modes by trapped energetic beam ions. *Physical Review Letters*, 52(13):1122–1125, 1984.

[68] A. Bock. *Correlation analysis methods for real-time localisation of magnetic islands in fusion plasmas*. Diplomarbeit, Technische Universität München, 2012.

[69] M. Reich, A. Bock, M. Maraschek, and the ASDEX Upgrade Team. NTM localization by correlation of the Te and dB/dt. *Fusion Science and Technology*, 61(May 2012):309 – 313, 2012.

[70] F. Felici, et al. Integrated real-time control of MHD instabilities using multi-beam ECRH/ECCD systems on TCV. *Nuclear Fusion*, 52(7):074001, 2012.

[71] M. García-Muñoz, et al. NTM induced fast ion losses in ASDEX Upgrade. *Nuclear Fusion*, 47(7):L10–L15, 2007.

[72] M. Gobbin, et al. Numerical simulations of fast ion loss measurements induced by magnetic islands in the ASDEX Upgrade tokamak. *Nuclear Fusion*, 49(9):095021, 2009.

[73] A. Herrmann and O. Gruber. ASDEX Upgrade - Introduction and Overview. *Fusion Science and Techology*, 44(3):569–577, 2003.

[74] E. R. Müller, K. Behringer, and H. Niedermeyer. Radiation losses and global energy balance for Ohmically heated discharges in ASDEX. *Nuclear Fusion*, 22(12):1651, 1982.

[75] M. Keilhacker and The ASDEX Team. The ASDEX Divertor Tokamak. *Nuclear Fusion*, 25(9):1045–1054, 1985.

[76] O. Vollmer, et al. Commissioning and performance of the new ASDEX Upgrade Neutral Beam Injector. In *SOFT Marsaille*, 1998.

[77] B. Streibl, P. T. Lang, F. Leuterer, J. M. Noterdaeme, and A. Stäbler. Machine design, fueling, and heating in ASDEX Upgrade. *Fusion Science and Technology*, 44(3):578–592, 2003.

[78] D. Wagner, et al. Present status of the new multifrequency ECRH system for ASDEX Upgrade. *IEEE Transactions on Plasma Science*, 36(2 PART 1):324–331, 2008.

[79] L. Giannone, et al. A data acquisition system for real-time magnetic equilibrium reconstruction on ASDEX Upgrade and its application to NTM stabilization experiments. *Fusion Engineering and Design*, 88(12):3299–3311, 2013.

[80] L. Giannone, et al. Real-time diamagnetic flux measurements on ASDEX Upgrade. *Review of Scientific Instruments*, 87(5):1–18, 2016.

[81] A. Mlynek, et al. Design of a digital multiradian phase detector and its application in fusion plasma interferometry. *Review of Scientific Instruments*, 81(3), 2010.

[82] A. Mlynek, L. Casali, O. Ford, and H. Eixenberger. Fringe jump analysis and implementation of polarimetry on the ASDEX Upgrade DCN interferometer. *Review of Scientific Instruments*, 85(11):1–5, 2014.

[83] W. Suttrop and A. G. Peeters. Practical Limitations to Plasma Edge Electron Temperature measurements by Radiometry of Electron Cyclotron Emission, 1996.

[84] S. K. Rathgeber, et al. Estimation of edge electron temperature profiles via forward modelling of the electron cyclotron radiation transport at ASDEX Upgrade. *Plasma Physics and Controlled Fusion*, 55(2):025004, 2013.

[85] B. Kurzan and H. D. Murmann. Edge and core Thomson scattering systems and their calibration on the ASDEX Upgrade tokamak. *Review of Scientific Instruments*, 82(10), 2011.

[86] R. J. Fonck, D. S. Darrow, and K. P. Jaehnig. Determination of plasma-ion velocity distribution via charge-exchange recombination spectroscopy. *Physical Review A*, 29(6):3288–3309, 1984.

[87] S. K. Rathgeber, et al. Estimation of profiles of the effective ion charge at ASDEX Upgrade with Integrated Data Analysis. *Plasma Physics and Controlled Fusion*, 52(9):095008, 2010.

[88] P. J. MC Carthy, W. Schneider, and P. Martin. The CLISTE Interpretive Equilibrium Code. *IPP Report 5/85*, 1999.

[89] R. Fischer, C. J. Fuchs, B. Kurzan, W. Suttrop, and E. Wolfrum. Integrated data analysis of profile diagnostics at ASDEX Upgrade. *Fusion Science and Technology*, 58(2):675–684, 2010.

[90] W. W. Heidbrink, D. Liu, Y. Luo, E. Ruskov, and B. Geiger. A code that simulates fast-ion Dα and neutral particle measurements. *Communications in Computational Physics*, 10(3):716–741, 2011.

[91] M. Weiland, et al. Enhancement of the FIDA diagnostic at ASDEX Upgrade for velocity space tomography. *Plasma Physics and Controlled Fusion*, 58(2):025012, 2016.

[92] R.C. Wolf, et al. Motional Stark Effect measurements of the local magnetic field in high temperature fusion plasmas. *Journal of Instrumentation*, 10(10):P10008–P10008, 2015.

[93] J. C. Kemp. Polarized light and its interaction with modulating devices. *Hinds Instruments, Inc., Hillsboro, OR*, page 27, 1987.

[94] Nikon Metrology. MCAx - Premium portable technology, 2017.

[95] T. Löbhard. *Kalibrierverfahren für die Motional Stark Effekt Diagnostik am Fusionsexperiment ASDEX Upgrade.* Diplomarbeit, Technische Universität München, 2011.

[96] R. T. Mumgaard. Engineering Upgrades to the Motional Stark Effect Diagnostic. Master thesis, Massachusetts Institute of Technology, 2015.

[97] R. T. Mumgaard. *Lower Hybrid Current Drive on Alcator C-Mod : Measurements with an Upgraded MSE Diagnostic and Comparisons to Simulation.* PhD thesis, Massachusetts Institute of Technology, 2015.

[98] Thorlabs. 360 Degree Continuous Rotation Stage with Stepper Motor Actuator NR360S, 2017.

[99] B. S. Victor, et al. Asymmetries in the motional Stark effect emission on the DIII-D tokamak. *Review of Scientific Instruments*, 87(11):11E126, 2016.

[100] J.P.H.E. Ongena, I. Voitsekhovitch, M. Evrand, and D. McCune. Numerical Transport Codes. *Transactions of Fusion Science and Technology*, 61(1):180–189, 2012.

[101] R.J. Hawryluk. An empirical approach to tokamak transport, 1981.

[102] Princeton Universtity. transpweb.pppl.gov, 2017.

[103] T. Oikawa, et al. Benchmarking of neutral beam current drive codes as a basis for the integrated modeling for ITER. *Proc. 22nd Int. Conf. on Fusion Energy*, 22, 2008.

[104] A. Pankin, D. McCune, R. Andre, G. Bateman, and A. Kritz. The tokamak Monte Carlo fast ion module NUBEAM in the national transport code collaboration library. *Computer Physics Communications*, 159(3):157–184, 2004.

[105] Y. R. Lin-Liu and F. L. Hinton. Trapped electron correction to beam driven current in general tokamak equilibria. *Physics of Plasmas*, 4(11):4179, 1997.

[106] S. P. Hirshman. Neoclassical current in a toroidally-confined multispecies plasma. *Physics of Fluids*, 1295(May 2013), 1978.

[107] S. P. Hirshman and D. J. Sigmar. Neoclassical transport of impurities in tokamak plasmas. *Nuclear Fusion*, 21(9):1079, 1981.

[108] S. P. Hirshman. Finite-aspect-ratio effects on the bootstrap current in tokamaks. *Physics of Fluids*, 31(10):3150–3152, 1988.

[109] M. Kraus. *Heiz- und Stromprofile bei Neutralteilcheninjektion in Tokamakplasmen.* Diplomarbeit, Technische Universität München, 2010.

[110] G. G. Lister. Fafner-a fully 3-d neutral beam injection code using monte carlo methods. 1985.

[111] M. Weiland. *Influence of RF heating and MHD instabilities on the fast-ion distribution in ASDEX Upgrade.* PhD thesis, Ludwig-Maximilians-Universität Muenchen, 2016.

[112] F. L. Hinton and R. D. Hazeltine. Theory of Plasma Transport in Toroidal Confinements Systems. *Rev. Mod. Phys.*, 48(2):239–308, 1976.

[113] M. N. Rosenbluth and R. D. Hazeltine. Plasma transport in Troidal confinement systems. *Physics of Fluids*, 15:116, 1972.

[114] T. Suzuki, et al. Experimental investigation and validation of neutral beam current drive for ITER through ITPA Joint Experiments. *Nuclear Fusion*, 51(8):083020, 2011.

[115] B. Sieglin, et al. Real time capable infrared thermography for ASDEX Upgrade. *Review of Scientific Instruments*, 86(11), 2015.

[116] T. Kalvas, et al. IBSIMU: A three-dimensional simulation software for charged particle optics. *Review of Scientific Instruments*, 81(2):16–19, 2010.

[117] F. Mink. Verbesserung der Bestimmung von Speziesverteilung und Strahlgeomet-

rie der Neutralinjektion an ASDEX Upgrade. Master's thesis, Ludwig-Maximilians-Universität, 2014.

[118] T. Lunt, et al. A new 3D viewer as an interface between the ASDEX Upgrade CAD models and data from plasma modelling and experiment. *Nuclear Instruments and Methods in Physics Research Section A: Accelerators, Spectrometers, Detectors and Associated Equipment*, 623(2):812–814, 2010.

[119] S. Martinov, et al. Three novel software tools for ASDEX Upgrade. *Fusion Engineering and Design*, 112:839–844, 2016.

[120] G. L. Bretthorst. *Bayesian spectrum analysis and parameter estimation*, volume 48. Springer Science & Business Media, 2013.

[121] W. Zwingmann, L.-G. Eriksson, and P. Stubberfield. Equilibrium analysis of tokamak discharges with anisotropic pressure. *Plasma Physics and Controlled Fusion*, 43(11):1441–1456, 2001.

[122] A. Evangelias and G. N. Throumoulopoulos. Axisymmetric equilibria with pressure anisotropy and plasma flow. *Plasma Physics and Controlled Fusion*, 58(4):045022, 2016.

[123] M. Fitzgerald, L. C. Appel, and M.J. Hole. EFIT tokamak equilibria with toroidal flow and anisotropic pressure using the two-temperature guiding-centre plasma. *Nuclear Fusion*, 53(11):113040, 2013.

[124] Z. S. Qu, M. Fitzgerald, and M. J. Hole. Analysing the impact of anisotropy pressure on tokamak equilibria. *Plasma Physics and Controlled Fusion*, 56(7):075007, 2014.

[125] O. M. Jones, et al. Fast-ion deuterium alpha spectroscopic observations of the effects of fishbones in the Mega-Ampere Spherical Tokamak. *Plasma Physics and Controlled Fusion*, 55(8):085009(10), 2013.

[126] T. Kass, et al. The fishbone instability in ASDEX Upgrade. *Nuclear Fusion*, 38(6):807–819, 1998.

[127] C. Perez von Thun, et al. Study of fast-ion transport induced by fishbones on JET. *Nuclear Fusion*, 52(9):094010, 2012.

[128] C.C. Petty, et al. High-beta, steady-state hybrid scenario on DIII-D. *Nuclear Fusion*, 56(1):016016, 2016.

[129] S. D. Pinches, et al. The HAGIS self-consistent nonlinear wave-particle interaction model. *Computer Physics Communications*, 111:133–149, 1998.

[130] J. A. Heikkinen and S. K. Sipilae. Power transfer and current generation of fast ions with large-kθ waves in tokamak plasmas. *Physics of Plasmas*, 2(10):3724, 1995.

[131] F. Jenko, W. Dorland, M. Kotschenreuther, and B. N. Rogers. Electron temperature gradient driven turbulence. *Physics of Plasmas*, 7(5):1904–1910, 2000.

[132] F. Jenko. genecode.org, 2017.

[133] N.N. Gorelenkov, S.D. Pinches, and K. Toi. Energetic particle physics in fusion research in preparation for burning plasma experiments. *Nuclear Fusion*, 54(12):125001, 2014.

[134] G. Y. Fu, et al. Global hybrid simulations of energetic particle effects on the n=1 mode in tokamaks: Internal kink and fishbone instability. *Physics of Plasmas*, 13(5):052517, 2006.

[135] B. Hu, R. Betti, and J. Manickam. Kinetic stability of the internal kink mode in ITER. *Physics of Plasmas*, 13(11):112505, 2006.

[136] M. Albergante, J. P. Graves, A. Fasoli, F. Jenko, and T. Dannert. Anomalous transport of energetic particles in ITER relevant scenarios. *Physics of Plasmas*, 16(11):112301, 2009.

[137] H. Zohm, et al. On the physics guidelines for a tokamak DEMO. *Nuclear Fusion*, 53(7):073019, 2013.

[138] F. Turco, et al. The high-βN hybrid scenario for ITER and FNSF steady-state mission. *Physics of Plasmas*, 22(5):056113, 2015.

[139] Y. Sakamoto, et al. Development of reversed shear plasmas with high bootstrap current fraction towards reactor relevant regime in JT-60U. *Nuclear Fusion*, 49(9):095017, 2009.

[140] C. D. Challis, et al. Stability and confinement optimisation in the range q0=1-3 at JET. *36th EPS Conference on Plasma Physics*, 33E:2–5, 2009.

[141] B. N. Wan, et al. Overview of EAST Experiments on the Development of High-Performance Steady-State Scenario. In *26th IAEA Fusion Energy Conference proceedings*, pages OV/2–2, 2016.

[142] Y.-K. Oh, et al. Overview of the KSTAR Research in Support of ITER and DEMO. In *26th IAEA Fusion Energy Conference proceedings*, volume 95, pages OV/2–4, 2016.

[143] A. Bock, et al. Non-Inductive Improved H-Mode Operation at ASDEX Upgrade. *Nuclear Fusion*, submitted, 2017.

[144] V. Mukhovatov, et al. Overview of physics basis for ITER. *Plasma Physics and Controlled Fusion*, 45(12A):A235–A252, 2003.

[145] R. Fischer, et al. Validation of the ohmic, neutral beam and bootstrap currents in non-inductive scenarios at ASDEX Upgrade. In *44th EPS Conference on Plasma Physics*, page P4.133, 2017.

[146] G. M. Staebler and F. L. Hinton. Currents in the scrape-off layer of diverted tokamaks. *Nuclear Fusion*, 29(10):1820–1824, 1989.

[147] P. J. Harbour. Current Flow Parallel to the Field in a Scrape-Off Layer. *Contributions to Plasma Physics*, 28(4-5):417–419, 1988.

[148] R. Hager and C. S. Chang. Gyrokinetic neoclassical study of the bootstrap current in the tokamak edge pedestal with fully non-linear Coulomb collisions. *Physics of*

Plasmas, 23(4), 2016.

[149] T Oikawa, et al. Reactor relevant current drive and heating by N-NBI on JT-60U. *Nuclear Fusion*, 41(11):1575–1583, 2001.

[150] P. A. Politzer. The bootstrap current and neutral beam current drive in DIII-D. *Fusion Science and Technology*, 48(2):1170–1177, 2005.

[151] C. B. Forest. Determination of the Noninductive Current Profile in Tokamak Plasmas. *Physical Review Letters*, 73(18):2444, 1994.

[152] E. L. Foley, F. M. Levinton, H. Y. Yuh, and L. E. Zakharov. The motional Stark effect diagnostic for ITER using a line-shift approach. *Review of Scientific Instruments*, 79(10):10F521, 2008.

[153] M. A. Makowski, et al. Optimization of the optical design of the ITER MSE diagnostic. *Review of Scientific Instruments*, 79(10):10F519, 2008.

[154] W. Kabsch. A solution for the best rotation to relate two sets of vectors. *Acta Crystallographica Section A*, 32(5):922–923, 1976.

[155] W. Kabsch. A discussion of the solution for the best rotation to relate two sets of vectors. *Acta Crystallographica Section A*, 34:827–828, 1978.

[156] Raspberry Pi Foundation. Raspberry Pi 3 Model B - Raspberry Pi, 2017.

Acknowledgements

In den Jahren, die ich mit der Erarbeitung der Inhalte und der Anfertigung dieser Dissertation verbracht habe, bin ich von vielen Personen in vielfältiger Weise unterstützt worden. Ohne sie wäre diese Arbeit gar nicht möglich gewesen. Deswegen möchte ich mich final nochmal bei all diesen Menschen bedanken. Im Speziellen danke ich:

- Frau **Prof. Dr.-Ing. Ursel Fantz** für die Möglichkeit, die Arbeit am Max-Planck-Institut für Plasmaphysik anzufertigen und für das kritische und detaillierte Hinterfragen meiner Ergebnisse und deren Darstellung.
- Herrn **Prof. Dr. Helmut Karl** für die Übernahme des Zweitgutachtens.
- **Dr. Christian Hopf** für die exzellente Betreuung, die stets offene Tür, die investierte Zeit und dafür, dass er mir immer wieder den richtigen Weg gewiesen hat.
- **Dr. Alexander Bock**, **Dr. Niek den Harder** und **Dr. Andreas Burckhart**, dass sie mir im wissenschaftlichen Diskurs neue Wege aufgezeigt und mir immer freundschaftlich unterstützend zur Seite gestanden haben.
- **Dr. Benedikt Geiger**, **Dr. Rainer Fischer** und **Dr. Giovanni Tardini** für ihre Hilfestellung bei der Formulierung und Lösung meiner wissenschaftlichen Fragestellungen und die produktive, zielführende Zusammenarbeit.
- dem gesamten **ASDEX Upgrade Team** und im Speziellen **Dr. Matthias Reich**, **Dr. Francouis Ryter**, **Dr. Jörg Stober**, **Dr. Alexander Mlynek**, **Dr. Markus Weiland**, **Dr. Louis Giannone** und **Dr. Valentin Igochine**, da die gesamte Arbeit nur durch die Zusammenarbeit mit diesen extrem hilfsbereiten Menschen möglich gewesen ist.
- **Josef Schäffler**, **Johannes Thalhammer**, **Josef Deimel** und **Erich Kühn** die für eine überragende Zuverlässigkeit der Neutralteilchen Injektion an ASDEX Upgrade sorgen und ohne die an erfolgreiche Experimente gar nicht zu denken wäre.
- der **ITED NNBI Gruppe** für den wiederholten gewinnbringenden wissenschaftlichen Diskurs und das Hinterfragen meiner Resultate aus einer anderen Perspektive.
- **Alexander Lebschy**, **Felician Mink** und **Dr. Florian Laggner** dafür, dass sie in meiner Zeit am IPP immer wieder für interessante Abwechslungen gesorgt haben, inklusive mehrerer einzigartiger Highlights.

Mein besonderer Dank gilt auch meiner Familie für ihren Beistand und natürlich auch meiner Freundin Claudia Hühn, die mich während der gesamten Zeit immer wieder ermutigt und unterstützt hat, meine Arbeit zu einem erfolgreichen Abschluss zu führen.

A. Appendix: MSE

A.1. Line of Sight Measurement

The precise knowledge of the line of sight geometry of the MSE system and the beam geometry is crucial for a correct interpretation of the MSE angles. For example is the MSE angles are used as a constraint for an equilibrium reconstruction or as input for the construction of a synthetic MSE diagnostic. Since the usual way of measuring the line of sight geometry is time consuming and the precision is not high enough, a new setup was designed. This setup was developed, a prototype was constructed and successfully tested. The measurement with the prototype can be seen in figure A.1 a).
The measurement takes place, like the conventional approach, during a maintenance opening of the vessel. For the measurement of a line of sight inside ASDEX Upgrade the fibers are illuminated from the detector side. The line of sight is now visible as a light beam in the torus. In the conventional approach these light beams were measured by aiming the pike of the probe of a Nikon 3D-joint-measurement arm MCAx30+ [94] to a light spot onto a mounted plate in the vessel. In this case the precision is determined by the eyesight and steadiness of the operator. In combination with spot diameters of several centimeters this can be improved. Additionally it is time consuming to aim and mount the plate at several positions.
To increase the accuracy, a new probe-head for the Nikon 3D-joint-Measurement-arm was designed. The main idea is to simultaneously measure the position and orientation of the new probe head and the position of the light spot on the probe head. To achieve the latter, the probe head has a camera looking onto a milky Plexiglas screen with a coordinate grid. The procedure can be seen in figure A.1 a). The positions of the grid points are measured during a calibration with respect to the measured probe-head position and its orientation. In post processing the position on the screen in the picture can be translated to the measurement position in the torus. A red light source is used and therefore only the red part of the image is used to find the position of the spot. An example can be seen in figure A.1 c), while A.1 b) shows the real picture with a magnified intensity of all color components by a factor of three.
A detailed description of the calibration of the setup and the way to translate the pixel position in a post processed picture to a measurement position can be found in Appendix A.2.
In figure A.2 a) a comparison between measurements in the usual way and with the new setup can be seen. In figure A.2 b) the angle between the direction vectors can be seen determined by the two different methods. With an average value of 0.16° this difference is

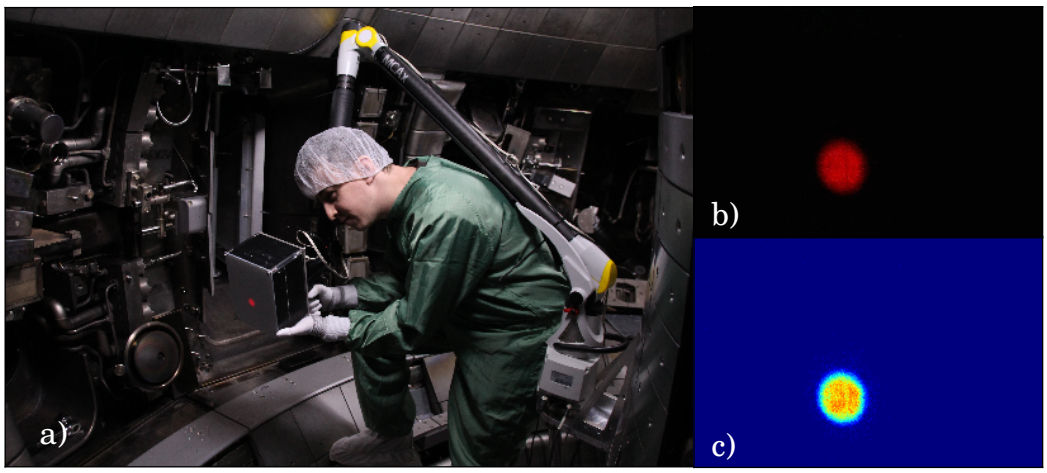

Figure A.1.: a) In-vessel measurement of a line of sight with the prototype setup. b) Captured picture and c) red component of the picture to evaluate, in pixels, the position and the extent of the line of sight.

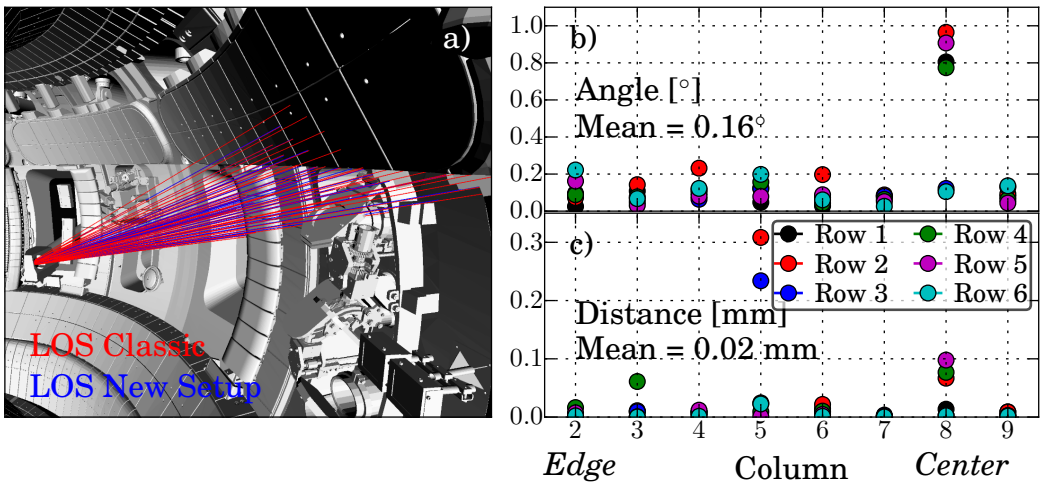

Figure A.2.: Comparison of the MSE lines of sight measured with the different methods. a) The red lines of sight corresponds to the measurement with classical technique and depicted in blue are the measurements with the new setup. In b) the enclosed angle between the corresponding direction vectors of the lines of sight and in c) the minimum distance between the corresponding lines of sight can be seen.

small and also the average minimum distance of 0.02 mm from figure A.2 c) shows good agreement between the two techniques. The trustworthiness of the old technique is only based on a comparison with former measurements, but in the case of deviations, there is no possibility to decide which measurement is right, unless the measurement is repeated. This repetition is only possible in a maintenance break and is very time consuming. Furthermore in this example the deviation for column 8 can be a hint for single and inaccurately measured points on these lines of sight with the classical technique. As there are only three points and no recorded pictures, it is impossible in post processing to identify and eliminate the inaccurately measured points.
Some lines of sight are not used for the MSE as for example the lines of sight in column 1 and column 10 are partially masked by the opening of the mirror box. These lines of sight are no longer used and also not evaluated. Example pictures showing the masking of them can be seen in appendix A.3 figure A.6. This is also a benefit from the new setup that it allows to document in the post processing the shape of the light beams and found deviations between the different lines of sight. Additionally the rows 1 and 6 with the largest distance to the beam axis are not used for the MSE diagnostic. This is due to the fact that, on the one hand, row 6 is used for FIDA measurements and, on the other hand, the number of detectors is limited, therefore the central channels with a higher signal level are used instead of the bottom row 1.
In figure A.3 the uncertainties for the measured lines of sight can be seen. It should be noticed that the measurement with the classical method has a higher scatter, because for this technique only 3 points per line of sight were taken. For the new technique at least 4 and up to 6 points were measured and fitted, but the scatter is much lower. The mean distance to the fitted line as well as the maximum distance to the fitted line is a factor 2 smaller for the new technique. Additionally it takes the same amount of time to measure 6 points per line of sight with the new technique, instead of 3 with the old technique. This is an important advantage, as working time in the open vessel is a scarce resource .
During the first measurements of the MSE lines of sight, several potential improvements and small issues appeared. This should be fixed for the next iteration and thus further decrease the uncertainties. A description of these improvements can be found in the following section A.4.

A.2. Postprocessing and Calibration of the New Line of Sight Measurement

The transfer function from pixel position to real position is based on a characterization of the setup in a lab measurement. Here the setup is fixed on a table and in a first step the Nikon 3D-joint-measurement-arm is connected to the setup to measure the reference position and the corresponding direction vectors, as can be seen in figure A.4 a). Afterwards the Nikon 3D-joint-measurement-arm is used to measure several points on the screen of the still fixed setup. The simultaneously taken pictures of the camera where used to match the grid points

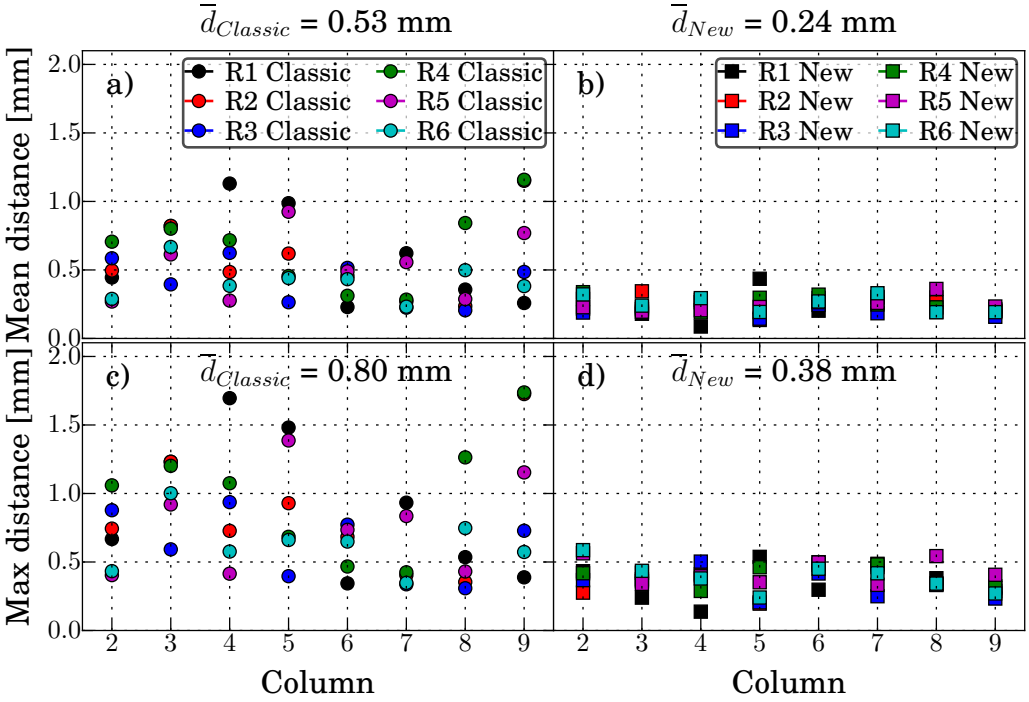

Figure A.3.: The mean distance of the measured points to the line of sight fitted with these measured point for the classical technique can be seen in a) and for the new setup in b). In c) and d) the maximum distance of the measured point to the fitted line can be seen. The uncertainty decreases by approximately a factor of 2 with the new technique.

in the picture, using the same coordinate system. This step can be seen in figure A.4 b).

This measurement is used to calculate two corresponding equations of the plane. The first one in 2D for the pixels in the image can be expressed as

$$\begin{pmatrix} x_{pix} \\ y_{pix} \end{pmatrix} = \begin{pmatrix} x_{0,pix} \\ y_{0,pix} \end{pmatrix} + a \cdot \begin{pmatrix} x_{1,pix} - x_{0,pix} \\ y_{1,pix} - y_{0,pix} \end{pmatrix} + b \cdot \begin{pmatrix} x_{2,pix} - x_{0,pix} \\ y_{2,pix} - y_{0,pix} \end{pmatrix} \tag{A.1}$$

with $\vec{x}_{0,pix}$, $\vec{x}_{1,pix}$ and $\vec{x}_{2,pix}$ three arbitrarily measured points on the plane which form linear independent vectors. $\vec{x}_{pix}$ is the searched pixel position, which can be expressed by a dedicated combination of the two scalars a and b. The second equation of plane is in 3D with the corresponding measured xyz positions to the three chosen pixel points with the same scalar values a and b for the corresponding xyz position to $\vec{x}_{pix}$

$$\begin{pmatrix} x \\ y \\ z \end{pmatrix} = \begin{pmatrix} x_0 \\ y_0 \\ z_0 \end{pmatrix} + a \cdot \begin{pmatrix} x_1 - x_0 \\ y_1 - y_0 \\ z_1 - z_0 \end{pmatrix} + b \cdot \begin{pmatrix} x_2 - x_0 \\ y_2 - y_0 \\ z_2 - z_0 \end{pmatrix}. \tag{A.2}$$

To minimize the uncertainties, the measured xyz positions are corrected along the plane normal to be in the fitted plane. The mean distance to the plane is 0.07 mm and the maximum distance is 0.3 mm within 70 measured points. Additionally the vectors $\vec{x}_{0,xyz}$, $\vec{x}_{1,xyz}$

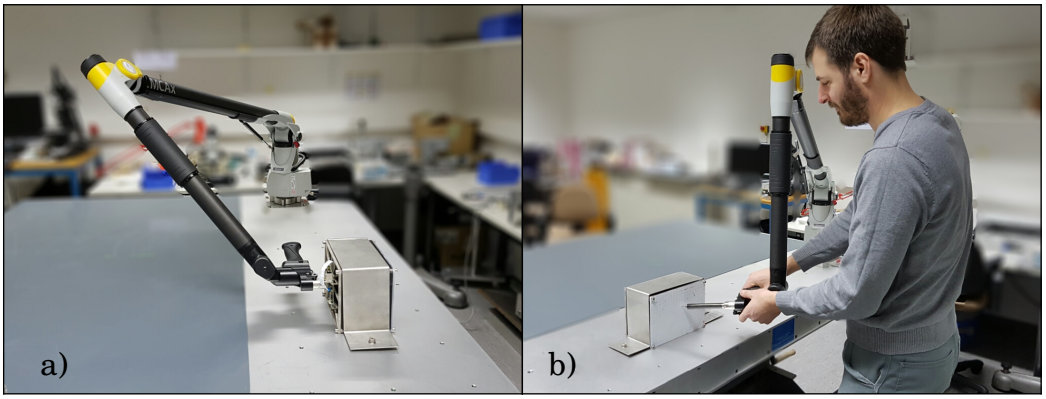

Figure A.4.: a) Measurement of the reference position and direction vectors with the setup fixed on a table. b) Measurement of grid points on the screen with simultaneously taken pictures to get the corresponding pixel position.

and $\vec{x}_{2,xyz}$ are expressed by the reference zero position of the arm added by a characteristic combination of the measured reference direction vectors.

$$\vec{x} = \vec{x}_{0,ref} + r \cdot \vec{x}_{x,ref} + s \cdot \vec{x}_{y,ref} + t \cdot \vec{x}_{z,ref} \tag{A.3}$$

By solving the equations (A.1) for a and b and calculation of equation (A.2) with these scalars it is possible to calculate the xyz position for every pixel position. With equation (A.3) the vectors can be transformed from the lab system to any arbitrary coordinate system.
Since the ratio between the distance of the camera to the screen and the diameter of the screen is small, a fish-eye camera was used. For a correct use the fish-eye and other distortions have to be corrected. This correction was achieved by a 5th-order 2D-interpolation of the distorted grid lines to a corresponding rectangular grid. An example of the correction can be seen in A.5.

In a last step the transformation of the Nikon 3D-joint-measurement-arm coordinate system to the ASDEX Upgrade coordinate was made. For this, multiple known points in the torus were measured with a corresponding probe head simultaneously measuring the corresponding vectors of the probe head holder. These vectors of the probe head holder at used to localise the new probe head. The measured points were used to express the transfer function using the Kabsch algorithm [154, 155]. This transfer function is used to translate the probe head vectors into the ASDEX Upgrade coordinate system.

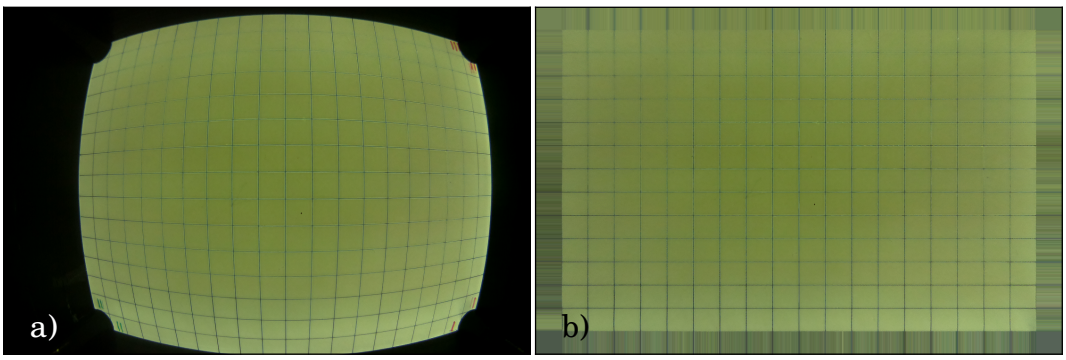

Figure A.5.: Distortion correction with a 2D-interpolation by an 5th-order spline fit. a) The uncorrected camera picture of the illuminated screen and b) same image after the correction.

A.3. Bad Lines of Sight of the MSE System

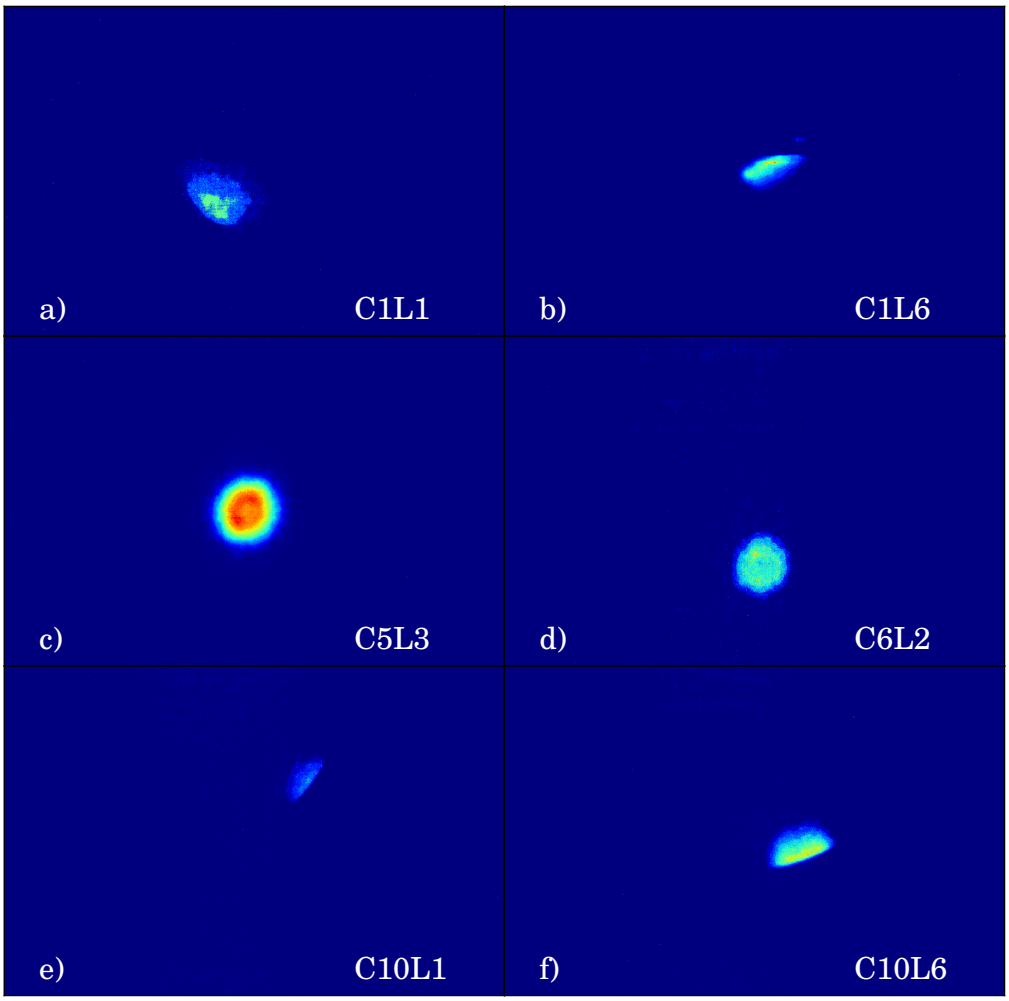

Figure A.6.: Red componend of example measurements of 6 mostly bad and therfore not used MSE lines of sight. c) is a useful example with a circular spot. d) has a much lower intensity and is therefore not useful, maybe due to a broken fiber. a), b), e) and f) have the problem that the light beam is partially masked by the mirror box.

A.4. Improvement Potentials for the Next LOS Prototype

During the first measurements of the MSE lines of sight several potential improvements and small issues appeared. A possible way do strongly decrease the time necessary to measure all 48 lines of sight is a rearrangement of the order of measuring the lines of sight. Instead of measuring several distances to the mirror for one line of sight and afterwards going to the next line of sight, at similar distances all lines of sight are measured and then at a new distance to the mirror. A first test leads to promising results, but further tests are necessary.
An improvement to the accuracy of the measurement could be a redesign of the base plate of the setup. In the prototype it is an aluminium matrix, to reduce the weight of the probe head. Unfortunately the braces are too thin and therefore not stiff enough leading to a small deviation, ending up in possible systematic uncertainties. To overcome this deformation, the next setup will be made as a pyramid of aluminum for mechanical stabilization and protection from stray light onto the camera, which is realized in the prototype by a 3D-printed box.
Another issue is the latency of the camera. At the moment the camera is connected to a Raspberry Pi 3 Model B [156] and triggered and read out via a network connection from the laptop connected to the Nikon 3D-joint-measurement-arm. This lead to a delay of several 100 ms from the sending of the trigger to the moment taking the picture with an exposure time of ~ 30 ms. In the next iteration of the setup a new camera should be used with a higher sensitivity, to decrease the exposure time and connected via USB direct to the laptop avoiding the detour through the Raspberry Pi. The direct connection should reduce the time between the sending of the trigger and the triggering of the camera. The uncertainty due to small movements during the triggering of the setup within this time, should be decreased. Also the delay between two measurements, which is at the moment in the order of 10 seconds, should be reduced by replacing the Raspberry by with a direct USB-connection to the camera.

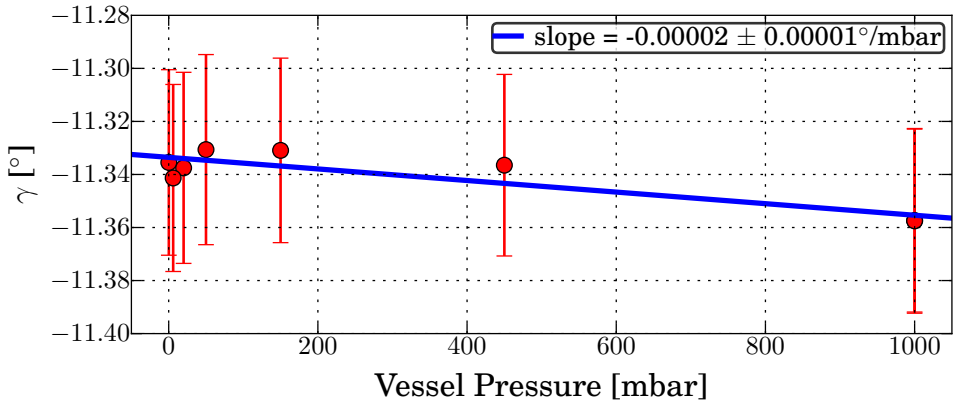

Figure A.7.: Measurement of polarization changes of an in-vessel lamp during the evacuation of ASDEX Upgrade.

A.5. Further Effects

A.5.1. Vacuum Effect

All calibration measurements are made in the vented torus. To investigate the influence of the vacuum on the polarization measurement, for example due to stress-induced birefringence, measurements were taken during the evacuation of ASDEX Upgrade. In figure A.7 the measured and non-linearly-corrected angle of a polarized in-vessel lamp versus the torus pressure can be seen.
In ASDEX Upgrade three in-vessel lamps are installed to test the diagnostic without plasma or investigate longterm stability. These lamps were upgraded during the maintenance opening of ASDEX Upgrade before the 2017 campaign. Until this maintenance break the polarization in the lamp was produced by reflection of fiber guided light on a metallic surface leading to a constant, but unknown polarization. The new design contains a polarizer that guarantees a constant polarization and allows to set a desired polarization during a maintenance break. The polarization was set to be in the range of the measured polarization of the plasma light.
One of these lamps was measured during the evacuation of the torus in preparation for the 2017 campaign. The change of $-0.02°$ during the change from the vented ($\sim$ 1000 mbar) to the mostly evacuated vessel ($\sim$1 mbar) is one order of magnitude smaller than the uncertainty of the measurement. Therefore the vacuum effect is negligible.

A.5.2. Long-term Stability

The stability of the MSE system was tested during the 2015/2016 campaign by measuring the light of the in-vessel lamp with similar boundary conditions. To avoid density and magnetic field effects the daily probe tests without plasma were used. These technical shots are

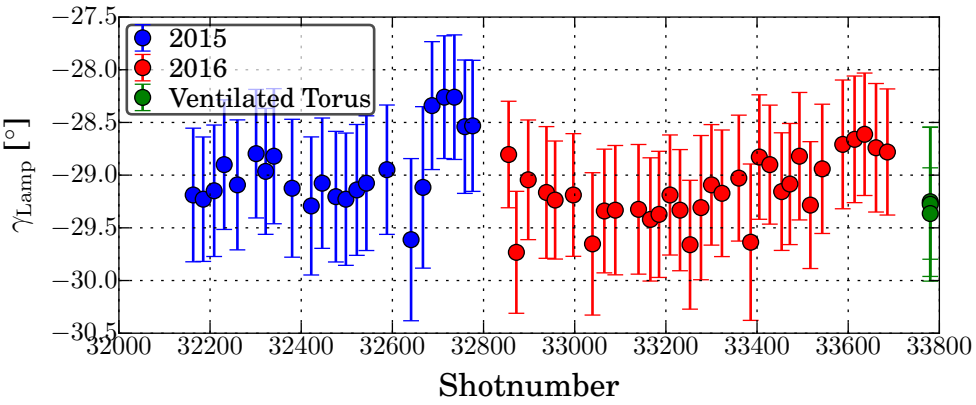

Figure A.8.: Averaged measurements of the polarized in-vessel light source in field and plasma-free probe tests, made every shot day for the 2015/2016 experimental campaign. In blue the probe tests from 2015 and in red the measurements in 2016. The green points are measurements of the same light source in the vented, field-free torus.

done in the beginning of each shot day, to perform a function test of a main part of the security related diagnostics and to test the toroidal field coils. Within 40 seconds multiple test are made. Amongst other things the toroidal field is ramped up to 1 T and back. The measurements shown here were taken in a field-free phase before the magnetic field ramp. In figure A.8 this scan over the full 2015/2016 campaign can be seen. Obviously there is a systematic drift, which is not linear, with a maximum angle change in the order of one degree. A possible explanation could be a coating of either the light source, for example during a boronization, or the first window during the plasma discharges. During the boronization process, the protection window is covered by a pneumatic shutter. A correlation test with temperature fluctuations in the torus hall due to different seasons was inconclusive. Another sign for coatings can be the drop of the angle after venting the torus. Here a possible thin coating can react with oxygen.
To tackle this problem, the three in-vessel lamps were upgraded with adjustable polarizer, described in section A.5.1. After the 2017 campaign they should additionally be equipped with different magnetic-field-sensitive shutters. The new polariser should guarantee constant polarization. If the drifts remains, the shutter should help to investigate the coating hypothesis of the lamps. While one lamp gets no shutter, the other two lamps get a shutter which is closed either with or without toroidal magnetic field. This guarantees that the two different cases are covered, either a drift caused by a coating during the boronization or a drift during coating or erosion caused by interaction with the plasma. The lamp without shutter can be used as reference. In the unlikely case of a shutter independent drift of all lamps, the reason must be placed on the diagnostic side.

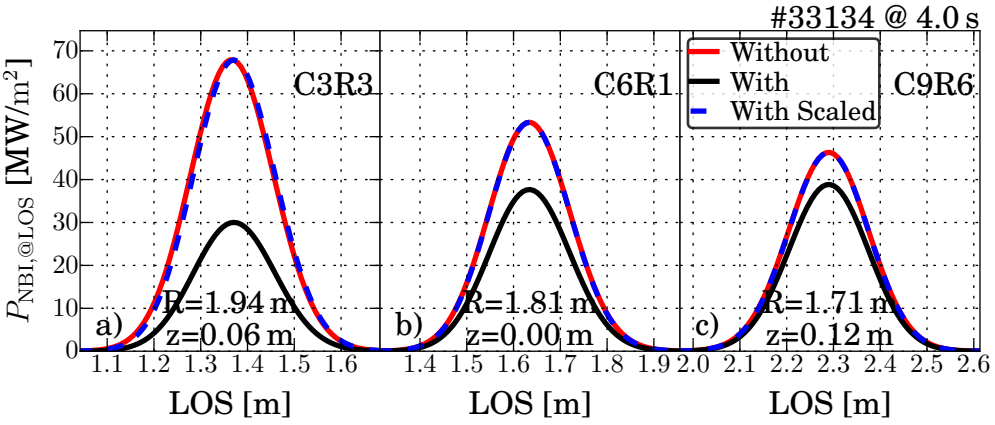

Figure A.9.: Beam power density along three different lines of sight of the MSE. In red calculated without beam attenuation and in black with beam attenuation for discharge #33134 at 4.0 s. The blue dashed lines are the calculations with beam attenuation scaled to the calculations without attenuation. The almost perfect agreement allows the neglecting of the beam attenuation.

A.5.3. Non Infinitesimal Beam Diameter

As written in section 3.2.1 and also visible in figure 4.3, the neutral beam 3 is a macroscopic object with a diameter on the order of several tenth of centimeters. To investigate the effect of the intersection of the lines of sight and the beam, the neutral beam power density along the lines of sight of the MSE is calculated, neglecting the beam attenuation along the beam axis. This is valid as the projection of the intersection to the beam axis is small, the result of the corresponding calculation can be seen in figure A.9. In a further step the expected MSE angles along the line of sight from an equilibrium of discharge #33134 are calculated. In figure A.10 the result for one line of sight can be seen. In figure A.10 a) in 2D the calculated time evolution of the MSE angle can be seen weighted with a color coded beam power density. Figure A.10 b) shows the power density of the neutral beam 3 along the line of sight versus the radial variable R and c) versus vertical variable z. The changes in R for this line of sight is smaller than 4 cm during the intersection with the beam at reasonable beam power densities. The change in z is in this case with 12 cm larger, but close to the mid-plane vertically the magnetic field vector is almost constant see reference [19]. Therefore the calculated angle spread is mainly from the change in R.
The MSE angle changes in a range of 0.5° for non-negligible beam power densities, for example higher than 10% of the maximum. For all lines of sight, the angle spread time averaged over the discharge versus the radial column can be seen in figure A.11 a). The minimum of 0.23° around column 6 can be explained by a minimum change in R during the beam intersection of these lines of sight.
The measured polarization is a superposition of all polarizations of the emitted light during the intersection with the beam. Due to the fact that the number of photons emitted from the beam corresponds with the power density, the expected angle is calculated as an average of the calculated angles in the Stokes vector weighted by the power density. The difference

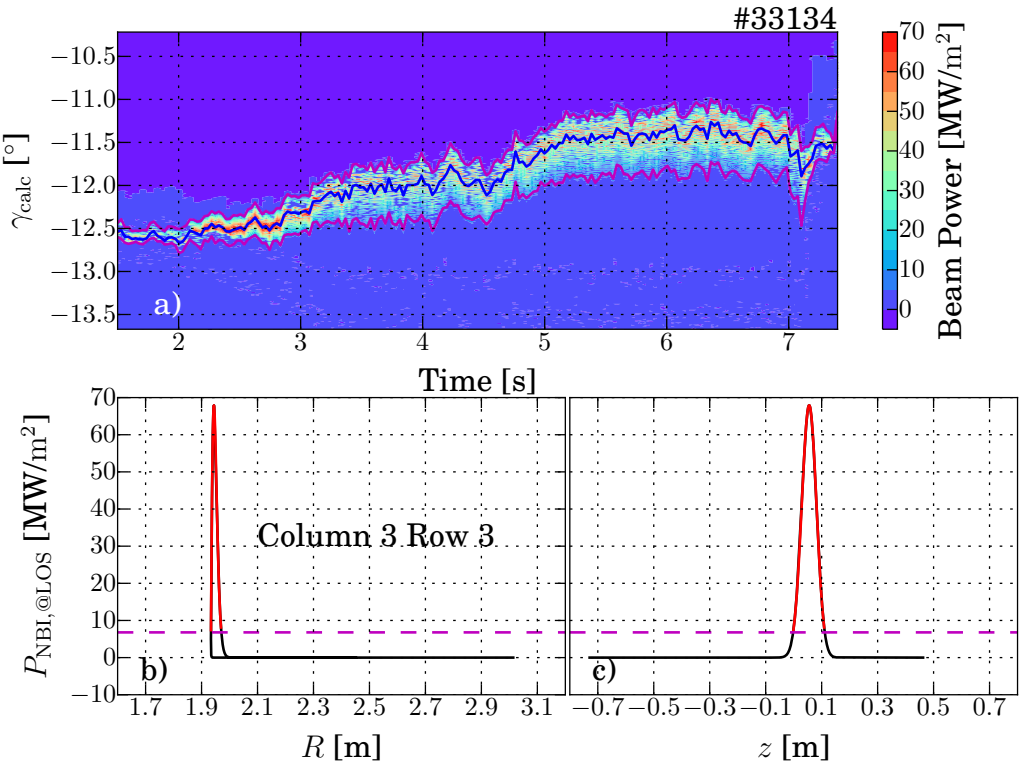

Figure A.10.: Expected MSE angle spread due to the non-infinitesimal beam diameter. a) The 2D calculation of the change of the MSE angles versus time from an equilibrium color coded weighted by the beam power density. b) Along the line of sight the beam power density versus R and in c) versus z.

to the calculated angles at the peak position can be seen in A.11 b). Towards the plasma center the deviation is increasing in this case, but the maximum deviation of 0.06° is well below the uncertainty of the measurement in the order of 0.2°. For an accurate comparison between measured and synthetic data from an equilibrium this has to be taken into account. Also in the equilibrium reconstruction constrained by the MSE this could have an effect. Nevertheless as long as the uncertainty of the measurement is much larger than this effect it can be neglected as higher order correction.

A.6. Polychromator

The polychromator is foreseen as replacement and upgrade for the photomultiplier based detector units. The polychromator system enables a parallel measurement of the π- and σ-component on a single line of sight. Furthermore the degree of polarization of the background radiation is measured, at wavelengths above and below the signal region. Assuming uniform polarization of the broadband background radiation and only linear wavelength dependence, the contribution of the polarized background in the signal region

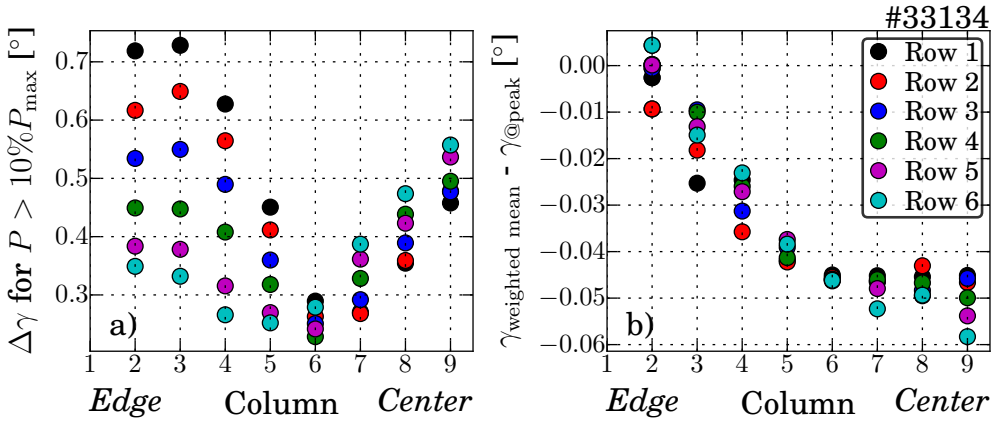

Figure A.11.: a) Time averaged the angle spread for reasonable beam power densities for all MSE lines of sight versus their radial column. b) The difference between the weighted mean in the Stokes components and the angle at the peak position.

can be interpolated and subtracted. The background is expected to be polarized due to polarizing reflection of light into a line of sight, for example from the divertor, on the metallic first wall. Such a polarized background was measured in the full metal first wall Tokamak Alcator C-MOD [96, 97], and there is also indication in ASDEX Upgrade for such background polarization [19].
The polychromator design used at ASDEX Upgrade is adapted from the one used at Alcator C-MOD. It was designed and constructed in cooperation with the MSE group of the MIT, developing, constructing and responsible for the MSE system of Alcator C-MOD. The optical design of the ASDEX Upgrade system is shown in the CAD drawing in figure A.12.

The light from four fibers, corresponding to four different lines of sight, is coupled into the polychromator. After a parallelizing collimating lens the light is reflected by an angled spherical mirror to the first detector unit next to the fiber input port. The first surface of the detector unit is a narrow band filter, transmitting only light in a 0.4 nm wide wavelength region and reflecting the remaining light. The path of light has an angle of incidence of $\sim 4°$ to the normal of the surface. The reflected light is mirrored on a second spherical mirror on the backside of the polychromator next to the first mirror towards the second detector unit. This back and forth reflection of light from a band pass filter and the mirrors to the next detector unit repeats three times. Four detector units get illuminated, cutting out a narrow part of the spectrum and reflecting the remaining light to the next detector unit.
The narrow band pass filter for the π- and σ-component are tunable in a narrow wavelength region by a feedback controlled temperature. Behind the filter an imaging lens focuses the light on the detector. In contrast to the MIT design, the image-preserving property of the optical system is used, to project the light of the single fibers on different quadrants of a 2x2 avalanche photodiode (APD) detector. This raytraced image on the different zones of the detector is shown in figure A.13 a).

The focusing lens can be seen in green on the left and the rays from the single fibers shown

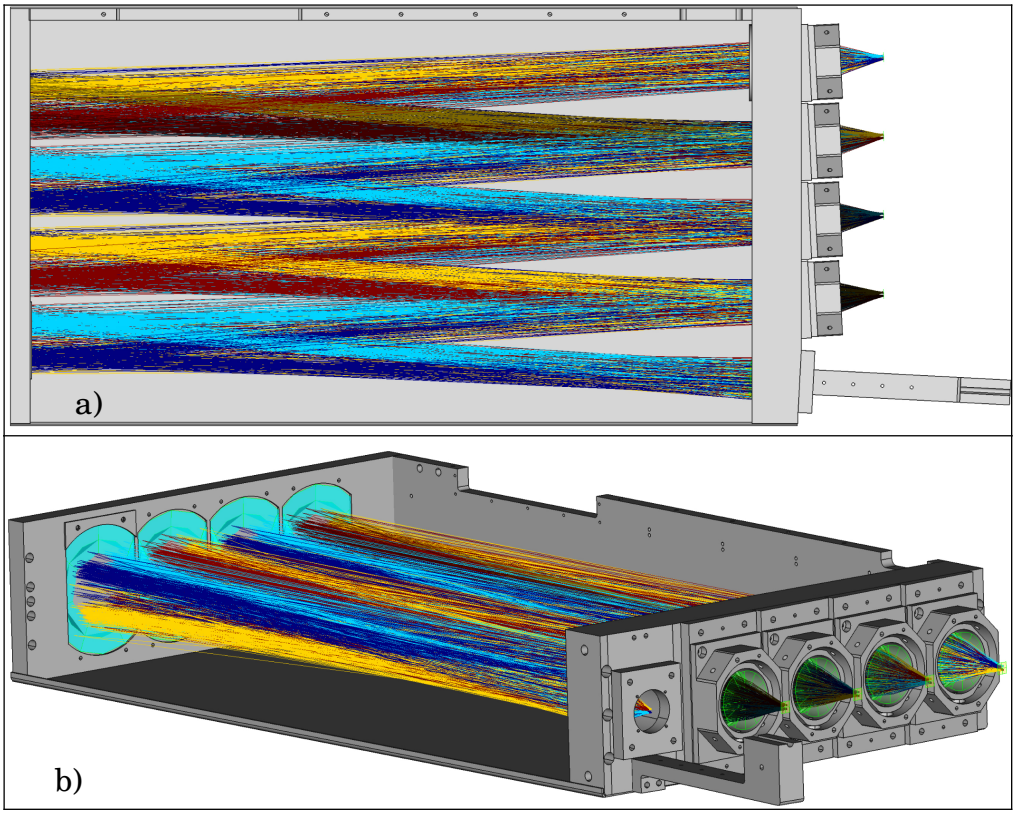

Figure A.12.: The mechanical and optical design of the ASDEX Upgrade polychromator. In the lower right corner is the fiber input, for four fibers. The light is relayed to and reflected on spherical mirrors mounted in the backplate, shown on the left side in b). The light is redirected to the detector units next to the input port. At the narrow band filter most of the light is reflected towards the next mirror and detector unit. The transmitted light in a dedicated wavelength region is focused after the filter onto the 2x2 APD detectors.

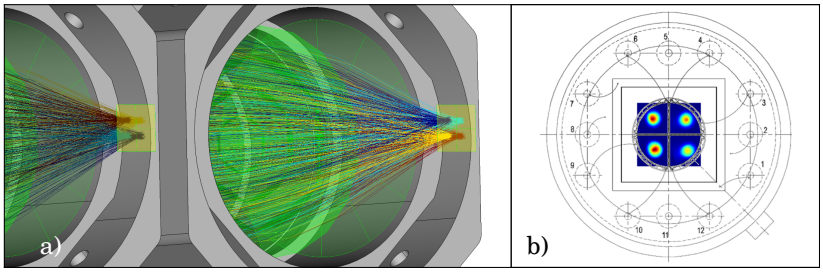

Figure A.13.: After the imaging lens behind the filter, the light of the different fibers is focused on separate detector quadrants. In a) the result from the raytracer for two different ports is shown. In b) a camera intensity measurement superimposed with a scaled drawing of the 2x2 APD detector can be seen.

in different colors are separated in the plane of the detector, indicated by the brownish squares. Figure A.13 b) shows a false color measurement from a camera mounted instead of the detector. This measurement is overlaid with a scaled drawing of the 2x2 APD detector. It shows good separation of the spots corresponding to the four fibers, with an expected crosstalk level in the single percent range. Furthermore the distance between the single spots is as expected from raytracing and fits on the different quadrants of the APD.
This enables the measurement of the light of individual lines of sight, so four lines of sight could be measured with each polychromator. This is possible at ASDEX Upgrade in contrast to Alcator C-Mod, where nine fibers are measured together on one APD. Because at ASDEX Upgrade a heating beam with 2.5 MW heating power is used for the MSE instead of a low power diagnostic beam. This leads to a higher number of emitted photons and in combination with the high sensitivity of the APD detectors the system is able to resolve the light of a single line of sight.
The possible combination of lines of sight simultaneously measurable in one polychromator is restricted by the transmitted wavelength through the tunable narrow bandpass filter. The angle of incidence of the light beam to the normal of the filter surface has a dominant influence on the transmitted wavelength. This transmitted wavelength could further be slightly adjusted by the temperature. The APDs are split in quadrants and the detectors and the input fiber holder are mounted in a way that the quadrants lying on top of each other are illuminated by light passing through the filter with the same angle of incidence. This two different angles of incidence at the filter are a consequence from the image-sustainability of the system. As the spherical mirrors reflecting light from some fibers on the left and of the other fibers on the right side, leading to a different reflection angle for the two groups. The angles of incidence to the normal of the filter surface of the two groups of lines of sight are $\sim 2.3°$ and $\sim 4.5°$. The wavelength shift from the angle change at the same temperature between the two different vertical groups enables the measurement on two radial positions. As the wavelength of the spectral lines are constant in wavelength along the vertical direction of the lines of sight, two lines of sight lying on top of each other are used at each of the two radial positions.
In figure A.14 measured emission spectra for one polychromator overlaid with the temperature optimized transmission curves of the four filters are shown.

In a) the transmission curves for the one fiber of the right vertical group is shown and in b) for both fibers of the left group. The background filters in green and orange are not tunable and have a wider transmission range. On the one hand the two fixed wavelength regions are chosen to be outside the Balmer α peak and its components and are also chosen to be in a region without interfering impurity lines. On the other hand the intensity of the polarized background emission is expected to be small with respect to the π- or σ-emission. Therefore to collect enough light from these wavelength regions the covered wavelength range of the filters is chosen to be wider.
The sequence of the filters in the different detector units is given by the different paths of light of the individual fibers. These paths could be approximated from figure A.12 and the alternating illumination of a quadrant from a single fiber in figure A.13 a). For example the light from the fiber indicated by the dark blue lines came from the lower right fiber of the fiber holder. After the reflection on the spherical mirror the lower right quadrant

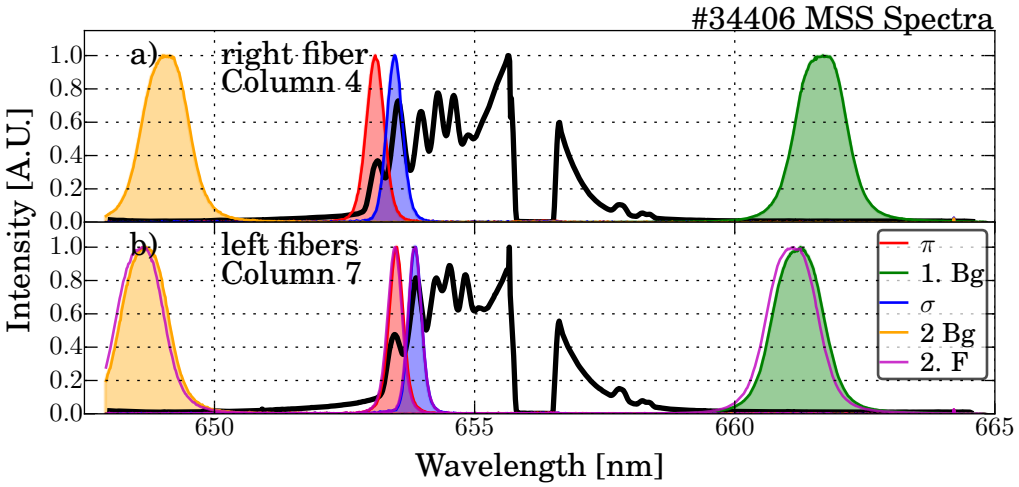

Figure A.14.: Measured filter transmission curves of one polychromator overlaid with measured spectra. In a) for one of the right fibers of the input fiber holder and in b) for the two left fibers. The second fiber is shown in magenta. The filter temperatures are optimized to measure on the columns 4 and 7.The spectra are measurements with the MSS spectrometer in discharge #34406 in the bottom row of the chosen columns.

of the first detector unit is illuminated. In the second detector unit this fiber illuminates the upper left quadrant and again the lower right in the detector unit three. In the last detector unit, like in the second one, the upper right quadrant is illuminated by the fiber shown in dark blue. As the behaviour is similar for the other fibers, the pattern is the same at every second detector unit and in between the diagonal quadrants are illuminated.
To the minimize the losses due to non-perfect reflectivity of the filters and mirrors in the signal region the first filter is chosen and tuned to the π component. Furthermore the π component is chosen first to suppress π emission in the later following σ measurement, because it is cut out. In the second detector unit the fibers are swapped, this leads to a change of the angles of incidence of the individual fibers. As the wavelength shift from the different angles of incidence is constant and also the temperature is only adjustable for the whole filter, it is not possible to measure the σ component in this detector unit. The wavelength shift could also be seen in the chosen background filters, shown in the different wavelength distance to the signal region in figure A.14. But due to the fact that the background is broadband the distance to the signal region does not hamper the measurement and ability to correct for the polarization of the background in the post processing. In the third detector unit the illuminated quadrants are the same as in the first detector unit. Therefore the σ component is measured corresponding to the π component from the first detector unit. In the fourth and last detector unit the second background filter is used.
Unfortunately during the first measurements an unintended not yet completely understood crosstalk between the different APD quadrands appears when illuminating with only one fiber. Therefore the first measurements to demonstrate the working principle are done with

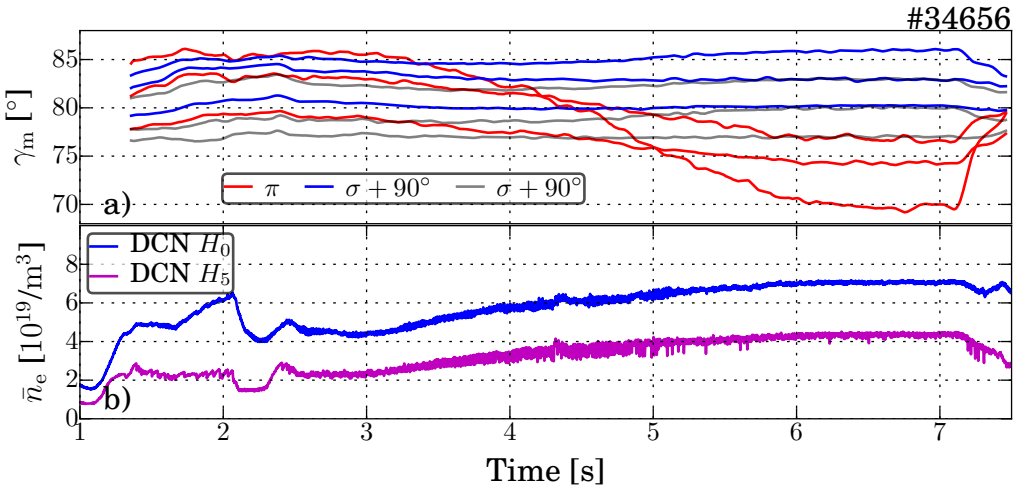

Figure A.15.: MSE angles measured with the conventional photo multiplier based MSE system are shown in a). In b) the central and edge line integrated density measured with the DCN interferometer is shown. The density increase in the plasma correlates with an increase of the divertor density. This increase leads to a strong deviation of the π channels from the 90° upshifted σ channels. The blue and red channels measuring on the same column with the same radial position and the grey channels are also σ measurements without a corresponding π measurement.

only a single fiber connected to a line of sight looking to the plasma.

A discharge to test the polychromator was designed based on the polarized background results of reference [19]. The pressure in the divertor was slightly ramped up, leading to an increase of the radiation in the lower plasma region. This light is expected to be reflected on the inner wall of ASDEX Upgrade into the lines of sight of the MSE and during the reflection on a metallic surface the light gets polarized. In figure A.15 the measured angles with the classical MSE system and the line integrated density are shown.

The measured angle of the six σ channels are 90° upshifted to theoretically match the corresponding π channels. The blue and red channels correspond to each other measuring next to each other in the same column at the same radial and slightly different vertical positions. It can be seen that the deviation of these channels strongly increases with increasing divertor density. The measured π angles decrease down to a nonphysical deviation of $-15°$, while the measured σ angles increase slightly at the same time. They also intersect each other which is physically very unlikely as this requires the integrated current between the two radial positions to be negative. Furthermore the central channels, shown with the higher angles, are more affected. This is due to the fact that the beam attenuation centrally decreases the intensity of the σ and π peak, therefore these channels are more affected by a polarized background with a constant intensity. Also the π channels are more affected with respect to the corresponding σ channels, as the measured intensity of the π peak is only half

the intensity of the σ peak. This is shown in the normalized black spectra in figure A.14. For the polychromator the correction of this background based on the following relation in the Stokes vector

$$\vec{S}_{\mathrm{tot}} = \vec{S}_{\pi/\sigma} + \vec{S}_{\mathrm{bg}} \tag{A.4}$$

$$\vec{S}_{\pi/\sigma} = \vec{S}_{\mathrm{tot}} - \vec{S}_{\mathrm{bg}}. \tag{A.5}$$

With $\vec{S}_{tot}$ the measured Stokes vector in the signal region, $\vec{S}_{bg}$ the Stokes vector of the background in the signal region and $\vec{S}_{\pi/\sigma}$ the Stokes vector of the plasma π or σ component. As reminder from section 4.1 in equation (4.1) the Stokes vector is defined as

$$\vec{S} = \begin{pmatrix} S_0 \\ S_1 \\ S_2 \\ S_3 \end{pmatrix} = I \begin{pmatrix} 1 \\ p\cos 2\gamma_{\mathrm{m}} \cos 2\chi \\ p\sin 2\gamma_{\mathrm{m}} \cos 2\chi \\ p\sin 2\chi \end{pmatrix}. \tag{A.6}$$

With the assumption that χ, the degree of ellipticity, is equal in all three Stokes vectors, the corrected MSE angle can be calculated from the ratio of S_2 and S_3 to

$$\gamma_{\mathrm{m},\pi} = \frac{1}{2} \arctan\left(\frac{(I_{\mathrm{tot}} p_{\mathrm{tot}} \sin(2\gamma_{\mathrm{m},tot}) - (I_{\mathrm{bg}} p_{\mathrm{bg}} \sin(2\gamma_{\mathrm{m},bg})}{(I_{\mathrm{tot}} p_{\mathrm{tot}} \cos(2\gamma_{\mathrm{m},tot}) - (I_{\mathrm{bg}} p_{\mathrm{bg}} \cos(2\gamma_{\mathrm{m},bg})} \right). \tag{A.7}$$

The angles in the different regions can be calculated similarly as written in section 4.1 in equation (4.3). The calculation of the intensities, negligible in the angle calculation of only a single Stokes vector, is a bit more complicated. The intensities measured in the different regions need to be normalized as the filters have a slightly different width and also the transmission differs. Furthermore the adjustment of the detectors and also the non perfect reflectivity of the mirrors and the filters outside the transmission region could have an impact. To bypass the determination of all these factors, the intensity of a polarized light source with a known relative intensity along the wavelength is measured. The in-vessel calibration lamp is used for a measurement of the intensities and in a second step the wavelength dependent intensity is measured with a relative calibrated spectrometer. The normalized lamp intensity together with the filter positions, including the intensity calibration factors can be seen in figure A.16.

For the polychromator the lamp needs to be measured as calibration and as only the relative intensities are necessary the measured intensities of this measurement must be normalized to this factors. The needed calibration factors could be used afterwards as intensity calibration for the polychromator. In a last step the measured background intensity needs to be interpolated to the signal region. Assuming only a linear wavelength dependence of the broad band polarized background, the two measurements of the background are averaged weighted by the wavelength distance to the signal region.
In figure A.17 the corresponding measurement of the first polychromator to the discharge shown before in figure A.15 can be seen.

In figure A.17 a) the measured angles of all four channels modulus 90° are shown. In the beginning up to 0.5 s, marked in magenta, the in-vessel lamp is switched on for the in-situ

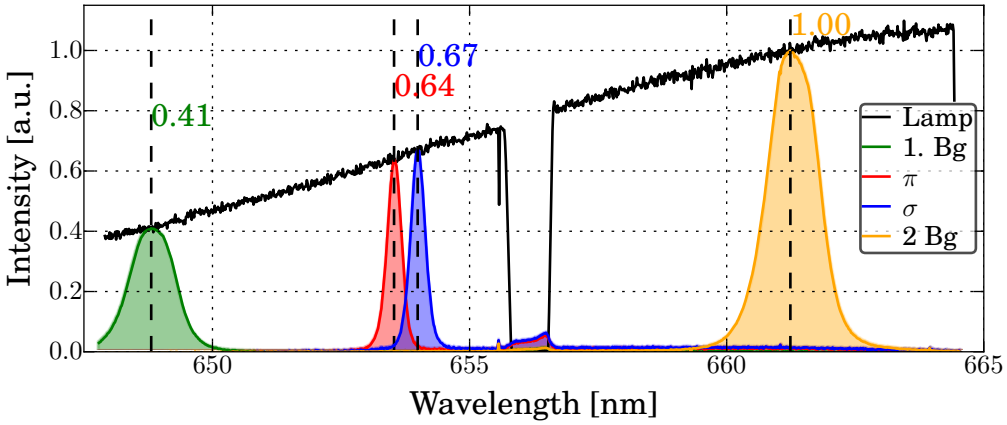

Figure A.16.: The relative intensity of the in-vessel lamp measured with a relative calibrated spectrometer can be seen. Furthermore the filter curves for one polychromator normalized to their intensity factors are shown.

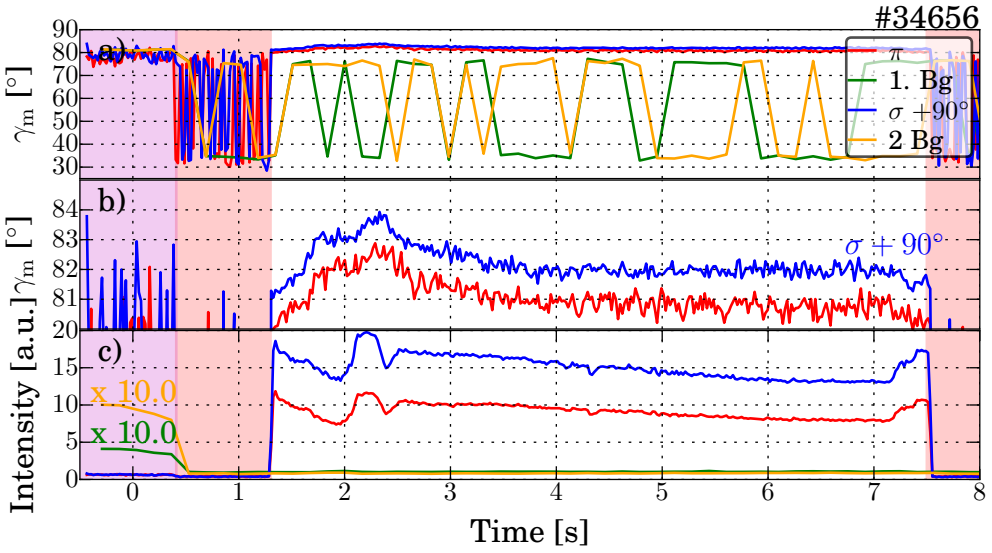

Figure A.17.: Corresponding measurement with the first polychromator to figure A.15. In a) the measured angles modulus 90° of the four channels can be seen, in b) zoomed to the π and σ measurement. In c) the time evolution of the calibrated intensities of the four channels are shown. The intensities of the background filters are up scaled by a factor of 10, as they are only in the order of 1% of the intensity of the π component.

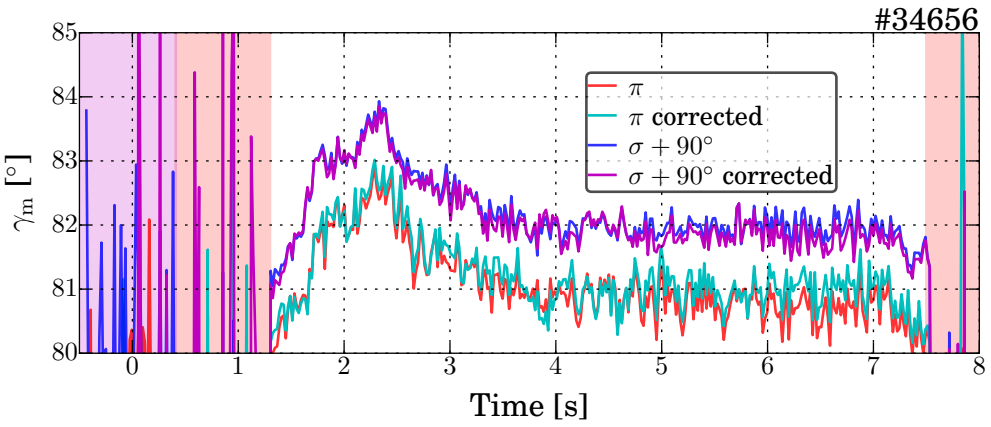

Figure A.18.: In red and blue the measured angles modulus 90° are shown. The corresponding corrected angles in cyan and magenta almost match the measurement. The reason is the intensity of the background only in the order of 1% with respect to the intensity in the signal region.

intensity calibration without the plasma. From 0.5 s to 1.2 s, marked in red, the lamp and the NBI beam 3 is off, therefore no polarized light could be measured. Beginning at 1.2 s the NBI beam 3 is switched on and the divertor density is increased to produce polarized background. At 7.5 s the discharge ends with switching of the NBI beam 3. Unfortunately in the zoomed section to the π and σ measurement in figure A.17 b) it can not be seen that the measurement is affected by any polarized background. The intensities shown in A.17 c) measured in the background channels are in the order of 1% of the intensities measured in the π and σ region and also do not increase during the discharge. This is also in agreement with a constant distance of 1° between the measured upshifted σ and π angle.
The comparison of the measured angles with the background corrected ones can be seen in figure A.18. It can be seen that there is almost no difference between the uncorrected and the corrected measurement. The maximum difference is with 0.3° in the same order as the statistical fluctuation of the measurement. Furthermore the difference between the π and σ component stays constant at 89°, also in the high divertor density phase, with the expected high polarized background. The reason for this behaviour in this special line of sight can be seen in figure A.19. In this CAD drawing the intersection of two MSE lines of sight with the inner wall of ASDEX Upgrade can be seen. In the measurement discussed above the green line of sight is used, but this line of sight ends in the A-port hosting the ECRH mirrors. The angle of incidence to this stainless steel surface strongly hampers reflection of light from the divertor into the line of sight. Because this light needs multiple reflections on multiple surfaces for the possible reflection for the divertor into the line of sight. Therefore it is not expected that an appreciable amount of light from the divertor is reflected into this line of sight. This leads to the measured absence of polarized background uncorrelated with light intensity in the divertor.
The second line of sight in figure A.19, marked in blue, is used to test the working principle of the polychromator. This line of sight ends on the in-vessel lamp, which is able to produce polarized light. In a further discharge the lamp is used to produce light with a known

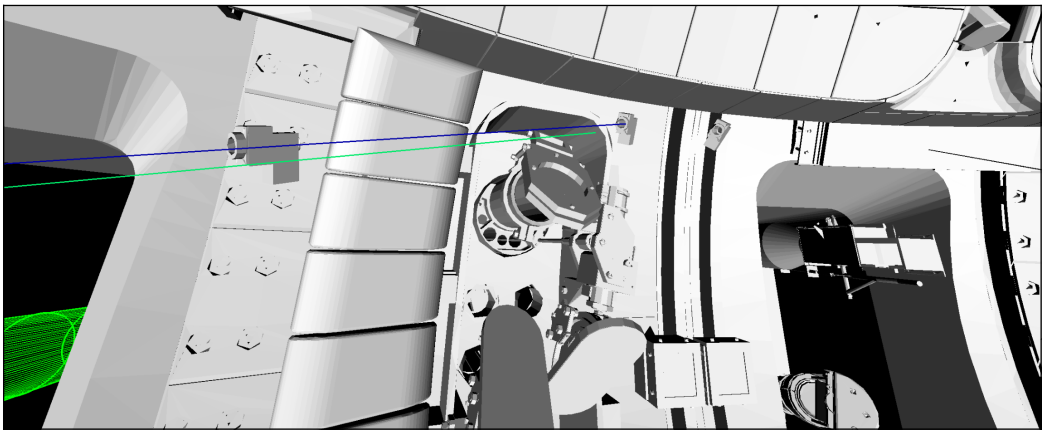

Figure A.19.: CAD drawing of ASDEX Upgrade with the intersection of two lines of sight of the MSE system with the inner wall. The polychromator used the green line of sight in discharge #34656 and the blue one in discharge #34669. The green line of sight ends in the ECRH A-port, which hampers light from the divertor to get reflected into it. The blue line of sight ends on the in-vessel lamp, producing polarized light.

polarization and intensity during the discharge, interfering with the plasma emission. In figure A.20 the polychromator measurement in this discharge can be seen.

In figure A.20 a) the measured angles in the different channels can be seen. The discharge starts again with a phase with only the lamp switched on and no plasma for the intensity calibration, the phases with only the lamp switched on are marked in magenta. Most interesting is the transition to the phase is marked in green. From 5.1 s on, during the plasma discharge, the lamp is switched on, producing synthetic and known polarized background. In this phase the angles reconstructed for the measurement in the background channels change from erratic fluctuations to the constant polarization angle of the lamp. In figure A.20 b) also a small angle change in the σ channel can be seen. For the π channel, the angle reconstruction is almost not able to reconstruct an angle any longer. This could be explained by the strong drop of the intensity of the π component shown in figure A.20 c). While in the σ and background channels the intensity strongly increases the intensity of the π channel drops almost to zero. In this special case the polarization angle of the lamp is almost similar to the angle from the plasma of the σ component and 90° to the π angle. Also the intensity of the polarized light from the lamp, measured with the background filter and interpolated to the π component is almost the same as the intensity of the π component of the plasma. The loss of measurable polarization could be explained looking at equation (A.4) and the definition of the Stokes vector in equation (A.6). The factor $2\gamma_\mathrm{m}$ in the sin and cos component of S_2 and S_3 in combination with the same intensity for the $\vec{S}_\pi$ and $\vec{S}_{bg}$ Stokes vectors, leads to a superposition of S_2 with $-S_2$ and S_3 with $-S_3$. Therefore in $\vec{S}_{tot,\pi}$ the components S_2 and S_3 are zero. As these components cover the linear polarization, in the measured Stokes vector $\vec{S}_{tot,\pi}$ no linear polarization can be found. In figure A.21 the corrected angles and the spectrograms of the single channels are shown.

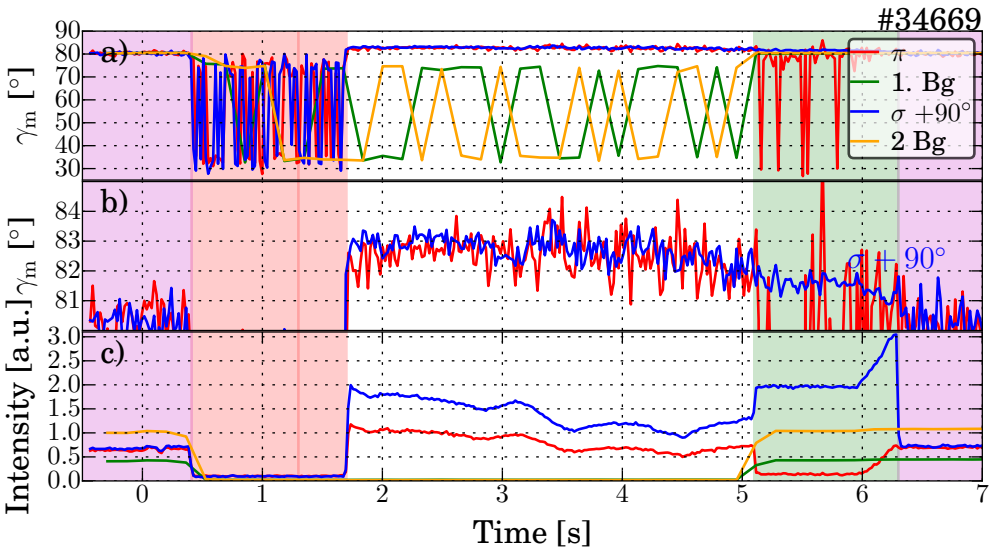

Figure A.20.: Polychromator measurement in a discharge, where the in-vessel lamp is used to produce synthetic background with a known polarization and intensity. In magenta the phases with only the lamp are shown and in green the phase were the lamp is superimposed with the plasma emission. In the red phase neither the lamp nor the NBI beam 3 is on. In a) and b) the measured angles modulus 90° are shown and in c) the intensity of the polarized light in the different channels.

Figure A.21 a) shows the correction of the σ channel. Unfortunately in this case the drop in the uncorrected angle from the superposition with the synthetic background is small, as the angle of the background is almost the same as the angle of the σ component from the plasma. But a small change could be seen in the green phase, with the combination of the plasma emission and the lamp, and this small change could be corrected using the background. More interesting is the π component in figure A.21 b). In this case the uncorrected measurement leads only to erratic fluctuation, but the correction recovers it almost to the value of the phase before, as expected.
The suppression of polarized light in the π channel by switching on the light can also be seen in figure A.21 c), where in the spectrogram from 5.1 s on the 40 kHz and 46 kHz component is not longer noticeable. In contrast in the spectrograms of the two background components in figure A.21 d) and f) the 40 kHz and 46 kHz components are only visible in phases with the lamp switched on. Finally in the phases after the discharge with only the lamp, marked in magenta, the corrected angles again starts to be erratic, as the only measured light in this phase is the synthetic background generated by the lamp and is subtracted by the correction.

In conclusion it is shown that the polychromator of ASDEX Upgrade works properly. On only a single line of sight the π component, the σ component and also in two regions the background could be measured. The π and σ component have a reasonable resolution at a good time resolution although only if one line of sight is used. This is an improvement in

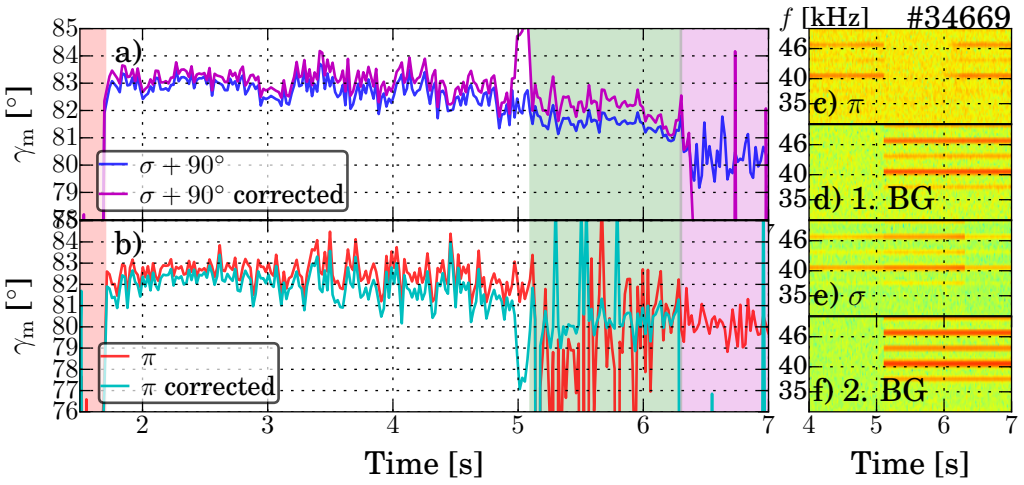

Figure A.21.: Correction of the polychromator measurement interfered by synthetic background from the in-vessel lamp. In a) and b) the comparison of the corrected angles for the σ and π component are shown. In c)-f) the spectrograms of the measured signals in the different components can be seen. In the spectrogram the 40 kHz and 46 kHz component correspond to the two polarization components. The loss of polarization of the π component can be seen in c) by the gap in the 40 kHz and 46 kHz band.

the accuracy of the radial and vertical position, as the classical photo multiplier based MSE system needs two lines of sight, lying vertically next to each other, to reach a good angle resolution. It could also be shown that the correction for polarized background in the π and σ component works well. Unfortunately this could only be shown for a discharge with a strong synthetic background from an in-vessel lamp. Because in the dedicated discharge, where the classical MSE seems to be affected by polarized background from the plasma, a line of sight was chosen for the polychromator, which is not affected by the background.
For the future the discharge with the polarized background should be repeated, but with the polychromator on a different line of sight, were the classical MSE saw an influence from the background. Also the cross talk of the 2x2 APD detectors needs to be understood and suppressed, this enables the simultaneous measurement of four lines of sight with one polychromator. Furthermore a more dedicated comparison with the classical MSE needs to be done in terms of fluctuations and the usefulness for the equilibrium reconstruction. In addition the deviation of the angular distance between the π and σ component from 90°, seen in discharge #34656 on a single line of sight, not explainable by polarized background, needs to be investigated further.

B. Appendix: Revision of Simulation Inputs

B.1. Beam Geometry

NBI Source	horizontal tilt	vertical tilt	nominal vertical tilt
Q5	-0.10°	+0.05°	+0.00°
Q6 On-Axis	-0.20°	-0.40°	-0.50°
Q6 Reference	-0.20°	+0.10°	+0.00°
Q6 Off-Axis	-0.20°	+0.40°	+0.30°
Q7 On-Axis	-0.10°	-0.25°	-0.50°
Q7 Reference	-0.10°	+0.20°	+0.00°
Q7 Off-Axis	-0.10°	+0.75°	+0.50°
Q8	-0.10°	+0.10°	+0.00°

Table B.1.: Horizontal and vertical correction angles for the NBI sources of box 2 to optically match the infrared measurements, with an accuracy in the order of ±0.05°.

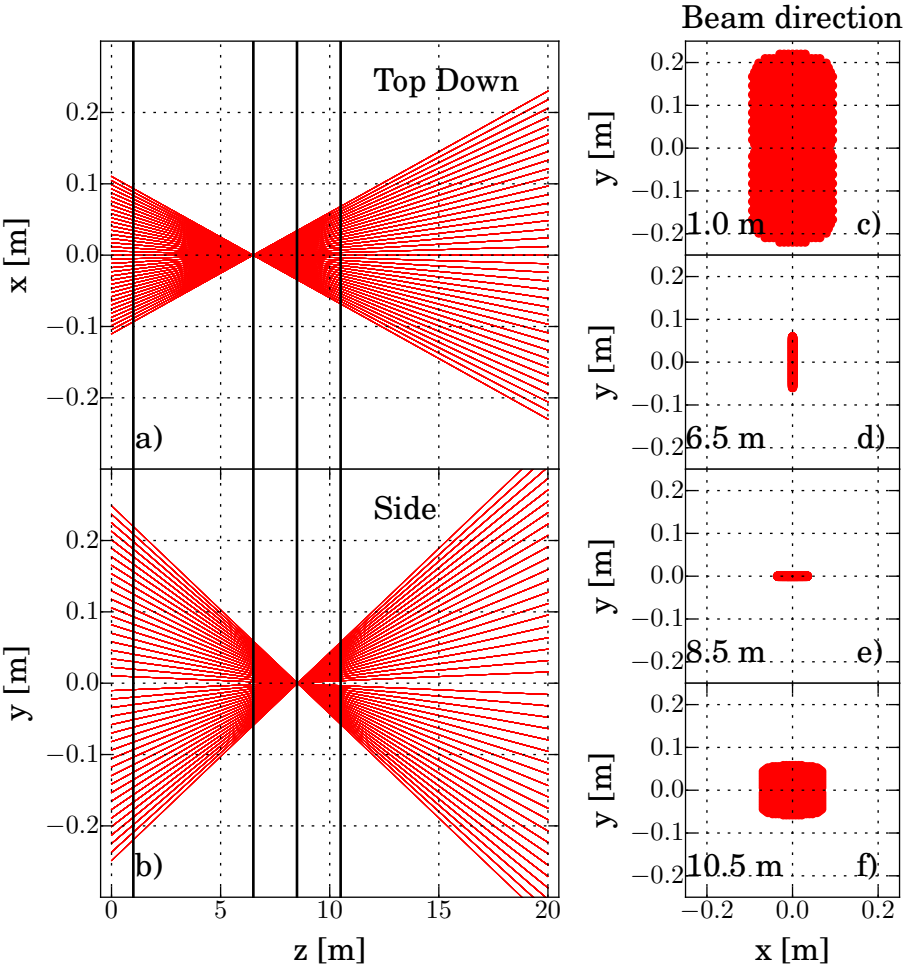

Figure B.1.: Geometry of all beamlets of a NBI Source of Box 1. Compare figure 6.9.

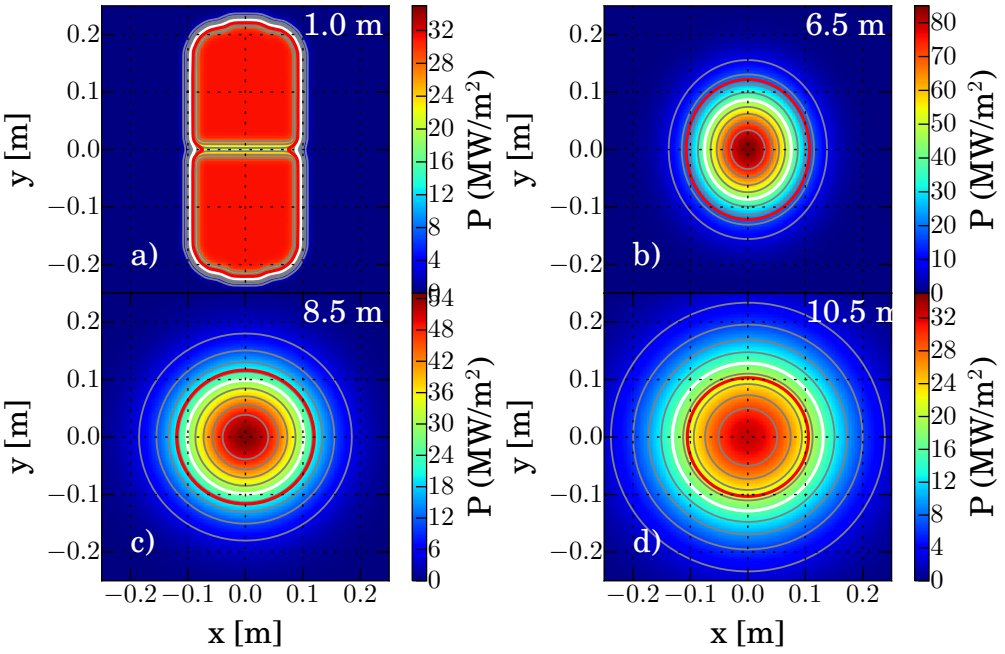

Figure B.2.: Power density profiles at four different positions along the beam axis of a beam of Box 1. Compare figure 6.10.

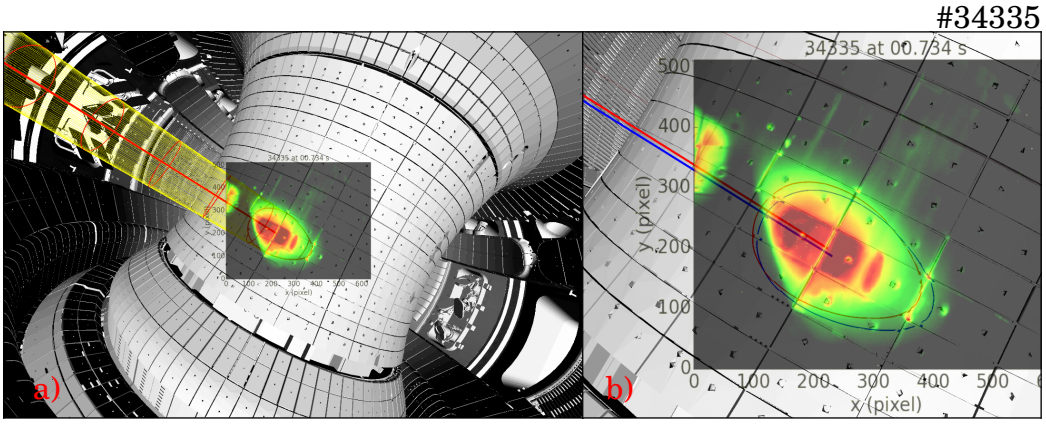

Figure B.3.: NBI Beam 5. The correction is a rotation of the source of -0.10° in horizontal and +0.05° in vertical direction. Compare figure 6.11.

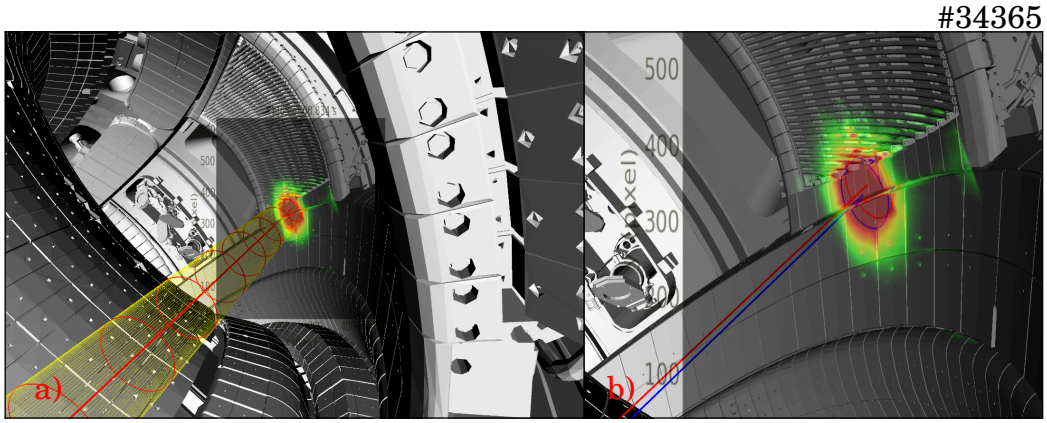

Figure B.4.: On-Axis case NBI Beam 6. The correction is a rotation of the source of -0.20° in horizontal and -0.40° in vertical direction. Compare figure 6.11.

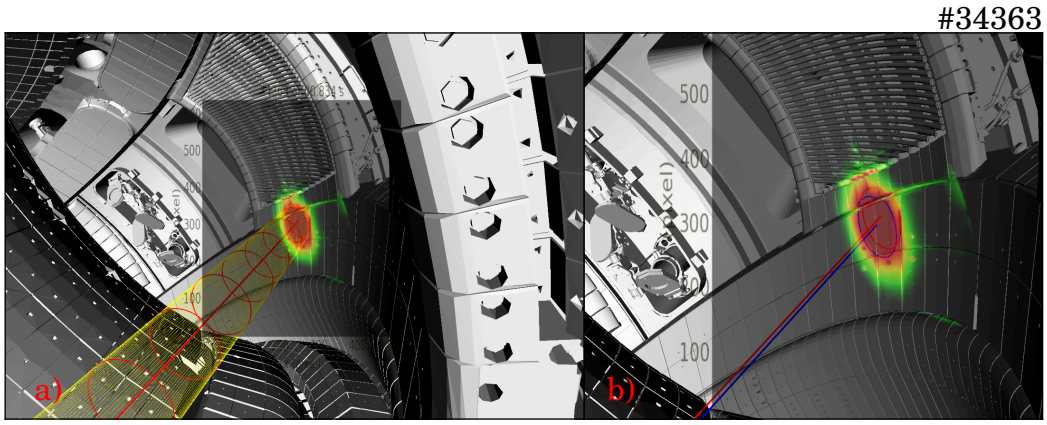

Figure B.5.: Reference position of NBI Beam 6. The correction is a rotation of the source of -0.20° in horizontal and +0.10° in vertical direction. Compare figure 6.11.

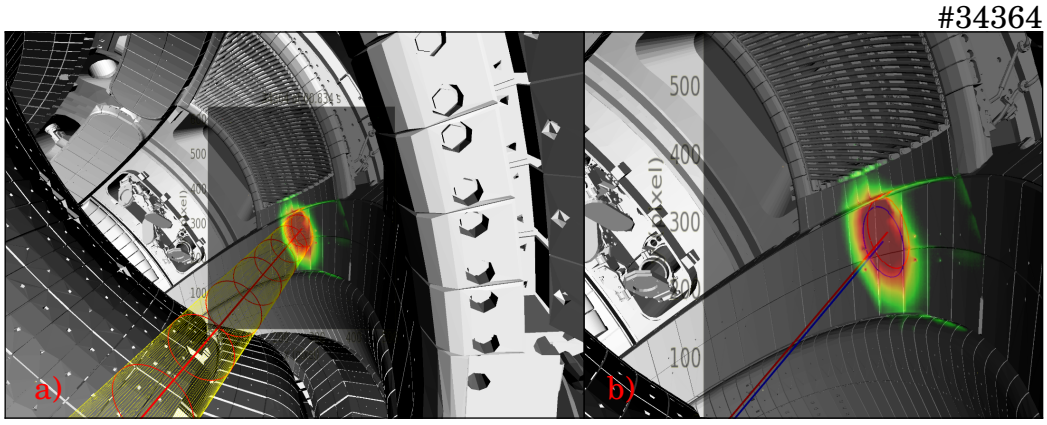

Figure B.6.: Off-Axis case NBI Beam 6. The correction is a rotation of the source of -0.20° in horizontal and +0.40° in vertical direction. Compare figure 6.11.

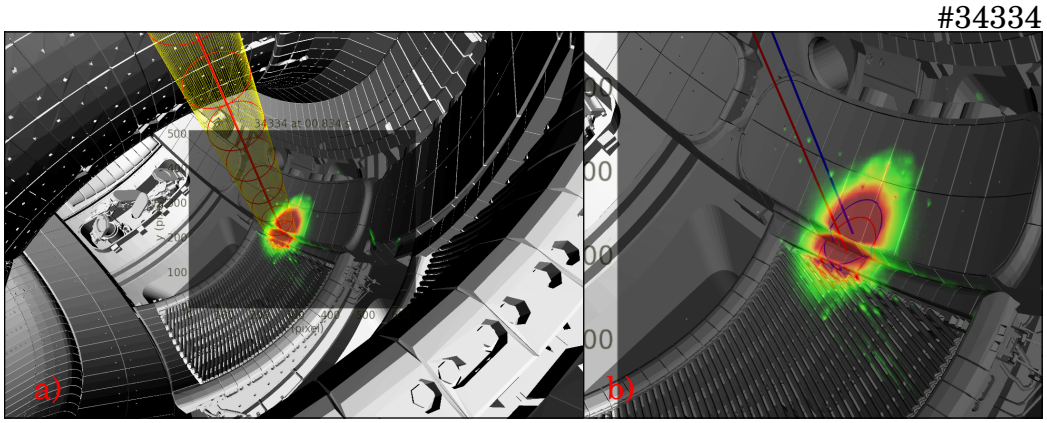

Figure B.7.: On-Axis case NBI Beam 7. The correction is a rotation of the source of -0.10° in horizontal and -0.25° in vertical direction. Compare figure 6.11.

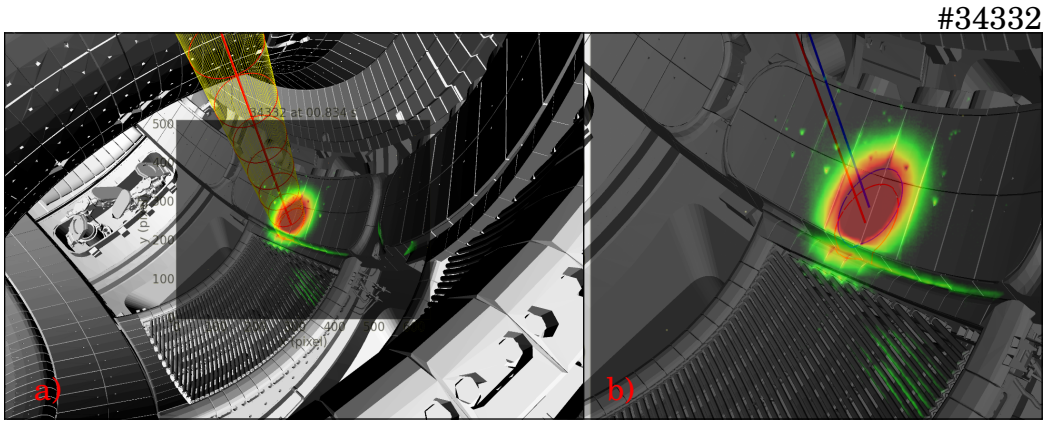

Figure B.8.: Reference position of NBI Beam 7. The correction is a rotation of the source of -0.10° in horizontal and +0.20° in vertical direction. Compare figure 6.11.

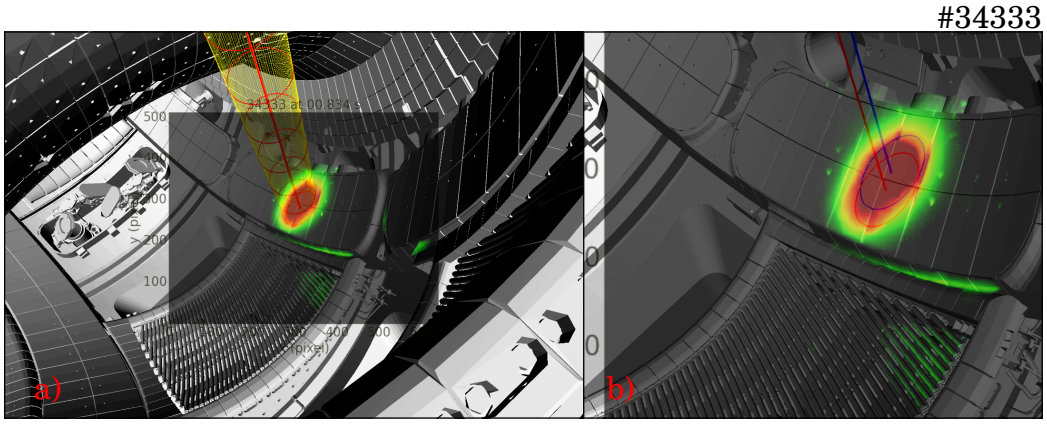

Figure B.9.: Off-Axis case NBI Beam 7. The correction is a rotation of the source of -0.10° in horizontal and +0.75° in vertical direction. Compare figure 6.11.

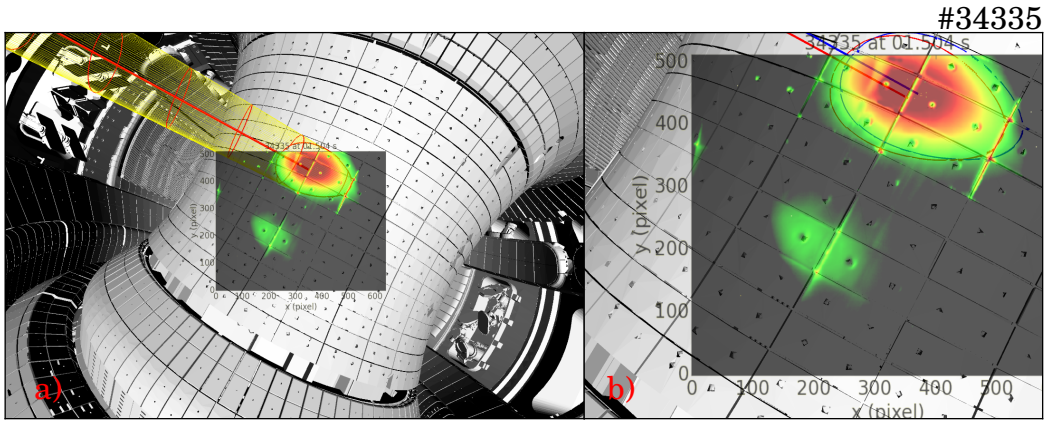

Figure B.10.: NBI Beam 8. The correction is a rotation of the source of -0.10 ° in horizontal and +0.10° in vertical direction. Compare figure 6.11.

B.1.1. Power Deposition

For a quantitative description of the neutral beam driven current and the fast ion distribution the beam power deposited in the plasma is necessary. In continuation of the correction of the injection geometry of the NBI beams in section 6.3.1 the power of each single NBI beam to the plasma is reviewed. A measurement of the power of the single beams can be performed in the beam box with the calorimeter. This calorimeter can be seen in a non-measurement position in figure 3.2 b) downstream after the magnet. This calorimeter can be used to dump the beam during conditioning pulses and the deposited power can be calculated from the measured temperature differences of the in- and out-flowing cooling water through the calorimeter panels. With the measured cooling water volume flow through the calorimeter the power can be calculated. This allows a measurement of the beam power close to the exit of the beam box. Unfortunately no direct measurement of the beam power and profile in the torus is possible. Therefore the beam losses on the path from the calorimeter position to the plasma had to be calculated.
These calculations are performed in collaboration with N. den Harder. The assumed main losses are due to geometrical deposition of power on the wall and other components like the beam exit scraper. In figure 6.10 the power density for all four beams of box 2 along the box axis from the box towards the torus can be seen, the corresponding figure for beam box 1 can be seen in figure B.12. On the basis of a CAD-model of the beam box, ASDEX Upgrade and the connecting duct the deposited power to the different components is calculated along the beam. In figure B.11 the power deposition on the different components can be seen. Figure B.11 a) shows the power densities on a reasonable scaling for the deposition on the inner wall of the torus. This leads to the conclusion that the dominant part of the power is deposited inside the torus as expected. However, figure B.11 b) use a different scaling for the power deposition and this scaling shows that a non-negligible part of the power is deposited on components along the path of the beam.
A ratio of the non-scraped power of the beam to the power at the calorimeter along the beam axis as function of the major radius of ASDEX Upgrade can be seen in figure

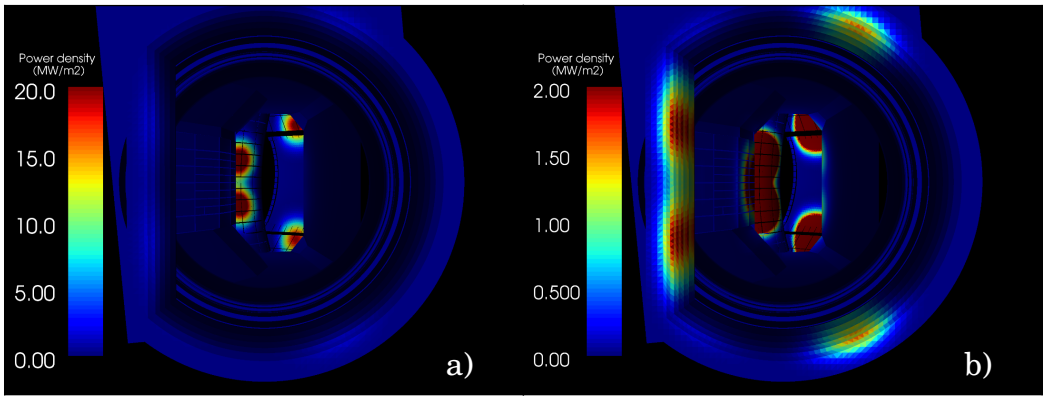

Figure B.11.: Calculated power deposition of the NBI beams of box 2. a) Use of a scaling for the deposition on the inner wall of ASDEX Upgrade, showing a reasonable transmission. b) Different scaling for the power density showing non-negligable power deposition on the beam exit scraper and in the duct.

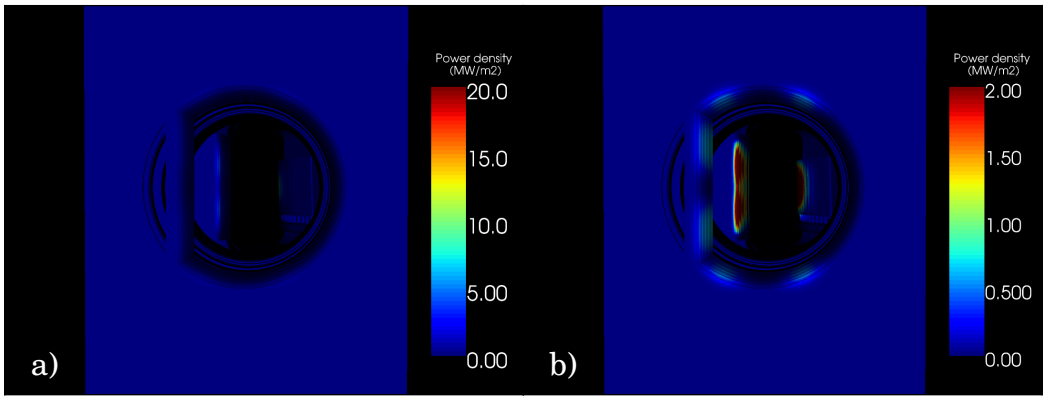

Figure B.12.: Calculated power deposition of the NBI beams of box 1. a) Use of a scaling for the not shown deposition on the inner wall of ASDEX Upgrade. b) Different scaling for the power density showing non-negligable power deposition on the beam exit scraper and in the duct.

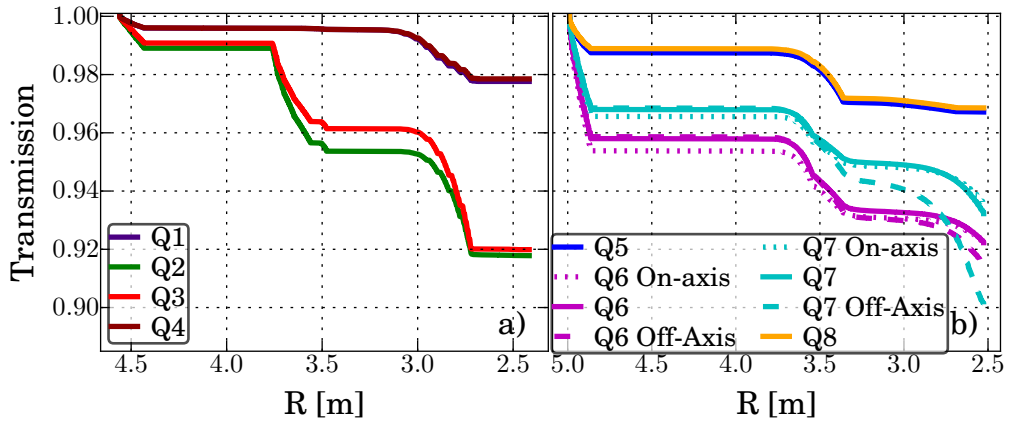

Figure B.13.: Transmission of the beam power from the calorimeter towards the plasma in a) for the beams of beam box 1 and in b) for the beams of beam box 2.

B.13. This represents the transmission through the duct connecting the NBI box with the torus. Figure B.13 a) shows the transmission for the beams of box 1 and b) of box 2. The calculations depends strongly on the divergence and focal length assumed for the beams. For these calculations the values measured in the master thesis of F. Mink [117] and verified with new measurements by N. den Harder are used. Up to now for all beams of both boxes a transmission of 85% were assumed based on calculations from the design phase around 1990. The change of the geometry of the duct for beam box 2 in 2000 was not taken into account and there are also differences in the transmission due to the steering ability of beam 6 and 7. In contrast to the old calculations the transmission of the duct towards the plasma, shown in table B.2, is slightly higher and differs also for the different sources. Furthermore in beam box 2 a new beam exit scraper was installed before the 2017 campaign, to protect duct components like the gate valve from too high power densities seen in the past.
A further influence on the transmission of the beam through the duct could come from background gas in the duct, leading to reionization. This would decrease the transmission as ions are deflected by the magnetic field from the torus and could not heat the plasma. Unfortunately there is no valid model for the pressure in the duct, but first rough estimations lead to a decrease of the transmission in the range of 1-2%. A further uncertainty could come from late neutralization of ions in the bending magnet. These small angle deflected neutrals could have trajectories ending in the calorimeter, but would not enter the plasma. These particle would lead to an overestimation of the power to the calorimeter. To calculate the fraction of small angle deflected neutrals the full magnetic field in the magnet and the neutralizer is need and a valid gas model in both. This is not done yet, but both uncertainties are under further investigation.

To measure the difference between the different NBI sources a discharge was designed that switches through all NBI sources individually at constant density. In addition, at the end of each single beam phase, NBI beam 3 is switched on for 70 ms to obtain measurements with the FIDA diagnostic. To measure the influence on the plasma the diamagnetic flux loop

NBI Source	Geometrical Transmission	New new Scraper
Q1	98.0%	-
Q2	92.0%	-
Q3	92.0%	-
Q4	98.0%	-
Q5	96.5%	95.5%
Q6 On-Axis	92.0%	92.0%
Q6 Reference	92.0%	92.0%
Q6 Off-Axis	91.5%	91.5%
Q7 On-Axis	93.5%	93.5%
Q7 Reference	93.0%	93.0%
Q7 Off-Axis	90.0%	90.0%
Q8	97.0%	95.5%

Table B.2.: The resulting geometrical transmission from figure B.13 at the end of the duct. Also the calculations for the new beam exit scraper installed in beam box 2 before the campaign 2017.

measurement (see section 3.3.1) is used. The measurements are compared with TRANSP simulations assuming different transmissions for all beams. The result can be seen in figure B.14. The calculation of the diamagnetic flux in TRANSP mainly based on the pressure profile. As only a single source is active the pressure profile is dominated by the thermal pressure, calculated from the input kinetic profiles. Unfortunately in this case the kinetic profiles seems to be underestimated. Therefore the comparison with TRANSP is not sensitive to minor changes in the beam power. Additionally in this case the change of the diamagnetic flux by switching on the beams seem to be strongly underestimated, for example due to the inaccurate kinetic profiles, as a nonphysically high beam transmission of 200% has to be assumed to match the data. However, a systematic uncertainty in the measurement can not be excluded. In anticipation to section 6.3.2 figure 6.21 the uncertainty of the TRANSP predicted diamagnetic flux due to the uncertainties of the kinetic inputs, this comparison is therefore at the moment not accurate enough to measure the small changes in the transmission.

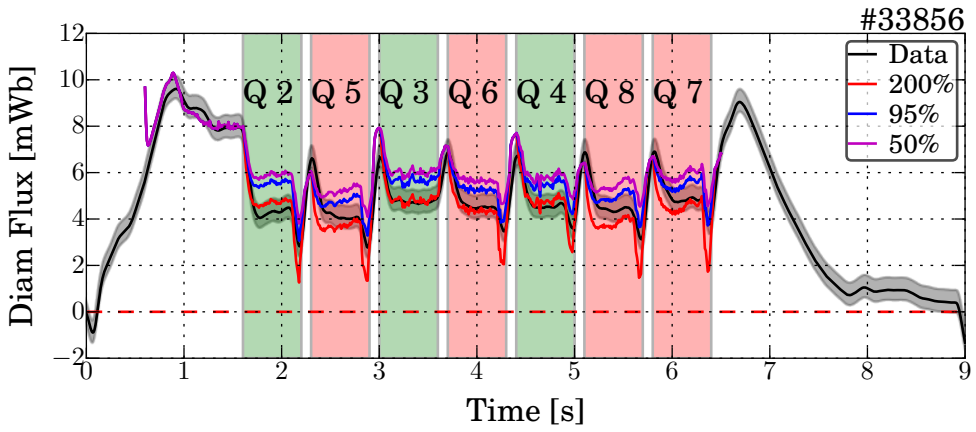

Figure B.14.: Diamagnetic Flux measurement in comparison with TRANSP.

B.2. Sensitivity Analysis

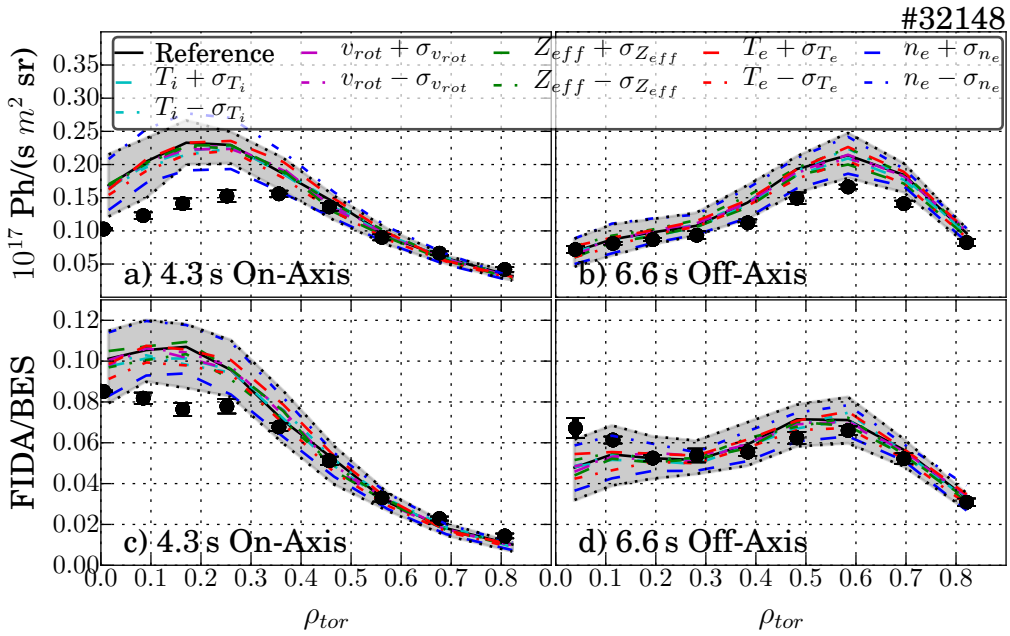

Figure B.15.: Influence of the profile uncertainties on the synthetic FIDA diagnostic for an on-axis and off-axis point in time. All different profiles are varied individually. The dominant influence of the electron density can be seen in figure 6.18.

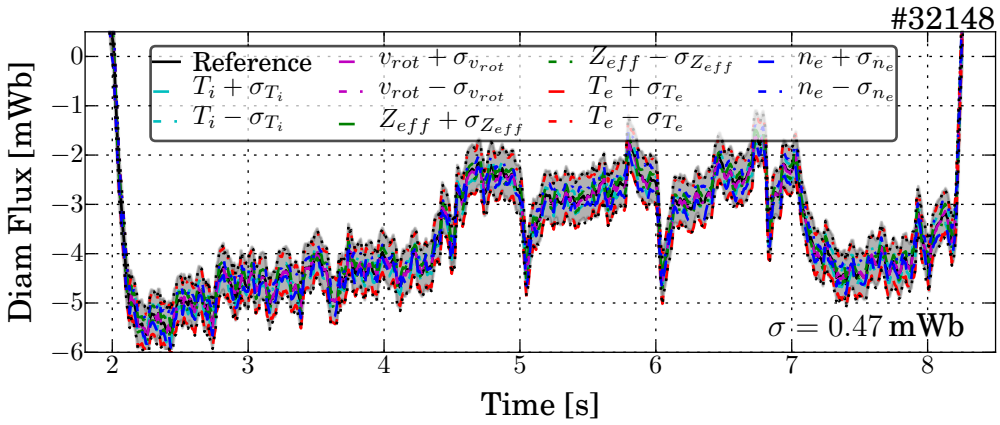

Figure B.16.: Influence of the assumed uncertainties of the kinetic profiles on the diamagnetic flux prediction. Dominated by the electron temperature uncertainty leading to a deviation of up to 0.47 mWb, this influence can be seen in figure 6.21. The measured diamagnetic flux is not shown.

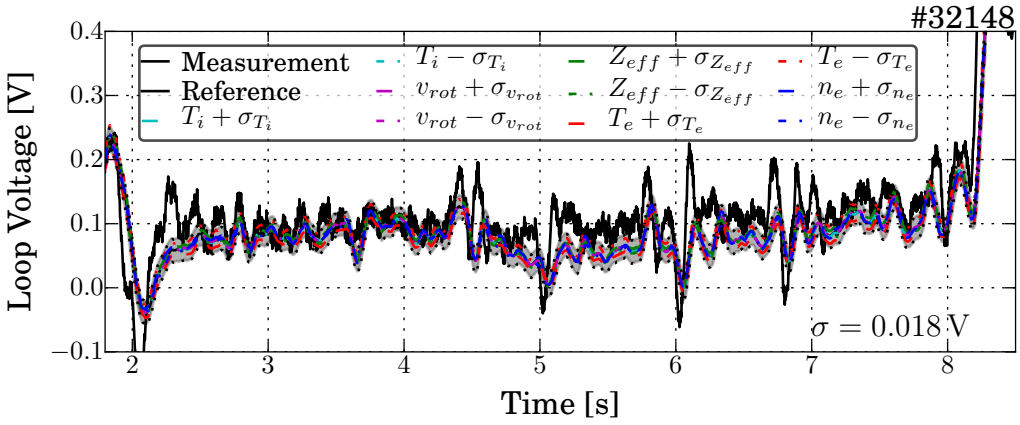

Figure B.17.: Sensitivity of the TRANSP predicted loop voltage due to variations of the kinetic profiles with respect to their uncertainties.

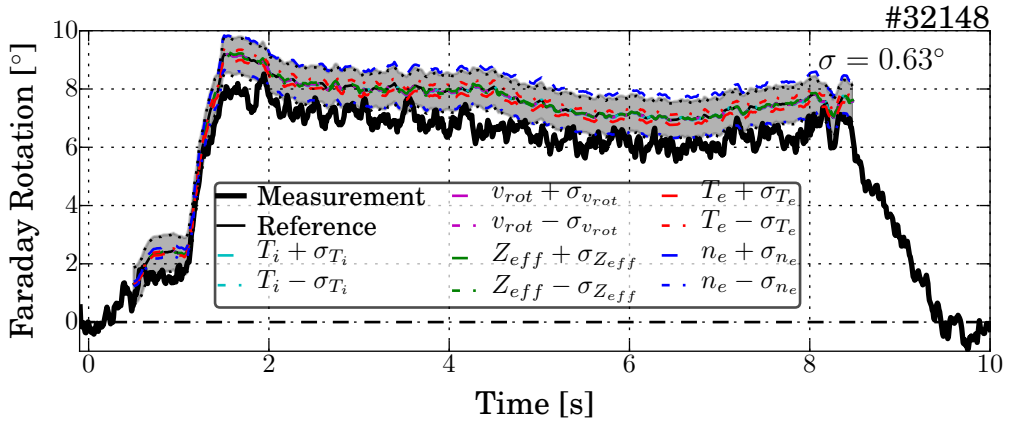

Figure B.18.: Sensitivity off the single polarimetry channel on the variation of the kinetic profiles with respect to their uncertainty.

B.3. Effective Charge Calculation

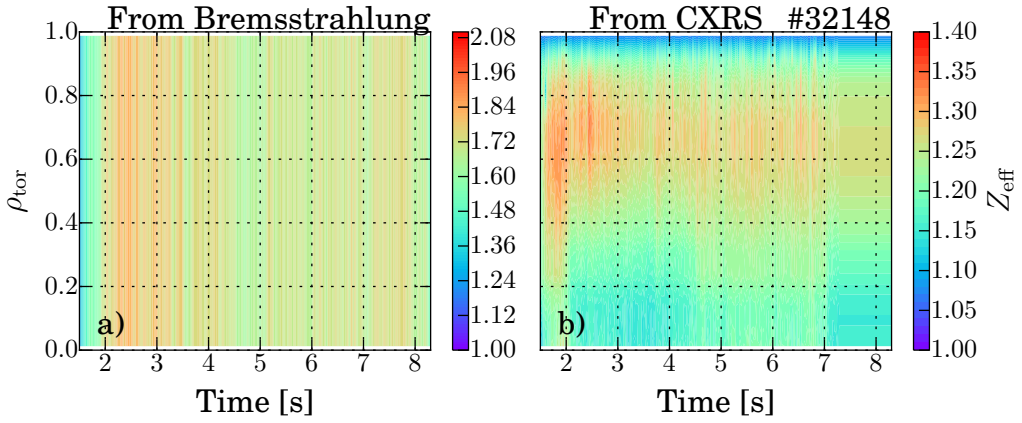

Figure B.19.: Profiles of the effective charge in discharge #32148. The profile in a) is calculated from the bremsstrahlung, but overestimate the effective charge. The profile in b) is calculated from the impurity densities measured by the charge exchange recombination spectroscopy by equation (3.10).

C. Appendix: Perturbation Induced Fast Ion Redistribution

C.1. FIDA Tomography: Fishbone Induced Fast Ion Redistribution

For the FIDA tomography lines of sight with a similar radial intersection with the beam of each of the five different optical heads are used. The lines of sight of the FIDA diagnostic are shown in figure 3.13. These lines, intersecting NBI beam 3 at similar radial position, should have different viewing directions. This enables a coverage of the full phase space with the combined weight functions of all the lines of sight, taking also different wavelength regions into account. The weight functions for the five different lines of sights can be seen in appendix C.3 in figure C.3.
With a combination of all the contained information the fast ion density in the phase space can be calculated from the FIDA measurements. This is done for one point in time in the on-axis phase, averaged over 8 frames. The resulting phase space resolved in pitch angle and energy, at one central radial position can be seen in figure C.1 a).
Unfortunately the line of sight looking almost vertically from above onto beam, covering the low pitch angle values (shown in magenta in figure 3.13 with the weight function from figure C.3 d)), is disturbed irrecoverably by the ELMs intense radiation in the divertor. Therefore the data of this line of sight are not usable, but without this line of sight the main information on the trapped particle is lost. Therefore the comparison with the TRANSP fast ion distribution functions is not as conclusive as expected.
The comparison of the three different TRANSP-predicted fast ion distributions in the phase space in figure C.1 b),c) and d) indicates only minor differences. Most obvious are the pronounced beam deposition peaks for the neoclassical prediction in C.1 b) from the NBI beam 3 at 60,keV and from beam 5 and 8 at 90 keV and 45 keV. Furthermore all beams deposit their half- or third energy component at 30 keV. As the beams have a slight co-current tangential steering the fast ions are produced dominantly with positive pitch angles and mainly as passing particles. In the simulations assuming anomalous fast ion diffusion in figure C.1 c) and d) the peaks are blurred out.
Beyond the deposition peaks the fast ion densities are quite similar, especially for negative pitch angles. The comparison with the tomographically reconstructed fast ion density is less conclusive, due to the fact the information for low pitch angle values is missing. Only the less pronounced deposition peaks in the tomography indicate a slightly better agreement with the fast ion distributions that assume central anomalous fast ion diffusion.

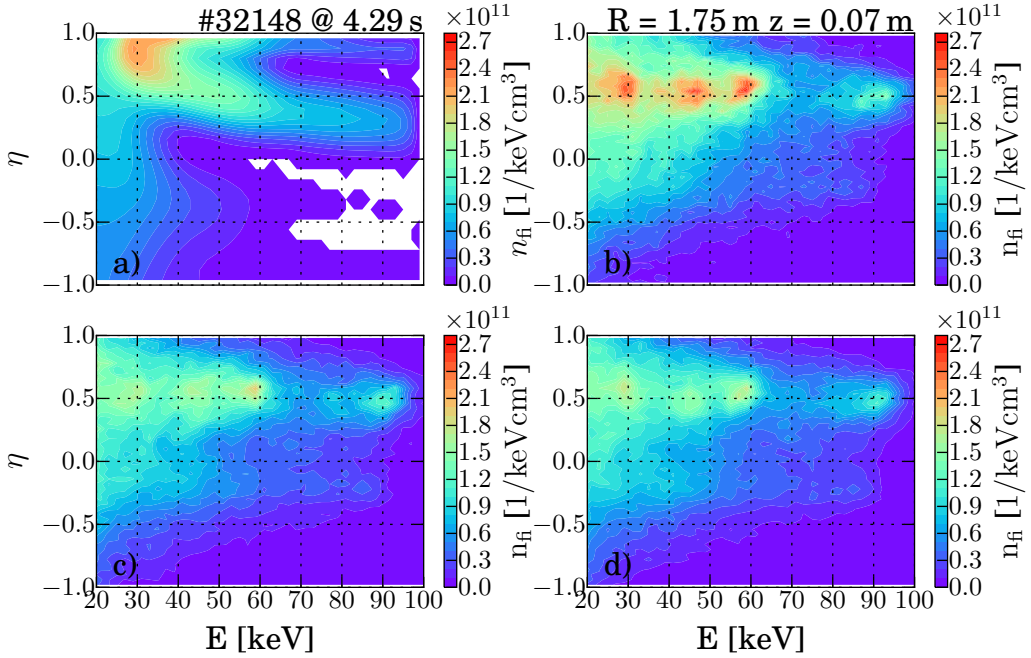

Figure C.1.: a) Fast ion distribution reconstructed from the FIDA tomography. In b),c) and d) the TRANSP predicted fast ion distribution can be seen for different simulations. In b) the neoclassical assumption, in c) the assumption of $D_{\mathrm{fi}} = 0.3\mathrm{m}^2/\mathrm{s}$ and in d) the assumption of $D_{\mathrm{fi}} = 0.5\mathrm{m}^2/\mathrm{s}$ for the profile shown in figure 6.32.

This is in agreement with the FIDA results shown before. Due to the fact, that the shown on-axis case is not conclusive, the off-axis case is not shown. Furthermore, as no anomalous fast ion transport is assumed in the off-axis phases, the predicted fast ion distribution should be the same and are so.

C.2. FIDA Tomography: Microturbulence Induced Fast Ion Redistribution

Different to the assumption in section 6.5.1 the assumed diffusion coefficients are different for trapped and passing particle and also energy resolved. Therefore again the fast ion distribution measured from the FIDA tomography should be compared with the TRANSP predictions. This comparison can be seen in figure C.2 in a) the fast ion distribution from the FIDA tomography is shown. In figure C.2 b) the fast ion distribution from TRANSP assuming neoclassical transport and in c) and d) the assumption of anomalous fast ion diffusion due to the microturbulent transport is shown. The difference between the simulations in c) and d) is that in c) only the diffusion for the passing particle from

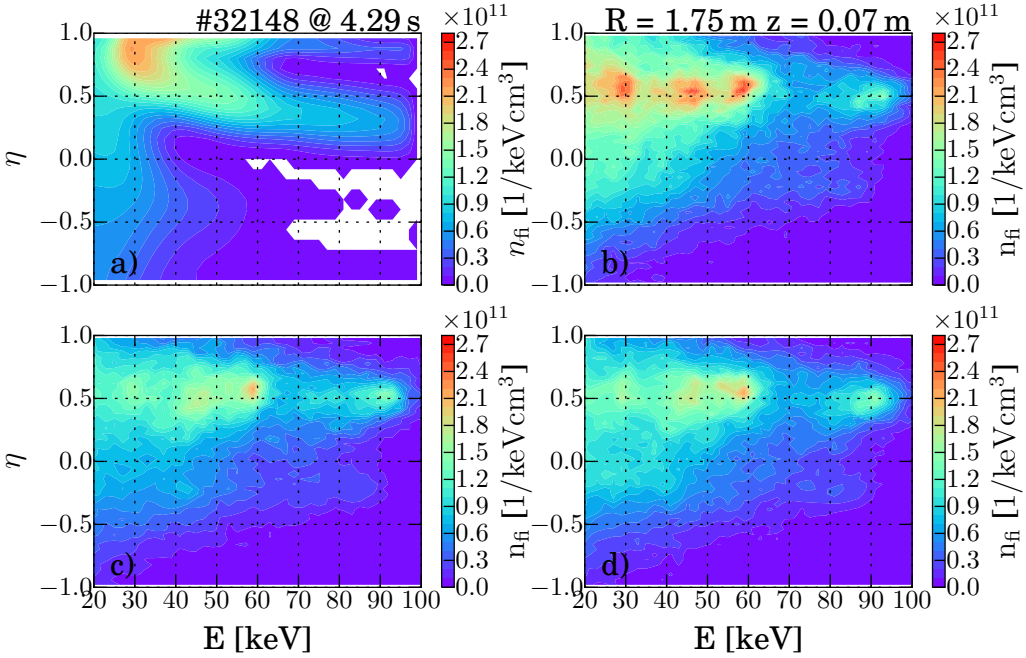

Figure C.2.: a) Fast ion distribution reconstructed from the FIDA tomography. In b),c) and d) the TRANSP predicted fast ion distribution can be seen for different simulations. In b) the neoclassical assumption, in c) only the diffusion coefficents for the passing particles from figure 6.36 are used and in d) both the diffusion for the passing and trapped fast ions are used.

figure 6.36 is assumed while d) takes also the trapped particle diffusion from figure 6.37 into account.
Unfortunately the result is again inconclusive as in section 6.5.1. The assumption of the energy dependent anomalous fast ion diffusion does not change the shape of the fast ion distribution in the phase space strong enough to gain information. Again only from the reduced maxima a slightly better agreement of the TRANSP fast ion distributions assuming anomalous fast ion diffusion with the reconstructed one from FIDA can be seen. The non usability of the vertical line of sight again strongly reduces the information on the trapped particles.

C.3. Weight Functions for FIDA Tomography

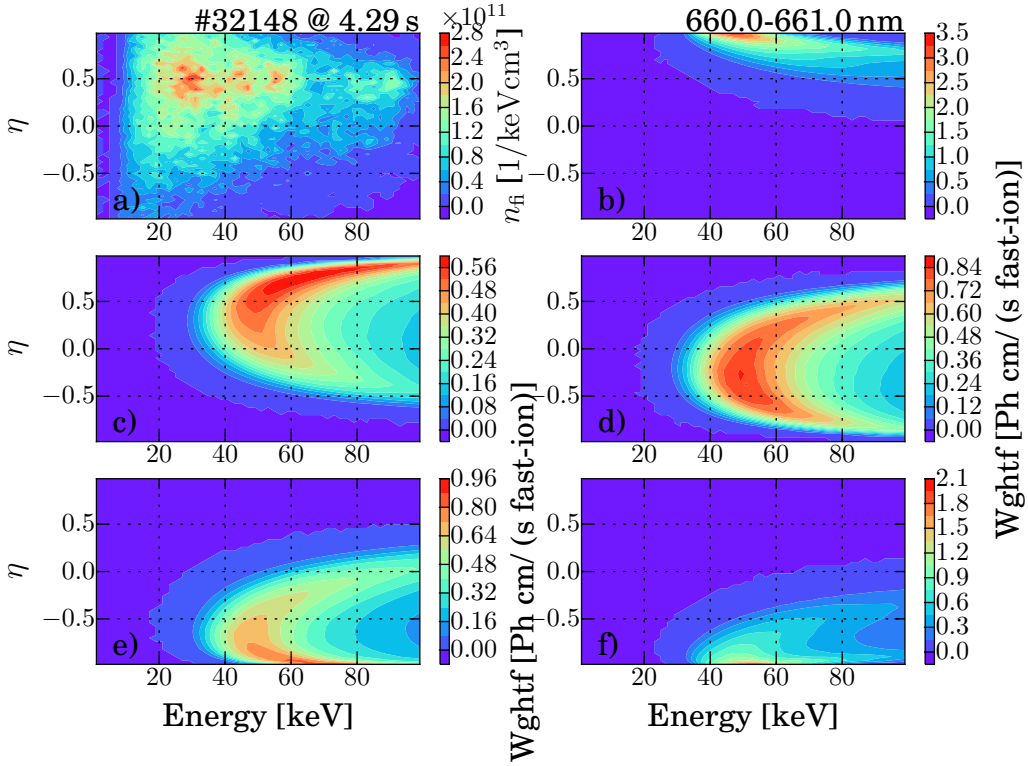

Figure C.3.: a) shows the fast ion distribution calculated by TRANSP. b)-f) shows the weight function of the five different lines of sight used for the FIDA tomography, but in this case only for the wavelength region from 660.-661.nm.

C.4. Anomalous Diffusion due to Microturbulence

$$D^{\mathrm{es}}_{\mathrm{fi,p}} = \frac{\sigma_{\mathrm{es,p}} \cdot \chi_{\mathrm{eff}}}{\eta^2} \cdot \left(\frac{E}{T_{\mathrm{e}}}\right)^{-1} \tag{C.1}$$

$$D^{\mathrm{es}}_{\mathrm{fi,p-FLR}} = \frac{\sigma_{\mathrm{es,p-FLR}} \cdot \chi_{\mathrm{eff}}}{\eta^2 \cdot (1-\eta^2)^{1/2}} \cdot \left(\frac{E}{T_{\mathrm{e}}}\right)^{-3/2} \tag{C.2}$$

$$D^{\mathrm{em}}_{\mathrm{fi,p}} = \sigma_{\mathrm{em,p}} \cdot \chi_{\mathrm{eff}} \cdot \left(\frac{\beta}{\beta_{\mathrm{crit}}}\right)^{2} \tag{C.3}$$

$$D^{\mathrm{em}}_{\mathrm{fi,p-FLR}} = \frac{\sigma_{\mathrm{em,p-FLR}} \cdot \chi_{\mathrm{eff}} \cdot (\beta/\beta_{\mathrm{crit}})^2}{(1-\eta^2)^{1/2}} \cdot \left(\frac{E}{T_{\mathrm{e}}}\right)^{-1/2} \tag{C.4}$$

$$D^{\mathrm{es}}_{\mathrm{fi,t}} = \frac{\sigma_{\mathrm{es,t}} \cdot \chi_{\mathrm{eff}} \cdot \epsilon_{\mathrm{t}}^{1/2}}{\eta \cdot (1-\eta^2)} \cdot \left(\frac{E}{T_{\mathrm{e}}}\right)^{-3/2} \tag{C.5}$$

$$D^{\mathrm{em}}_{\mathrm{fi,t}} = \frac{\sigma_{\mathrm{em,t}} \cdot \chi_{\mathrm{eff}} \cdot (\beta/\beta_{\mathrm{crit}})^2 \cdot \epsilon_{\mathrm{t}}^{1/2} \cdot \eta}{1-\eta^2} \cdot \left(\frac{E}{T_{\mathrm{e}}}\right)^{-1/2} \tag{C.6}$$

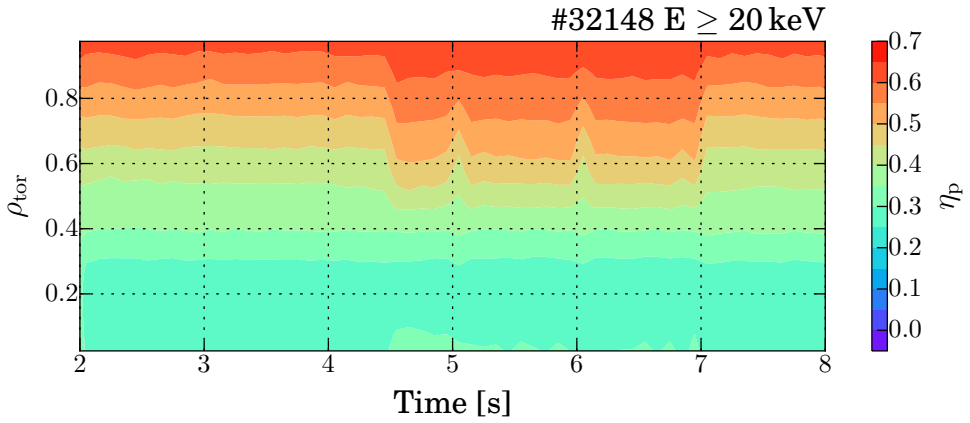

Figure C.4.: Energy averaged pitch angle distribution for passing fast ions above 20 keV as input for equations (6.1-6.6/C.1-C.6).

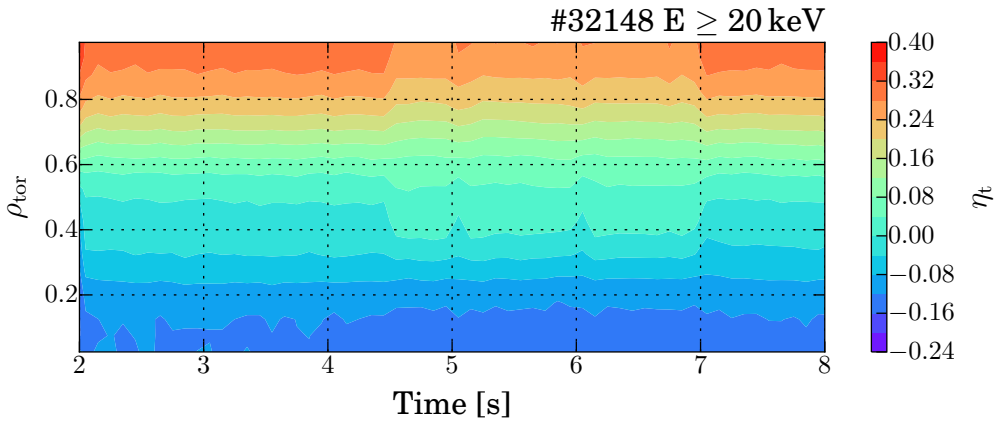

Figure C.5.: Energy averaged pitch angle distribution for trapped fast ions above 20 keV as input for equations (6.1-6.6/C.1-C.6).

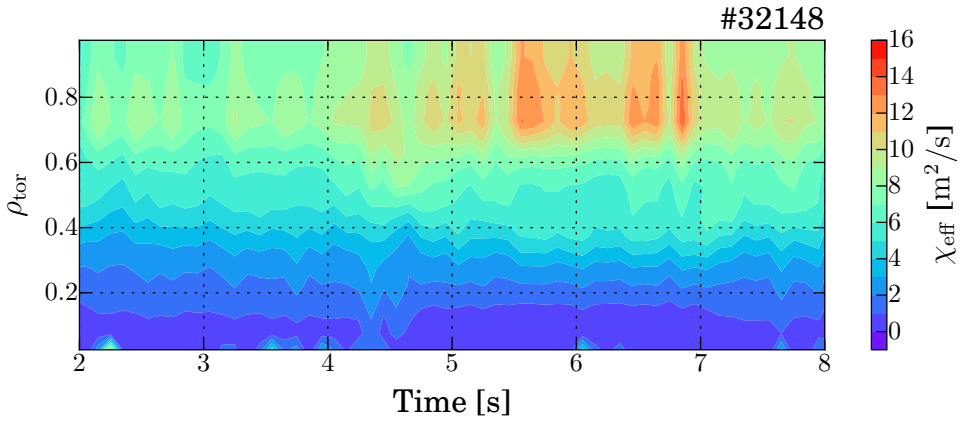

Figure C.6.: Effective heat diffusivity χ_{eff} as sum of the ion and electron heat diffusivity calculated by TRANSP.

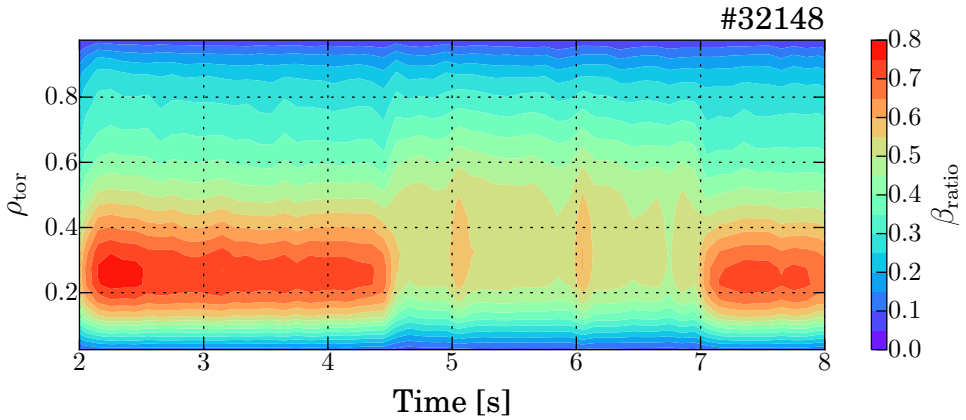

Figure C.7.: Local ratio $\beta/\beta_{\text{crit}}$ with β_{crit} from the Troyon limit with a factor $g = 3.5$.

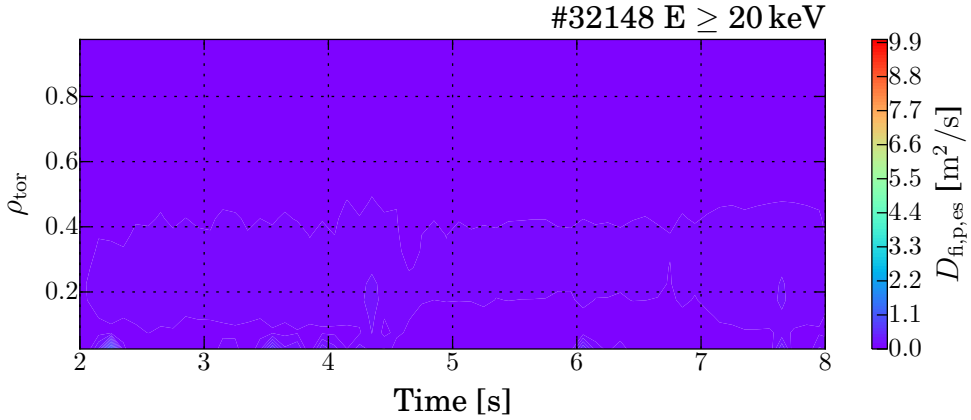

Figure C.8.: $D^{es}_{fi,p}$ Energy averaged anomalous fast ion diffusion coefficient for passing fast ions by electrostatic perturbation from equation (6.1/C.1) including the finite Larmor radius approximation of equation (6.2/C.2). Based on the model from Pueschel et al. [33].

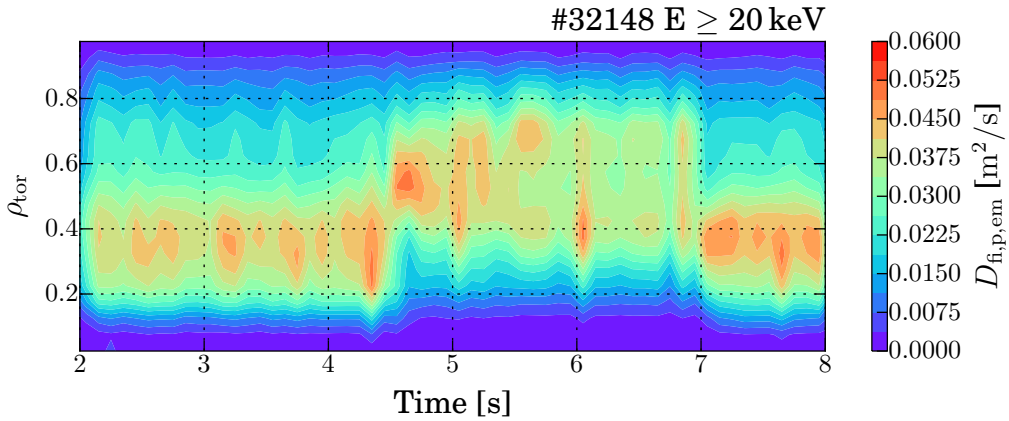

Figure C.9.: $D^{em}_{fi,p}$ Energy averaged anomalous fast ion diffusion coefficient for passing fast ions by electromagnetic perturbation from equation (6.3/C.3) including the finite Larmor radius approximation of equation (6.4/C.4). Based on the model from Pueschel et al. [33].

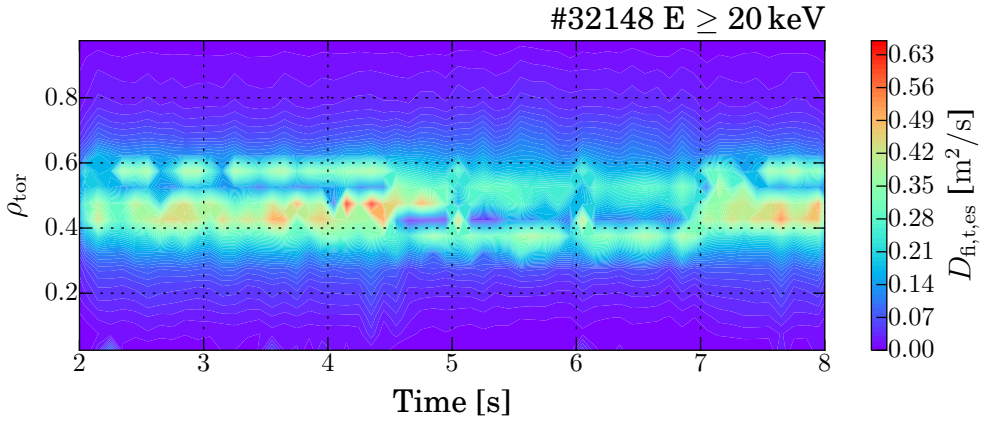

Figure C.10.: $D^{es}_{fi,t}$ Energy averaged anomalous fast ion diffusion coefficient for trapped fast ions by electrostatic perturbation from equation (6.5/C.5). Based on the model from Pueschel et al. [33].

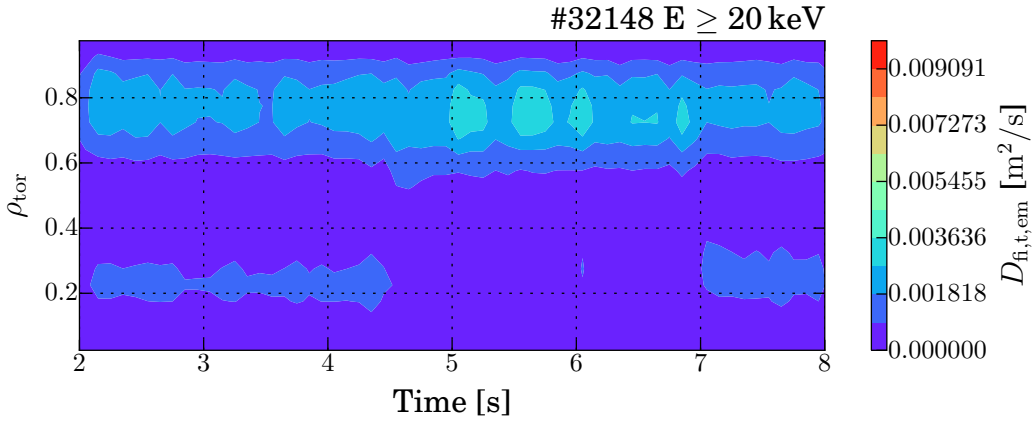

Figure C.11.: $D^{em}_{fi,t}$ Energy averaged anomalous fast ion diffusion coefficient for trapped fast ions by electromagnetic perturbation from equation (6.6/C.6). Based on the model from Pueschel et al. [33].

C.5. Anomalous Diffusion due to Microturbulence in Discharges #18703, #27237 and #28071

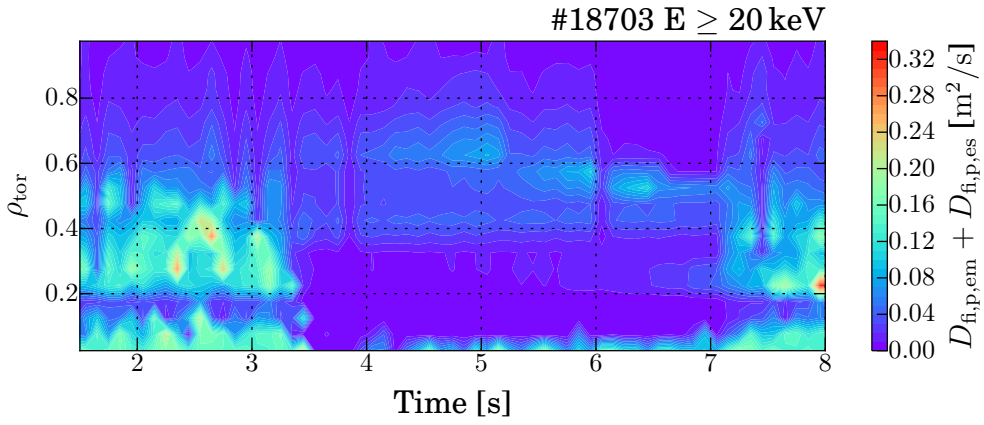

Figure C.12.: Fast ion diffusion coefficients for the passing particle from the equations (6.1) to (6.4) describing the redistribution of fast ions in the plasma due to electrostatic and electromagnetic microturbulence based on [33].

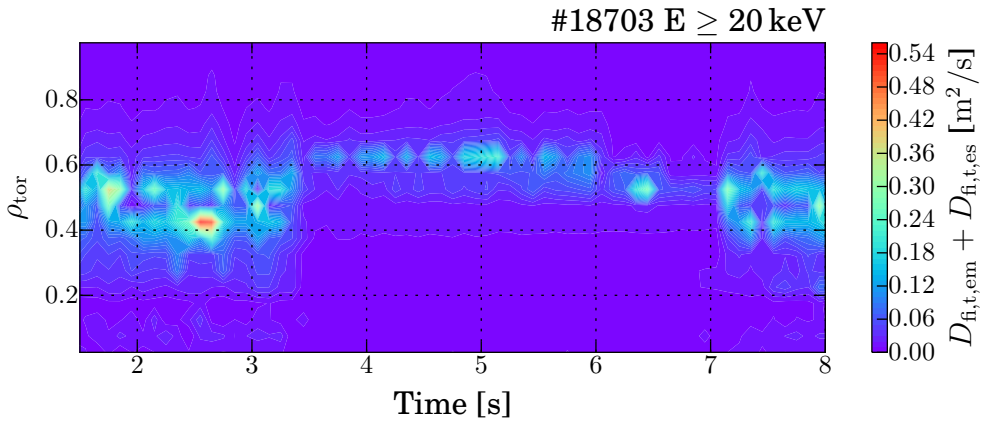

Figure C.13.: Regarding to figure C.12 the fast ion diffusion coefficients for the trapped particle from the equations (6.5) and (6.6).

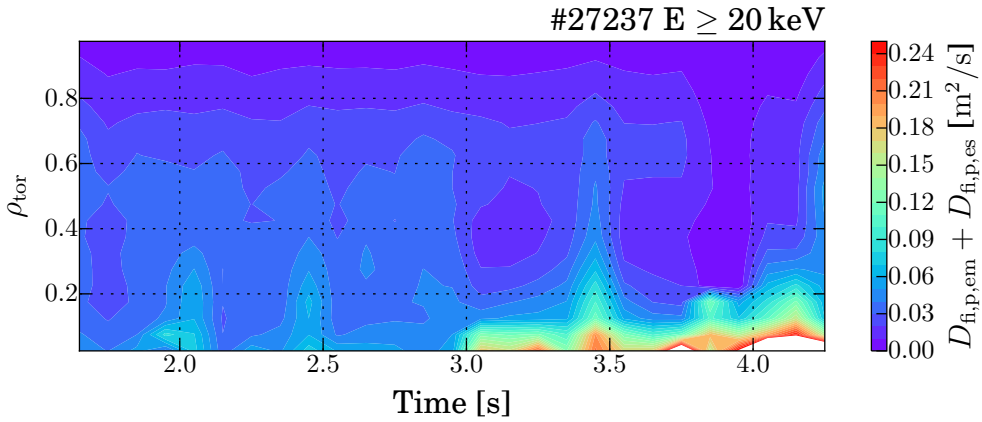

Figure C.14.: Fast ion diffusion coefficients for the passing particle from the equations (6.1) to (6.4) describing the redistribution of fast ions in the plasma due to electrostatic and electromagnetic microturbulence based on [33].

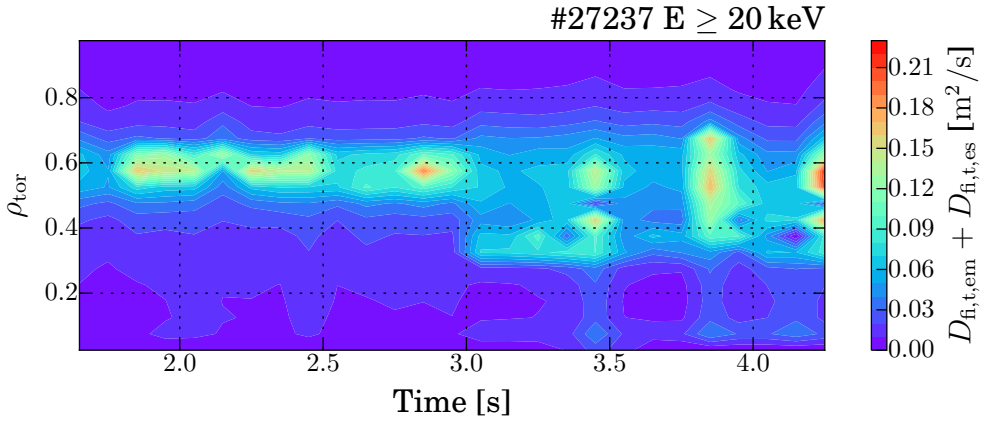

Figure C.15.: Regarding to figure C.14 the fast ion diffusion coefficients for the trapped particle from the equations (6.5) and (6.6).

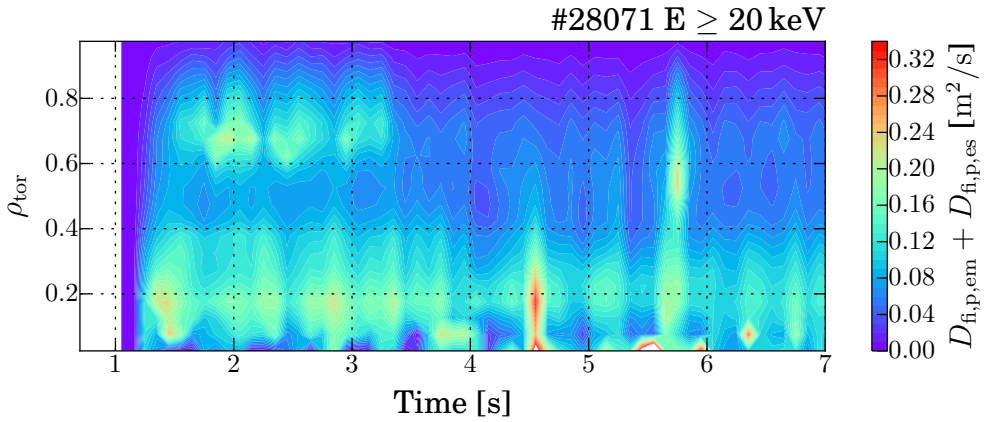

Figure C.16.: Fast ion diffusion coefficients for the passing particle from the equations (6.1) to (6.4) describing the redistribution of fast ions in the plasma due to electrostatic and electromagnetic microturbulence based on [33].

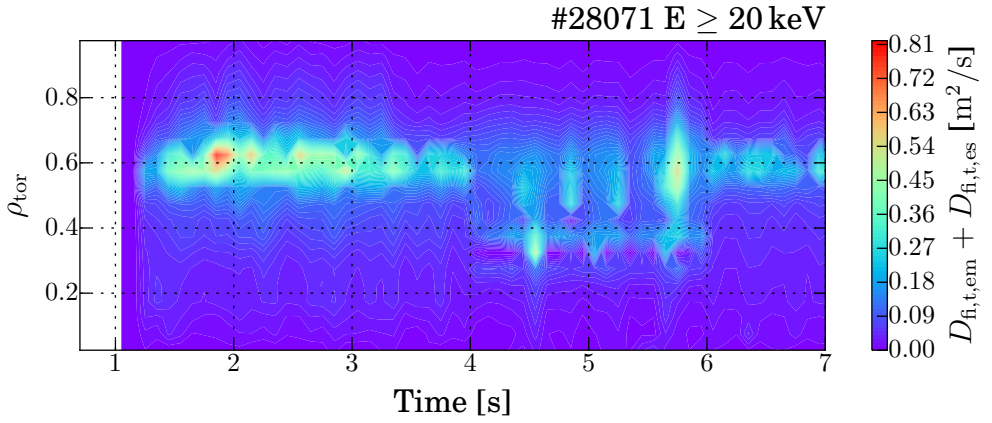

Figure C.17.: Regarding to figure C.16 the fast ion diffusion coefficients for the trapped particle from the equations (6.5) and (6.6).

D. Appendix: Quantitative Investigation of Non-Inductive Current Drive

D.1. Discharge Overview of #33379

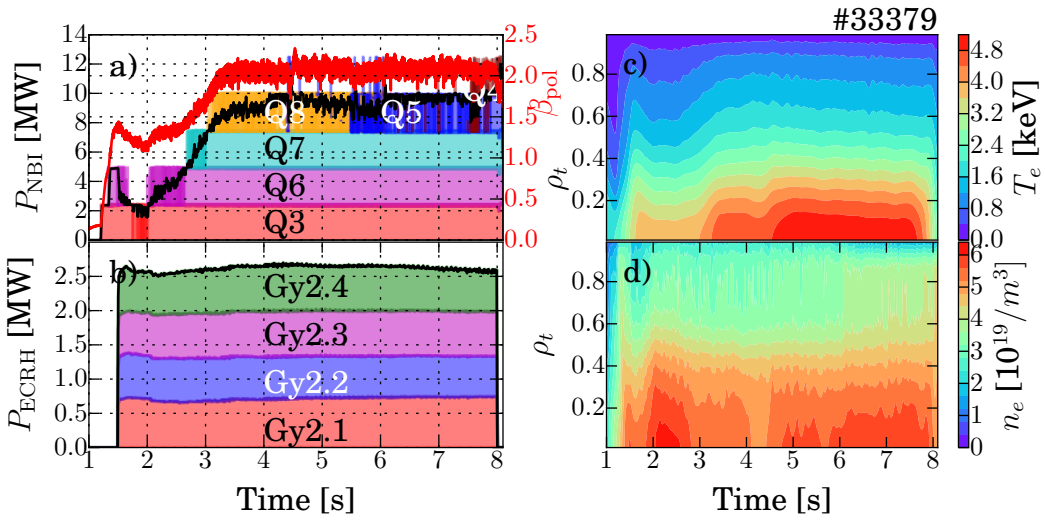

Figure D.1.: Discharge overview, with the neutral beam power and the control parameter β_{pol} in a) and the electron cyclotron resonance heating power in b). In c) the electron temperature and in d) the electron density profiles are shown.

D.2. Current in the Central Solenoid

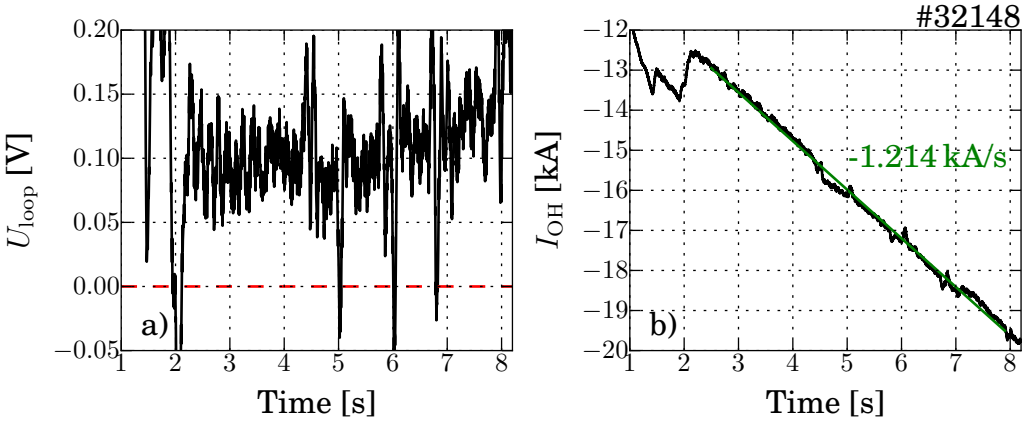

Figure D.2.: In a) the loop voltage measurement and in b) the current in the central solenoid is shown. This discharge got an inductive current fraction in the order of 50% and more, leading to a strongly negative slope in the current of the central solenoid and a loop voltage, above zero.

D.3. Anomalous Fast Ion Diffusion due to Microturbulence in Discharges #33134

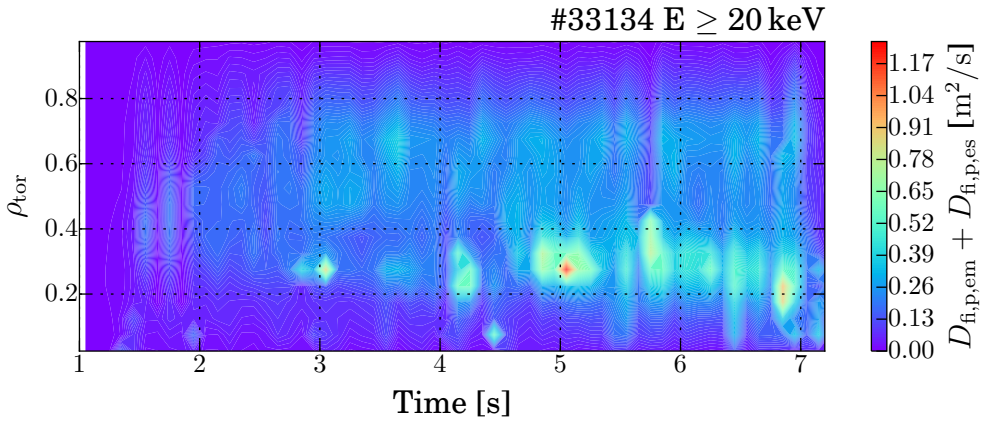

Figure D.3.: Fast ion diffusion coefficients for the passing particle from the equations (6.1) to (6.4) describing the redistribution of fast ions in the plasma due to electrostatic and electromagnetic microturbulence based on [33].

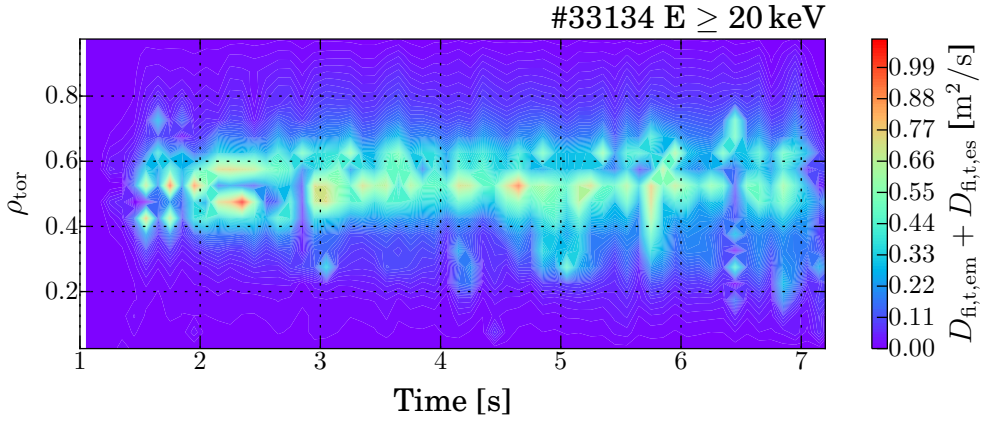

Figure D.4.: Regarding to figure D.3 the fast ion diffusion coefficients for the trapped particle from the equations (6.5) and (6.6).

Acronyms

BS bootstrap current **Section 2.4.4**

CXRS charge exchange recombination spectroscopy **Section 3.3.6**

ECCD electron cyclotron current drive **Section 2.4.3**

ECE electron cyclotron emission **Section 3.3.4**

ECRH electron cyclotron resonance heating **Sections 2.4.3 and 3.2.2**

ELM edge localized mode **Section 2.3 and Reference** [46]

FIDA fast ion D-alpha spectroscopy **Section 3.3.8**

H-mode high confinement mode **Section 2.3**

IDA integrated data analysis **Section 3.3.7**

IDE integrated data equilibrium **Section 2.1.1**

IPP Max-Planck Institut für Plasma Physik

ITER Latin word for "The Way" **References** [8–10]

MHD magnetohydrodynamic **Reference** [57]

MSE motional Stark effect polarimetry **Chapter 4**

NBCD neutral beam current drive **Section 2.4.2**

NBI neutral beam injection **Sections 2.4.2 and 3.2.1**

NTM neoclassical tearing mode **Section 2.5.3**